Technische Universität München

MAX-PLANCK-INSTITUT FÜR QUANTENOPTIK

Chemistry in a quantum medium

Bose polarons, ultracold molecules, and quantum computing

PhD Thesis - Arthur Christianen

Technische Universität München
TUM School of Natural Sciences

Chemistry in a quantum medium

Bose polarons, ultracold molecules, and quantum computing

Arthur Christianen

Vollständiger Abdruck der von der TUM School of Natural Sciences der Technischen Universität München zur Erlangung des akademischen Grades eines

Doktors der Naturwissenschaften (Dr. rer. nat.)

genehmigten Dissertation.

Vorsitz: Prof. Jonathan J. Finley, PhD

Prüfer der Dissertation:
1. Hon-Prof. J. Ignacio Cirac, PhD
2. Prof. Dr. Michael Knap
3. Prof. Dr. Richard Schmidt

Die Dissertation wurde am 31.08.2023 bei der Technischen Universität München eingereicht und durch die TUM School of Natural Sciences am 25.10.2023 angenommen.

Summary

Important processes in chemistry and physics, such as solvation and superconductivity, depend on interactions between particles and their environments. However, most media which particles are naturally immersed into, are too complex for a bottom-up theoretical description. In this thesis, we explore how we can still investigate in-medium processes in a fundamental way. To this end, we study the model system of an impurity atom immersed in a Bose-Einstein condensate (BEC) of ultracold atoms, focusing in particular on chemical processes such as molecule formation. A BEC is the ideal medium in this regard, since it is dilute, controllable and well-characterizable, while still showing non-trivial quantum medium effects.

First, we introduce the relevant concepts of ultracold scattering and the tools of the Gaussian-state variational approach we employ. In this framework, we demonstrate how to describe the ground-state of a weakly-interacting BEC without involving the Born approximation to describe the underlying scattering processes.

We subsequently show how the BEC acts as a "quantum solvent" by dressing the impurity to form a quasiparticle called the Bose polaron. In case of a weakly-interacting BEC, we find that the impurity can trigger a collapse of the surrounding BEC by mediating attractive interactions. This collapse is connected to a three-body scattering resonance of the impurity with two bosons from the BEC, which is shifted due to many-body effects. In presence of explicit repulsion between the bosons, a phase diagram emerges, where the polaronic instability manifests itself as a first-order phase transition ending in a critical point. Beyond this point, the instability is prevented by the interboson interactions and instead there is a smooth crossover between the polaron and a few-body bound state. We show that this phase diagram can be qualitatively captured in an analytical model, and that both the instability and crossover regimes are accessible in realistic experiments. Deep in the crossover regime, we find theoretically and experimentally that the coupling to the BEC triggers the formation of a qualitatively new quasiparticle, which can be described as the coherent superposition of dimer, trimer, and free-impurity states.

The complexity of the medium could be increased by considering ultracold molecules instead of ultracold atoms. However, the molecules themselves already undergo pairwise chemical reactions, making it difficult to bring a gas of ultracold molecules to degeneracy. We have previously proposed that the molecular loss mechanism is the formation of long-lived collision complexes, followed by photoexcitation by the trapping laser. Here we discuss how some experiments confirm the theoretical predictions, while others disagree by orders of magnitude, and we explore possible theoretical explanations for this mystery.

Finally, we consider how we can simulate complex quantum systems on near-term digital quantum computers. Quantum computers should simulate quantum dynamics exponentially more efficiently than classical computers, but current quantum computers suffer from noise and cannot perfectly represent the desired Hamiltonians. Adopting the perspective of Floquet theory, we propose a protocol and an error-mitigation strategy that would allow near-term experiments to observe prethermalization despite these experimental imperfections.

Zusammenfassung

Wichtige Prozesse in der Chemie und Physik, wie Solvatisierung und Supraleitung, hängen von Wechselwirkungen zwischen Teilchen und ihrer Umgebung ab. Die meisten Medien, in die Teilchen natürlicherweise eingebettet sind, sind jedoch zu komplex für eine theoretische Beschreibung von unten nach oben. In dieser Dissertation untersuchen wir, wie wir dennoch in-Medium Prozesse auf fundamentale Weise erforschen können. Zu diesem Zweck untersuchen wir das Modellsystem eines Verunreinigungsatoms, das in einem Bose-Einstein-Kondensat (BEC) von ultrakalten Atomen eingebettet ist, wobei wir uns insbesondere auf chemische Prozesse wie die Molekülbildung konzentrieren. Ein BEC ist in dieser Hinsicht das ideale Medium, da es verdünnt, kontrollierbar und gut charakterisierbar ist, gleichzeitig aber auch nicht-triviale quantenmechanische Effekte im Medium zeigt.

Zunächst stellen wir die relevanten Konzepte der Ultrakaltstreuung und die Werkzeuge des von uns verwendeten Gauß'schen Zustandsvariationansatzes vor. In diesem Rahmen zeigen wir, wie der Grundzustand eines schwach wechselwirkenden BEC beschrieben werden kann, ohne die Born-Approximation zur Beschreibung der zugrunde liegenden Streuprozesse heranzuziehen.

Anschließend zeigen wir, wie das BEC als "quantenmechanisches Lösungsmittel" fungiert, indem es die Verunreinigungspartikel verkleidet, um ein Quasiteilchen namens Bose-Polaron zu bilden. Im Falle eines schwach wechselwirkenden BEC stellen wir fest, dass die Verunreinigung einen Kollaps des umgebenden BEC auslösen kann, indem sie attraktive Wechselwirkungen vermittelt. Dieser Kollaps ist mit einer Dreikörper-Streuungsresonanz der Verunreinigung mit zwei Bosonen des BEC verbunden, die aufgrund von Vielteilcheneffekten verschoben wird. In Anwesenheit von expliziter Abstoßung zwischen den Bosonen entsteht ein Phasendiagramm, in dem sich die polaronische Instabilität als Phasenübergang erster Ordnung manifestiert, der in einem kritischen Punkt endet. Jenseits dieses Punktes wird die Instabilität durch die Wechselwirkungen zwischen den Bosonen verhindert, und stattdessen erfolgt ein sanfter Übergang zwischen dem Polaron und einem gebundenen Zustand mit wenigen Teilchen. Wir zeigen, dass dieses Phasendiagramm qualitativ in einem analytischen Modell erfasst werden kann und dass sowohl die Instabilität als auch die Übergangsregime in realistischen Experimenten zugänglich sind. Tief im Übergangsbereich finden wir theoretisch und experimentell heraus, dass die Kopplung an das BEC die Bildung eines qualitativ neuen Quasiteilchens auslöst, das als kohärente Überlagerung von Dimer-, Trimer- und freien Verunreinigungszuständen beschrieben werden kann.

Die Komplexität des Mediums könnte erhöht werden, indem man statt ultrakalter Atome ultrakalte Moleküle in Betracht zieht. Allerdings unterliegen die Moleküle selbst bereits paarweise chemischen Reaktionen, was es schwierig macht, ein Gas aus ultrakalten Molekülen zur Entartung zu bringen. Wir haben zuvor vorgeschlagen, dass der Verlust von Molekülen durch die Bildung langlebiger Kollisionskomplexe und anschließende Photoanregung durch den Fanglaser verursacht wird. Hier diskutieren wir, wie einige Experimente die theoretischen Vorhersagen bestätigen, während andere um Größenordnungen davon abweichen, und erforschen mögliche theoretische Erklärungen für dieses Rätsel.

Schließlich betrachten wir, wie komplexe Quantensysteme auf digitalen Quantencomputern in naher Zukunft simuliert werden können. Quantencomputer sollten die Quantendynamik exponentiell effizienter simulieren können als klassische Computer, aber gegen-

wärtige Quantencomputer leiden unter Rauschen und können die gewünschten Hamiltonfunktionen nicht perfekt darstellen. Unter Verwendung der Floquet-Theorie schlagen wir ein Protokoll und eine Fehlerausgleichsstrategie vor, die es ermöglichen würden, Prethermalisierung trotz dieser experimentellen Unvollkommenheiten in naher Zukunft zu beobachten.

List of Publications

Included in this thesis

Bose polarons

[1] Arthur Christianen, J. Ignacio Cirac, Richard Schmidt,
Chemistry of a Light Impurity in a Bose-Einstein Condensate,
Physical Review Letters 128, 183401 (2022)

[2] Arthur Christianen, J. Ignacio Cirac, Richard Schmidt,
Bose polaron and the Efimov effect: A Gaussian-state approach,
Physical Review A 105, 053302 (2022)

[3] Arthur Christianen, J. Ignacio Cirac, Richard Schmidt,
Phase diagram for strong coupling Bose polarons,
preprint (2023), arXiv:2306.09075 [cond-mat.quant-gas]

[4] Carsten Robens*, Arthur Christianen*, Alex Y. Chuang, Yiqi Ni, Richard Schmidt, Martin W. Zwierlein,
Superpositions of dimers and trimers formed from Bose polarons,
in preparation, *: equal contributions

Ultracold Molecules

[5] Roman Bause, Andreas Schindewolf, Renhao Tao, Marcel Duda, Xing-Yan Chen, Goulven Quéméner, Tijs Karman, Arthur Christianen, Immanuel Bloch, Xin-Yu Luo,
Collisions of ultracold molecules in bright and dark optical dipole traps,
Physical Review Research 3, 033013 (2021)

[6] Arthur Christianen and Gerrit C. Groenenboom and Tijs Karman,
Lossy quantum defect theory of ultracold molecular collisions,
Physical Review A 104, 043327 (2021)

[7] Roman Bause, Arthur Christianen, Andreas Schindewolf, Immanuel Bloch, Xin-Yu Luo,
Ultracold Sticky Collisions: Theoretical and Experimental Status,
The Journal of Physical Chemistry A 127, 729-741 (2023)

Quantum Computing

[8] Yilun Yang, Arthur Christianen, Sandra Coll-Vinent, Vadim Smelyanskiy, Mari Carmen Bañuls, Thomas E. O'Brien, Dominik S. Wild, J. Ignacio Cirac,
Simulating Prethermalization Using Near-Term Quantum Computers,
PRX Quantum 4, 030320 (2023)

Not included in this thesis

Sorted by order of publication, the publications marked with an asterisk are based on work done before my PhD

[9]* Arthur Christianen, Tijs Karman, Rodrigo A. Vargas-Hernández, Gerrit C. Groenenboom, Roman V. Krems
Six-dimensional potential energy surface for NaK–NaK collisions: Gaussian process representation with correct asymptotic form,
The Journal of Chemical Physics 150, 064106 (2019)

[10]* Arthur Christianen, Tijs Karman, Gerrit C. Groenenboom,
Quasiclassical method for calculating the density of states of ultracold collision complexes,
Physical Review A 100, 032708 (2019)

[11]* Arthur Christianen, Martin W. Zwierlein, Gerrit C. Groenenboom, Tijs Karman,
Photoinduced Two-Body Loss of Ultracold Molecules,
Physical Review Letters 123, 123402 (2019)

[12]* Arthur Christianen, John Sous,
Exploring universal and nonuniversal regimes of trimers from three-body interactions in one-dimensional lattices,
Physical Review A 101, 063610 (2020)

[13]* Taha Selim, Arthur Christianen, Ad van der Avoird, Gerrit C. Groenenboom,
Multi-channel distorted-wave Born approximation for rovibrational transition rates in molecular collisions,
The Journal of Chemical Physics 155, 034105 (2021)

[14] Oriana K. Diessel, Jonas von Milczewski, Arthur Christianen, Richard Schmidt,
Probing molecular spectral functions and unconventional pairing using Raman spectroscopy,
preprint (2022), arXiv:2209.11758 [cond-mat.quant-gas]

[15] Dibyendu Sardar, Arthur Christianen, Hui Li, John L. Bohn,
Four-body singlet potential-energy surface for reactions of calcium monofluoride,
Physical Review A 107, 032822 (2023)

[16]*, Baruch Margulis, Karl P. Horn, Daniel M. Reich, Meenu Upadhyay, Nitzan Kahn, Arthur Christianen, Ad van der Avoird, Gerrit C. Groenenboom, Markus Meuwly, Christiane P. Koch, Edvardas Narevicius,
Tomography of Feshbach resonance states,
Science 380, 77-81 (2023)

[17], Yilun Yang, Arthur Christianen, Mari Carmen Bañuls, Dominik S. Wild, J. Ignacio Cirac,
Phase-Sensitive Quantum Measurement without Controlled Operations,
preprint (2023), arXiv:2308.10796 [quant-ph]

Contents

Summary i

Zusammenfassung ii

List of publications iv

1 Introduction 1
- 1.1 Physics and chemistry in a medium . . . 1
- 1.2 Ultracold gases . . . 2
- 1.3 Chemistry in a quantum medium . . . 5
- 1.4 Bose polarons . . . 6
- 1.5 Ultracold molecules . . . 7
- 1.6 Quantum computing . . . 7
- 1.7 Outline of this thesis . . . 8
- 1.8 Units, notation and conventions . . . 8

A Ultracold scattering and Gaussian states 10

2 Scattering of ultracold atoms 11
- 2.1 Formulation of the scattering problem . . . 11
- 2.2 Ultracold scattering . . . 12
- 2.3 Scattering of alkali atoms and molecules . . . 17
- 2.4 The three-body problem . . . 20
- 2.5 Numerical methods . . . 23

3 Gaussian-state variational approach 26
- 3.1 Coherent states . . . 26
- 3.2 Gaussian states . . . 27
- 3.3 The time-dependent variational principle . . . 31
- 3.4 Equations of motion for Gaussian states . . . 32

4 Gaussian states and Bose-Einstein condensates 35
- 4.1 Introduction . . . 35
- 4.2 Bogoliubov theory . . . 37
- 4.3 Variational optimization . . . 39
- 4.4 Beyond-Gaussian state solution . . . 43
- 4.5 Conclusion and discussion . . . 48

B Bose polarons 50

5 Polaronic instability and shifted Efimov resonance 52
- 5.1 Introduction . . . 52

5.2 Theoretical model . . . 55
5.3 Cooperative binding effect . . . 60
5.4 The Efimov effect and the Bose polaron . . . 68
5.5 Discussion and experimental proposal . . . 74
5.6 Conclusion and Outlook . . . 76

6 Phase diagram for strong-coupling Bose polarons 78
6.1 Introduction . . . 78
6.2 Theoretical and computational methods . . . 79
6.3 Repulsion . . . 83
6.4 Results: Polaronic instability or smooth crossover? . . . 86
6.5 Analytical model . . . 96
6.6 Conclusion and Outlook . . . 103
Appendices . . . 105
6.A Computation of Gaussian integrals . . . 105

7 Dimer-trimer superpositions from Bose polarons 109
7.1 Introduction . . . 109
7.2 Theoretical description . . . 110
7.3 Experimental details . . . 114
7.4 Results . . . 115
7.5 Conclusion/Outlook . . . 119

C Ultracold molecules 120

8 Sticky collisions of ultracold molecules 121
8.1 Introduction . . . 121
8.2 Theory framework . . . 123
8.3 Experimental verification . . . 128
8.4 Testing the theoretical assumptions . . . 130
8.5 Conclusion and outlook . . . 134

D Quantum Computing 136

9 Prethermalization on near-term digital quantum computers 137
9.1 Introduction . . . 137
9.2 The prethermalized expectation value problem . . . 139
9.3 Error mitigation . . . 145
9.4 Summary and outlook . . . 151
Appendices . . . 152
9.A Definition of problems . . . 152
9.B The Magnus expansion . . . 154
9.C Phase- and amplitude-damping noise . . . 155

Outlook 157

Acknowledgments 161

Bibliography 163

Chapter 1. Introduction

1.1 Physics and chemistry in a medium

The properties of particles and objects are strongly influenced by their surrounding environments. We use this to our advantage every day when we are cooking, doing our laundry, or cleaning, but such medium effects are in particular also important in a scientific context. Any organic chemist can tell you that some chemical reactions happen in one medium but not in another, and that a carefully chosen solvent can thus help to efficiently synthesize complex molecules [18, 19]. In turn, any condensed-matter physicist can tell you how classic superconductivity arises from attractive interactions between electrons mediated by excitations of the surrounding crystal lattice [20].

Understanding these medium effects using a bottom-up theoretical description is tremendously challenging, however. Consequently, theorists need to either resort to much simplified models or complex computational techniques, and often both, without a guarantee of success. In practice, this means that solvents for chemical reactions need to be picked empirically via trial and error, with the help of intuition and heuristic models [18, 19]. The same holds for finding superconductors with a high critical temperature [21]. The reason that medium effects are often difficult to model theoretically is that they inherently involve many particles at the same time.

The scenarios where a truly bottom-up description is successful are those with a large degree of experimental control, so that a precise theoretical model can be formulated and tested. Good examples are collision experiments, where people let dilute beams of particles intersect each other in the vacuum. The most famous case is of course the Large Hadron Collider [22–24] at CERN, where the aim is to study the most fundamental properties of nature and to stringently test the predictions of the Standard Model. Collision experiments of atoms and molecules are not as well known [16, 25], but these can similarly challenge modern quantum chemistry. Other excellent examples are the high-resolution spectroscopy experiments on narrow atomic transitions in simple atoms to test quantum electrodynamics [26], and measurements on the dipole moment of the electron using ultracold molecules [27, 28] to constrain physics leading to time-reversal-symmetry breaking. In these cases, the involved particles are brought into complete isolation so that the processes of interest can be studied to extreme accuracy.

The natural question thus emerges whether we can study medium effects while still keeping some of the controllability and cleanliness of these in-vacuum experiments. This seems to be contradictory, since a system being dilute seems to immediately imply that the particles spend most of their time in isolation, hence experiencing no medium effects (at least in a non-relativistic setting where the vacuum is not a medium itself). However, we will see that this is no longer true when gases are cooled to ultracold temperatures.

1.2 Ultracold gases

1.2.1 Quantum degeneracy in solids and gases

The reason that gases behave differently at very low temperatures is the concept of wave-particle duality in quantum mechanics. The crucial parameter here is the De Broglie wavelength

$$\lambda = \frac{h}{p} \approx \frac{h}{\sqrt{mk_BT}}, \tag{1.1}$$

where we used that $\langle p \rangle = \sqrt{mk_BT}$ to relate the momentum to the temperature. When the wave functions of identical particles in a system start to overlap, their quantum statistics (whether the particles are bosonic or fermionic) starts to become important.

Electrons in a metal are already in the degenerate regime at room temperature, with a wavelength of approximately 10 nm and an interparticle distance set by the lattice spacing, which is usually about 0.5 nm. As a result, electrons in a metal behave quantum mechanically, in the simplest case as a Fermi gas.

For atoms in gases to also reach the degenerate regime, much lower temperatures are needed. Since atoms are a factor 10^4-10^5 heavier than electrons, reaching the same de Broglie wavelengths requires them to be as cold as 100 mK. Moreover, even these temperatures are not sufficient, since the interparticle distances in gases are much larger than in solids. The experimentally realized ultracold gases are even much more dilute than air, and have typical interparticle distances on the order of 200 nm. A quick computation thus tells us that the temperature needs to go down to about 100 nK to reach a similar wavelength-to-distance ratio as the case of electrons in solids.

How atoms will behave in the degenerate regime depends on their quantum statistics, which is in turn determined by their total number of electrons and nucleons. If the sum of the number of electrons and the number of nucleons is even, the atom is a boson, and otherwise it is a fermion. This implies that suddenly the isotope of the atom starts to play an important role, in contrast to the generic case in chemistry and condensed matter, where the isotopes usually do not matter very much.

1.2.2 Reaching the degenerate regime

For most chemical species, and under usual conditions, cooling a gas to low temperatures leads to a phase transition to a liquid or solid state. However, studies of the formation of rain droplets in the atmosphere teach us that the spontaneous nucleation of water droplets is very slow, and that rain-droplet formation is usually triggered due to the presence of preformed nucleation centers such as dust particles [29]. If a gas is therefore cooled in absence of such nucleation centers, and if spontaneous cluster formation due to multi-particle collision processes is suppressed, liquid droplets or clusters are very unlikely to form.

Here enters the technique of laser cooling [30, 31]. This method was first proposed in 1975 [32], and uses the concept of radiation pressure to slow atoms down. The general idea is to use the Doppler effect to always exert this radiation pressure on the atoms in the direction in which they are moving, ultimately bringing the atoms almost to a standstill. This technique works on the single-atom level, and therefore does not trigger any droplet formation. Without special tricks, the ultimate limit to laser cooling is the recoil limit, set by the momentum that a single photon imparts on an atom which is standing still. The temperature scale that can usually be reached with laser cooling is on the order of

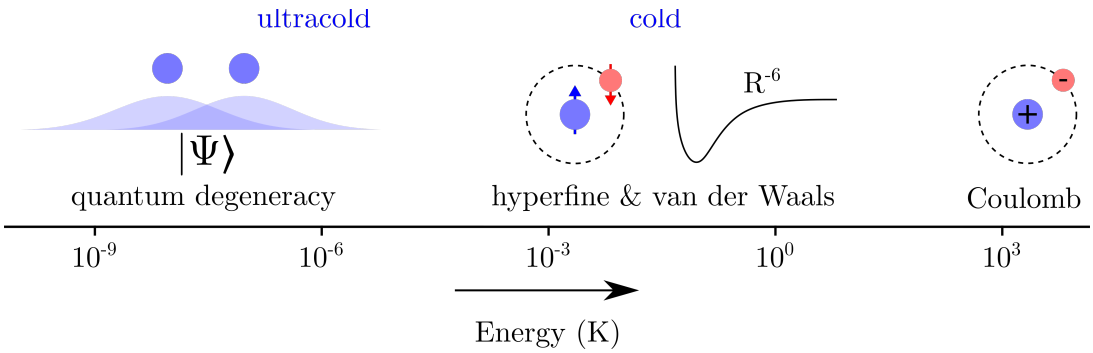

Figure 1.1: Energy scales in atoms and ultracold gases in terms of the equivalent temperature in kelvin. The Coulomb interactions inside atoms or molecules are very strong and take place on the order of more than 1000 K. The typical energy scales associated with van der Waals interactions between neutral atoms, and hyperfine interactions inside atoms, range from 1mK to 1K. Atomic and molecular collisions in this regime are called "cold". Even lower energy collisions are referred to as "ultracold". Quantum degeneracy occurs when the de Broglie wavelength of the particles becomes comparable to the interparticle distance (for simplicity, only the nuclei are shown in the picture). This typically occurs in the temperature regime from 1 nK-1 μK.

microkelvins. Hence, this brings the system close to but not quite into the degenerate regime.

Once atoms are this cold they can also be trapped by laser light, in optical dipole traps [33]. These are based on a different concept than laser cooling, namely that atoms are polarized by the electromagnetic field of light. As a result, the intensity profile of the laser forms a potential for the atoms. In the typical scenario, the laser is far red-detuned with respect to atomic transitions, so that the energy of the atoms is lowered in presence of the laser light. By creating a standing wave of the laser, one can also create so-called optical lattices for the atoms. Atoms trapped in optical lattices are often used as "quantum simulators" which natively implement the paradigmatic Hubbard model from condensed-matter physics [34, 35].

To cool the system beyond the recoil limit, evaporative cooling can be applied [36]. The idea of evaporative cooling is simple: if one by one the hottest atoms disappear, the remaining gas becomes colder and colder. To achieve this, the depth of the trapping potential is slowly lowered so that the atoms with the highest energy can escape. Crucial here is that the remaining atoms rethermalize, and therefore it is important that there are collisions between the particles, and that these collisions do not lead to loss. There is no limit to the temperatures that can be reached via evaporative cooling other than the number of atoms or other mechanisms that lead to heating. Indeed, temperatures far below a nanokelvin have been reached [37, 38].

The atoms traditionally used for these experiments are alkali atoms, since they have a simple electronic structure amenable to laser cooling. The ground-state phases of matter of these atoms are metallic solids. Nevertheless, ultracold gases can be long-lived, since pairwise collisions between atoms in their ground-states are always elastic and therefore no energy can be released. Only higher-order collision processes can trigger the formation of bound clusters. These processes are suppressed due to the low densities, but they can still in the end be limiting factors to the lifetime of an ultracold gas, see Sec. 2.4.1.

Before moving on, it is instructive to compare the temperature of these ultracold gases with the internal energy scales of the atoms, depicted in Fig. 1.1. The electronic ener-

gies and energy gaps inside the atoms are of 1000s of kelvins and the electrons therefore already behave quantum mechanically on these energy scales. The first quantum effects in the nuclear motion are usually only observed at temperatures lower than 1 kelvin. In this regime, the wavelengths of the atoms are similar to the range of the van der Waals interactions, meaning that atomic collisions start to have quantum features. Collisions in this regime are referred to as "cold" and this is the typical temperature regime where molecular-beam experiments operate which aim to study the fundamentals of chemistry [16, 25, 39, 40]. This is also the energy scale of the coupling between the nuclear spins and the electronic spins, leading to the hyperfine structure of the atoms. In chemistry the hyperfine structure is usually not important, but if the atoms are cooled to "ultracold" (below 1 mK) temperatures, even this energy scale becomes orders of magnitude larger than the translational energy. This shows that somehow these ultracold gases are a very unnatural state of matter, where the kinetic energy of the atoms is orders of magnitude smaller than any of their natural energy scales.

1.2.3 Bose-Einstein condensation

When bosons are cooled to ultracold temperatures they form a *Bose-Einstein condensate* (BEC). Other than fermions, bosons do not obey the Pauli principle and they can therefore all occupy the same energy level. Indeed, the definition of a BEC is that a single-particle eigenstate of the system is occupied by a macroscopic number of particles. This remarkable phase of matter was observed for the first time only in 1995 [41, 42], in a system of ultracold atoms. Excellent reviews on BECs are given in Refs. [43, 44]. Here we will summarize the key characteristics.

The phase transition of Bose-Einstein condensation can be described relatively simply in a thermodynamic framework if we take into account the Bose-Einstein statistics of the particles [45]. In a grand-canonical ensemble the average population $\bar{n}_i$ of a single-particle energy level ϵ_i of a bosonic system is given by

$$\bar{n}_i = \frac{1}{\exp[(\epsilon_i - \mu)/k_B T] - 1}. \tag{1.2}$$

We can now set the chemical potential μ so that $\sum_i \bar{n}_i = N$, and take $\epsilon_0 = 0$, with $\epsilon_{i\neq 0} > \epsilon_0$. In this case $\mu < 0$. Now we consider what happens when $\mu \to 0^-$ and $|\mu| \ll \epsilon_1$. In this case the number of particles in the excited states N_{ex} is only dependent on the temperature.

$$N_{ex} = \sum_{i>0} \frac{1}{\exp(\epsilon_i/k_B T) - 1}. \tag{1.3}$$

If $N_{ex} < N$ this is consistent and the remaining particles are in the condensate mode, if $N_{ex} > N$, the chemical potential must deviate from 0. Therefore the condition that $N_{ex} = N$ sets the critical temperature for the phase transition. For a three-dimensional harmonic oscillator, in the case of large particle number, one finds

$$N_{ex} = \zeta(3)\Big[\frac{k_B T}{\hbar\omega}\Big]^3, \tag{1.4}$$

where $\omega = (\omega_x\omega_y\omega_z)^{1/3}$ and ζ is the Riemann zeta-function. This expression can simply be translated into a critical temperature

$$k_B T_C = 0.94\hbar\omega N^{1/3}. \tag{1.5}$$

Remarkable here is the presence of $N^{1/3}$ in the expression. One might naively expect that condensation happens when the kinetic energy of the particles $k_B T$ becomes comparable

to the harmonic oscillator energy $\hbar\omega$, but the physics is not so simple, it is truly a collective phenomenon following from the bosonic statistics of the particles.

Interactions also play a key role in BECs, but we postpone this discussion until Chapter 4, where this will be addressed in detail.

1.3 Chemistry in a quantum medium

Having discussed the degenerate regimes that ultracold atoms reach when cooled to ultracold temperatures, we now move to the main topic of this thesis: "Chemistry in a quantum medium". By now we have encountered our quantum medium, but where does the chemistry come in?

Let us for now adopt the chemistry perspective, and consider the BEC as a solvent in which we immerse a solute. As a solute, we simply take an atom of a different kind. Such a system can be realized by making a density-imbalanced mixture of ultracold atoms of different chemical species, or by transferring some of the medium atoms to a different internal state.

It is well known in chemistry that when a particle is dissolved, it locally deforms the medium around itself, forming a so-called solvation layer. The typical example is the case of table salt dissolved in water, where the dipolar water molecules reorient themselves to have favorable charge-dipole interactions with the sodium and chloride ions. This distinguishes a solution from a mixture of (non-degenerate) gases for example, because the gases do not reorganize themselves on a microscopic level. The question is now whether and how a "solvation layer" manifests itself in a BEC.

It turns out that indeed, the BEC is locally deformed around the solute atom, which we will call "impurity" in the following. If the impurity-boson interactions are attractive then the density of the BEC is locally enhanced around the impurity, and when the effective interactions with the BEC are repulsive, the density of the condensate close to the impurity is decreased. The correlations between the impurity and the BEC atoms, and the correlations the impurity mediates in the BEC, are qualitatively depicted in Fig. 1.2

Aside from the formation of the solvation layer, there are two actual chemical processes which the impurity can undergo. The first one we have already implicitly mentioned, and is called three-body recombination. This process involves the impurity simultaneously scattering with two particles from the condensate. One of the particles can then form a deeply bound molecule with the impurity, and the third particle can take away the released energy. This process leads to loss from the trap of all of the involved particles. The second chemical process is less detrimental and often actually desired: the controlled formation of weakly bound Feshbach molecules. This can be achieved by magnetically or optically changing the interaction strength between the impurity and the bath, and transferring the system from a free state to a bound state between a boson and the impurity. In this case there is no third atom involved, and there is no large release of potential energy. Both of these processes can be studied both in a thermal gas, so in absence of medium effects, and in a BEC. This would allow us to clearly distinguish these cases, and to truly observe how medium effects are manifested in such a degenerate quantum gas.

What do we gain from studying in-medium chemistry in such a degenerate gas? Well, firstly we now have a medium which we can describe up to controllable approximations from the first principles of quantum mechanics. A simpler state than a BEC from the theory perspective does barely exist, because almost all particles occupy the same single-particle eigenstate and there are only weak correlations. Furthermore, we can work to good approximation at zero temperature, avoiding the complications which arise at finite

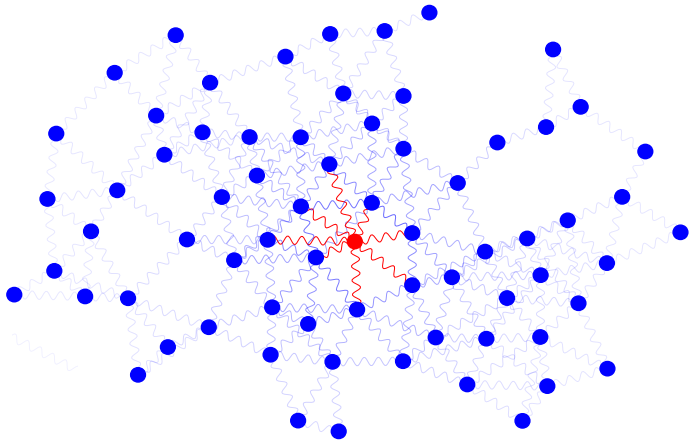

Figure 1.2: Illustration of the correlations that the impurity atom induces inside a weakly-interacting Bose-Einstein condensate.

temperature. Thus, even though we will need to invoke more approximations to solve the Hamiltonian for the quantum-impurity problem, our starting point is now at least from the principles of quantum mechanics. This is unheard of when describing the molecular dynamics for chemical reactions in liquid solvents. Moreover, we will discuss below how the way the impurity is dressed by the BEC is strongly reminiscent of condensed-matter physics, allowing us to create novel connections between the phenomena from chemistry and from many-body physics. Finally, experiments on ultracold gases give us unique ways to probe the quantum states of the formed molecules in a way that is impossible in traditional chemistry.

1.4 Bose polarons

To truly appreciate the effect the background BEC is having as a quantum solvent we need to introduce some concepts from condensed-matter physics. Indeed, the way in which the impurity distorts the background BEC is conceptually different from the conventional case of a solute immersed in water. In our case the impurity namely deforms the BEC coherently, forming a quasiparticle called the Bose polaron.

The concept of a polaron was originally coined by Landau [46] in 1933 to describe the motion of electrons in an ionic lattice, where the electron polarizes and locally deforms the crystal lattice around itself. In this case the electron is also dressed by bosonic excitations of the environment, namely phonons. A paradigmatic theoretical model to describe this system was introduced by Fröhlich [47]. In its simplest form, the model Hamiltonian can be written as

$$\hat{\mathcal{H}} = \frac{\hat{P}^2}{2M} + \sum_{\boldsymbol{k}} \omega_{\boldsymbol{k}} \hat{b}^\dagger_{\boldsymbol{k}} \hat{b}_{\boldsymbol{k}} + \int_{\boldsymbol{k}} V_{\boldsymbol{k}} e^{i\boldsymbol{k}\hat{\boldsymbol{R}}} (\hat{b}^\dagger_{\boldsymbol{k}} + \hat{b}_{\boldsymbol{k}}). \tag{1.6}$$

Here the impurity of mass M is described in first quantization with position and momentum operators $\hat{\boldsymbol{R}}$ and $\hat{\boldsymbol{P}}$, and the bosonic excitations with dispersion $\omega_{\boldsymbol{k}}$ with creation and annihilation operators $\hat{b}^\dagger_{\boldsymbol{k}}$ and $\hat{b}_{\boldsymbol{k}}$. The third term in the expression describes how the impurity can create or destroy excitations in the medium with momentum-dependent coupling $V_{\boldsymbol{k}}$.

Tempere *et al.* [48] showed that the Bose polaron Hamiltonian describing an impurity in a BEC has exactly this structure for weak interactions. They proposed that the cold-

atom system could serve as a quantum simulator for interesting strong-coupling physics predicted in the Fröhlich model which could not directly be realized in solids.

However, it turned out that at strong coupling the polarons in ultracold gases behave rather differently than electrons in a solid. In particular, the Fröhlich model only allows the impurity to create and destroy excitations from the bath, but not to actually interact with them [49]. In the cold-atom case these interactions with the excitations from the medium are crucial at strong coupling: this can even lead to the formation of molecules! Therefore the different behavior from the electron-phonon case is not so surprising, because bound-state formation is unusual between electrons and phonons.

Still the general condensed-matter picture that the impurity forms a Bose polaron quasiparticle persists and it is thus intriguing to ask how this affects the chemical processes and the molecules which can be formed. We will highlight in this thesis that these chemical processes in a quantum medium show qualitatively new, and interesting phenomena, which are accessible in realistic experiments.

1.5 Ultracold molecules

When discussing chemistry at ultracold temperatures one cannot leave out a discussion about ultracold molecules [39, 40, 50, 51]. From the viewpoint of chemistry, cold and ultracold molecules offer exciting possibilities to tune the outcomes of reactions with external fields, and to prepare the reactants and image the products in a quantum-state specific way. Indeed, several kinds of ultracold molecules have now been realized in the lab.

In the light of our discussion, a natural thought would be to use ultracold molecules instead of ultracold atoms as our impurity or as our medium. This takes us one step closer to the complexity of real chemical systems. Unfortunately, reaching the degenerate regime has proven to be very challenging for molecules, because they can undergo chemical reactions upon collision, preventing the use of evaporative cooling. For some molecules such reactions should be expected, since rearrangement reactions are predicted to be allowed [52]. However, even molecules for which these reactions are forbidden seem to disappear every time they collide [7]. The mechanism by which these molecules disappear is still not understood. Naturally, before considering in-medium chemistry in this case, we should first understand the chemical reactions between the individual particles, and be able to make such a medium.

A proposed mechanism for the molecular loss is that molecules stick together upon collision and form long-lived collision complexes [10, 53, 54], which can subsequently be destroyed by the laser light of the optical dipole trap [11]. In Chapter 8 of this thesis we will discuss the seemingly contradictory experiments probing these phenomena, along with potential theoretical explanations for some of these effects. Even though we do not consider medium effects here, still the ultracold nature of the collisions turns out to be crucial, and other interesting connections to many-body physics show up.

1.6 Quantum computing

So far we have discussed ways to construct model systems where we can study chemistry in a medium with a bottom-up theoretical approach, by considering chemistry in a Bose-Einstein condensate. However, instead of reducing the complexity compared to real-life settings, we can also increase the capabilities of our computers, so that we are able to deal with more complex simulations. This is very challenging if we are interested in simulating

quantum systems, since in this case the computational cost for classical computers increases exponentially with the number of involved particles, both in memory and time.

Feynman proposed to resolve this issue by creating computers which themselves are making use of quantum mechanics: using "quantum computers" to simulate quantum systems [55, 56]. In the last decades there has been rapid progress in this direction, and indeed it has been shown that for some tasks quantum simulators can already outperform classical computers [57]. Unfortunately, quantum computers suffer from decoherence and noise, which introduce errors in the computations [58]. So far, this has prevented us to solve important open problems using quantum computers.

There is a large ongoing effort to reduce the noise and create fault-tolerant quantum computers, using the principles of quantum error correction, but this is expected to still take a long time. Instead, another direction of research is to see if we can still find applications for today's "noisy intermediate-scale quantum" computers [58]. In Chapter 9 of this work, we study how to extract thermodynamic properties of condensed-matter models from near-term quantum computers.

1.7 Outline of this thesis

To summarize, aside from this introduction this thesis consists of four parts, which are again subdivided into chapters.

Part A serves to give an in-depth introduction into the concepts and methods being used later in the thesis. In Chapter 2 we will discuss the topic of ultracold scattering, which is crucial to gain a deep understanding of the physics of ultracold gases. Furthermore, in Chapter 3 we will introduce the methodology of the variational approach with bosonic Gaussian states used in Chapter 4 and Part B. Then, as a starting point for the further discussions, we will study how scattering processes manifest themselves in weakly interacting BECs, as describes by Gaussian states. We present a novel approach for deriving the quantum corrections in BECs, in particular focusing on the explicit use of finite-range potentials. This chapter is based on a manuscript in preparation.

Part B consists of three chapters all devoted to Bose polarons. This is the core of this thesis, and describes the work of Refs. [1–4]. In Chapter 5 we introduce the new concept of a polaronic instability caused by three-body correlations. In Chapter 6 we develop a unified model for the ground state of the Bose polaron problem across a wide range of parameter regimes. In Chapter 7 we describe the formation of coherent dimer-trimer superpositions in a BEC, in collaboration with the experimental group of Martin Zwierlein.

Part C only contains a single chapter, Chapter 8, which describes the recent developments in the field of sticky collisions of ultracold molecules, and contains content from Refs. [5–7]. The introduction of this chapter also describes work done before my PhD in Refs. [10, 11].

Chapter 9 (Part D) is based on Ref. [8], where we propose how the phenomenon of prethermalization, combined with error mitigation, allows one to do interesting experiments on near-term digital quantum computers.

The thesis concludes with an outlook and acknowledgments.

1.8 Units, notation and conventions

Throughout this thesis we will use atomic units in equations unless mentioned otherwise. Hence, we set $\hbar = 1$, the elementary charge $e = 1$, the Coulomb constant $(4\pi\epsilon_0)^{-1} = 1$

and the electron mass $m_e = 1$. We follow literature conventions for the units in which we express our variables in the text and figures.

We will indicate operators with hats $\hat{O}$, vectors using boldface $\boldsymbol{v}$, and we usually (but not always) write matrices as captial letters. Furthermore, we denote three-dimensional integrals over position and momentum as

$$\int_{\boldsymbol{r}} = \int d^3r, \tag{1.7}$$

$$\int_{\boldsymbol{k}} = \frac{1}{(2\pi)^3} \int d^3k. \tag{1.8}$$

We have chosen to absorbe the factors $\frac{1}{(2\pi)^3}$ from Fourier transforms fully into the momentum integrals.

Part A. Ultracold scattering and Gaussian states

Abstract

The dynamics of ultracold gases is to a large degree governed by the scattering properties of the constituent atoms or molecules. In Chapter 2 we introduce the most important concepts of two-body scattering at ultracold temperatures, such as the scattering length, universality, and Feshbach resonances. We also extend the discussion to three-body physics and introduce the chemical reaction of three-body recombination and the three-body universal phenomena described by the Efimov effect.

In Chapter 3 we introduce the bosonic Gaussian-state framework for the purpose of variational calculations. We explain how to compute expectation values and we derive the equations of motion for imaginary-time evolution.

In Chapter 4 we apply the Gaussian-state framework to derive quantum corrections in BECs, as an illustrative example of how a Gaussian state can incorporate pairwise scattering processes in a BEC. Quantum corrections in BECs have drawn recent attention, because they can stabilize Bose-Bose mixtures or dipolar condensates against collapse, leading to the formation of exotic phases such as quantum droplets or supersolids. Here we show how to recover the first-order quantum corrections in the variational Gaussian-state framework, focusing explicitly on finite-range interactions. The Gaussian-state description correctly renormalizes the mean-field energy, but it fails to reproduce the expression of the beyond-mean-field terms. We show that this can be resolved by extending the Gaussian-state Ansatz to also include triplets of excitations.

Chapter 2. Scattering of ultracold atoms

2.1 Formulation of the scattering problem

Let us consider the scattering process of two particles in a three-dimensional, non-relativistic setting. In the center-of-mass frame of the particles, the Hamiltonian for such a process is given by

$$\hat{\mathcal{H}} = \hat{\mathcal{H}}_1(\{\hat{O}_1\}) + \hat{\mathcal{H}}_2(\{\hat{O}_2\}) - \frac{1}{2\mu_r R}\frac{\partial}{\partial R^2}R + \frac{\hat{L}^2}{2\mu_r R^2} + V(R, \{\hat{O}_1\}, \{\hat{O}_2\}). \tag{2.1}$$

Here $\hat{\mathcal{H}}_i$ is the Hamiltonian for particle i, which depends on a set operators $\{\hat{O}_i\}$ acting on the internal degrees of freedom of that subsystem. The third and fourth term describe the kinetic energy with respect to the radial and angular motion respectively, where R is the distance between the particles, μ_r is the reduced mass of the system, and $\hat{L}$ is the angular momentum operator.

In case of atomic or molecular collisions it is standard to take the Born-Oppenheimer equation and describe the motion of the nuclei as adiabatic from the electronic perspective. We therefore assume that the electrons always occupy their motional ground state for the instantaneous nuclear positions. In this case the Hamiltonian (2.1) applies to the scattering of the nuclei, with an interaction potential V determined by the electronic energy for the given nuclear geometry.

We can then express the eigenstates of this Hamiltonian in terms of a basis of eigenstates of the non-interacting Hamiltonian ($V = 0$). These are the simultaneous eigenstates of $\hat{\mathcal{H}}_1$, $\hat{\mathcal{H}}_2$, and $\hat{L}$, which are typically referred to as "channels". Thus, the wave function can be written as

$$\langle R|\psi\rangle = \frac{1}{R}\sum_{\alpha\beta lm} \psi_{\alpha\beta,lm}(R)|\alpha,\beta;l,m\rangle, \tag{2.2}$$

where α and β label the eigenstates of $\hat{\mathcal{H}}_1$ and $\hat{\mathcal{H}}_2$ respectively, and l and m indicate the typical angular momentum quantum numbers. Now we bundle the labels for the initial and final states as $i = (\alpha_i, \beta_i, l_i, m_i)$ and $f = (\alpha_f, \beta_f, l_f, m_f)$ respectively. For initial scattering channel i, the asymptotic scattering wave function takes the form

$$\psi_i(R \to \infty) = R\big[h^{(2)}_{l_i}(k_i R) + \sum_f h^{(1)}_{l_f}(k_f R) S_{fi}\big]. \tag{2.3}$$

Here $h^{(1)}$ and $h^{(2)}$ are spherical Hankel functions of the first and second kind, which describe the outgoing and ingoing spherical waves, respectively. The S-matrix describes the phase and amplitude of the wave function in the outgoing channels. In absence of loss-mechanisms, the S-matrix is unitary, so that the norm of the wave function is conserved during the scattering process. For the non-interacting problem, the exact regular solutions of the Schrödinger equation are spherical Bessel functions $j_l(kR) = h^{(1)}_l(kR) + h^{(2)}_l(kR)$. Therefore, if $S = \mathbb{I}$, the ingoing wave function is (at least asymptotically) completely unaffected by the scattering process. More generally, the diagonal elements of S describe *elastic* collisions, where the collision channel does not change. However, the scattering

wave function can still undergo some phase shift δ_l, which is related to S via $S_l = e^{2i\delta_l}$. The off-diagonal elements of S describe the probability amplitudes for inelastic collisions.

From the S-matrix one can compute the collision cross section σ via

$$\sigma_{i\to f} = \frac{\Delta\pi}{k_i^2}|1 - S_{fi}|^2. \tag{2.4}$$

Here $\Delta = 1$ for distinguishable particles and $\Delta = 2$ for indistinguishable particles. This factor compensates for the fact that for indistinguishable particles half of the partial waves are forbidden due to the exchange symmetry. Identical bosons can only scatter with even l and identical fermions can only scatter with odd l. From the collision cross section one can compute the collision rate coefficient

$$\beta_{i\to f} = \langle \sigma_{i\to f} v \rangle, \tag{2.5}$$

as an average over the distribution of relative collision velocities v.

For elastic collisions one can express the collision cross section in terms of the phase shift as

$$\sigma_l(k) = \frac{(2l+1)4\pi\Delta \sin(\delta_l)^2}{k^2}. \tag{2.6}$$

Here we have assumed the scattering cross section is independent of m, which is true in absence of external fields. The factor $2l + 1$ follows from summing over these different m-contributions.

2.2 Ultracold scattering

2.2.1 Wigner threshold laws

Let us now consider elastic, single-channel scattering processes at very low temperatures. Important insight was already obtained by Wigner by studying collisions at exactly $E = 0$ [59, 60]. In this case, the Schrödinger equation which the scattering wave function obeys outside the range of the potential simply reads

$$-\frac{1}{2\mu_r}\frac{\partial^2}{\partial R^2}\psi(R) + \frac{l(l+1)}{2\mu_r R^2}\psi(R) = 0. \tag{2.7}$$

From solving this equation we find that $\psi(R)$ needs to be of the form

$$\psi(R) = AR^{l+1} + BR^{-l}. \tag{2.8}$$

For comparison, we can rewrite Eq. (2.3) in terms of spherical Bessel functions. Up to some prefactor, this gives

$$\psi(R) = R\big[j_l(kR) - \tan(\delta_l) y_l(kR)\big], \tag{2.9}$$

$$\approx R\big[(kR)^l - \tan(\delta_l)(kR)^{-l-1}\big], \tag{2.10}$$

where in the second line we have taken the dominant terms in the limit of $kR \to 0$. Given that Eq. (2.10) should smoothly connect to Eq. (2.8), we find that the phase shift needs to obey

$$\tan(\delta_l) \sim k^{2l+1}. \tag{2.11}$$

For small k, $\tan(\delta_l) \approx \sin(\delta_l)$, and we can thus insert this into Eq. (2.6), resulting in

$$\sigma \sim (2l+1)4\pi\Delta k^{4l}. \tag{2.12}$$

This simple formula has drastic consequences. It immediately implies that for $k \to 0$, the collision cross section for $l > 0$ is strongly suppressed. This is simple to understand qualitatively because for $l > 0$ the kinetic energy associated with the rotational motion, $\frac{l(l+1)}{2\mu_r R^2}$, forms a barrier in the long range of the effective radial potential (the centrifugal barrier). The lower the energy of the collision, the smaller the probability that the colliding particles tunnel through this barrier to reach the short-range region of the collision. For $l = 0$ there is no centrifugal barrier, and the collision cross section approaches a constant value of

$$\sigma_0 = 4\pi\Delta a^2. \tag{2.13}$$

The parameter a is called the *scattering length*. The scattering length is an important parameter which will come back throughout this thesis and which quantifies the effective interaction strength between the scattering particles. Note that even though the collision cross section is constant in the low-energy limit, the collision rate still depends on the temperature. That is because the average collision velocity in Eq. (2.5) strongly decreases as a function of temperature.

Going beyond the scattering length, one can systematically expand the s-wave phase shift in terms of the scattering momentum. This gives rise to the so-called *effective range expansion*

$$k\cot(\delta_0) = -\frac{1}{a} + \frac{r_{\text{eff}}k^2}{2} + \mathcal{O}(k^4). \tag{2.14}$$

Here r_{eff} is the effective range, describing the first momentum dependent term for the low-energy scattering process. In most cases, r_{eff} is similar to the range of the interaction potential. This implies that for ultracold collisions $|r_{\text{eff}}k| \ll 1$, and that the scattering cross section becomes momentum independent in the relevant range of momenta.

Note that for identical fermions the lowest allowed partial wave has $l = 1$. This implies that fermionic collision rates are strongly suppressed at ultracold temperatures. As a result, ultracold fermionic gases are usually to good approximation non-interacting. Another consequence is that evaporative cooling does not work well for a gas of identical fermions, since there are no collisions which lead to efficient thermalization.

2.2.2 Scattering length

From the formula of the collision cross section (Eq. (2.13)) it is clear that the s-wave scattering length parameterizes the effective "size" of the scattered object, which reflects the effective interaction strength. The scattering length also has a direct impact on the shape of the wave function. Inserting Eq. (2.14) in Eq. (2.10) namely gives us

$$\psi(R) \sim R - a. \tag{2.15}$$

We show some illustrative examples of low-energy scattering wave functions in Fig. 2.1. From left to right, the figures show the cases of $a = 0$, $a > 0$, $a \to \infty$, and $a < 0$ for a collision of ^{23}Na with ^{40}K at a collision energy corresponding to $3\mu K$. The blue curves indicate the wave function in the open scattering channel, whereas in red the wave function contributions from the closed channels are shown, which will be discussed in more detail below.

When $a = 0$ the asymptotic scattering wave function perfectly resembles the solution of the non-interacting problem. The potential sits at the minimum of the wave function amplitude, also indicating that its impact will be minimal. In the opposite case of $a \to \infty$, the potential sits at the peak of the amplitude of the long-range wave function, showing this gives rise to the strongest interaction strength. In fact, the point where $a = \infty$ is

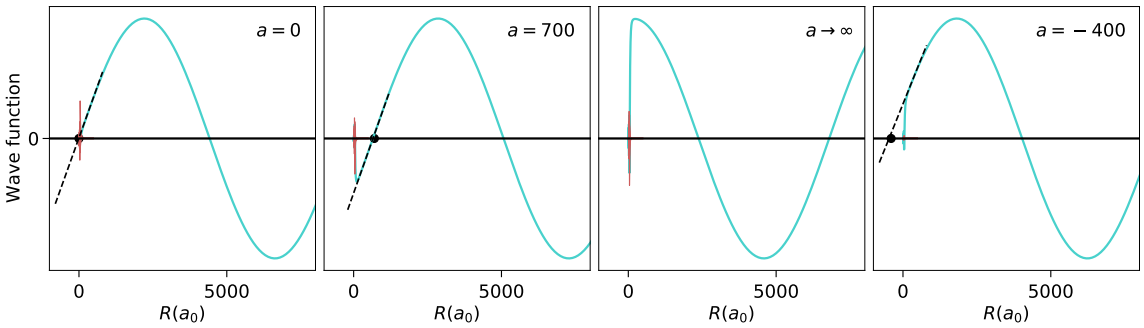

Figure 2.1: Plots of the real part of the ^{23}Na-^{40}K scattering wave function amplitude as a function of the interparticle distance at a collision energy of 3μK at various scattering lengths. The open-channel contribution to the wave function is shown in blue, the closed-channel contributions are shown in red. The black dashed lines indicate the slope of the scattering wave function close at the edge of the potential. The x-intercept of this line is close to the scattering length (the deviations are due to the finite scattering energy). The scattering lengths are also indicated by the black dots.

exactly the point where a new bound state of zero energy emerges in the potential. When the energy of a quasi-bound state matches the collision energy this is called a scattering resonance. Since the collision energy is practically zero in our case, the scattering resonance happens exactly when a quasi-bound state crosses the scattering threshold to become a real bound state.

The point of $a \to \infty$ is often called *unitarity*, or the interactions are called *unitary*. This name is slightly confusing since the S-matrix is always unitary, and a more accurate term would be *unitarity-limited*. This just means that the collision cross section is maximal given the constraint that the S-matrix is unitary. From Eq. (2.6) we see that this happens when $\sigma = \frac{4\pi}{k^2}$, since $\sin(\delta)^2 \leq 1$.

2.2.3 Universality

In Fig. 2.2 we zoom in on the short-range of the scattering wave function of Fig. 2.1 . The different colored lines correspond to different scattering channels, where each channel corresponds to a certain combination of hyperfine states of the two initial atoms. The dotted vertical line indicates the van der Waals length, which is a measure typically used to indicate the length scale of the interatomic interaction potential. Indeed, we clearly see that the scale at which the wave function varies at short range is vastly different from the scale of the long-range oscillations in Fig. 2.1, where we did not have the resolution to observe the character of the short-range wave function. However, the wavelength of the collisions occurring in ultracold gases is even longer than what we have shown in Fig. 2.1. Therefore, the natural question to ask is whether for the many-body processes appearing on the length scale of the BEC, the short-range details of the interactions are important.

In the end, it turns out that if a system is sufficiently dilute, and (almost) all collisions are pairwise, only the outcomes of the collision processes matter, and that therefore the scattering length is all the necessary information required to describe the long-range dynamics of the system properly. The only importance of the exact short-range contribution to the scattering processes is therefore to determine the scattering length. This immediately has the implication, that *any interaction potential* yielding the same scattering length will lead to the same many-body dynamics on length scales much larger than the range of the potential. This phenomenon is an example of *universality*.

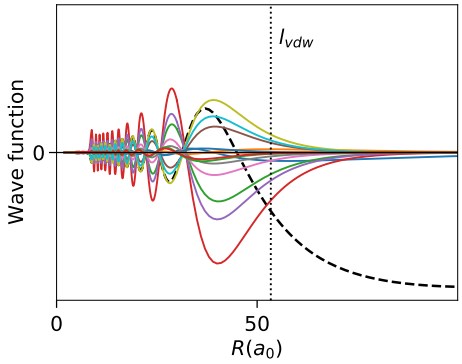

Figure 2.2: Short range of the ^{23}Na ^{40}K-scattering wave function as a function of the interparticle distance at a magnetic field of 101 gauss. The different scattering channels are indicated with the different colors. The open-channel wave-function contribution is indicated as the dashed black line, and the vertical dotted line indicates the van der Waals length.

Universality is one of the reasons that ultracold systems are so amenable to theoretical descriptions, and attractive for quantum simulation. Indeed, it would be very cumbersome to have to take into account the complex short-range character of the scattering wave function in many-body calculations. Fortunately, universality now implies that the same many-body dynamics would be found if we use a simple model potential with the same scattering length. In fact, even if the underlying physical potential has many bound states, we can take a model potential without any bound states.

This last statement has another important implication, since an ultracold gas such as a BEC is not the ground state of the realistic system. Instead, the true ground state of the collection of alkali atoms is a metal, where all the particles are separated by distances even much smaller than the van der Waals length. In contrast, in the model system where the potentials do not have any bound states, the BEC can be the true ground state. This makes the theoretical computation of the BEC-properties much simpler, since it is much easier to find the ground state of a system than to look for a special excited state in the spectrum. Finding a good description for the BEC, including its collective dynamics, is therefore much more straightforward with these model potentials.

When considering the ground state, also the *sign* of the scattering length becomes much more meaningful. In a thermal gas the sign of the interactions is not very important, only the collision cross section really matters. Since the collision cross section depends on a^2, the magnitude of a determines the strength of the interactions, and that is all the necessary information in this case. However, when we are truly searching for the ground state of the system, the sign of the interactions can make an essential difference.

It turns out that a positive scattering length is felt as an effective repulsion and a negative scattering length as an effective attraction, even though the underlying physical potential can have both attractive and repulsive contributions. This can be understood from the observation that a strictly repulsive potential *always* has a positive scattering length on the order of the range of the potential, because the wave function is expelled from the potential. For attractive potentials, we have the opposite case. If there are no bound states in the potential, the scattering length of an attractive potential is always negative. This is because the phase accumulates faster inside the potential. In an attractive potential the scattering length is not limited by the length scale of the potential, because exactly at the point where a bound state appears in the potential, the scattering length

diverges.

Note that with such a theoretical replacement of the interaction potentials, one might not call the many-body calculations fully *ab initio* any more. However, note that this approximation is very-well justifiable theoretically, only invoking the principles of quantum mechanics. It has further been verified in countless experiments.

As a final remark on the universal phenomena: also the bound state which crosses or appears from the continuum at the resonance has universal properties. Indeed, here we can again use the Wigner threshold laws. For $E < 0$ and $l = 0$, the Schrödinger equation has the asymptotic solution

$$\psi(R) = A\exp(-\kappa R) + B\exp(\kappa R). \tag{2.16}$$

This is only normalizable in case $B = 0$, so with the short range boundary condition set by the Wigner threshold law, we simply find that $\kappa = \frac{1}{a}$. Close to the resonance, the bound state energy is thus given by the simple expression

$$E^{(0)}_{\text{dimer}} = -\frac{1}{2\mu_r a^2}. \tag{2.17}$$

The range of validity of this simple expression can be extended by taking into account the effective range. Directly from the effective range expansion, one can derive

$$E^{(1)}_{\text{dimer}} = -\frac{1}{2\mu r^2_{\text{eff}}}\Big(1 - \sqrt{1 - \frac{2r_{\text{eff}}}{a}}\Big)^2. \tag{2.18}$$

2.2.4 Momentum space formulation

For the purpose of many-body calculations, it is often more convenient to work in momentum-space. The scattering problem can also be formulated entirely in momentum space, using the Lippmann-Schwinger equation

$$|\psi^{(\pm)}\rangle = |\phi\rangle + \frac{1}{E - \hat{\mathcal{H}}_0 \pm i\epsilon}\hat{V}|\psi^{(\pm)}\rangle. \tag{2.19}$$

Here $|\psi^{(\pm)}\rangle$ are the ingoing and outgoing scattering solutions and $|\phi\rangle$ are the eigenstates of non-interacting Hamiltonian $\hat{\mathcal{H}}_0$ at the corresponding energy E. Here the operator $\hat{V}$ corresponds to the interaction potential. For simplicity, let us consider single-channel scattering. In this case the free eigenstates are just momentum eigenstates. Thus, we find

$$|\psi^{(\pm)}_{\boldsymbol{k}}\rangle = |\boldsymbol{k}\rangle + \int_{\boldsymbol{q}} \frac{2\mu_r|\boldsymbol{q}\rangle}{k^2 - q^2 \pm i\epsilon}\langle\boldsymbol{q}|\hat{V}|\psi^{(\pm)}_{\boldsymbol{k}}\rangle \equiv |\boldsymbol{k}\rangle + \int_{\boldsymbol{q}} \frac{2\mu_r|\boldsymbol{q}\rangle}{k^2 - q^2 \pm i\epsilon}T^{(\pm)}_{\boldsymbol{q},\boldsymbol{k}}. \tag{2.20}$$

Here we have defined the (on-shell) T-matrix. From this equation one can easily arrive at a self-consistent equation for the T-matrix,

$$T^{(\pm)}_{\boldsymbol{q},\boldsymbol{k}} = V_{\boldsymbol{q},\boldsymbol{k}} + \int_{\boldsymbol{q}'} \frac{2\mu_r V_{\boldsymbol{q},\boldsymbol{q}'}T^{(\pm)}_{\boldsymbol{q}',\boldsymbol{k}}}{k^2 - q'^2 \pm i\epsilon}. \tag{2.21}$$

For low momenta, the T-matrix can be related to the scattering length. In this case we have

$$\lim_{\boldsymbol{q},\boldsymbol{k}\to 0} T_{\boldsymbol{q},\boldsymbol{k}} = \frac{2\pi a}{\mu_r}. \tag{2.22}$$

A popular approximation is to set

$$T_{\boldsymbol{q},\boldsymbol{k}} = V_{\boldsymbol{q},\boldsymbol{k}}, \tag{2.23}$$

and neglect the second term in Eq. (2.21). This is called the (first-order) Born approximation, and this plays a central role in the description of BECs via the well-known Gross-Pitaevskii equation. In this case one chooses a model potential so that $V_{00} = \int_{\boldsymbol{r}} V(\boldsymbol{r}) = \frac{2\pi a}{\mu_r}$. We will discuss this in more detail in Chapter 4.

2.3 Scattering of alkali atoms and molecules

2.3.1 Atomic structure and interaction potentials

Having discussed the general themes in ultracold scattering, we consider now the scattering of alkali atoms. This is the type of atom that was used in the first ultracold gas experiments, because of the simple electronic structure amenable to laser cooling. Today, more types of atoms are being used, but alkali atoms remain the most common.

As we have discussed, in many-body calculations it is not strictly necessary to incorporate the detailed internal atomic structure and short-range scattering physics. Nevertheless, the internal structure of atoms still plays an important role in ultracold-atom experiments, because it can be used to *tune* the scattering length. This is the ideal scenario, where the complexity of the problem allows us for tunability, but does not require us to make the many-body models more difficult. Furthermore, knowing this detailed internal structure enables us to theoretically compute the scattering properties from the microscopic potentials, so that the many-body models accurately capture the experimental conditions.

Alkali atoms have a single unpaired electron, which occupies an s-orbital. The nucleus of the atom also has a spin, and the coupling between this nuclear spin and the electron spin gives rise to the hyperfine structure of the atom. The typical energy splittings between the hyperfine states are on the order of $100 - 1000$ MHz or in terms of equivalent temperature, tens of mK. Since the hyperfine coupling term does not commute with the magnetic-field term, the character of the hyperfine eigenstates depend strongly on the magnetic field. Over a typical magnetic-field range of 0-1000 Gauss (0-100 mT) the spectrum changes from hyperfine-dominated to magnetic-field dominated. Convenient collections on alkali atom properties are given for example in Refs. [61, 62].

The interaction potentials for ultracold atoms can generally be divided into a long-range and a short-range part. In the long-range the van der Waals interaction is dominant, and it has the form

$$V_{LR} = -\frac{C_6}{R^6}, \tag{2.24}$$

where the C_6 coefficient quantifies the strength of the interaction. Accurate values of the C_6 coefficients calculated for ultracold atoms are readily available in the literature [63, 64]. The characteristic length scale associated with this potential is called the *van der Waals length*

$$L_{vdw} = \frac{(2\mu_r C_6)^{1/4}}{2}, \tag{2.25}$$

and is typically on the order of about $50a_0$. Another parameter which is often used is the *mean scattering length* $\bar{a} = \frac{4\pi L_{vdw}}{\Gamma(\frac{1}{4})^2} \approx 0.956 L_{vdw}$ [65].

To be precise, atoms have one even longer range interaction, which is the magnetic-dipole interaction between the unpaired spins. However, for alkali atoms the magnetic

moments are relatively small, and this effect can therefore usually be neglected. This is, however, no longer the case for strongly magnetic atoms such as chromium, erbium or dysprosium, where the magnetic dipole interaction can give rise to interesting phenomena [66].

At short distances ($\lesssim 20a_0$), the atoms start to have strong chemical interactions. This is mostly due to the unpaired electrons, which enable the two alkali atoms to form a strong chemical bond if the electrons are in the singlet configuration. In case the electronic spins are in the triplet configuration, the Pauli principle prevents the formation of strong bonds, leading to a much more shallow potential. The typical depth of the singlet potentials is on the order of a few 1000K and of the triplet potentials on the order of 100K. Accurate interaction potentials can be constructed with the help of vibrational spectroscopy experiments, see e.g. Refs. [67, 68]. The resulting potentials typically bring one already close to the scattering length profiles found in ultracold gas experiments, and the potential depths can then be slightly tuned to get to near-perfect agreement with the experimentally measured scattering lengths (see for example Refs. [69, 70]).

2.3.2 Magnetic Feshbach resonances

The nuclear spins do not play any direct role in the short-range interactions. However, because the atoms are asymptotically in their hyperfine ground state, the competition between the hyperfine coupling and the magnetic field determines the spin admixture of the atoms and therefore the admixture of the triplet and the singlet potential they experience. This has the consequence that the scattering length of the ultracold atoms can be tuned via the magnetic field.

However, just changing the singlet-triplet admixture of the scattering states is only part of the story. Indeed, it turns out that the typical energy scale of the least-bound states in the van der Waals potentials, which is set by the van der Waals length, is of similar order as the hyperfine energy. Consequently, the relative energy of the (quasi-)bound states in different hyperfine channels can be tuned with respect to the collision channel. When the bound-state energies are then tuned to zero at the collision threshold, this gives rise to a zero-energy scattering resonance, where the scattering length diverges. This kind of resonance is called a *magnetic Feshbach resonance*, and these resonances commonly occur for ultracold alkali atoms.

In Fig. 2.3 the scattering resonances are shown for the scattering of ^{23}Na and ^{40}K. In Fig. 2.3a) the hyperfine states are given by ($|F = 1, m_F = 1\rangle$ and $|F = 9/2, m_F = -9/2\rangle$ for ^{23}Na and ^{40}K respectively. In Fig. 2.3b) the state for ^{23}Na is the same, and for ^{40}K it is $|F = 9/2, m_F = -7/2\rangle$. The total magnetic moment M is conserved in the collisions, and is given by $-7/2$ for a) and $-5/2$ for b). The atoms are in the lowest asymptotic states corresponding to these values of M, so that there are only elastic collisions. In blue the scattering lengths are shown as a function of magnetic field, in red the bound-state energies of the bound states crossing the continuum at the resonances.

We see two a) and three b) adjacent resonances with different widths. The appearance of these kind of patterns of resonances is common and originates from the multiplicity of bound states. Indeed, since the interaction potentials are independent of the nuclear spin, bound states which only differ by their nuclear spin have almost the same energy. The width of the resonances is determined by the coupling strength to the ingoing channel. The general rule here is that the electron spin is much easier to change than the nuclear spin. Hence, the more different the nuclear states of the bound state are compared to the scattering state, the weaker the coupling, and the smaller the resonance width.

Magnetic Feshbach resonances can also be used as an experimental tool to create ul-

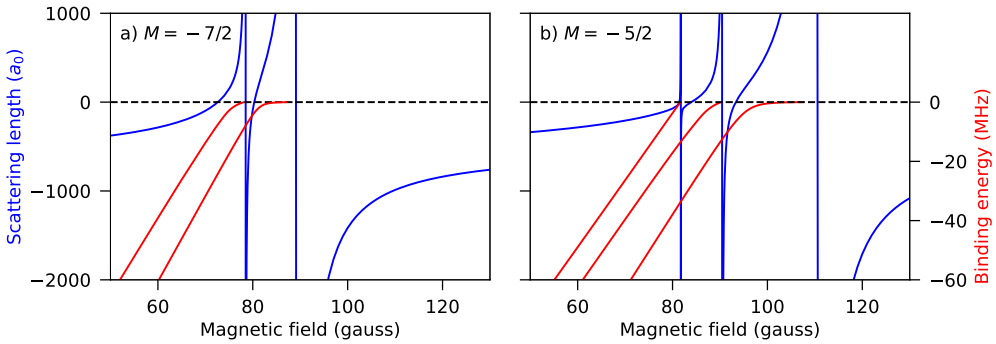

Figure 2.3: Scattering length (blue, in a_0) and binding energies (red, in MHz) of ^{23}Na and ^{40}K as a function of magnetic field. For ^{23}Na the internal state is $|F = 1, m_F = 1\rangle$, for ^{40}K the internal state is a) $|F = 9/2, m_F = -9/2\rangle$ and b) $|F = 9/2, m_F = -7/2\rangle$.

tracold molecules. For this there are two procedures, magneto- and radiofrequency (rf)-association. In case of magneto-association one starts on the negative scattering length side of the resonance, where the quasibound state lies above the collision threshold. However, close to the resonance the scattering particles still spend some time in this virtual state before dissociating again. The idea is to then quickly sweep the magnetic field to turn the quasi-bound molecules into really bound molecules. In the degenerate case this simple picture breaks down, and polaron physics plays an important role. This will be discussed in great detail in Part B of this thesis. In the second procedure an rf-photon is used to transfer one of the atoms from a hyperfine state in which there is no molecule, to a hyperfine state where there is a shallow bound state. This protocol has a close connection to *injection spectroscopy* which is done for polarons. This will be discussed in more detail in Chapter 7.

2.3.3 Scattering of ultracold molecules

Having discussed the scattering of alkali atoms, let us now briefly discuss the scattering of heteronuclear ultracold molecules, the topic of Chapter 8. We focus in particular on singlet bialkali molecules in their ground state.

In addition to van der Waals interactions, heteronuclear molecules can have dipole-dipole interactions. The long-range potential therefore takes the form

$$V_{LR} = \frac{\boldsymbol{d_1} \cdot \boldsymbol{d_2} - 3(\boldsymbol{d_1} \cdot \hat{\boldsymbol{R}}) \cdot (\boldsymbol{d_2} \cdot \hat{\boldsymbol{R}})}{R^3} - \frac{C_6}{R^6}. \tag{2.26}$$

Here $\boldsymbol{d_1}$ and $\boldsymbol{d_2}$ are the molecular dipole moments in the laboratory frame, and $\hat{R}$ is the direction of the vector connecting the molecular centers of mass. Having these long-ranged anisotropic interactions is one of the most important motivations for creating ultracold molecules, since this gives interesting new options for quantum simulation.

Importantly, molecules in their rotational eigenstates do not have a lab-frame dipole moment and thus no dipolar interactions. To induce the dipolar interactions, the molecules need to be polarized using an electric field by mixing rotational states. Alternatively, microwaves can be used.

The polarizability of the molecular dipoles also plays an important role for the van der Waals interactions. For alkali atoms the C_6 coefficient is determined by the electronic polarizability, but dipolar molecules are easier to polarize rotationally than electronically.

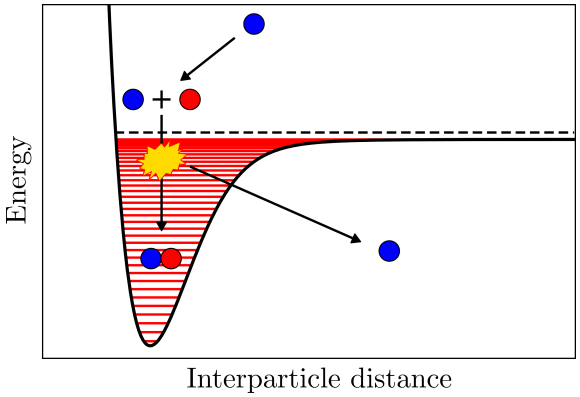

Figure 2.4: Illustration of the three-body recombination process. We schematically show the interaction potential between two atoms as a function of the interparticle distance, where the red horizontal lines indicate the bound state energy levels. When three particles collide, two of them can decay into one of these bound states, while the released energy is turned into kinetic energy.

Hence, the rotational C_6 coefficient is orders of magnitude larger than the electronic C_6 coefficient [71], except for very weakly dipolar molecules such as KRb and LiNa. As a result, the van der Waals length for molecules is much larger than for atoms. For example, for scattering of two NaK molecules, the van der Waals length is given by $\sim 250a_0$, compared to $50a_0$ for scattering between Na and K atoms.

The internal structure of the molecules, aside from the electronic and nuclear spins, consists of vibrational and rotational states. Since the interaction potential between the molecules depends on the nuclear positions of the atoms, there are complex couplings between the different vibrational and rotational states when the molecules approach each other. The spins in bialkali molecules are less important than for ultracold alkali atoms, since the electronic spins are coupled into a singlet. Consequently, there is no strong coupling between the electronic and the nuclear spins. The coupling among the nuclear spins themselves, and the coupling between the nuclear spin and the motional degrees of freedom is also weak.

2.4 The three-body problem

2.4.1 Three-body recombination

Because ultracold gases are dilute, almost all scattering processes are pairwise, and higher order processes are suppressed. However, this does not mean that these higher processes are not important at all, because three-body scattering processes are in the end limiting the lifetime of BECs, especially for large scattering lengths. Whereas pairwise collisions of ground-state atoms are always elastic, this is no longer true for three-body collisions. The chemical reaction which can occur is visualized in Fig. 2.4. The bound states inside the pairwise potentials are not accessible when two particles scatter, but when a third particle simultaneously collides with the other two, this third particle can take away the energy that is released when the other two particles decay into this bound state. The kinetic energy which is released in this process is orders of magnitude larger than the trapping energy, and this process therefore leads to loss of all the involved particles. This can be measured in experiment.

In a thermal gas the three-body recombination rate equation [72] is given by

$$\frac{dn}{dt} = -3L_3 n^3, \tag{2.27}$$

where L_3 is the recombination rate and n is the density of bosons. Here we have assumed that all three particles (and not more) are lost in the recombination process. It has been shown that this loss is suppressed in BECs by a factor 1/3! due to the symmetry of the bosonic wave function of identical particles, and is therefore given by $\frac{dn}{dt} = -\frac{1}{2}L_3 n^3$ [73]. This shows once more that BECs are truly different from thermal gases.

Importantly, for bosons $L_3 \sim a^4$, and the three-body recombination rate therefore increases faster with a than the elastic two-body scattering rate, which scales as a^2. At high scattering lengths, three-body recombination can therefore become seriously detrimental to the lifetime of ultracold gases.

However, the simple a^4 scaling is not the whole story, because there are also scattering resonances. Indeed, just like the two-body scattering rate shows a resonance when two-body bound states cross the continuum, the three-body scattering rate shows a resonance when a three-body bound state becomes bound. These three-body bound states have special universal properties and form a topic of considerable theoretical interest.

2.4.2 Thomas collapse and the Efimov effect

From a theoretical perspective, the three-body problem is much richer than the two-body problem. It can be considered as the smallest instance of a true many-body problem. Indeed, already in the classical case there exists no closed-form solution of the three-body problem, and finding the possible types of orbits in the three-body problem is still an active field of research [74].

Quantum mechanically, the three-body problem also has remarkable features. A first surprising discovery was made by Thomas already in 1935 [72, 75]. He considered a scenario of three identical particles interacting via purely pairwise potentials. The pairwise potential would only host a single bound state with energy E_2. He considered the three-body binding energy, while varying the range and depth of the potentials for fixed E_2. He found, that in the limit of the range of the two-body potential going to zero, the three-body binding energy diverges! This is referred to as the *Thomas collapse*. Note that in this limit the depth of the potential also diverges, but that E_2 still has the same fixed and finite value. Classically, the three-body energy would also diverge in this limit, but so would the dimer energy. This shows that the quantum-mechanical zero-point energy plays an interesting role in the three-body problem. Furthermore, this shows that just fixing the two-body binding energy or the scattering length, is not sufficient to fully characterize the three-body problem. To this end another parameter needs to be introduced, which is often simply referred to as the *three-body parameter*. Various parameters can be used at the three-body parameter, but they always somehow specify the range of the potential.

The most famous quantum three-body effect was discovered by Efimov in 1970 [72, 76, 77]. He considered the same scenario as Thomas, involving three identical particles with short-ranged pairwise interactions. Efimov considered the case of the scattering length going to infinity, in absence of any (deep) bound states in the pairwise potential. Indeed, Efimov showed that in this case, where a two-body bound state just appears in the potential, there exists an infinite number of three-body bound states in the spectrum. But that is not all, he also showed that these bound states obey a geometric scaling relation: the ratio of the binding energies of subsequent bound states is given by a universal scaling factor λ_0^2, with $\lambda_0 \approx 22.7$. These three-body bound states are already bound at unitarity,

and they therefore appear from the continuum at attractive scattering lengths. Also the scattering lengths at these resonances are separated by the universal scaling factor λ_0. Hence, these are the three-body bound states which give rise to the resonances in the three-body recombination rate we discussed before. Even though the Efimov effect was originally considered in the context of nuclear physics, it was first observed in the field of ultracold atoms in 2006 [78]. The observation was indeed a resonance in the three-body recombination signal, showing that the recombination is not only detrimental, but that it can also be used to probe interesting three-body physics. In case of three identical bosons, observing Efimov resonances beyond the first one is usually difficult, since they are all very close to unitarity, where the three-body recombination loss is anyway high.

2.4.3 Van der Waals universality

A natural question to now ask, concerns the role of the "three-body parameter" we introduced in the framework of the Efimov effect. Indeed, it turns out that the range of the potential determines the scattering length a_- of the first Efimov resonance, and also the energy of the lowest bound state at unitarity. Indeed, if the range of the potential would go to zero, a_- would also go to zero, and the three-body energy at unitarity would diverge.

The next question which comes to mind is how universal these three-body features are. Clearly it is no longer the case that only the scattering length is sufficient to describe all the relevant physics. Nevertheless, one might expect that some form of universality still exists. Originally this was debated, but it was experimentally shown [79, 80] that there is some universality in the way that a_- depends on the length scale of the potential. It turned out that in several cold-atom experiments the same ratio of a_- to L_{vdw} was observed. Therefore this universality is called "van der Waals universality". The origin of van der Waals universality is discussed in Refs. [81–83] , but this type of universality is more qualitative than the universality for two-body scattering; there exist for example no simple formulas like Eq. (2.17) or (2.18) to describe the trimer energy close to resonance, or for the value of a_- itself.

In Part B the Efimov effect plays a prominent role, but we will not delve deeper into the van der Waals universality. In Chapter 7 we directly compare our results to experiments by choosing model potentials which give rise to the same scattering length and effective range as the realistic atomic potentials including the hyperfine structure. In Chapter 5 and 6 we do not directly compare to experiments, but here the results might be compared to experimental data by rescaling the units so that a_- matches the experiment.

2.4.4 Heteronuclear and many-body Efimov effect

In our work we are interested in an impurity immersed in a Bose-Einstein condensate. This gives rise to two differences compared to the scenarios we just discussed. Now one particle is distinguishable from the others, and since the BEC contains a very large number of particles, in principle we are not limited to only the formation of three-body bound states.

Indeed, for three particles it has been shown that the Efimov effect also extends to the heteronuclear case [77, 84–87]. We typically consider the scenario of an impurity interacting with two bosons which do not (or very weakly) interact with each other. In this case the mass ratio between the impurity and the bosons is extremely important [77, 84]. It has been shown that the heteronuclear Efimov effect is very weak (the scaling ratio λ_0 and a_- become very large) if the impurity is heavier than the bosons, but very strong if the impurity is much lighter than the bosons. This is intuitive, since the interactions between the two bosons now need to be mediated by the impurity, which is most efficient when

the impurity is light. For an infinitely heavy impurity the problem factorizes into two independent two-body problems and there is consequently no Efimov effect. For the case of an extreme mass imbalance, for a ^{6}Li impurity immersed in ^{133}Cs, for the first time even the second Efimov resonance from the geometric series was observed [86, 87].

What about going beyond three particles? We have already seen that a three-body bound state can be bound when no two-body bound state is yet possible. In the simple case of N particles with pairwise interactions, it is easy to understand that the Efimov effect also extends beyond three particles. The total kinetic energy namely only scales with N, whereas the interaction energy scales with N^2. Since the interactions are attractive, this should lead to more and more deeply bound states for increasing particle number. Indeed, in Ref. [88, 89] it was confirmed numerically that adding more particles lowers the energy. Experimentally, a four-body and five-body Efimov resonances were observed [90, 91]. In contrast, in the heteronuclear case it is much less obvious that the Efimov effect extends beyond three particles. Here, both the interaction and kinetic energies scale with N. This topic will be discussed in much more detail in Chapter 5.

In the Bose polaron problem, the question emerges how the Efimov effect manifests itself in a medium. This question has been investigated in detail before in the case of Bose-Einstein condensates where the interactions have been quenched to unitarity $a \to \infty$ [92–100]. While here certainly interesting phenomena were observed, unfortunately the system is extremely unstable due to recombination. Furthermore, theoretically describing a quench to unitarity is extremely hard due to the rapid build-up of correlations. One of the motivations for studying the Bose polaron problem at strong interactions is therefore to see if we can gain new insights into the in-medium Efimov effect, in a problem which seems more tractable because the correlations are only localized around the impurity.

2.5 Numerical methods

Having discussed the theory background, we will now consider how to solve the scattering problem numerically. For numerical approaches to solve the three-body problem, see for example Refs. [101, 102]. We will discuss here the solution of the two-body problem, i.e., how to find the eigenstates of the Hamiltonian of the form 2.1. We used this approach for example to construct Figs. 2.1, 2.2, 2.3, and for matching the experimental results in Chapter 7. Furthermore, understanding this methodology will be useful for Chapter 8.

In case of the scattering problem, the Schrödinger equation is usually solved by making use of its structure as a second-order differential equation in terms of R and applying the correct boundary conditions. In this work, the renormalized Numerov method is used, which was introduced for this problem by Johnson [103]. One can derive a second-order differential equation for the radial motion in the following way:

$$\hat{\mathcal{H}}|\Psi\rangle = E_{tot}|\Psi\rangle, \tag{2.28}$$

$$\frac{1}{2\mu R}\frac{\partial^2}{\partial R^2}R|\Psi\rangle = \hat{\mathcal{H}}_{Li,1} + \hat{\mathcal{H}}_{Li,2} + \hat{V}(R) - E_{tot}|\Psi\rangle, \tag{2.29}$$

$$\frac{\partial^2}{\partial R^2}\psi_i(R) = \sum_\beta \langle i|2\mu_r\big[E_j + \hat{V}(R) - E_{tot}\big]|j\rangle\psi_j(R), \tag{2.30}$$

$$\frac{\partial^2}{\partial R^2}\boldsymbol{\psi} = W\boldsymbol{\psi}(R). \tag{2.31}$$

Here $|j\rangle$ denotes the channel with asymptotic energy E_j. The centrifugal term is absorbed

into the potential $\hat{V}(R)$. In the last line we defined the matrix W_{ij} as :

$$W_{ij} = 2\mu\big[E_j\delta_{ij} + \langle i|\hat{V}(R)|j\rangle - E_{tot}\delta_{ij}\big]. \tag{2.32}$$

Since none of the terms on the left-hand side couple the wave functions for different values of R, we can now solve this second-order differential equation. If we now discretize R with step size Δ and expand the differential equation to fourth order, which is known as the Numerov method, we obtain

$$\boldsymbol{\psi}_{n+1} - 2\boldsymbol{\psi}_n + \boldsymbol{\psi}_{n-1} = \frac{\Delta^2}{12}\Big(\Big[\frac{\partial^2\boldsymbol{\psi}}{\partial R^2}\Big]_{n+1} + 10\Big[\frac{\partial^2\boldsymbol{\psi}}{\partial R^2}\Big]_{n} + \Big[\frac{\partial^2\boldsymbol{\psi}}{\partial R^2}\Big]_{n-1}\Big) + \mathcal{O}(\Delta^6), \tag{2.33}$$

$$\boldsymbol{\psi}_{n+1} - 2\boldsymbol{\psi}_n + \boldsymbol{\psi}_{n-1} = \frac{\Delta^2}{12}(W_{n+1}\boldsymbol{\psi}_{n+1} + 10W_n\boldsymbol{\psi}_n + W_{n-1}\boldsymbol{\psi}_{n-1}) + \mathcal{O}(\Delta^6). \tag{2.34}$$

The index n here denotes the grid point. The short range of the potential usually has a repulsive barrier, so by using the boundary condition that $\boldsymbol{\psi}(R \to 0) = 0$ one can propagate the wave function radially outward. However, it turns out to be much more numerically stable to not propagate the wave function itself, but the ratio between the wave function on subsequent grid points, the so-called Q-matrix:

$$Q_{n+1}\boldsymbol{\psi}_{n+1} = \boldsymbol{\psi}_n. \tag{2.35}$$

This approach is typically referred to as the *renormalized Numerov method*. By using Eq. (2.34), one can get to the following equation for the Q-matrix

$$Q_{n+1} = (12\mathbb{I} - 10F_n - F_{n-1}Q_n)^{-1}F_{n+1}. \tag{2.36}$$

Here $F_n = \mathbb{I} - \frac{\Delta^2}{12}W_n$. We will now discuss both scattering and bound state calculations using the Numerov method, which differ by the application of the boundary conditions.

2.5.1 Scattering calculations with the Numerov method

When considering scattering calculations, the total energy of the system is equal to or larger than the energy of at least one of the asymptotic channels. In this case it is guaranteed that a solution of the Schrödinger equation exists at this energy, which will asymptotically be of the form of Eq. (2.3). If we have propagated the wave function until outside of the potential range, the asymptotic wave function can be extracted from the final two Q-matrices.

Up to this point we have only needed to use real variables. Therefore, we use boundary conditions in terms of spherical Bessel functions (with the so-called K-matrix) to match to the Q-matrices, and only transform to the S-matrix afterwards. The asymptotic wave function in terms of the K-matrix can be written as

$$\psi_K = f_n - g_nK, \tag{2.37}$$

$$\psi_S = 2i\psi_K(\mathbb{I} + iK)^{-1}, \tag{2.38}$$

where the second equation shows how to transform from the K-matrix boundary condition to the S-matrix condition we have defined in Eq. (2.3). In Eq. (2.37), $\boldsymbol{f}$ and $\boldsymbol{g}$ are given by:

$$(f_n)_{ij} = \delta_{ij}k_i^{1/2}R_n j_l(k_iR_n), \tag{2.39}$$

$$(g_n)_{ij} = \delta_{ij}k_i^{1/2}R_n y_l(k_iR_n). \tag{2.40}$$

Here j_l and y_l are spherical Bessel functions of the first and second kind. We can now extract the K-matrix from the final Q-matrices by

$$K = (g_{n-1} - Q_n g_n)^{-1}(f_{n-1} - Q_n f_n). \tag{2.41}$$

To avoid divergences, we propagate far enough outward that only open channels have significant contributions. The S-matrix can be obtained from the K-matrix as

$$S = (\mathbb{I} - iK)^{-1}(\mathbb{I} + iK). \tag{2.42}$$

To compute the scattering wave function one can first compute the asymptotic wave function using Eq. (2.37) and then propagate the wave function backward with the Q-matrices. In this case the Q-matrices need to be stored during the propagation.

2.5.2 Bound states calculations with the Numerov method

When $E < 0$, there are no scattering solutions to the Schrödinger equation, and furthermore, there is only a solution at a discrete set of energies. Still the Numerov approach can be used. In this case the asymptotic boundary condition for large R is that $\boldsymbol{\psi}(R \to \infty) = 0$. One can now do both a forward propagation starting from small R and a backward propagation starting from large R. At some point, the forward Q-matrix $Q^{(f)}$ and the backward Q-matrix $Q^{(b)}$, will correspond to the same interval, *i.e.*

$$\boldsymbol{\psi}_n = Q^{(f)}_{n+1}\boldsymbol{\psi}_{n+1}, \tag{2.43}$$

$$Q^{(b)}_{p+1}\boldsymbol{\psi}_n = \boldsymbol{\psi}_{n+1}. \tag{2.44}$$

When these equations have a common solution, there exists a solution to the Schrödinger equation with the correct boundary conditions. This condition can be rephrased as

$$(Q^{(f)}_{n+1} - [Q^{(b)}_{p+1}]^{-1})\boldsymbol{\psi} = 0. \tag{2.45}$$

For general energies this is not the case, but if we diagonalize this matrix and track its eigenvalues as a function of energy, we can systematically find the zero crossings and approach the bound-state energy to arbitrary precision. The bound-state wave function can then be constructed using the corresponding eigenvector, and by propagating the wave function using the already computed Q-matrices.

Chapter 3. Gaussian-state variational approach

In this Chapter we will discuss the Gaussian-state variational method for bosonic quantum systems. This is a form of self-consistent mean-field theory including up to pairwise inter-boson correlations. For a more complete and mathematical treatment of Gaussian states and variational methods (for both bosons and fermions) I recommend Refs. [104, 105]. For a review on variational methods using Gaussian states and beyond, see Ref. [106].

We will use the Gaussian-state formulation in terms of creation and annihilation operators $\hat{b}^\dagger$, $\hat{b}$ with the standard canonical commutation relations

$$[\hat{b}_i, \hat{b}_j^\dagger] = \delta_{i,j}. \tag{3.1}$$

In quantum optics it is more common to use the quadrature representation with operators $\hat{x}$ and $\hat{p}$. However, the two formulations are completely equivalent.

3.1 Coherent states

Let us start by introducing the simpler coherent states. A coherent state is defined as the eigenstate of a bosonic annihilation operator. Considering a single-mode case, this corresponds to

$$\hat{b}|\phi\rangle = \phi|\phi\rangle. \tag{3.2}$$

The state $|\phi\rangle$ can be written as

$$|\phi\rangle = \hat{U}_c|0\rangle = \exp(\phi\hat{b}^\dagger - \phi^*\hat{b})|0\rangle, \tag{3.3}$$

since

$$[\hat{b}, \hat{U}_c] = \phi\hat{U}_c, \tag{3.4}$$

and with this property, Eq. (3.2) is satisfied. The unitary operator $\hat{U}_c$ is called a displacement operator. Since $\hat{U}_c^\dagger\hat{U}_c = \hat{\mathbb{I}}$, the state is automatically normalized. Applying the unitary displacement to another operator formulated in terms of creation and annihilation operators, simply gives

$$\hat{U}_c^\dagger f(\hat{b}^\dagger, \hat{b})\hat{U}_c = f(\hat{b}^\dagger + \phi^*, \hat{b} + \phi). \tag{3.5}$$

From Eq. (3.5) one can deduce that

$$\hat{U}_c^{-1}(\phi) = \hat{U}_c^\dagger(\phi) = \hat{U}_c(-\phi), \tag{3.6}$$

$$\hat{U}_c(\alpha + \phi) = \hat{U}_c(\alpha)\hat{U}_c(\phi). \tag{3.7}$$

Other than that, an important property of the set of coherent states is that it forms an overcomplete basis for the bosonic Hilbert space. The identity operator can be written as

$$\hat{\mathbb{I}} = \frac{1}{\pi}\int |\phi\rangle\langle\phi| d\Re(\phi) d\Im(\phi). \tag{3.8}$$

Finally, let us note that all the properties discussed above can be readily generalized to the multimode case, where

$$\hat{U}_c = \exp(\sum_i \phi_i \hat{b}_i^\dagger - \phi_i^* \hat{b}_i), \tag{3.9}$$

$$[\hat{b}_i, \hat{U}_c] = \phi_i \hat{U}_c. \tag{3.10}$$

3.2 Gaussian states

The form of the state 3.3 can be systematically extended by also adding a Gaussian part. In this case

$$|\psi\rangle = \hat{U}_c \hat{U}_G |0\rangle = \exp(\phi \hat{b}^\dagger - \phi^* \hat{b}) \exp(\frac{1}{2}[\xi \hat{b}^\dagger \hat{b}^\dagger - \xi^* \hat{b}\hat{b}])|0\rangle. \tag{3.11}$$

In the multimode case, ξ now gets two indices:

$$|\psi\rangle = \hat{U}_c \hat{U}_G |0\rangle = \exp(\sum_i \phi_i \hat{b}_i^\dagger - \phi_i^* \hat{b}) \exp(\frac{1}{2} \sum_{ij} \xi_{ij} \hat{b}_i^\dagger \hat{b}_j^\dagger - \xi_{ij}^* \hat{b}_i \hat{b}_j)|0\rangle. \tag{3.12}$$

A state which can be written in this form, is called a *Gaussian state*. In the quantum optics literature, this is often also referred to as a squeezed state. The operator $\hat{U}_G$ is again unitary by construction, and is in particular called a Gaussian unitary. It acts on creation and annihilation operators in the following way,

$$\hat{U}_G^\dagger \hat{B}_i \hat{U}_G = \sum_j S_{ij} \hat{B}_j, \tag{3.13}$$

where we have defined

$$\hat{\boldsymbol{B}} = \begin{pmatrix} \hat{\boldsymbol{b}} \\ \hat{\boldsymbol{b}}^\dagger \end{pmatrix}. \tag{3.14}$$

For clarification, in the case of N modes, the first N entries of $\hat{\boldsymbol{B}}$ correspond to $\hat{\boldsymbol{b}}$, and the second N enties to $\hat{\boldsymbol{b}}^\dagger$. The matrix S is a $2N \times 2N$ matrix, and it is symplectic. The symplectic property of the matrix implies that

$$S \Sigma S^\dagger = \Sigma, \tag{3.15}$$

for

$$\Sigma = [\hat{\boldsymbol{B}}, \hat{\boldsymbol{B}}^\dagger] = \begin{pmatrix} \mathbb{I} & 0 \\ 0 & -\mathbb{I} \end{pmatrix}. \tag{3.16}$$

Note that also $S^\dagger$ is symplectic.

In terms of ξ, S is given by

$$S = \exp[\begin{pmatrix} 0 & \xi \\ \xi^* & 0 \end{pmatrix}]. \tag{3.17}$$

For real ξ we get

$$S = \begin{pmatrix} \cosh \xi & \sinh \xi \\ \sinh \xi & \cosh \xi \end{pmatrix}. \tag{3.18}$$

For this case, it is easy to see that S obeys Eq. (3.15). If we now define new operators

$$\hat{\boldsymbol{A}} = \begin{pmatrix} \hat{\boldsymbol{a}} \\ \hat{\boldsymbol{a}}^\dagger \end{pmatrix} = S \hat{\boldsymbol{B}}, \tag{3.19}$$

these will again obey the commutation relations. We namely see that

$$[\hat{\boldsymbol{A}}, \hat{\boldsymbol{A}}^\dagger] = [S\hat{\boldsymbol{B}}, \hat{\boldsymbol{B}}^\dagger S^\dagger] = S\Sigma S^\dagger = \Sigma. \tag{3.20}$$

If we again have an arbitrary function of creation and annihilation operators, the Gaussian transformation will take it to

$$\hat{U}_G^\dagger f(\hat{\boldsymbol{B}})\hat{U}_G = f(S\hat{\boldsymbol{B}}). \tag{3.21}$$

Now let us compute expectation values of this operator with respect to the vacuum state

$$\langle\psi_G|f(\hat{\boldsymbol{B}})|\psi_G\rangle = \langle 0|f(S\hat{\boldsymbol{B}})|0\rangle, \tag{3.22}$$

where we have defined $\hat{U}_G|0\rangle = |\psi_G\rangle$. Since we are computing expectation values with respect to the vacuum, the result will only be nonzero if every creation operator is paired with exactly one annihilation operator on its left, and every annihilation operator with a creation operator on its right. As a result, we can use Wick's theorem to compute the expectation values. However, since Wick's theorem holds after the transformation with the Gaussian unitary, it must also hold before the transformation, because every creation or annihilation operator is transferred to one other creation or annihilation operator. Therefore, computing expectation values with respect to a Gaussian state breaks down to applying Wick's theorem and then computing the pair correlators (see below for an example).

The pairwise expectation values can be computed using $\langle 0|\hat{B}_i(\hat{B}^\dagger)_j|0\rangle = \frac{1}{2}[\delta_{ij} - \Sigma_{ij}]$, via

$$\langle\psi_G|\hat{B}_i(\hat{B}^\dagger)_j|\psi_G\rangle = \sum_{k,l}\langle 0|S_{il}\hat{B}_k(\hat{B}^\dagger)_l S^\dagger_{lj}|0\rangle = \frac{1}{2}(\Gamma_{ij} - \Sigma_{ij}), \tag{3.23}$$

where we have defined the covariance matrix Γ as

$$\Gamma = SS^\dagger = \begin{pmatrix} \mathbb{I} + 2G & 2F \\ 2F^* & \mathbb{I} + 2G^* \end{pmatrix}, \tag{3.24}$$

with

$$G_{ij} = \langle 0|\hat{b}_j^\dagger \hat{b}_i|0\rangle, \tag{3.25}$$

$$F_{ij} = \langle 0|\hat{b}_i \hat{b}_j|0\rangle. \tag{3.26}$$

Let us now demonstrate the example of computing a four-point correlator.

$$\begin{aligned}\langle\psi_G|\hat{b}_i^\dagger\hat{b}_j^\dagger\hat{b}_k\hat{b}_l|\psi_G\rangle &= \langle\psi_G|\hat{b}_i^\dagger\hat{b}_j^\dagger|\psi_G\rangle\langle\psi_G|\hat{b}_k\hat{b}_l|\psi_G\rangle + \langle\psi_G|\hat{b}_i^\dagger\hat{b}_k|\psi_G\rangle\langle\psi_G|\hat{b}_j^\dagger\hat{b}_l|\psi_G\rangle \\ &\qquad + \langle\psi_G|\hat{b}_i^\dagger\hat{b}_l|\psi_G\rangle\langle\psi_G|\hat{b}_j^\dagger\hat{b}_k|\psi_G\rangle, \\ &= F^*_{ij}F_{kl} + G_{ik}G_{jl} + G_{il}G_{jk}. \end{aligned} \tag{3.27}$$

In the first step we have applied Wick's theorem, and written the four-point correlator in terms of its pairwise correlators. In the second step we have simply filled in the values of F and G.

The covariance matrix plays a special role in the Gaussian-state theory, because due to Wick's theorem it fully specifies the state in a unique way, except for an overall phase. This does not hold for the matrix ξ, which has some redundancy. The covariance matrix does not have $2N \times 2N$ free parameters, however, since it inherits constraints on its elements following from S being symplectic. Other than the obvious constraints from the form of Eq. 3.24, this therefore leads to the further constraint that

$$G + G^2 = FF^*. \tag{3.28}$$

3.2.1 Non-unitary formulation

In some cases it can be more practical to write the Gaussian state in a different way, by partially normal ordering the Gaussian unitary $\hat{U}_G$. Indeed, it can be shown [105, 107] that a Gaussian unitary can always be decomposed as

$$\hat{U}_G = \exp(\frac{1}{2}\sum_{ij} \xi_{ij}\hat{b}_i^\dagger\hat{b}_j^\dagger - \xi_{ij}^*\hat{b}_i\hat{b}_j), \tag{3.29}$$

$$= \mathcal{N}\exp(\frac{1}{2}\sum_{ij}\xi'_{ij}\hat{b}_i^\dagger\hat{b}_j^\dagger)\exp(\frac{1}{2}\sum_{ij}\xi''_{ij}\hat{b}_i^\dagger\hat{b}_j)\exp(\frac{1}{2}\sum_{ij}\xi'''_{ij}\hat{b}_i\hat{b}_j). \tag{3.30}$$

When we act with this operator on the vacuum, we see that the last two parts disappear, leading to

$$\hat{U}_G|0\rangle = \mathcal{N}\exp(\frac{1}{2}\sum_{ij}\xi'_{ij}\hat{b}_i^\dagger\hat{b}_j^\dagger)|0\rangle = \hat{V}_G|0\rangle. \tag{3.31}$$

In this case the operator $\hat{V}_G$ is different from $\hat{U}_G$, and in particular non-unitary, but the way they act on the vacuum is the same. Therefore, also the Gaussian states constructed from $\hat{U}_G$ or $\hat{V}_G$ are the same. The commutation relations of $\hat{V}_G$ with respect to the creation and annihilation operators are simpler than those of $\hat{U}_G$, and are given by

$$[\hat{b}_i, \hat{V}_G] = \sum \xi'_{ij}\hat{b}_j^\dagger\hat{V}_G, \tag{3.32}$$

$$[\hat{b}_i^\dagger, \hat{V}_G] = 0. \tag{3.33}$$

In the following we will work with this representation of the Gaussian state, and therefore omit the accents on ξ'. With this new definition, it is more straightforward to write the pairwise correlation functions in terms of ξ. This time we compute these expectation values directly, instead of expressing them in terms of the symplectic matrix S. Let us first consider G,

$$G_{ij} = \langle 0|\hat{V}_G^\dagger\ \hat{b}_j^\dagger\hat{b}_i\ \hat{V}_G|0\rangle. \tag{3.34}$$

Commuting the creation and annihilation operators past the Gaussian operators we find

$$G_{ij} = \langle 0|(\hat{b}_j^\dagger + \sum_l \hat{b}_l\xi_{lj}^*)\hat{V}_G^\dagger\hat{V}_G(\hat{b}_i + \sum_k \hat{b}_k^\dagger\xi_{ki})|0\rangle, \tag{3.35}$$

$$= \sum_{lk}\xi_{lj}^*\xi_{ki}\langle 0|\hat{V}_G^\dagger\ \hat{b}_l\hat{b}_k^\dagger\ \hat{V}_G|0\rangle, \tag{3.36}$$

$$= \sum_{lk}\xi_{lj}^*\xi_{ki}(G_{lk} + \delta_{lk}). \tag{3.37}$$

The recursive relation we have obtained in the end can be solved via a geometric series

$$G = \sum_{n=1}^{\infty}(\xi\xi^*)^n = \xi\xi^*[\mathbb{I} - \xi\xi^*]^{-1} \equiv \xi\xi^* X. \tag{3.38}$$

Similarly, for F we derive

$$F_{ij} = \langle 0|\hat{V}_G^\dagger\ \hat{b}_i\hat{b}_j\ \hat{V}_G|0\rangle, \tag{3.39}$$

$$= \sum_k \xi_{ki}\big(\delta_{jk} + \xi_{lj}\langle 0|\hat{V}_G^\dagger\ \hat{b}_l^\dagger\hat{b}_k^\dagger\ \hat{V}_G|0\rangle\big), \tag{3.40}$$

$$= \xi_{ij} + \sum_{kl}\xi_{ik}\xi_{lj}F_{kl}^*, \tag{3.41}$$

which leads to

$$F = \sum_{n=0}^{\infty} (\xi\xi^*)^n \xi = [\mathbb{I} - \xi\xi^*]^{-1}\xi = X\xi. \tag{3.42}$$

Having direct expressions for F and G in terms of ξ is convenient, since F and G appear in the energy expectation values and the elements of ξ are the true independent variational parameters.

From the geometric series we can immediately derive the following identities

$$F\xi^* = G, \tag{3.43}$$

$$G\xi + \xi = F. \tag{3.44}$$

These equations and their complex conjugates immediately also lead to Eq. (3.28).

3.2.2 Overlap of Gaussian states

Let us now compute the overlap of two Gaussian states, which will also give us an expression for the norm $\mathcal{N}$. We denote the unnormalized Gaussian states as

$$|\boldsymbol{\phi}, \xi\rangle = \exp(\sum_i \phi_i \hat{b}_i^\dagger - \phi_i^* \hat{b}) \exp(\frac{1}{2}\sum_{ij} \xi_{ij} \hat{b}_i^\dagger \hat{b}_j^\dagger)|0\rangle. \tag{3.45}$$

To compute the overlap of two Gaussian states, we first use that

$$\langle 0, 0|\boldsymbol{\phi}, \xi\rangle = \exp(-\frac{1}{2}\sum_i |\phi_i|^2) \exp(\frac{1}{2}\sum_{ij} \phi_i^* \xi_{ij} \phi_j^*). \tag{3.46}$$

Using Eqs. (3.6) and (3.7) this can be simply generalized to

$$\langle \boldsymbol{\alpha}, 0|\boldsymbol{\phi}, \xi\rangle = \exp(\frac{1}{2}\sum_i \alpha_i^*\phi_i - \phi_i^*\alpha_i - |\phi_i - \alpha_i|^2) \exp[\frac{1}{2}\sum_{ij} (\phi_i - \alpha_i)^* \xi_{ij} (\phi_j - \alpha_j)^*], \tag{3.47}$$

$$= \exp(\frac{\boldsymbol{\alpha}^*\boldsymbol{\phi} - \boldsymbol{\phi}^*\boldsymbol{\alpha}}{2}) \exp(-\frac{|\boldsymbol{\phi} - \boldsymbol{\alpha}|^2}{2}) \exp[\frac{1}{2}(\boldsymbol{\phi} - \boldsymbol{\alpha})^* \xi (\boldsymbol{\phi} - \boldsymbol{\alpha})^*]. \tag{3.48}$$

We can now compute the overlap of two Gaussian states by inserting the completeness relation of coherent states (3.8)

$$\langle \boldsymbol{\phi}', \xi' | \boldsymbol{\phi}, \xi\rangle = \frac{1}{\pi^N} \int \langle \phi', \xi' | \alpha, 0\rangle \langle \alpha, 0 | \phi, \xi\rangle d^N\Re(\alpha) d^N\Im(\alpha). \tag{3.49}$$

If we plug in Eq. (3.47) this yields a Gaussian integral which we can solve explicitly. After carrying out the integration and some further algebra, we find the overlap

$$\langle \boldsymbol{\phi}', \xi' | \boldsymbol{\phi}, \xi\rangle = \frac{1}{\sqrt{\det(\mathbb{I} - \xi\xi'^*)}} \exp(\frac{\boldsymbol{\phi}'^*\boldsymbol{\phi} - \boldsymbol{\phi}^*\boldsymbol{\phi}'}{2}) \exp\left\{\frac{1}{2}[\boldsymbol{\phi}'^* - \boldsymbol{\phi}^* - (\boldsymbol{\phi}' - \boldsymbol{\phi})\xi'^*](\mathbb{I} - \xi\xi'^*)^{-1}[\boldsymbol{\phi} - \boldsymbol{\phi}' - \xi(\boldsymbol{\phi}^* - \boldsymbol{\phi}'^*)]\right\}. \tag{3.50}$$

Indeed, when $\xi' = 0$, we recover Eq. (3.47). For the norm of a Gaussian state we obtain

$$\langle \boldsymbol{\phi}, \xi | \boldsymbol{\phi}, \xi\rangle = [\det(\mathbb{I} - \xi\xi^*)]^{-1/2}. \tag{3.51}$$

This implies that our normalization factor is given by $\mathcal{N} = [\det(\mathbb{I} - \xi\xi^*)]^{1/4}$ in Eq. (3.31).

3.3 The time-dependent variational principle

In this section we discuss how to efficiently use a Gaussian state as a variational Ansatz to approximate the ground state of the Hamiltonian. As an approach to optimize the variational parameters we can use *imaginary-time evolution*. Before deriving the equations of motion, let us discuss the *time-dependent variational principle*. The time-dependent variational principle is discussed in detail mathematically in Ref. [104]. Here we give the basic idea, and we derive the equations of motion for imaginary-time evolution with Gaussian states.

The idea behind the time-dependent variational principle is that variational approaches are not only suitable to find ground states, but that they can also be used to simulate dynamics. An intuitive formulation is the McLachlan variational principle. We start from the time-dependent Schrödinger equation

$$i\partial_t|\psi(t)\rangle = \hat{\mathcal{H}}|\psi(t)\rangle. \tag{3.52}$$

If the form of the state is restricted to be parameterized in terms of a vector of variational parameters $\boldsymbol{x}$, so that $|\psi(t)\rangle = |\psi[\boldsymbol{x}(t)]\rangle$, then the time-dependent Schrödinger equation can generally not be satisfied. Instead, one can minimize the difference between the time-evolved state and the real time-evolution

$$\frac{\partial}{\partial(\partial_t \boldsymbol{x})}||i\partial_t - \hat{\mathcal{H}}|\psi[\boldsymbol{x}(t)]\rangle||^2 = 0. \tag{3.53}$$

We can also apply the time-dependent variational principle to minimize the energy, by doing imaginary-time evolution instead of real-time evolution. It is relatively simple to explain how this works. In case of exact real-time evolution, we can write the time evolution in terms of the energy eigenstates $|E\rangle$,

$$|\psi(t)\rangle = \sum_j \exp(-iE_j t)|E\rangle\langle E|\psi\rangle. \tag{3.54}$$

If we now replace the real time t by the imaginary time $\tau = -it$, we get instead

$$|\psi(\tau)\rangle = \sum_j \exp(-E_j \tau)|E\rangle\langle E|\psi\rangle. \tag{3.55}$$

We can shift the Hamiltonian so that the ground state energy is 0 and all excited states have positive energies. Then, the wave-function amplitude of all excited eigenstates decay exponentially, the higher the energy is, the faster the decay. Therefore the average energy of the state decreases. When $\tau \to \infty$, only the ground-state energy remains, if it has nonzero overlap with the initial state. If the overlap with the ground state is zero, then at least the lowest energy state that $|\psi\rangle$ has overlap with remains. More rigorously, we need to take care that the norm of the wave function is conserved. We can write the imaginary time Schrödinger equation as

$$\partial_\tau|\psi(\tau)\rangle = -[\hat{\mathcal{H}} - E(\tau)]|\psi(\tau)\rangle, \tag{3.56}$$

where $E(\tau) = \langle\psi(\tau)|\hat{\mathcal{H}}|\psi(\tau)\rangle$. Projecting this equation from the left with $\langle\psi(\tau)|$ will now give 0, showing that the addition of $E(\tau)$ makes that the norm of the wave function is conserved. Now the McLachlan variational principle can be written completely analogously to the real-time evolution scenario

$$\frac{\partial}{\partial(\partial_\tau \boldsymbol{x})}||\partial_\tau + \hat{\mathcal{H}} - E(\tau)|\psi(\tau)\rangle||^2 = 0. \tag{3.57}$$

3.4 Equations of motion for Gaussian states

We now take a Gaussian state of the form of Eq. (3.31) and minimize the energy using imaginary-time evolution and McLachlan's variational principle. The first step is to make the replacement that

$$\partial_\tau = \sum_i \partial_\tau x_i \partial_{x_i}, \tag{3.58}$$

yielding

$$\partial_{x_j} E + \sum_i \partial_\tau x_i \big[\langle\psi(\boldsymbol{x})|\overleftarrow{\partial_{x_i}}\partial_{x_j}|\psi(\boldsymbol{x})\rangle + \langle\psi(\boldsymbol{x})|\overleftarrow{\partial_{x_j}}\partial_{x_i}|\psi(\boldsymbol{x})\rangle\big] = 0. \tag{3.59}$$

Note that for complex variables, one should consider the real and imaginary parts as independent variational parameters. This can also be formulated in terms of the variables and their complex conjugates. Hence, the Gaussian-state parameter vector $\boldsymbol{x}$ consists of $\mathcal{N}$, $\mathcal{N}^*$, $\boldsymbol{\phi}$, $\boldsymbol{\phi}^*$, ξ and ξ^*. The derivatives $\partial_{x_i}|\psi\rangle$ are given by:

$$\partial_{\mathcal{N}}|\psi\rangle = \frac{1}{\mathcal{N}}|\psi\rangle, \tag{3.60}$$

$$\partial_{\mathcal{N}^*}|\psi\rangle = 0, \tag{3.61}$$

$$\partial_{\phi_i}|\psi\rangle = [\hat{b}_i^\dagger - \frac{\phi_i^*}{2}]|\psi\rangle, \tag{3.62}$$

$$\partial_{\phi_i^*}|\psi\rangle = [-\hat{b}_i + \frac{\phi_i}{2}]|\psi\rangle, \tag{3.63}$$

$$\frac{\partial}{\partial\xi_{ij}}|\psi\rangle = \hat{U}_\phi \hat{b}_i^\dagger \hat{b}_j^\dagger \hat{V}_G|0\rangle, \tag{3.64}$$

$$\frac{\partial}{\partial[\xi_{ij}]^*}|\psi\rangle = 0. \tag{3.65}$$

Let us now denote $\boldsymbol{x'}$ as the vector $\boldsymbol{x}$ without $\mathcal{N}$ and $\mathcal{N}^*$. If we take $x_j = \mathcal{N}$ in Eq. (3.59),

$$0 = \frac{\partial_\tau \mathcal{N}^*}{|\mathcal{N}|^2} + \frac{1}{\mathcal{N}} \sum_i \partial_\tau x_i' \langle\psi(\boldsymbol{x})|\overleftarrow{\partial_{x_i'}}|\psi(\boldsymbol{x})\rangle. \tag{3.66}$$

Multiplying this equation by $|\mathcal{N}|^2\mathcal{N}$ and adding it to the complex conjugate, we exactly recover the equation for the norm

$$0 = \mathcal{N}\partial_\tau\mathcal{N}^* + \mathcal{N}^*\partial_\tau\mathcal{N} + |\mathcal{N}|^2 \sum_i \partial_\tau x_i' \big[\langle\psi(\boldsymbol{x})|\overleftarrow{\partial_{x_i'}}|\psi(\boldsymbol{x})\rangle + \langle\psi(\boldsymbol{x})|\partial_{x_i'}|\psi(\boldsymbol{x})\rangle\big] = \partial_\tau\langle\psi(\boldsymbol{x})|\psi(\boldsymbol{x})\rangle. \tag{3.67}$$

This shows that the equations of motion for $\mathcal{N}$ take care of the conservation of the norm. For the other variational parameters one finds

$$\begin{aligned} 0 = \partial_{x_j'} E + \frac{\partial_\tau \mathcal{N}}{\mathcal{N}} \langle\psi(\boldsymbol{x})|\overleftarrow{\partial_{x_j'}}|\psi(\boldsymbol{x})\rangle + \frac{\partial_\tau \mathcal{N}^*}{\mathcal{N}^*} \langle\psi(\boldsymbol{x})|\partial_{x_j'}|\psi(\boldsymbol{x})\rangle \\ + \sum_i \partial_\tau x_i' \big[\langle\psi(\boldsymbol{x})|\overleftarrow{\partial_{x_i'}}\partial_{x_j'}|\psi(\boldsymbol{x})\rangle + \langle\psi(\boldsymbol{x})|\overleftarrow{\partial_{x_j'}}\partial_{x_i'}|\psi(\boldsymbol{x})\rangle\big]. \end{aligned} \tag{3.68}$$

Inserting now Eq. (3.66) gives:

$$\begin{aligned} 0 = \partial_{x_j'} E + \sum_i \partial_\tau x_i' \Big[\langle\psi(\boldsymbol{x})|\overleftarrow{\partial_{x_i'}}\partial_{x_j'}|\psi(\boldsymbol{x})\rangle - \langle\psi(\boldsymbol{x})|\overleftarrow{\partial_{x_i'}}|\psi(\boldsymbol{x})\rangle\langle\psi(\boldsymbol{x})|\partial_{x_j'}|\psi(\boldsymbol{x})\rangle \\ + \langle\psi(\boldsymbol{x})|\overleftarrow{\partial_{x_j'}}\partial_{x_i'}|\psi(\boldsymbol{x})\rangle - \langle\psi(\boldsymbol{x})|\overleftarrow{\partial_{x_j'}}|\psi(\boldsymbol{x})\rangle\langle\psi(\boldsymbol{x})|\partial_{x_i'}|\psi(\boldsymbol{x})\rangle\Big]. \end{aligned} \tag{3.69}$$

For $x'_j = \phi_j$ we find

$$0 = \eta^*_j + \sum_i \partial_\tau \phi^*_i [\mathbb{I} + 2G_{ij}] - 2\sum_i \partial_\tau \phi_i F^*_{ij}, \tag{3.70}$$

where $\eta^*_j = \partial_{\phi_j} E$. In practice, taking a simplified equation for ϕ

$$\partial_\tau \boldsymbol{\phi} = -\boldsymbol{\eta}, \tag{3.71}$$

gives the same result with comparable efficiency. For $x'_j = \xi_{qp}$ we get

$$0 = \partial_{\xi_{qp}} E + \sum_{ij} \partial_\tau \xi^*_{ij} X_{iq} X_{jp}. \tag{3.72}$$

The energy E is most simply expressed in terms of F and G because of Wick's theorem. If we thus define

$$\mathcal{E}_{ij} = \frac{\partial E}{\partial G_{ji}}, \tag{3.73}$$

$$\Delta_{ij} = 2\frac{\partial E}{\partial F^*_{ij}}, \tag{3.74}$$

then we can express these derivatives in terms of ξ via

$$\frac{\partial X_{ij}}{\partial \xi_{mn}} = X_{im}(\xi^* X)_{nj} = X_{im} F^*_{nj}, \tag{3.75}$$

$$\frac{\partial X_{ij}}{\partial \xi^*_{mn}} = (X\xi)_{im} X_{nj} = F_{im} X_{nj}. \tag{3.76}$$

This yields the total expression

$$\frac{\partial E}{\partial \xi} = \frac{1}{2}[X^* \mathcal{E}^* F^* + F^* \mathcal{E} X + X^* \Delta^* X + F^* \Delta F^*]. \tag{3.77}$$

Inserting this into Eq. (3.72) and multiplying from the left and right with $[X^*]^{-1}$ and X^{-1} we finally find

$$\partial_\tau \xi^* = -[\Delta^* + \mathcal{E}^* \xi^* + \xi^* \mathcal{E} + \xi^* \Delta \xi^*]. \tag{3.78}$$

This derivation can straightforwardly be applied also to the real-time evolution case. The equations of motion for ξ for real-time evolution are also given in Appendix G of Ref. [106]. The equations of motion are usually formulated in terms of the covariance matrix Γ [2, 106, 108]. We can retrieve this also from our expression. Indeed, using Eqs. (3.38), (3.42), (3.75), and (3.76) we find

$$\partial_\tau G = \partial_\tau X = X \partial_\tau \xi F^* + F \partial_\tau \xi^* X = -\big[(X+G)\Delta F^* + X\mathcal{E}G + h.c.\big], \tag{3.79}$$

$$\partial_\tau F = X \partial_\tau \xi + \partial_\tau X \xi = -\big[X\Delta + F\mathcal{E}^* + 2F\Delta^* F + (X+G)\Delta G^* + (X+G)\mathcal{E}F\big]. \tag{3.80}$$

After some algebra, one can find this corresponds to the equation of motion of the covariance matrix corresponding to

$$\partial_\tau \Gamma = \Sigma \mathscr{H} \Sigma - \Gamma \mathscr{H} \Gamma. \tag{3.81}$$

where

$$\mathscr{H} = \begin{pmatrix} \mathcal{E} & \Delta^* \\ \Delta & \mathcal{E}^* \end{pmatrix}. \tag{3.82}$$

For imaginary-time evolution, it is numerically more stable to work with ξ instead of Γ. The reason behind this is that the elements of ξ are linearly independent, and that all realizations of ξ lead to a proper Gaussian state, as long as the norm of the state stays finite. Numerical errors in ξ are therefore not very detrimental. This is not true for the covariance matrix Γ, which has some built-in constraints, see Eq. (3.28). Due to numerical errors, these constraints can be violated, taking the evolution outside of the space of allowed Gaussian states. This can give rise to unphysical results, putting a stricter constraint on the numerical step size. For real-time evolution these considerations are less important, because there the actual time-evolution itself is the subject of interest, instead of only the final approximation to the ground state.

3.4.1 Iterated Bogoliubov theory

Instead of explicitly evolving the equations of motion, one can instead also use a method called "iterated Bogoliubov theory" [109]. This involves iteratively solving $\eta = 0$ for ϕ and $\Sigma\mathscr{H}\Sigma - \Gamma\mathscr{H}\Gamma = 0$ for Γ. The latter can be solved via symplectic diagonalization. If one can find a symplectic S_d so that

$$S_d^\dagger \mathscr{H} S_d = D, \tag{3.83}$$

for diagonal D, then $\Gamma = S_d S_d^\dagger$ solves the equation, as can be seen from

$$\Sigma\mathscr{H}\Sigma = S_d\Sigma S_d^\dagger \mathscr{H} S_d \Sigma S_d^\dagger = S_d \Sigma D \Sigma S_d^\dagger = S_d D S_d^\dagger = \Gamma\mathscr{H}\Gamma. \tag{3.84}$$

Williamson's theorem states that for a positive definite and Hermitian $\mathscr{H}$, such a matrix S_d always exists [110].

Chapter 4. Gaussian states and Bose-Einstein condensates

4.1 Introduction

When a bosonic gas is cooled to the degenerate regime, this leads to the formation of a Bose-Einstein condensate, where the single-particle ground state of the system is macroscopically occupied (see Sec. 1.2.3). Since the BEC is playing a central role in this thesis as the "quantum medium", having a good understanding of the interactions inside the BEC itself is important. Furthermore, before studying quantum effects in chemical processes in a BEC, it is good to first understand the quantum effects in the weakly-interacting case. That is therefore the aim of this Chapter.

We consider, a dilute, weakly-interacting, three-dimensional BEC, so that $n_0^{-1/3} \gg a$. The general Hamiltonian for the Bose gas is simple to write down,

$$\hat{\mathcal{H}} = \int_{\boldsymbol{k}} (\frac{k^2}{2m} - \mu)\hat{b}^\dagger_{\boldsymbol{k}}\hat{b}_{\boldsymbol{k}} + \frac{1}{2}\int\int d\boldsymbol{r}d\boldsymbol{r'}V(\boldsymbol{r}-\boldsymbol{r'})\hat{b}^\dagger_{\boldsymbol{r}}\hat{b}^\dagger_{\boldsymbol{r'}}\hat{b}_{\boldsymbol{r}}\hat{b}_{\boldsymbol{r'}} + \int_{\boldsymbol{r}} V_{\text{ext}}(\boldsymbol{r})\hat{b}^\dagger_{\boldsymbol{r}}\hat{b}_{\boldsymbol{r}}, \tag{4.1}$$

$$= \int_{\boldsymbol{k}} (\frac{k^2}{2m} - \mu)\hat{b}^\dagger_{\boldsymbol{k}}\hat{b}_{\boldsymbol{k}} + \frac{1}{2}\int_{\boldsymbol{K}}\int_{\boldsymbol{q}}\int_{\boldsymbol{p}} V_{\boldsymbol{pq}}\ \hat{b}^\dagger_{\boldsymbol{K}/2+\boldsymbol{q}}\hat{b}^\dagger_{\boldsymbol{K}/2-\boldsymbol{q}}\hat{b}_{\boldsymbol{K}/2+\boldsymbol{p}}\hat{b}_{\boldsymbol{K}/2-\boldsymbol{p}} + \int_{\boldsymbol{r}} V_{\text{ext}}(\boldsymbol{r})\hat{b}^\dagger_{\boldsymbol{r}}\hat{b}_{\boldsymbol{r}}. \tag{4.2}$$

Here μ indicates the chemical potential, V indicates the interboson interaction potential, and V_{ext} the potential in which the bosons are trapped. In a BEC, the wavelength of the particles is much larger than the interparticle distance, and as a result, mean-field theory is expected to work well. A standard approach to describe the ground state of the BEC is thus to approximate the wave function as [44]

$$\Psi(\boldsymbol{r_1}, ...\boldsymbol{r_N}) = \phi(\boldsymbol{r_1})....\phi(\boldsymbol{r_N}), \tag{4.3}$$

where all particles have the same spatial distribution and there are no interparticle correlations. In the Gaussian-state framework we aim to employ here, it is more natural to describe the BEC using a coherent state,

$$|\Psi\rangle = \exp[\int_{\boldsymbol{r}} \phi(\boldsymbol{r})\hat{b}^\dagger_{\boldsymbol{r}} - \phi^*(\boldsymbol{r})\hat{b}_{\boldsymbol{r}}]|0\rangle, \tag{4.4}$$

but this leads to the same mean-field result. In both of these cases there are no interparticle correlations, and the scattering processes are not explicitly included. This means that we are implicitly using the Born approximation, where the T-matrix is just given by the bare potential, see Eq. (2.23). Since we want our effective description to still have the correct scattering length, the realistic potential needs to be replaced by a model potential which has the desired scattering length on the level of the Born approximation. The most convenient choice is to take a *contact interaction*

$$V(\boldsymbol{r}-\boldsymbol{r'}) = \frac{4\pi a}{m}\delta(\boldsymbol{r}-\boldsymbol{r'}). \tag{4.5}$$

We can now use Eq. (4.4) as a variational Ansatz and apply the time-dependent variational principle. This leads to the *Gross-Pitaevskii equation* (GPE) [111, 112]

$$i\partial_t\phi = [-\frac{\nabla^2}{2m} - \mu + V_{\text{ext}}(\boldsymbol{r}) + \frac{4\pi a}{m}|\phi(\boldsymbol{r})|^2]\phi(\boldsymbol{r}). \tag{4.6}$$

This simple equation turns out to describe the dynamics of weakly-interacting Bose-Einstein condensates remarkably well.

In the homogeneous case where $V_{\text{ext}}(\boldsymbol{r}) = 0$, one simply sees that a stationary state is achieved when the condensate has a completely flat density profile, and that the resulting density n_0 is set by the chemical potential

$$\mu = \frac{4\pi a|\phi(\boldsymbol{r})|^2}{m} = \frac{4\pi a n_0}{m}. \tag{4.7}$$

In this work we are interested what happens if we go beyond mean-field theory: if we actually consider the scattering processes that take place without using the Born approximation. Indeed, the form of the first-order beyond-mean-field correction is already known since the work by Lee, Huang and Yang in 1957 [113] and is therefore called the LHY correction. They showed that the chemical potential including this correction, is given by

$$\mu_{LHY} = \frac{4\pi n_0 a}{m}(1 + \frac{32}{3\sqrt{\pi}}\sqrt{n_0 a^3}). \tag{4.8}$$

This leads to the following energy density

$$E_{LHY} = \frac{2\pi n_0^2 a}{m}(1 + \frac{128}{15\sqrt{\pi}}\sqrt{n_0 a^3}). \tag{4.9}$$

The combination $n_0 a^3$ is called the *gas parameter* and quantifies the effective diluteness of the BEC and how well mean-field theory works. In ultracold gases this parameter is typically not more than 10^{-4} [44]. As we will discuss later in the thesis, however, if strongly-interacting quantum impurities are introduced, the densities reached in the polaron clouds can be much higher.

At first sight the LHY-correction seems to have a reasonable form, where the first-order correction depends on the small gas parameter. However, when considering it more carefully one may notice something striking: the LHY-correction is positive! This may seem surprising, since allowing for more correlations in the variational wave function should by definition lower the energy. The reason this is apparently not the case in the LHY-expression, is that we have applied the Born approximation to compute the mean-field term, assuming there were no interboson correlations. By going beyond-mean field, we start to take into account these correlations, and this also means we need to relax the Born approximation and describe the scattering processes more properly. We will see that from this procedure the positive LHY correction arises.

Lee, Huang and Yang originally derived this correction using an improved pseudopotential involving the derivative of a delta function, but the simplest way that the LHY correction can be derived, is via the Bogoliubov approximation. Here we will consider the Gaussian-state framework introduced in Chapter 3, and we will show that in this framework, the Bogoliubov approach is not self-consistent. We will demonstrate how to resolve this and derive the LHY correction self-consistently and variationally. It turns out that this actually requires going beyond Gaussian states. We will keep the form of the potential arbitrary, and show the connection between the variational wave function

and the T-matrix describing the scattering process. For reference, approaches using diagrammatics have been developed for example by Beliaev [114], and have been reviewed in Ref. [115, 116]. Recently, mathematically rigorous proofs [117, 118] have confirmed the form of the LHY correction, with an approach more similar to what is done here.

Before continuing, let us discuss more about the relevance of these LHY corrections. Indeed, because the gas parameter is very small, LHY corrections are barely observable in a simple single-component BEC. However, in the last decade scenarios have been proposed and experimentally realized where LHY corrections play a critical role: quantum droplets. This phase of matter has been realized in mixtures of two species of BEC [119–122], or in dipolar gases [66, 123, 124]. Indeed, in these cases two mean-field terms can be brought to almost cancel, suddenly making the LHY contribution important. When the sum of the two mean-field terms is negative then the system would be predicted to collapse when only considering the mean-field terms. However, since the LHY correction is positive and scales with a higher order of the density, the LHY correction can stabilize this collapse. This gives rise to self-bound quantum droplets.

4.2 Bogoliubov theory

To start, let us first consider the simplest way one can obtain the LHY correction (4.8): via Bogoliubov theory [125]. The first step is to displace the Hamiltonian with the background BEC: to replace all the creation/annihilation operators acting on the BEC mode by $\phi = \sqrt{n_0}$. In case we write the BEC wave function as a coherent state, this follows directly from the action of the displacement unitary on the Hamiltonian. For the homogeneous Bose gas this gives

$$\begin{aligned}\hat{\mathcal{H}}_{\text{disp}} = \hat{U}_c^\dagger \hat{\mathcal{H}} \hat{U}_c = \Omega\frac{U\phi^4}{2} - \Omega\mu\phi^2 + \int_{\boldsymbol{k}} (\frac{k^2}{2m} - \mu)\hat{b}_{\boldsymbol{k}}^\dagger \hat{b}_{\boldsymbol{k}} \\ + \frac{\phi^2}{2}\int_{\boldsymbol{q}} [V_{q0}(\hat{b}_{\boldsymbol{q}}^\dagger \hat{b}_{-\boldsymbol{q}}^\dagger + \hat{b}_{\boldsymbol{q}}\hat{b}_{-\boldsymbol{q}} + 2\hat{b}_{\boldsymbol{q}}^\dagger \hat{b}_{\boldsymbol{q}}) + 2U\hat{b}_{\boldsymbol{q}}^\dagger \hat{b}_{\boldsymbol{q}}] \\ + \phi\int_{\boldsymbol{K}}\int_{\boldsymbol{q}} [\hat{b}_{\boldsymbol{K/2+q}}^\dagger \hat{b}_{\boldsymbol{K/2-q}}^\dagger \hat{b}_{\boldsymbol{K}} V_{\boldsymbol{K/2},\boldsymbol{q}} + h.c.] \\ + \frac{1}{2}\int_{\boldsymbol{K}}\int_{\boldsymbol{q}}\int_{\boldsymbol{p}} V_{\boldsymbol{pq}}\ \hat{b}_{\boldsymbol{K/2+q}}^\dagger \hat{b}_{\boldsymbol{K/2-q}}^\dagger \hat{b}_{\boldsymbol{K/2+p}} \hat{b}_{\boldsymbol{K/2-p}}, \quad (4.10)\end{aligned}$$

where Ω is the volume of the system, which we take to infinity. We have further defined $U = \int_{\boldsymbol{r}} V(\boldsymbol{r})$. In the Bogoliubov approach one first finds the ground state at this level of theory, taking a contact interaction, and setting $\mu = Un_0$. The second step is the *Bogoliubov approximation*. This approximation entails truncating the displaced Hamiltonian to quadratic order in the creation and annihilation operators:

$$\begin{aligned}\frac{\hat{\mathcal{H}}_{\text{Bog}}}{\Omega} = (\frac{U\phi^4}{2} - \mu\phi^2) + \int_{\boldsymbol{k}} (\frac{k^2}{2m} - \mu)\hat{b}_{\boldsymbol{k}}^\dagger \hat{b}_{\boldsymbol{k}} \\ + \frac{\phi^2}{2}\int_{\boldsymbol{q}} [V_{\boldsymbol{q}0}(\hat{b}_{\boldsymbol{q}}^\dagger \hat{b}_{-\boldsymbol{q}}^\dagger + \hat{b}_{\boldsymbol{q}}\hat{b}_{-\boldsymbol{q}} + 2\hat{b}_{\boldsymbol{q}}^\dagger \hat{b}_{\boldsymbol{q}}) + 2U\hat{b}_{\boldsymbol{q}}^\dagger \hat{b}_{\boldsymbol{q}}]. \quad (4.11)\end{aligned}$$

Since this Hamiltonian is quadratic, the ground state can exactly be written as a Gaussian state $\hat{U}_G|0\rangle$. Equivalently, one can transform the creation and annihilation operators into

new quasiparticle operators

$$\beta_{\boldsymbol{k}}^\dagger = \hat{U}_G^\dagger \, b_{\boldsymbol{k}}^\dagger \, \hat{U}_G = u_k b_{\boldsymbol{k}}^\dagger - v_k b_{-\boldsymbol{k}}, \tag{4.12}$$

$$\beta_{\boldsymbol{k}} = \hat{U}_G^\dagger \, b_{\boldsymbol{k}} \, \hat{U}_G = u_k b_{\boldsymbol{k}} - v_k b_{-\boldsymbol{k}}^\dagger. \tag{4.13}$$

This is typically referred to as the *Bogoliubov transformation*. In terms of the new quasiparticle operators, the Hamiltonian can be written as

$$\frac{1}{\Omega}\hat{U}_G^\dagger \hat{\mathcal{H}}_{Bog} \hat{U}_G = -\frac{U\phi^4}{2} + \frac{1}{2}\int_{\boldsymbol{k}} (\omega_k - \frac{k^2}{2m} - V_{\boldsymbol{k},\boldsymbol{0}}\phi^2) + \int_{\boldsymbol{k}} \omega_k \beta_{\boldsymbol{k}}^\dagger \beta_{\boldsymbol{k}}, \tag{4.14}$$

where

$$\omega_k = \sqrt{\frac{k^4}{4m^2} + \frac{V_{\boldsymbol{k}0}\phi^2 k^2}{m}}, \tag{4.15}$$

$$u_k = \sqrt{\frac{1}{2}\left(\frac{\frac{k^2}{2m} + V_{\boldsymbol{k}0}\phi^2}{\omega_k} + 1\right)}, \tag{4.16}$$

$$v_k = -\sqrt{\frac{1}{2}\left(\frac{\frac{k^2}{2m} + V_{\boldsymbol{k}0}\phi^2}{\omega_k} - 1\right)}. \tag{4.17}$$

Let us now carefully consider the second term, which should give rise to the LHY correction

$$\begin{aligned} E_{LHY} &= \frac{1}{2}\int_{\boldsymbol{k}} (\omega_k - \frac{k^2}{2m} - V_{\boldsymbol{k},\boldsymbol{0}}\phi^2), \\ &= \frac{1}{8\pi^2 m} \lim_{\Lambda\to\infty} \int_0^\Lambda k^2 dk \, (\sqrt{k^4 + 4mU\phi^2 k^2} - k^2 - 2mU\phi^2), \\ &= \frac{8m^{3/2}U^{5/2}\phi^5}{15\pi^2} - \frac{1}{8\pi^2 m} \lim_{\Lambda\to\infty} (2m^2U^2\phi^4\Lambda). \end{aligned} \tag{4.18}$$

We see that this integral is UV-divergent! This originates from the fact that the Gaussian state can renormalize the interboson interactions, and that we therefore should not have taken the Born approximation in the beginning. This issue is usually resolved by adding the next-order term in the Born expansion to the mean-field term

$$E\text{corr} = \int_{\boldsymbol{k}} \frac{mU^2\phi^4}{k^2}. \tag{4.19}$$

This term counteracts the UV-divergent term, and one remains with the first term in Eq. (4.18), which upon insertion of $U = \frac{4\pi a}{m}$ exactly returns the LHY correction (4.9).

There are more issues with the Bogoliubov approach. In fact, also the expectation value of the state with respect to the quartic term which was dropped diverges. It takes the following form

$$E_q = \frac{U}{2}(\int_{\boldsymbol{k}} u_k v_k)^2 + U(\int_{\boldsymbol{k}} v_k^2)^2. \tag{4.20}$$

This gives

$$E_q = \frac{U}{2}\Big[\frac{mU\phi^2}{2\pi^2} \lim_{\Lambda\to\infty} \big(\sqrt{k^2 + 4U\phi^2}\big)_0^\Lambda\Big]^2 + U\Big[\frac{(mU\phi^2)^{3/2}}{3\pi^2}\Big]^2. \tag{4.21}$$

The regular terms of both contributions scale like $\phi^6 U^4 \sim n_0^3 U^4$, and can therefore be neglected justifiably. However, the first term also has a contribution which is UV-divergent.

Even though it scales with U^3, the density dependence of this UV-divergent term is n_0^2, which is the same as for the mean-field term. From the variational perspective, a divergence in the energy density of the quartic term clearly means this term should not have been neglected. Another issue is that the back-action of the excitations on top of the condensate on the condensate itself is not considered, which would also lead to a change in the chemical potential.

One important quantity to characterize the quantum fluctuations is the depletion, the number of particles outside of the BEC-mode. The depletion can be computed as

$$n_d = \langle \int_{|\boldsymbol{k}|>0} \hat{b}^\dagger_{\boldsymbol{k}} \hat{b}_{\boldsymbol{k}} \rangle = \int_{\boldsymbol{k}} v^2_{\boldsymbol{k}} = \frac{(mU\phi^2)^{3/2}}{3\pi^2} = \frac{8n_0\sqrt{n_0 a^3}}{3\sqrt{\pi}}. \tag{4.22}$$

The typical argument for dropping the contributions of the quartic terms is that these terms scale as n_d^2. This is indeed true for the second term in Eq. (4.20), where this can be seen immediately, but for the first term in Eq. (4.20) this is false for the UV-divergent part. To understand this, it is important to consider the nature of the wave function, which is a Gaussian state. In particular, this means that excitations are always created *in pairs*. Therefore the number of pairs $n_p = \frac{n_d}{2}$. However, since there are also interactions *inside* every pair, one contribution of the quartic term will not scale with the square of the density of pairs, $\sim n_p^2$, but as the density of pairs times their internal energy.

Interestingly, even though the Bogoliubov approach seems ill-motivated in the present analysis, it still captures the correct low-energy properties, such as the LHY-correction, the depletion, and the excitation spectrum. Indeed, one way to understand the validity of Bogoliubov theory is via quantum field theory. Here the presence of UV-divergences is common and not frowned upon. In the field-theory framework, the approximation is typically to truncate up to a certain number of vertices in the Feynman diagrams, which would in our case just truncate the expression at a given order of U. Indeed, the UV-divergence going with U^2 in Eq. (4.18) would then justifiably be cured by going to the next-order Born approximation as written in Eq. (4.19). The UV-divergence in Eq. (4.21) scales with U^3 and would therefore be disregarded at the quadratic order in U. This divergence would then be cured by other diagrams of order U^3.

In the remainder of this Chapter we will consider how to approach this problem self-consistently in a variational framework.

4.3 Variational optimization

The Gaussian-state wave function for a homogeneous BEC has the form

$$|\psi\rangle = \hat{U}_c \hat{U}_G |0\rangle = \hat{U}_c \hat{V}_G |0\rangle = \exp[\int_{\boldsymbol{r}} \phi \hat{b}^\dagger_{\boldsymbol{r}} - h.c.] \exp(\int_{\boldsymbol{k}} \xi_{\boldsymbol{k}} \hat{b}^\dagger_{\boldsymbol{k}} \hat{b}^\dagger_{-\boldsymbol{k}}) |0\rangle. \tag{4.23}$$

Importantly, compared to Eq. (3.31) the correlation matrix ξ has only one index instead of two. This follows from momentum-conservation, which implies that only pairs of particles with opposite momenta are created. As a result, the matrix multiplications in the equations for G (3.38) and F (3.42) now become element-wise. Furthermore, since we are looking for the ground state, we can assume ϕ and ξ to be real. This leads to

$$G_{\boldsymbol{k}} = \frac{\xi^2_{\boldsymbol{k}}}{1 - \xi^2_{\boldsymbol{k}}}, \tag{4.24}$$

$$F_{\boldsymbol{k}} = \frac{\xi_{\boldsymbol{k}}}{1 - \xi^2_{\boldsymbol{k}}}. \tag{4.25}$$

Since the wave function now includes pairwise correlations between the bosons, it is able to describe pairwise scattering processes. Therefore, taking the Born approximation is no longer justified. As a result, already obtaining the mean-field energy is not completely trivial, since the renormalization of the bare coupling also needs to come out of the Gaussian-state calculation. The advantage of taking into account the correlations explicitly, is that we see directly how the scattering length emerges as the effective interaction strength in the many-body model, and how the scattering processes are described in the wave function.

To this end, let us compute the expectation value of the Hamiltonian with respect to the Gaussian state. Using Wick's theorem, we obtain the energy density

$$E = \frac{1}{\Omega}\langle 0|\hat{V}_G^\dagger \hat{U}_c^\dagger \hat{\mathcal{H}} \hat{U}_c \hat{V}_G|0\rangle = \frac{U}{2}\phi^4 - \mu\phi^2 + \int_{\boldsymbol{k}} (\frac{k^2}{2m} - \mu) G_{\boldsymbol{k}} + \phi^2 \int_{\boldsymbol{k}} F_{\boldsymbol{k}} V_{\boldsymbol{k},0}$$
$$+ \phi^2 \int_{\boldsymbol{k}} G_{\boldsymbol{k}}(U + V_{\boldsymbol{k},0}) + \frac{1}{2}\int_{\boldsymbol{k}}\int_{\boldsymbol{k'}} F_{\boldsymbol{k}} F_{\boldsymbol{k'}} V_{\boldsymbol{k},\boldsymbol{k'}} + \int_{\boldsymbol{K}}\int_{\boldsymbol{k}} G_{\boldsymbol{K}/2+\boldsymbol{k}} G_{\boldsymbol{K}/2-\boldsymbol{k}}(U + V_{2\boldsymbol{k},0}). \quad (4.26)$$

Since G and F are not linearly independent, it is now convenient to express this in terms of our variational parameter $\xi_{\boldsymbol{k}}$:

$$E(\boldsymbol{\xi}) = \frac{U}{2}\phi^4 - \mu\phi^2 + \int_{\boldsymbol{k}} (\frac{k^2}{2m} - \mu)\frac{\xi_{\boldsymbol{k}}^2}{1-\xi_{\boldsymbol{k}}^2} + \phi^2 \int_{\boldsymbol{k}} \frac{\xi_{\boldsymbol{k}}}{1-\xi_{\boldsymbol{k}}^2} V_{\boldsymbol{k},0} + \phi^2 \int_{\boldsymbol{k}} \frac{\xi_{\boldsymbol{k}}^2}{1-\xi_{\boldsymbol{k}}^2}(U + V_{\boldsymbol{k},0})$$
$$+ \frac{1}{2}\int_{\boldsymbol{k}}\int_{\boldsymbol{k'}} \frac{\xi_{\boldsymbol{k}}}{1-\xi_{\boldsymbol{k}}^2}\frac{\xi_{\boldsymbol{k'}}}{1-\xi_{\boldsymbol{k'}}^2} V_{\boldsymbol{k},\boldsymbol{k'}} + \int_{\boldsymbol{K}}\int_{\boldsymbol{k}} \frac{\xi_{\boldsymbol{K}/2+\boldsymbol{k}}^2}{1-\xi_{\boldsymbol{K}/2+\boldsymbol{k}}^2}\frac{\xi_{\boldsymbol{K}/2-\boldsymbol{k}}^2}{1-\xi_{\boldsymbol{K}/2-\boldsymbol{k}}^2}(U + V_{2\boldsymbol{k},0}). \quad (4.27)$$

4.3.1 The mean field term

To obtain the zeroth order term, we only keep terms scaling with at most $n_0^2 \sim \phi^4 \sim \xi^2$ (note that $\mu \sim n_0$). The expression then takes the simple form

$$E_0(\boldsymbol{\xi}) = \frac{U}{2}\phi^4 - \mu\phi^2 + \int_{\boldsymbol{k}} \frac{k^2}{2m}\xi_{\boldsymbol{k}}^2 + \int_{\boldsymbol{k}} \xi_{\boldsymbol{k}} V_{\boldsymbol{k},0}\phi^2 + \frac{1}{2}\int_{\boldsymbol{k}}\int_{\boldsymbol{k'}} \xi_{\boldsymbol{k}}\xi_{\boldsymbol{k'}} V_{\boldsymbol{k},\boldsymbol{k'}}. \quad (4.28)$$

Surprisingly, we see that the hierarchy of the initial displaced Hamiltonian does not fully determine the hierarchy of terms even for this zeroth-order approximation. We have namely kept a term originating from the quartic term of the Hamiltonian, which is discarded in Bogoliubov theory, and we have discarded a term (the $\phi^2 G$ term) which Bogoliubov theory keeps.

From this starting point, we can now simply minimize the energy as a function of ϕ and ξ. Note that also this is different from Bogoliubov theory, where ϕ and μ are fixed in the beginning. In the variational framework it is important to self-consistently find the ground state and to therefore also treat ϕ as a variational parameter. In the end we can fix the total density via the chemical potential. After some simple algebra we find

$$\mu^{(0)} = U\phi^2 + \int_{\boldsymbol{k}} \xi_{\boldsymbol{k}}^{(0)} V_{\boldsymbol{k},0}, \quad (4.29)$$

$$0 = \frac{k^2}{m}\xi_{\boldsymbol{k}}^{(0)} + \phi^2 V_{\boldsymbol{k},0} + \int d^3k' \xi_{\boldsymbol{k'}}^{(0)} V_{\boldsymbol{k},\boldsymbol{k'}}. \quad (4.30)$$

Eq. (4.30) closely resembles the Schrödinger equation for zero-energy scattering in momentum space (see Sec. 2.2.4). Therefore it is no surprise that the resulting ξ can be expressed in terms of the T-matrix from Eq. (2.21)

$$\xi_{\boldsymbol{k}}^{(0)} = -\frac{m\phi^2 T_{\boldsymbol{k},0}}{k^2}. \quad (4.31)$$

We can now compare more closely the wave function of the BEC, consisting of the coherent and the Gaussian part, and the momentum-space scattering wave function in Eq. (2.20) at zero collision energy. Both in the BEC-case and in the scattering case the wave function consists of one part which describes the undisturbed wave function and a part which describes the scattering. Indeed, in the many-body wave function the coherent state corresponds to the population of the momentum-zero mode, and the Gaussian part takes care of the pairwise scattering. We thus see directly how the T-matrix and the scattering length enter the picture in the Gaussian-state framework.

An expression for the chemical potential can be obtained by inserting Eq. (4.31) in Eq. (4.29)

$$\mu^{(0)} = U\phi^2 - \int_{\boldsymbol{k}} \frac{\phi^2 \; m \; T_{\boldsymbol{k},0} V_{\boldsymbol{k},0}}{k^2} = \frac{4\pi a \phi^2}{m}. \tag{4.32}$$

Here, note the similarity to Eq. (2.21). We have additionally used Eq. (2.22).

In conclusion, we have now retrieved the mean-field term by renormalization of the scattering wave function. This confirms that the result obtained on the level of the Born approximation (4.7) was correct, and that this approximation is thus justified, at least at this level of theory. Let us emphasize again, that already to obtain this zeroth-order term, a quartic term in the Hamiltonian is needed which is dropped on the level of the Bogoliubov approximation.

4.3.2 Quantum corrections

To attempt to extract the quantum corrections, we can add back the lowest-order terms we dropped, the chemical potential term in the dispersion of ξ and the $G\phi^2$ term. This gives rise to modified equations:

$$\mu^{(1)} = U\phi^2 + \int_{\boldsymbol{k}} \xi^{(1)}_{\boldsymbol{k}} V_{\boldsymbol{k},0} + 2\int_{\boldsymbol{k}} [\xi^{(1)}_{\boldsymbol{k}}]^2 (U + V_{\boldsymbol{k},0}), \tag{4.33}$$

$$0 = 2\big[\frac{k^2}{2m} - \mu^{(0)} + \phi^2(U + V_{\boldsymbol{k},0})\big]\xi^{(1)}_{\boldsymbol{k}} + \phi^2 V_{\boldsymbol{k},0} + \int_{\boldsymbol{k}'} \xi^{(1)}_{\boldsymbol{k}'} V_{\boldsymbol{k},\boldsymbol{k}'}. \tag{4.34}$$

We see that there is an additional energy cost for the created pairs due to interactions with the condensate. Eq. (4.34) can be rewritten as

$$\xi^{(1)}_{\boldsymbol{k}} = -\frac{m}{k^2 - 2m\mu^{(0)} + 2m(U + V_{\boldsymbol{k},0})\phi^2}(\phi^2 V_{\boldsymbol{k},0} + \int_{\boldsymbol{k}'} \xi^{(1)}_{\boldsymbol{k}'} V_{\boldsymbol{k},\boldsymbol{k}'}). \tag{4.35}$$

This can approximately be solved as

$$\xi^{(1)}_{\boldsymbol{k}} \approx -\frac{m(\phi^2 + c)T_{\boldsymbol{k},0}}{k^2 - 2m\mu^{(1)} + 2m(U + V_{\boldsymbol{k},0})\phi^2}, \tag{4.36}$$

where we can determine the constant c by:

$$\begin{aligned}(\phi^2 - c)T_{\boldsymbol{k},\boldsymbol{0}} &= \phi^2 V_{\boldsymbol{k},\boldsymbol{0}} - \int_{\boldsymbol{k}'} \frac{m(\phi^2 + c)V_{\boldsymbol{k},\boldsymbol{k}'} T_{\boldsymbol{k}',0}}{k'^2 - 2m\mu^{(0)} + 2m(U + V_{\boldsymbol{k},0})\phi^2}, \\ &\approx \phi^2 V_{\boldsymbol{k},\boldsymbol{0}} + \frac{m(\phi^2 + c)V_{\boldsymbol{k},0}T_{0,0}}{4\pi}\sqrt{4mU\phi^2 - 2m\mu^{(0)}} - \int_{\boldsymbol{k}'} \frac{m(\phi^2 + c)V_{\boldsymbol{k},\boldsymbol{k}'}T_{\boldsymbol{k}',0}}{k'^2}.\end{aligned} \tag{4.37}$$

Neglecting c in the second term, and using again Eq. (2.21), we find that

$$c = \frac{m\phi^2 T_{0,0}}{4\pi}\sqrt{4mU\phi^2 - 2m\mu^{(0)}} + \mathcal{O}(\phi^4). \tag{4.38}$$

To obtain an expression for $\mu^{(1)}$ we also need to solve integrals of the form

$$\begin{aligned}\int_{\boldsymbol{k}} [\xi_{\boldsymbol{k}}^{(1)}]^2 (U + V_{\boldsymbol{k},\boldsymbol{0}}) &\approx \int_{\boldsymbol{k}} \frac{(m\phi^2 T_{\boldsymbol{k},0})^2 (U + V_{\boldsymbol{k},0})}{[k^2 - 2m\mu^{(0)} + 2m(U + V_{\boldsymbol{k},\boldsymbol{0}})\phi^2]^2} [U + V_{\boldsymbol{k},\boldsymbol{0}}], \\ &\approx \frac{2U(m\phi^2 T_{0,0})^2}{2\pi^2} \int \frac{k^2 dk}{(k^2 - 2m\mu^{(0)} + 4mU\phi^2)^2}, \\ &\approx \frac{2U(m\phi^2 T_{\boldsymbol{k},0})^2}{8\pi\sqrt{4mU\phi^2 - 2m\mu^{(0)}}} = 2Un_d, \end{aligned} \tag{4.39}$$

In the second line we have made the approximation that the range of the potential is much smaller than the interparticle distance. This means that $V_{\boldsymbol{k},0} \approx U$ for the relevant integration range for determining the leading term of the integral. For this leading-order result, the c-term does not play a role. The depletion on this level of theory is given by

$$n_d = \int_{\boldsymbol{k}} \langle \hat{b}_{\boldsymbol{k}}^\dagger \hat{b}_{\boldsymbol{k}}^\dagger \rangle = \int_{\boldsymbol{k}} G_{\boldsymbol{k}} \approx \int_{\boldsymbol{k}} [\xi_{\boldsymbol{k}}^{(1)}]^2. \tag{4.40}$$

Plugging this in, and using Eq. (2.21), we find

$$\mu^{(1)} = \frac{4\pi a\phi^2}{m} + 2n_d U + a\phi^2 \mu^{(0)} \sqrt{4mU\phi^2 - 2m\mu^{(0)}}. \tag{4.41}$$

We can now identify the total density as $n_0 = \phi^2 + n_d$. Inserting this, and the definition of n_d into the above equation, we find our final expression

$$\mu^{(1)} = \frac{4\pi a n_0}{m} (1 + \frac{5a\phi}{4} \sqrt{4mU - 8\pi a}). \tag{4.42}$$

Clearly, we have not recovered the familiar LHY expression (4.8). The prefactor of the square root is incorrect, and the expression still depends on the bare coupling strength U.

To identify what is missing in the description, it is important to understand the origin of the LHY correction. Indeed, the additional terms which we added to obtain the LHY correction describe the interactions of the created pairs of excitations with the background condensate. However, at this point we have not yet included a mechanism for these interactions to be renormalized. As a result, the bare coupling still appears. From this insight we can also understand why the LHY correction is correctly recovered by Bogoliubov theory. Here the quadratic interboson repulsion term describing the correction is included. There is no mechanism to renormalize this term, but that is also not needed, because the coupling is used on the level of the Born approximation: the renormalized coupling has been inserted by hand.

Before moving on, let us discuss why the LHY correction appears at all. Having identified that the origin of the LHY term is the interaction between the excitations from the BEC and the particles in the BEC itself, the presence of the LHY correction implies that there is a difference between the two interactions. Otherwise there would be no additional interaction-energy penalty for the presence of these excitations. As explained very well by Leggett [44], this energy penalty follows from the *exchange interactions*. The argument goes as follows. Let us consider a wave function of two bosons

$$\Psi(\boldsymbol{r_1}, \boldsymbol{r_2}) = \langle \boldsymbol{r}_1, \boldsymbol{r}_2 | \Psi \rangle = \phi(\boldsymbol{r}_1)\chi(\boldsymbol{r}_2). \tag{4.43}$$

If $\phi = \chi$ the wave function is symmetric under exchange of the bosons, leading to an interaction energy (in case of contact interactions) of

$$E_U = U \int_{\boldsymbol{r}} |\phi(\boldsymbol{r})|^4. \tag{4.44}$$

If instead ϕ and χ are orthogonal, the wave function needs to be symmetrized

$$\Psi(\boldsymbol{r_1}, \boldsymbol{r_2}) = \langle \boldsymbol{r}_1, \boldsymbol{r}_2 | \Psi \rangle = \frac{1}{\sqrt{2}} \big[\phi(\boldsymbol{r}_1)\chi(\boldsymbol{r}_2) + \phi(\boldsymbol{r}_2)\chi(\boldsymbol{r}_1) \big]. \tag{4.45}$$

Evaluating now again the expectation value of the interaction energy, we find instead

$$E_U = 2U \int_{\boldsymbol{r}} |\phi(\boldsymbol{r})|^2 |\chi(\boldsymbol{r})|^2. \tag{4.46}$$

Therefore, we see that bosons in different modes occupying the same space, such as two different momentum modes, have stronger repulsive interactions than bosons in the same mode. This is essential for the appearance of the LHY term. We indeed recognize that also in our energy functional (4.26), disregarding renormalization of the interactions for a moment, the interactions in the BEC are given by $\frac{1}{2} n_0^2 U$, whereas the interaction between excitations and the BEC are given by $2 n_0 n_d U$. Note here that one of the factors two is simply from the square $(n_0 + n_d)^2$. For repulsive interactions, this additional exchange interactions form a mechanism which stabilizes the BEC and makes excitations out of the BEC additionally unfavorable.

4.4 Beyond-Gaussian state solution

4.4.1 Three-body effects

We now proceed to resolve the renormalization of the interaction between the pairs of excitations which are created and the particles in the background condensate. Let us first take a step back and consider again the general form of the displaced Hamiltonian in Eq. (4.10). All terms have contributed to the mean-field term or the LHY correction, except for the cubic term. The expectation value of the cubic term is zero, since the Gaussian state only creates excitations in pairs. Since we are considering a translationally invariant system, the total momentum of these pairs is zero.

This makes the issue apparent: when one of the constituent particles of the pair scatters with one of the particles from the condensate, the total momentum of this scattering process is *not* zero. Therefore these kind of scattering processes are not correctly renormalized by the variational wave function. Indeed, these processes can be described by the cubic term in the Hamiltonian, and require an extension of the variational wave function. Note that when the calculations are done in a trap [108], this issue might be partially resolved, because then momentum is not conserved.

The natural way to extend the variational Ansatz is to also allow a term with triples of excitations in the exponent. The state then takes the following form:

$$|\psi\rangle = \hat{U}_G \hat{U}_T |0\rangle, \tag{4.47}$$

$$= \hat{U}_G \exp\Big[\frac{1}{\sqrt{2}} \int_{|\boldsymbol{k}|<\Lambda} \int_{|\boldsymbol{p}|>\Lambda} \int_{|\boldsymbol{q}|>\Lambda} \delta(\boldsymbol{k}+\boldsymbol{p}+\boldsymbol{q}) (\alpha_{\boldsymbol{kpq}}\, b^\dagger_{\boldsymbol{k}} b^\dagger_{\boldsymbol{p}} b^\dagger_{\boldsymbol{q}} - h.c.) \Big] |0\rangle. \tag{4.48}$$

In general, exponentials with arguments cubic in the creation and annihilation operators give rise to problems with the normalization of the wave function [107]. Formally, when expanding the power series of the exponential, this gives rise to divergences when computing expectation values. However, for sufficiently small α and especially in the continuum limit, the power series converges and remains stable for many terms before diverging. Hence, when the power series of the exponential is truncated in this stable regime, the resulting

expression still behaves to very high order in perturbation theory as an exponential function. This argument will be made more rigorous in other works, but for our purpose now this normalization problem can safely be ignored.

Further, we have introduced the intermediate momentum scale Λ, because we are trying to describe processes where a single low-momentum excitation from a pair collides with a particle from the condensate. During the collision process, the particles can occupy high momentum modes set by the inverse length scale of the potential. Therefore the triplets need to contain one low-momentum excitation and two high-momentum excitations.

Since $\hat{U}_T$ is unitary, the state is guaranteed to be normalized. Moreover, for small α we can compute expectation values using that

$$\hat{b}_{\boldsymbol{x}}\hat{U}_T|0\rangle = \begin{cases} \hat{U}_T \int_{|\boldsymbol{p}|>\Lambda}\int_{|\boldsymbol{q}|>\Lambda} \delta(\boldsymbol{x}+\boldsymbol{p}+\boldsymbol{q})\frac{\alpha_{\boldsymbol{xpq}}}{\sqrt{2}}\hat{b}^\dagger_{\boldsymbol{p}}\hat{b}^\dagger_{\boldsymbol{q}} + \mathcal{O}(\alpha^3)|0\rangle, & \text{if } x<\Lambda, \\ \hat{U}_T \int_{|\boldsymbol{k}|<\Lambda}\int_{|\boldsymbol{q}|>\Lambda} \delta(\boldsymbol{x}+\boldsymbol{p}+\boldsymbol{q})\sqrt{2}\alpha_{\boldsymbol{kxq}}\hat{b}^\dagger_{\boldsymbol{k}}\hat{b}^\dagger_{\boldsymbol{q}} + \mathcal{O}(\alpha^3)|0\rangle, & \text{if } x>\Lambda. \end{cases} \tag{4.49}$$

As a result, computing expectation values up to order α^2 is still straightforward. Note that the same holds also for Gaussian states.

We can now rewrite the Gaussian operator in the Gaussian state into a Gaussian unitary (see Chap. 3), and use this to transform the Hamiltonian. This is exactly analogous to performing a Bogoliubov rotation (but not the Bogoliubov approximation), and we obtain the energy functional for α. The variables $u_{\boldsymbol{k}}$ and $v_{\boldsymbol{k}}$ can be expressed in terms of $\xi_{\boldsymbol{k}}$ as

$$u_{\boldsymbol{k}} = \frac{1}{\sqrt{1-\xi^2_{\boldsymbol{k}}}}, \tag{4.50}$$

$$v_{\boldsymbol{k}} = \frac{\xi_{\boldsymbol{k}}}{\sqrt{1-\xi^2_{\boldsymbol{k}}}}. \tag{4.51}$$

Up to leading order, the energy takes the following form

$$\begin{aligned} E_\alpha = &\int_{|\boldsymbol{k}|<\Lambda}\int_{|\boldsymbol{p}|>\Lambda}\int_{|\boldsymbol{q}|>\Lambda} (\omega_{\boldsymbol{k}}+\omega_{\boldsymbol{p}}+\omega_{\boldsymbol{q}})\alpha^2_{\boldsymbol{kqp}}\delta(\boldsymbol{k}+\boldsymbol{p}+\boldsymbol{q}) \\ &+ 2\sqrt{2}\phi\int_{|\boldsymbol{k}|<\Lambda}\int_{|\boldsymbol{p}|>\Lambda}\int_{|\boldsymbol{q}|>\Lambda} v_{\boldsymbol{k}}u_{\boldsymbol{q}}u_{\boldsymbol{p}}V_{\boldsymbol{k}/2,(\boldsymbol{p}-\boldsymbol{q})/2}\alpha_{\boldsymbol{kqp}}\delta(\boldsymbol{k}+\boldsymbol{p}+\boldsymbol{q}) \\ +\int_{|\boldsymbol{k}|<\Lambda}\int_{|\boldsymbol{p}|,|\boldsymbol{p'}|>\Lambda}\int_{|\boldsymbol{q}|,|\boldsymbol{q'}|>\Lambda} &u_{\boldsymbol{q}}u_{\boldsymbol{p}}u_{\boldsymbol{q'}}u_{\boldsymbol{p'}}\alpha_{\boldsymbol{kpq}}\alpha_{\boldsymbol{kp'q}}\delta(\boldsymbol{k}+\boldsymbol{p}+\boldsymbol{q})\delta(\boldsymbol{k}+\boldsymbol{p'}+\boldsymbol{q'})V_{(\boldsymbol{p}-\boldsymbol{q})/2,(\boldsymbol{p'}-\boldsymbol{q'})/2}. \end{aligned} \tag{4.52}$$

Here we have only kept the leading-order terms, using that $v_{\boldsymbol{k}}$ only has a large contribution for small k. The effective quadratic part of the Hamiltonian after the Gaussian unitary transformation is diagonal, because otherwise the energy could have been minimized further within the Gaussian-state manifold. It therefore gives rise to the new dispersion $\omega_{\boldsymbol{k}}$, of which we leave the exact form unspecified for now. The cubic and quartic terms are transformed similarly. For the cubic term the leading-order term is linear in ξ, whereas for the quartic term the zeroth-order term is already non-zero, and therefore dominant.

Generally $k \ll q, p$. In this case $\boldsymbol{q} = -\boldsymbol{p}-\boldsymbol{k} \approx -\boldsymbol{p}$, $\omega_{\boldsymbol{p}} \approx \frac{p^2}{2m}$, and $u_{\boldsymbol{p}} \approx 1$. Then Eq. (4.52) simplifies to

$$\begin{aligned} E_\alpha = &\int_{|\boldsymbol{k}|<\Lambda}\int_{|\boldsymbol{p}|>\Lambda}\frac{p^2}{m}\alpha^2_{\boldsymbol{kp-p}} + \sqrt{2}\phi\int_{|\boldsymbol{k}|<\Lambda}\int_{|\boldsymbol{p}|>\Lambda} v_{\boldsymbol{k}}(V_{\boldsymbol{k},\boldsymbol{p}}+V_{0,\boldsymbol{p}})\alpha_{\boldsymbol{kp-p}} \\ &+\int_{|\boldsymbol{k}|<\Lambda}\int_{|\boldsymbol{p}|,|\boldsymbol{p'}|>\Lambda}\alpha_{\boldsymbol{kp-p}}\alpha_{\boldsymbol{kp'-p'}}V_{\boldsymbol{p},\boldsymbol{p'}}. \end{aligned} \tag{4.53}$$

Minimizing this energy functional gives

$$0 = \frac{p^2}{m}\alpha_{\boldsymbol{kp-p}} + \frac{(V_{\boldsymbol{k},\boldsymbol{p}} + V_{0,\boldsymbol{p}})}{\sqrt{2}}\phi v_{\boldsymbol{k}} + \int_{\boldsymbol{q}} V_{\boldsymbol{q},\boldsymbol{p}}\alpha_{\boldsymbol{kq-q}}, \tag{4.54}$$

We can again solve this equation in terms of the T-matrix

$$\alpha_{\boldsymbol{kp-p}} = -\frac{m\phi v_{\boldsymbol{k}}(T_{\boldsymbol{p},\boldsymbol{k}} + T_{\boldsymbol{p},\boldsymbol{0}})}{\sqrt{2}p^2}. \tag{4.55}$$

Plugging this back into Eq. (4.53), gives

$$\begin{aligned} E_\alpha &= \phi^2 \int_{\boldsymbol{k}} v_{\boldsymbol{k}}^2 \int_{\boldsymbol{p}} \frac{(T_{\boldsymbol{p},\boldsymbol{k}} + T_{\boldsymbol{p},0})^2}{2p^2} - \phi^2 \int_{\boldsymbol{k}} v_{\boldsymbol{k}}^2 \int_{\boldsymbol{p}} \frac{m(V_{\boldsymbol{p},\boldsymbol{k}} + V_{\boldsymbol{p},0})(T_{\boldsymbol{p},\boldsymbol{k}} + T_{\boldsymbol{p},0})}{p^2} \\ &+ \phi^2 \int_{\boldsymbol{k}} v_{\boldsymbol{k}}^2 \int_{\boldsymbol{p}} \int_{\boldsymbol{p'}} \frac{m(T_{\boldsymbol{p},\boldsymbol{k}} + T_{\boldsymbol{p},0})}{p^2} \frac{m(T_{\boldsymbol{p'},\boldsymbol{k}} + T_{\boldsymbol{p'},0})}{p'^2} V_{\boldsymbol{p},\boldsymbol{p'}}, \\ &= -\phi^2 \int_{\boldsymbol{k}} v_{\boldsymbol{k}}^2 \int_{\boldsymbol{p}} \frac{m(V_{\boldsymbol{p},\boldsymbol{k}} + V_{\boldsymbol{p},\boldsymbol{0}})(T_{\boldsymbol{p},\boldsymbol{k}} + T_{\boldsymbol{p},0})}{2p^2}, \\ &= (\frac{4\pi a}{m} - U)2\phi^2 \int_{\boldsymbol{k}} G_{\boldsymbol{k}}, \end{aligned} \tag{4.56}$$

where we used that $G_{\boldsymbol{k}} = v_{\boldsymbol{k}}^2$.

Adding this term to the energy functional of the Gaussian state (4.26), we find that in the term giving rise to the LHY energy, the bare coupling U is replaced by the renormalized coupling $\frac{4\pi a}{m}$. If one follows the entire derivation of subsection 4.3.2, one finds that this replacement carries all the way through until the end, the equation for $\mu^{(1)}$. Including the three-body correction this now becomes

$$\mu^{(1)} = \frac{4\pi a n_0}{m}[1 + 5a^{3/2}\phi\sqrt{\frac{\pi}{2}}]. \tag{4.57}$$

The term does not contain the bare coupling any more, but the prefactor $5\sqrt{\pi/2} \approx 6.26$ is different from the LHY result of $\frac{32}{3\sqrt{\pi}} \approx 6.02$. This is because for small k, the truncation up to quadratic order of ξ was not warranted. Including the correct three-body contribution to the energy functional, we will now fully solve the equations and obtain the correct LHY-correction.

4.4.2 LHY result

To obtain the full LHY results, we will first derive general expressions in terms of the T-matrix. Aside from the case of short-range interactions, we show that we can then also apply the result to the case of dipolar interactions. We will now work with the energy functional

$$\begin{aligned} E \approx \frac{1}{\Omega}\langle 0|\hat{U}_T^\dagger \hat{U}_G^\dagger \hat{U}_c^\dagger \hat{\mathcal{H}} \hat{U}_c \hat{U}_G \hat{U}_T|0\rangle &= \frac{U}{2}\phi^4 - \mu\phi^2 + \int_{\boldsymbol{k}} (\frac{k^2}{2m} - \mu)G_{\boldsymbol{k}} + \phi^2 \int_{\boldsymbol{k}} F_{\boldsymbol{k}} V_{\boldsymbol{k},0} \\ &+ \phi^2 \int_{\boldsymbol{k}} G_{\boldsymbol{k}}(\frac{8\pi a}{m} - U + V_{\boldsymbol{k},0}) + \frac{1}{2}\int_{\boldsymbol{k}} \int_{\boldsymbol{k'}} F_{\boldsymbol{k}} F_{\boldsymbol{k'}} V_{\boldsymbol{k},\boldsymbol{k'}}. \end{aligned} \tag{4.58}$$

We have dropped the G^2, because this term has no contribution yet on this level of theory. We now derive equations for ϕ and ξ without truncating, which yields

$$0 = -2\mu\phi + 2\phi^3 U + \frac{2\phi}{(2\pi)^3}\int_{\boldsymbol{k}}(F_{\boldsymbol{k}} + G_{\boldsymbol{k}})V_{\boldsymbol{k},0} + \frac{2\phi(\frac{8\pi a}{m} - U)}{(2\pi)^3}\int_{\boldsymbol{k}} G_{\boldsymbol{k}}, \tag{4.59}$$

$$0 = 2\big[\frac{k^2}{2m} - \mu + (\frac{8\pi a}{m} - U)\phi^2 + \phi^2 V_{\boldsymbol{k},0}\big]\xi_{\boldsymbol{k}} + (1 + \xi_{\boldsymbol{k}}^2)(\phi^2 V_{\boldsymbol{k},0} + \int_{\boldsymbol{q}} V_{\boldsymbol{k},\boldsymbol{q}} F_{\boldsymbol{q}}). \tag{4.60}$$

Now we can define

$$\mathcal{E}_{\boldsymbol{k}} = \frac{k^2}{2m} - \mu + (\frac{8\pi a}{m} - U)\phi^2 + \phi^2 V_{\boldsymbol{k},0}, \tag{4.61}$$

$$\Delta_{\boldsymbol{k}} = \phi^2 V_{\boldsymbol{k},0} + \int_{\boldsymbol{q}} V_{\boldsymbol{k},\boldsymbol{q}} F_{\boldsymbol{q}}. \tag{4.62}$$

This way we find:

$$\xi_{\boldsymbol{k}} = \frac{-\mathcal{E}_{\boldsymbol{k}} + \sqrt{\mathcal{E}_{\boldsymbol{k}}^2 - \Delta_{\boldsymbol{k}}^2}}{\Delta_{\boldsymbol{k}}}, \tag{4.63}$$

$$F_{\boldsymbol{k}} = \frac{-\Delta_{\boldsymbol{k}}}{2\sqrt{\mathcal{E}_{\boldsymbol{k}}^2 - \Delta_{\boldsymbol{k}}^2}}, \tag{4.64}$$

$$G_{\boldsymbol{k}} = \frac{\mathcal{E}_{\boldsymbol{k}}}{2\sqrt{\mathcal{E}_{\boldsymbol{k}}^2 - \Delta_{\boldsymbol{k}}^2}} - \frac{1}{2}. \tag{4.65}$$

For large k, $F_{\boldsymbol{k}} \approx \xi_{\boldsymbol{k}}$ and motivated by the previous analysis, we write

$$F_{\boldsymbol{k}} = -\frac{m\phi^2 T_{\boldsymbol{k},\boldsymbol{0}}}{k^2} + \delta F_{\boldsymbol{k}}, \tag{4.66}$$

$$\Delta_{\boldsymbol{k}} = \phi^2 T_{\boldsymbol{k},\boldsymbol{0}} + \int_{\boldsymbol{q}} V_{\boldsymbol{k},\boldsymbol{q}} \delta F_{\boldsymbol{q}}. \tag{4.67}$$

Up to leading order, $\mathcal{E}_{\boldsymbol{k}}$ is given by

$$\mathcal{E}_{\boldsymbol{k}} \approx \frac{k^2}{2m} + \phi^2 T_{\boldsymbol{k},0}. \tag{4.68}$$

For large momenta only the kinetic part of $\mathcal{E}$ matters, and for small momenta $\frac{4\pi a}{m} - U + V_{\boldsymbol{k},\boldsymbol{0}} \approx T_{\boldsymbol{k},\boldsymbol{0}}$. For short-range interactions this is exact, for dipolar interactions this is true in the Born approximation for the angle-dependent contributions.

This means that

$$\mathcal{E}_{\boldsymbol{k}}^2 - \Delta_{\boldsymbol{k}}^2 \approx \frac{k^2}{2m}(\frac{k^2}{2m} + 2\phi^2 T_{\boldsymbol{k},0}). \tag{4.69}$$

The depletion is given by

$$\begin{aligned} n_d = \int_{\boldsymbol{k}} G_{\boldsymbol{k}} &\approx \int_{\boldsymbol{k}} \Big[\frac{\frac{k^2}{2m} + \phi^2 T_{\boldsymbol{k},0}}{2\sqrt{\frac{k^2}{2m}(\frac{k^2}{2m} + 2\phi^2 T_{\boldsymbol{k},0})}} - \frac{1}{2}\Big], \\ &\approx \frac{1}{(2\pi)^3}\int d\Omega \int_0^\infty dk\, \Big[\frac{k}{2}\sqrt{k^2 + 4m\phi^2 T_{\boldsymbol{k},0}} - \frac{mk\phi^2 T_{\boldsymbol{k},0}}{\sqrt{k^2 + 4m\phi^2 T_{\boldsymbol{k},0}}} - \frac{k^2}{2}\Big], \\ &\approx \frac{2}{3}m^{3/2}\phi^3 \frac{1}{(2\pi)^3}\int d\Omega \lim_{k\to 0} T_{\boldsymbol{k},0}^{3/2}. \end{aligned} \tag{4.70}$$

Here we have implicitly split the integrals in small-k and large-k parts. In the small-k part, the T-matrix is independent of k, and for large k the contribution of the $T\phi^2$-terms is negligible compared to the kinetic energy terms. Therefore the k-dependence of T is not important in either part of the integrals, and does not need to be considered.

The equation for $F_{\boldsymbol{k}}$ becomes

$$F_{\boldsymbol{k}} = -\frac{\phi^2 V_{\boldsymbol{k},0} + \int_{\boldsymbol{q}} V_{\boldsymbol{k},\boldsymbol{q}} F_{\boldsymbol{q}}}{2\sqrt{\frac{k^2}{2m}(\frac{k^2}{2m} + 2\phi^2 T_{\boldsymbol{k},0})}}. \tag{4.71}$$

Following a procedure similar to the solution of Eq. (4.36), we find

$$F_{\boldsymbol{k}} = \frac{-(\phi^2 + 3n_d)T_{\boldsymbol{k},0}}{2\sqrt{\frac{k^2}{2m}(\frac{k^2}{2m} + 2\phi^2 T_{\boldsymbol{k},0})}}. \tag{4.72}$$

For μ, we now obtain

$$\begin{aligned}\mu &= \phi^2 U + \int_{\boldsymbol{k}} [F_{\boldsymbol{k}} + G_{\boldsymbol{k}}]V_{\boldsymbol{k}} + (\frac{8\pi a}{m} - U)\int_{\boldsymbol{k}} G_{\boldsymbol{k}}, \\ &= \frac{4\pi a n_0}{m} + 4n_d(\frac{4\pi a}{m} - U) + \frac{8m^{3/2}\phi^3}{3}\frac{1}{(2\pi)^3}\int d\Omega V_{\boldsymbol{k}} T_{\boldsymbol{k},0}^{3/2}. \end{aligned} \tag{4.73}$$

$$\tag{4.74}$$

If we consider the case of short-range interactions

$$\lim_{k\to 0} T_{\boldsymbol{k},0} = \frac{4\pi a}{m}. \tag{4.75}$$

Then

$$n_{dep} = \frac{8}{3\sqrt{\pi}}(a\phi^2)^{3/2}, \tag{4.76}$$

$$\mu = \frac{4\pi a n_0}{m}(1 + \frac{32\sqrt{n_0 a^3}}{3\sqrt{\pi}}). \tag{4.77}$$

We have indeed recovered the familiar LHY result (4.8) we also found from Bogoliubov theory.

4.4.3 Dipolar interactions

Aside from short-range interactions, we can also consider dipolar interactions. Let us assume the dipoles are aligned in the z-direction and take a dipolar interaction of the form

$$V(\boldsymbol{r}) = \frac{C_d}{4\pi r^3}(1 - 3\cos^2\theta_r), \tag{4.78}$$

where θ_r is the angle between vector $\boldsymbol{r}$ and the z-direction. One can now define a dipolar length a_d analogous to the scattering length, which will be given by

$$a_{dd} = \frac{C_d \mu_r}{6\pi}. \tag{4.79}$$

In momentum space, the low-momentum contributions to the potential take the following form

$$\lim_{\boldsymbol{q}\to 0} V_{\boldsymbol{q},0} = U + \frac{2\pi a_d}{\mu_r}(3\cos^2\theta_{\boldsymbol{q}} - 1). \tag{4.80}$$

For dipolar potentials, the angle-dependent term is typically well described on the level of the Born approximation [126, 127]. This means that the low-momentum T-matrix can be written as

$$\lim_{\boldsymbol{q}\to 0} T_{\boldsymbol{q},0} = \frac{2\pi}{\mu_r}\big[a + a_d(3\cos^2\theta_{\boldsymbol{q}} - 1)\big]. \tag{4.81}$$

Here it is important to note that for fixed U, a_d can have a significant impact also on the scattering length a. Furthermore, for dipolar interactions $V_{0,0}$ and $T_{0,0}$ are not uniquely defined, and depend on the direction in which the limit to infinite system size is taken. In our equations we will assume the completely isotropic case, so that $V_{0,0} = U$ and $T_{0,0} = \frac{2\pi a}{\mu_r}$. The mean-field term is therefore the same as for the contact-interaction case.

If we now define $\epsilon_d = \frac{a_d}{a}$, we find

$$n_d = \frac{2}{3}m^{3/2}\phi^3\frac{1}{(2\pi)^3}\int d\Omega\Big(\frac{4\pi a}{m}\Big)^{3/2}\big[1 + \epsilon_d(3\cos^2\theta_{\boldsymbol{k}} - 1)\big]^{3/2}, \tag{4.82}$$

$$n_d = \frac{4\phi^3 a^{3/2}}{3\sqrt{\pi}}(1-\epsilon_d)^{3/2}\int_0^1 dy\frac{1}{\sqrt{y}}\big[1 + \frac{3\epsilon_d}{1-\epsilon_d}y\big]^{3/2}, \tag{4.83}$$

$$n_d = \frac{8\phi^3 a^{3/2}}{3\sqrt{\pi}}\mathcal{Q}_3(\epsilon_d), \tag{4.84}$$

where Q_l is defined in terms of the hypergeometric function ${}_2F_1$:

$$Q_l(\epsilon_d) = (1-\epsilon_d)^{l/2}\ {}_2F_1\big(-l/2, 1/2; 3/2, \frac{3\epsilon_d}{\epsilon_d - 1}\big). \tag{4.85}$$

In this case

$$\mu = \frac{4\pi a n_0}{m} + \frac{8m^{3/2}\phi^3}{3}\frac{1}{(2\pi)^3}\big(\frac{4\pi}{m}\big)^{5/2}\int d\Omega\big[a + a_d(3\cos^2\theta_{\boldsymbol{k}} - 1)\big]^{5/2}, \tag{4.86}$$

$$= \frac{4\pi a n_0}{m}[1 + \frac{32\sqrt{n_0 a^3}}{3\sqrt{\pi}}Q_5(\epsilon_d)]. \tag{4.87}$$

$$\tag{4.88}$$

This agrees with the result of Refs. [128, 129].

4.5 Conclusion and discussion

We have studied how to variationally derive the first-order quantum-fluctuation correction in Bose-Einstein condensates at zero temperature, for explicit finite-range interactions. Even though Bogoliubov theory already recovers this correction, the Bogoliubov approach is not self-consistent. When we formulated the problem self-consistently within the Gaussian-state variational framework, we found that pairwise interboson correlations are not sufficient to recover the LHY correction. Indeed, we showed that the interactions of the pairwise excitations with the background BEC are the origin of the LHY correction, and that these interactions are not renormalized on the Gaussian-state level of theory. We demonstrated that by including three-body correlations in the wave function, this issue can be resolved, leading to the classic LHY result. We retrieved our final equations in terms of the T-matrix, allowing us to readily generalize the result to the case of dipolar scattering. Also in this case, our result is in agreement with the literature.

Even though the approach we used here is not the most straightforward way to derive the LHY corrections, it allows for a physical interpretation how the actual scattering

processes in the BEC influence its energy. This approach can further be extended to also derive higher-order LHY corrections.

This study also provides a good background for studies of the Bose polaron problem using Gaussian states, since we have now clearly verified that at least the main contribution to the interboson interaction energy is correctly renormalized. We have also identified which terms in the energy functional gives rise to the renormalization effect. This will turn out useful when constructing an approximate energy functional for the Bose polaron in Chapter 6.

Altogether this was a good first step towards our goal of developing a deep understanding of scattering processes in a quantum medium, and their description in terms of Gaussian states and beyond.

Part B. Bose polarons

Abstract

When an impurity atom is immersed in a Bose-Einstein condensate it forms a Bose polaron. We study the fate of the attractive Bose polaron for a sweep of the boson-impurity interaction strength across a Feshbach resonance. In particular, we study the role of the Efimov effect and three-body correlations. We find that the chemical processes that the impurity can undergo with the bath atoms, are significantly affected by the degeneracy of the background medium.

In Chapter 5 we consider the case of weak interactions in the background BEC which we describe using the Bogoliubov approximation. We use a Gaussian-state approach in the reference frame of the impurity to describe the polaron cloud. First we demonstrate that the heteronuclear Efimov effect extends beyond three particles, and that when more particles bind to the impurity, the binding energy per particle increases, showing *cooperative binding*. Since these many-body bound states are lower in energy than the polaron, the polaron is no longer the ground state of the system, but only a metastable excited state. For a large range of interaction strengths, there is no efficient decay mechanism from the polaron into the large clusters, but at a certain critical scattering length the impurity starts to efficiently mediate attractive interactions, triggering a collapse of the BEC into the deeply bound Efimov clusters. The onset of this instability is closely tied to the three-body Efimov resonance, but it is shifted due to the polaronic dressing of the impurity.

In presence of explicit repulsion between the bosons from the BEC a competition emerges between the impurity-mediated attraction and the intrinsic interboson repulsion. In Chapter 6 we develop a quantum-chemistry inspired variational approach to incorporate the interboson repulsion and to study this competition in detail. We find that the polaronic instability persists for modest interboson repulsion if the impurity is light, and that it can be interpreted as a first-order transition. If the interboson repulsion is increased, this transition terminates in a critical point, beyond which there is instead a smooth crossover. In the crossover regime the polaron gradually changes into a few-particle molecule for increasing interaction strength. We find an analytical model with a simplified wave function which can qualitatively capture this phase diagram, and show that it can be interpreted in terms of the well-known Landau model. Furthermore, we find that both the instability and crossover regimes are accessible with realistic experimental parameters.

In Chapter 7 we explore in more detail the crossover regime, and the nature of the

dressed molecules which are formed. We consider the concrete system of a ^{40}K impurity in a BEC of ^{23}Na, in collaboration with the experimental group of Martin Zwierlein. In their injection spectroscopy experiments, an attractive polaron state is initially prepared, after which the impurity is transferred via a radiofrequency transition to a final state with a large positive scattering length. In a thermal gas this would lead to the production of Feshbach molecules, but in presence of the BEC we find that the formed molecules experience a substantial many-body dressing. Indeed, we show that not just dimer states are formed, but superpositions of a dimer, a trimer, and a free impurity state. This highlights how molecule formation proceeds qualitatively different in presence of a background BEC, showing a remarkable example of chemistry in a quantum medium.

Chapter 5. Polaronic instability and shifted Efimov resonance

The content of this chapter is based on the two companion papers

[1] Arthur Christianen, J. Ignacio Cirac, Richard Schmidt,
Chemistry of a Light Impurity in a Bose-Einstein Condensate,
Physical Review Letters 128, 183401 (2022)

[2] Arthur Christianen, J. Ignacio Cirac, Richard Schmidt,
Bose polaron and the Efimov effect: A Gaussian-state approach,
Physical Review A 105, 053302 (2022),

The presentation in this chapter follows Ref. [2]. In the introduction, excerpts from Ref. [3] are used.

5.1 Introduction

How can molecules form in a quantum gas of ultracold atoms? Original studies in this direction were performed in Fermi-Fermi mixtures to probe the crossover from a Bardeen-Cooper-Schrieffer (BCS) state, where pairs of fermions form Cooper pairs, to a BEC of diatomic molecules, where the fermions have formed bound states [130–135]. This BCS-to-BEC crossover was originally discussed in the context of condensed matter [136] and is another example of an interesting phenomenon first observed with ultracold atoms.

In the density-imbalanced limit, a precursor of the BCS-to-BEC crossover is already observed in the Fermi polaron problem [137–142] of a single impurity immersed in a Fermi sea. In this model, there is a sharp transition from a polaronic state to a molecular state. Here the molecule is formed by an impurity bound to a single fermion from the bath (except in the very-mass imbalanced case [143]). The reason only one particle from the bath binds to the impurity, is simply the Pauli exclusion principle.

In the Bose polaron case [144–146] this Pauli constraint is obviously absent, and it is known from the Efimov effect that forming bound states with multiple bosons is actually favorable. Therefore, already at this point is seems clear that the phenomenology for the Bose polaron case will not be as straightforward as in the Fermi polaron case. Furthermore, the formation of Feshbach molecules is not the only chemical process of interest here, because the Efimov resonance also leads to an enhanced probability for the three-body recombination reaction. Hence, if the many-body physics somehow affects this resonance, it will also have a direct impact on the chemical recombination rate.

It has indeed been established theoretically that the Efimov effect is important in the Bose polaron framework [147–149], but the exact role the Efimov effect plays is still debated. For the Fermi polaron, descriptions allowing for only few excitations from the Fermi gas have been successful [137, 140], and when variations of such approaches are applied to the Bose polaron case [147–150], one finds a smooth crossover from the polaron

into a dimer, trimer or tetramer. These results were corroborated with quantum Monte Carlo studies, for equal mass or heavy impurities [150, 151].

However, in absence of interboson interactions it is clear that a few excitations are not enough to capture the polaron properties. Indeed, for non-interacting bosons the polaron energy will diverge at unitarity because the bosons accumulate in the boson-impurity bound state which emerges in the spectrum at negative energy. This effect persists in presence of interboson repulsion treated using the Bogoliubov approximation, as shown with a coherent-state approach in Ref. [152]. Here, they found an analytical expression for the polaron energy, given by

$$E_{MF} = \frac{2\pi n_0}{\mu_r(a^{-1} - a_0^{-1})}. \tag{5.1}$$

Here a_0 is positive and given in Eq. (5.11). Thus, on the Bogoliubov level, the interboson repulsion only has the effect of shifting the scattering length of the divergence from unitarity to a positive value, but qualitatively the picture does not change. In Ref. [153] a divergence of the polaron energy was predicted already at negative scattering lengths, using a renormalization-group approach. Even though we do not expect these divergences to happen in presence of realistic interboson repulsion, this still shows that approaches based on the truncation of the number of excitations from the BEC are missing something, for they do not capture the behavior in case of a non-interacting BEC.

Since a divergence of the polaron energy arises when a two-body bound state appears, the natural question is whether something similar happens for a three-body bound state. The first three-body bound state appears at a_-, the scattering length of the first Efimov resonance. As a_- is negative, an instability arising from three-body effects would happen already for weaker interactions than the divergence in energy predicted by the coherent-state approach.

In this Chapter we investigate the occurrence and the properties of such a polaronic instability due to three-body effects. To this end, we employ a Gaussian-state approach in the reference frame of the impurity. This systematically extends the coherent-state Ansatz to include pairwise interboson correlations, and three-body correlations involving the impurity. As a result, we can describe both the many-body physics of the creation of a macroscopic polaron cloud and the few-body physics of the Efimov effect. In particular, we study how these two phenomena affect each other. We focus on the case of light impurities, for which the impurity can efficiently mediate interactions between the bosons, and the Efimov effect is thus most prominent [77, 84, 86, 87, 148, 154]. In Chapter 6 we will then introduce explicit repulsion in the BEC, and compare our Gaussian-state approach to the double-excitation approach [147, 149, 150].

One of our key results, illustrated in Fig. 5.1, is that even at negative scattering lengths, the polaron is no longer the ground state when three-body correlations are taken into account. This finding is a result of large Efimov clusters that emerge deep in the energy spectrum. However, the polaron remains a metastable excited state up to a critical scattering length a^*, at which an energy barrier protecting the polaron from decaying into Efimov clusters disappears. This critical scattering length can be interpreted as a many-body shifted Efimov resonance.

Our results find an intuitive explanation when first considering the question how the heteronuclear Efimov effect extends to the case of more than three particles. As discussed in Section 2.4.4, for the homonuclear case this extension to larger particle numbers is well understood [77, 89] and four- and five particle Efimov clusters have been experimentally observed [90, 91]. However, in the case where the bosons only interact attractively with the impurity, but do not interact or interact only repulsively with each other, there is no

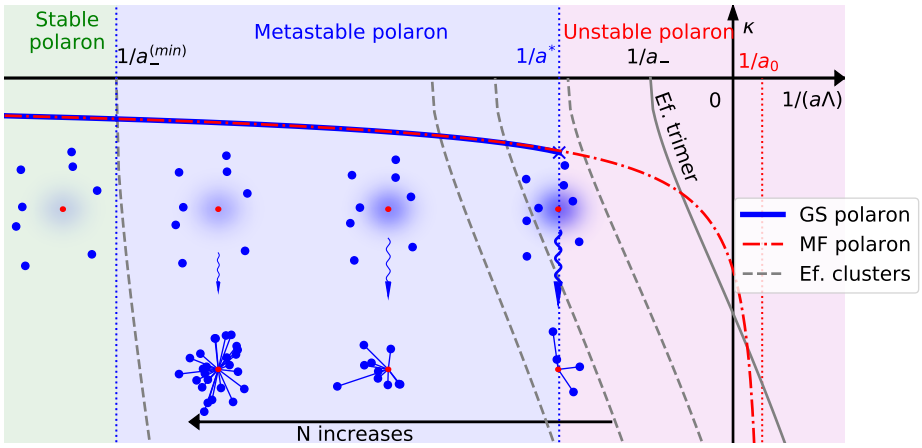

Figure 5.1: Illustration of the main results of this work. Here we show the wave number $\kappa = -\frac{\sqrt{M|E|}}{\Lambda}$ of the polaron found using Gaussian States (blue) and mean-field theory (red dash-dotted) as a function of the inverse scattering length $(1/a\Lambda)$. In gray the wave number of the Efimov trimer (solid line), and larger Efimov clusters (dashed lines) is shown. Note that the dashed lines are only representative and not all possible Efimov clusters are displayed. For small scattering lengths (green area), the polaron is the ground state of the system and a stable quasiparticle. For $|a| > |a_-^{(min)}|$, the smallest scattering length at which an Efimov cluster can be formed, the polaron turns into a metastable excited state, which can decay into the large Efimov clusters via many-body scattering processes. These scattering processes become more likely as the absolute value of the scattering length increases. When a critical scattering length a^* is reached, the polaron ceases to exist as a well-defined quasiparticle. At this point scattering of the polaron with one or two more bath particles can lead to the rapid decay into an Efimov cluster. In contrast, in mean field theory, the polaron remains stable up to a positive scattering length a_0, at which an infinite number of particles piles up in two-body bound states formed with the impurity.

general picture for the existence of clusters with increasing size.

Here we assume weakly interacting bosons and use a single-channel model to describe the interactions with the impurity. We show that in this scenario, similar to the homonuclear case, clusters of increasing particle number become more and more tightly bound. We will refer to this effect as "cooperative binding". This term originates from chemistry, where it pertains to particles cooperating with each other to lead to ever stronger binding, such as in the famous example of oxygen binding to hemoglobin.

Strikingly, we find that the cooperative binding effect has a profound impact on the stability of Bose polarons. This is also illustrated in Fig. 5.1, where we schematically plot the wave number of the polaron state found from Gaussian (blue solid line) and coherent states (red dash-dotted line) as a function of the dimensionless scattering length. The result from coherent states is referred to as mean-field theory. The gray solid line indicates the position of the lowest three-body Efimov state in vacuum, appearing at the three-atom scattering threshold at a_-. The gray dashed lines indicate the lowest Efimov clusters of increasing particle number, which shift to the left as a function of particle number. Using simple arguments, we prove that there is a minimum scattering length $a_-^{(min)}$ needed to form any Efimov cluster, which is indicated as the boundary of the green shaded area in Fig. 5.1.

The background color of the figure indicates the stability of the polaron. In the green area, no Efimov cluster can be formed, meaning that the polaron is the ground state of the extended Fröhlich Hamiltonian [49]. When crossing $a_-^{(min)}$ into the blue area, the polaron is no longer the absolute ground state, but becomes a metastable excited state. For scattering lengths $|a| < |a^*|$, the decay of the polaron into Efimov clusters, indicated by wiggly vertical arrows, is extremely slow and requires the simultaneous scattering of a large number of bosons on the polaron. However, as the magnitude of the scattering length increases, both the number of particles in the polaron cloud increases and the number of particles needed to form a bound state decreases. As a result, the decay processes will become more and more pronounced. When a^* is crossed into the red area, already scattering of only one or two additional bosons is sufficient to cause the breakdown of the polaron into an Efimov cluster. Since these decay processes are included in our Gaussian-state Ansatz, the local energy minimum of the polaron on our variational manifold disappears, meaning the polaron is no longer a metastable quasiparticle. Since the field of the background BEC couples the different particle number clusters, we find a cascade of the wave function into ever larger Efimov clusters.

One remarkable outcome of our study is that $|a^*|$ is smaller than $|a_-|$. This is caused by the fact that the polaron can decay immediately into larger clusters than the Efimov trimer, requiring smaller scattering lengths due to the cooperative binding. In experiments, the formation of these large Efimov clusters will cause rapid chemical recombination into deeply bound states not included in our model. Furthermore, the shift of the Efimov resonance means that the experimentally observed resonant recombination signal will be modified by the degeneracy of the BEC. This provides a fascinating example of how chemistry is modified in a quantum medium and how polaron-cloud formation can enhance chemical reactivity in a nontrivial way.

The structure of the Chapter is as follows: after introducing our theoretical methods in Section 5.2, we prove in Section 5.3 that our Gaussian-state Ansatz incorporates Efimov physics. Moreover, we present evidence for the cooperative binding effect extending to large particle numbers, and we elucidate the origin of this effect. We demonstrate that many-body Efimov clusters form the ground state of the Hamiltonian. Then, in Section 5.4, we use the Gaussian-state Ansatz to calculate the energy of the polaron as a function of scattering length and density, and we demonstrate its abrupt instability. In Section 5.5 we discuss the limitations of our approach and how our results can be probed experimentally. We conclude in Section 5.6 with an outlook on future work.

5.2 Theoretical model

5.2.1 Hamiltonian

We consider a three-dimensional homogeneous BEC of bosons of mass m described by creation and annihilation operators $\hat{b}^\dagger$ and $\hat{b}$, with interaction potential $V_{BB}(\boldsymbol{r'} - \boldsymbol{r})$ and a chemical potential μ_B. In this BEC we immerse one impurity of mass M described in first quantization with momentum and position operators $\hat{\boldsymbol{P}}$ and $\hat{\boldsymbol{R}}$. The impurity-boson interaction potential is given by $V_{IB}(\boldsymbol{r} - \hat{\boldsymbol{R}})$. This gives rise to the Hamiltonian

$$\hat{\mathcal{H}}_0 = -E_{bg} + \int_{\boldsymbol{k}} \Big(\frac{k^2}{2m} - \mu_B\Big)\hat{b}^\dagger_{\boldsymbol{k}}\hat{b}_{\boldsymbol{k}} + \frac{\hat{\boldsymbol{P}}^2}{2M} + \int_{\boldsymbol{r}} V_{IB}(\boldsymbol{r} - \hat{\boldsymbol{R}})\hat{b}^\dagger_{\boldsymbol{r}}\hat{b}_{\boldsymbol{r}} + \frac{1}{2}\int_{\boldsymbol{r'}}\int_{\boldsymbol{r}} V_{BB}(\boldsymbol{r'} - \boldsymbol{r})\hat{b}^\dagger_{\boldsymbol{r'}}\hat{b}^\dagger_{\boldsymbol{r}}\hat{b}_{\boldsymbol{r'}}\hat{b}_{\boldsymbol{r}}. \quad (5.2)$$

Here E_{bg} indicates the energy of the background BEC. The first step, just as in the Chapter 4, is to displace the background BEC using

$$\hat{U}_{n_0} = \exp[\int_{\boldsymbol{r}} \sqrt{n_0}(\hat{b}^\dagger_{\boldsymbol{r}} - \hat{b}_{\boldsymbol{r}})]. \tag{5.3}$$

How we subsequently treat the interboson repulsion is the largest difference between this Chapter and the following Chapter 6. In the present Chapter, we first take the Bogoliubov approximation in the background BEC, as discussed in Sec. 4.2. In Chapter 6 we do not take the Bogoliubov approximation and proceed with the coherent-state description of the background BEC.

Important is the way in which the impurity degrees of freedom are treated. In the system as a whole, the total momentum is conserved. As a result, the momentum of one of the particles can be specified exactly if we know this total momentum and the sum of the momenta of all the other particles. Here, we choose this one particle to be the impurity. Concretely, we apply a unitary translation operator to the Hamiltonian, which brings us to the reference frame where the impurity is at the center. Key here is to use the total momentum of the background bosons as the generator for this translation. The resulting transformation is called the Lee-Low-Pines (LLP) transformation [152, 155], and is given by

$$\hat{U}_{LLP} = \exp(-i\hat{\boldsymbol{R}} \int_{\boldsymbol{k}} \boldsymbol{k}\ \hat{b}^\dagger_{\boldsymbol{k}} \hat{b}_{\boldsymbol{k}}). \tag{5.4}$$

We now discuss the case where we first take the Bogoliubov approximation. In this case

$$\begin{aligned}\hat{\mathcal{H}} = \hat{U}^\dagger_{LLP}\hat{\mathcal{H}}_{\mathrm{Bog}}\hat{U}_{LLP} = \int_{\boldsymbol{k}} \omega_k \hat{\beta}^\dagger_{\boldsymbol{k}}\hat{\beta}_{\boldsymbol{k}} + \frac{[\boldsymbol{P} - \int_{\boldsymbol{k}} \boldsymbol{k}\ \hat{\beta}^\dagger_{\boldsymbol{k}}\hat{\beta}_{\boldsymbol{k}}]^2}{2M} + gn_0 \\ + g\sqrt{n_0}\int_{\boldsymbol{k}}^{\Lambda} W_k[\hat{\beta}^\dagger_{\boldsymbol{k}} + \hat{\beta}_{-\boldsymbol{k}}] + g\int_{\boldsymbol{k}}^{\Lambda}\int_{\boldsymbol{k'}}^{\Lambda} \big[V^{(1)}_{k,k'}\hat{\beta}^\dagger_{\boldsymbol{k}}\hat{\beta}_{\boldsymbol{k'}} + \frac{V^{(2)}_{k,k'}}{2}(\hat{\beta}^\dagger_{\boldsymbol{k}}\hat{\beta}^\dagger_{\boldsymbol{k'}} + \hat{\beta}_{-\boldsymbol{k}}\hat{\beta}_{-\boldsymbol{k'}})\big].\end{aligned} \tag{5.5}$$

where

$$W_k = \frac{k}{\sqrt{2m\omega_k}}, \tag{5.6}$$

$$V^{(1)}_{k,k'} = \frac{W_k W_{k'}}{2} + \frac{1}{2(W_k W_{k'})}, \tag{5.7}$$

$$V^{(2)}_{k,k'} = \frac{W_k W_{k'}}{2} - \frac{1}{2(W_k W_{k'})}. \tag{5.8}$$

The Bogoliubov creation and annihilation operators $\hat{\beta}^\dagger$, $\hat{\beta}$ and the Bogoliubov dispersion $\omega_{\boldsymbol{k}}$ are defined in Eqs.(4.12),(4.13) and (4.15), respectively.

In the Bogoliubov case it is most convenient to write everything in momentum space and to use a separable model potential, in our case a regularized contact interaction. This regularization is done by introducing a high-momentum cutoff Λ in the momentum-integrals. In this case Λ^{-1} plays the role of the range of the potential, and for that reason also the role of the three-body parameter in the three-body problem (see Sec. 2.4.2). For the regularized contact interaction, we can exactly solve the Lippmann-Schwinger equation (2.21) to relate the coupling strength g to the boson-impurity scattering length a,

$$g^{-1} = \frac{\mu_r}{2\pi a} - \frac{\mu_r \Lambda}{\pi^2}. \tag{5.9}$$

Even on the coherent-state level, the pairwise impurity-boson correlations are included, and the boson-impurity interactions are renormalized. At this point we can also recognize that if we drop the quadratic term in Eq. (5.5), we exactly retrieve the Fröhlich model of Eq. (1.6). From our current analysis we therefore see that the Fröhlich model is missing the correct renormalization of the boson-impurity interactions.

Note that in Eq. (5.5) the impurity-position operator has disappeared from the Hamiltonian, because the impurity position has been translated to the center of the reference frame. Consequently, the momentum operator now commutes with the Hamiltonian, and can thus be replaced by the number vector $\boldsymbol{P}$, which now has the meaning of the total momentum of the system. Compared to Eq. (5.2), the LLP-transformation thus leads to a replacement of the impurity momentum by the total momentum of the system minus the total momentum of the bosons.

We are interested in the ground state of the system, and therefore we set the total momentum of the system to zero. Note that this does not mean that the impurity is stationary. Indeed, despite the fact that $\langle \hat{\boldsymbol{P}} \rangle = 0$, $\langle \hat{\boldsymbol{P}}^2 \rangle$ is nonzero in the laboratory frame, and it is these fluctuations in the impurity momentum (and its resulting kinetic energy) that will be crucial for our findings. What remains of the LLP-term is the square of the interboson momentum. Normal ordering this term leads to a quadratic term which modifies the bosonic dispersion, replacing the impurity mass by its reduced mass, and a true quartic term, which represents the impurity-mediated interaction between the bosons. The total Hamiltonian is thus given by

$$\hat{\mathcal{H}} = \int_{\boldsymbol{k}} (\omega_k + \frac{k^2}{2M}) \hat{\beta}^\dagger_{\boldsymbol{k}} \hat{\beta}_{\boldsymbol{k}} + \frac{1}{2M} \int_{\boldsymbol{k}'} \int_{\boldsymbol{k}} \boldsymbol{k}' \cdot \boldsymbol{k} \; \hat{\beta}^\dagger_{\boldsymbol{k}'} \hat{\beta}^\dagger_{\boldsymbol{k}} \hat{\beta}_{\boldsymbol{k}'} \hat{\beta}_{\boldsymbol{k}} + g n_0 + g\sqrt{n_0} \int_{\boldsymbol{k}}^{\Lambda} W_k [\hat{\beta}^\dagger_{\boldsymbol{k}} + \hat{\beta}_{-\boldsymbol{k}}]$$
$$+ g \int_{\boldsymbol{k}}^{\Lambda} \int_{\boldsymbol{k}'}^{\Lambda} \big[V^{(1)}_{k,k'} \hat{\beta}^\dagger_{\boldsymbol{k}} \hat{\beta}_{\boldsymbol{k}'} + \frac{V^{(2)}_{k,k'}}{2} (\hat{\beta}^\dagger_{\boldsymbol{k}} \hat{\beta}^\dagger_{\boldsymbol{k}'} + \hat{\beta}_{-\boldsymbol{k}} \hat{\beta}_{-\boldsymbol{k}'}) \big]. \quad (5.10)$$

To summarize: when the impurity is integrated out it has a threefold effect on the bosons. It modifies their dispersion, it plays the role of an external potential, and it mediates interactions between the bosons. Surprisingly, this mediated interaction arises from the kinetic energy term of the Hamiltonian. Note that this term even persists when there are no interactions between the bosons and the impurity. That is because the impurity must now impose the momentum conservation of the system. The total momentum of the impurity must always cancel the total momentum of the bosons, and the state of the bosons is therefore directly correlated with the energy of the impurity.

On the coherent-state level one can at this point analytically find a solution for the polaron energy in terms of the scattering length. This is given by Eq. (5.1), where

$$a_0^{-1} = \frac{2\Lambda}{\pi} - \frac{1}{\mu_r \pi} \int_0^{\Lambda} dk \frac{k^2 W_k^2}{\omega_k + \frac{k^2}{2M}}. \quad (5.11)$$

5.2.2 Spherical symmetry

The final Hamiltonian (5.10), where the total momentum of the system is set to zero, is still spherically symmetric even in the reference frame of the impurity. Therefore the angular momentum in all directions is conserved. To make optimal use of this symmetry, we shift from a plane-wave to a spherical-wave description. The spherical wave modes are defined via

$$\hat{\beta}^\dagger_{\boldsymbol{k}} = (2\pi)^{3/2} k^{-1} \sum_{lm} i^l Y^*_{lm}(\boldsymbol{\Omega}_k) \hat{\beta}^\dagger_{klm}. \quad (5.12)$$

In terms of real-space coordinates, they take the following form

$$\langle \boldsymbol{r}|\hat{\beta}^\dagger_{klm}|0\rangle = j_\lambda(kr)Y_{lm}(\boldsymbol{\Omega}_r)k\sqrt{\frac{2}{\pi}}, \tag{5.13}$$

where the Y_{lm} are spherical harmonics. Here l and m respectively indicate the angular momentum and its projection on the z-axis, in the reference frame where the impurity is at the center.

We can also rewrite the Hamiltonian into these spherical wave operators:

$$\hat{\mathcal{H}} = \sum_{lm}\int_k(\omega_k + \frac{k^2}{2M})\hat{\beta}^\dagger_{klm}\hat{\beta}_{klm} + \hat{\mathcal{H}}_{\mathrm{QLLP}} + gn_0 + \frac{g\sqrt{n_0}}{\pi\sqrt{2}}\int_k k\ W_k(\hat{\beta}^\dagger_{k00} + \hat{\beta}_{k00})$$
$$+ \frac{g}{2\pi^2}\int_{k_1}\int_{k_2}\left[k_1k_2\ V^{(1)}_{k_1,k_2}\hat{\beta}^\dagger_{k_100}\hat{\beta}_{k_200} + \frac{V^{(2)}_{k_1,k_2}}{2}(\hat{\beta}^\dagger_{k_100}\hat{\beta}^\dagger_{k_200} + \hat{\beta}_{k_100}\hat{\beta}_{k_200})\right]. \tag{5.14}$$

Now the integral $\int_k = \int_0^\Lambda dk$ only denotes the integral over the magnitude of k. The quartic Lee-Low-Pines term $\mathcal{H}_{\mathrm{QLLP}}$ takes a non-trivial form in the spherical wave basis. To construct it we need to consider integrals of the type

$$I = (2\pi)^3\int_{\boldsymbol{k}}\boldsymbol{k}k^{-2}i^{l-l'}Y^*_{lm}(\boldsymbol{\Omega}_1)Y_{l'm'}(\boldsymbol{\Omega}_1), \tag{5.15}$$

$$= \int_k \sin(\theta)d\theta d\phi\begin{pmatrix}k_1\sin(\theta)\cos(\phi)\\ k_1\sin(\theta)\sin(\phi)\\ k_1\cos(\theta)\end{pmatrix}i^{l-l'}Y^*_{lm}(\theta,\phi)Y_{l'm'}(\theta,\phi), \tag{5.16}$$

$$= \int_k k\sin(\theta)d\theta d\phi\sqrt{\frac{4\pi}{3}}\begin{pmatrix}\frac{1}{\sqrt{2}}[Y_{1,-1}(\theta,\phi) - Y_{1,1}(\theta,\phi)]\\ \frac{i}{\sqrt{2}}[Y_{1,-1}(\theta,\phi) + Y_{1,1}(\theta,\phi)]\\ Y_{1,0}(\theta,\phi)\end{pmatrix}i^{l-l'}Y^*_{lm}(\theta,\phi)Y_{l'm'}(\theta,\phi). \tag{5.17}$$

At this point, we can use the following identity for the integral over three spherical harmonics,

$$\int\sin(\theta)d\theta d\phi Y^*_{lm}(\theta,\phi)Y_{l'm'}(\theta,\phi)Y_{l''m''}(\theta,\phi) =$$
$$\sqrt{\frac{(2l+1)(2l'+1)(2l''+1)}{4\pi}}(-1)^m\begin{pmatrix}l & l' & l''\\ 0 & 0 & 0\end{pmatrix}\begin{pmatrix}l & l' & l''\\ -m & m' & m''\end{pmatrix}, \tag{5.18}$$

where we have used the Wigner $3j$-symbols $\begin{pmatrix}l & l' & l''\\ -m & m' & m''\end{pmatrix}$, which are closely related to Clebsch-Gordan coefficients. Importantly, for these symbols to be nonzero, l, l' and l'' need to satisfy the triangular inequalities, and for the lower row we need to have $-m+m'+m''=0$.

After some algebra, and filling in the values of the $3j$-symbols, we obtain for the

$\hat{\mathcal{H}}_{\mathrm{QLLP}}$-term

$$\hat{\mathcal{H}}_{\mathrm{QLLP}} = \sum_{ll'mm'} \int_k \int_{k'} \frac{kk'}{\sqrt{(2l+1)(2l+3)(2l'+1)(2l'+3)}}$$
$$\Bigg[\sqrt{(l-m+1)(l+m+1)(l'-m'+1)(l'+m'+1)} [2\hat{\beta}^\dagger_{k(l+1)m}\hat{\beta}^\dagger_{k'l'm'}\hat{\beta}_{klm}\hat{\beta}_{k'(l'+1)m'}$$
$$- \hat{\beta}^\dagger_{k(l+1)m}\hat{\beta}^\dagger_{k'(l'+1)m'}\hat{\beta}_{klm}\hat{\beta}_{k'l'm'} - \hat{\beta}^\dagger_{klm}\hat{\beta}^\dagger_{k'l'm'}\hat{\beta}_{k(l+1)m}\hat{\beta}_{k'(l'+1)m'}]$$
$$+ \sqrt{(l-m+1)(l-m+2)(l'+m'+1)(l'+m'+2)}$$
$$[\hat{\beta}^\dagger_{k(l+1)(m-1)}\hat{\beta}^\dagger_{k'(l'+1)(m'+1)}\hat{\beta}_{klm}\hat{b}_{k'l'm'} + \hat{\beta}^\dagger_{klm}\hat{\beta}^\dagger_{k'l'm'}\hat{\beta}_{k(l+1)(m-1)}\hat{\beta}_{k'(l'+1)(m'+1)}]$$
$$+ \sqrt{(l-m+1)(l-m+2)(l'-m'+1)(l'-m'+2)}\ \hat{\beta}^\dagger_{k(l+1)(m-1)}\hat{\beta}^\dagger_{k'l'm'}\hat{\beta}_{klm}\hat{\beta}_{k'(l'+1)(m'-1)}$$
$$+ \sqrt{(l+m+1)(l+m+2)(l'+m'+1)(l'+m'+2)}\ \hat{\beta}^\dagger_{k(l+1)(m+1)}\hat{\beta}^\dagger_{k'l'm'}\hat{\beta}_{klm}\hat{\beta}_{k'(l'+1)(m'+1)} \Bigg]. \tag{5.19}$$

Note that this term takes exactly the same form without the Bogoliubov transformation in terms of the original bosonic creation and annihilation operators.

5.2.3 Gaussian states for the polaron problem

Having considered the Hamiltonian in the spherical wave basis, we can now impose the same symmetry on our Gaussian state, which then takes the form

$$|\mathrm{GS}\rangle = \mathcal{N} \exp\Big[\int_k (\phi_k \hat{\beta}^\dagger_{k00} - h.c.)\Big] \exp\Big[\sum_{lm} (-1)^m \int_k \int_{k'} \xi^{(l)}_{k,k'} \hat{\beta}^\dagger_{klm}\hat{\beta}^\dagger_{kl-m}\Big]|0\rangle. \tag{5.20}$$

The difference from the presentation in Chapter 3 is that we are here dealing with continuous variables, and the difference with Chapter 4 is that we do not have the full translational symmetry. We take the Gaussian state to be a zero angular-momentum eigenstate, which gives strong restrictions to the form of the Gaussian-state wave function. Indeed, this implies that the coherent contribution only creates particles with zero angular momentum zero. If this were not the case, then the state would be a superposition of many contributions with different angular momenta, and not an angular-momentum eigenstate. We therefore drop the angular momentum indices of $\boldsymbol{\phi}$. Similarly, the Gaussian contribution can only create pairs with zero angular momentum. As a result, the particles created in the pairs need to have the same l and opposing values of m. Furthermore, this needs to be true regardless of the choice of the z-axis, so therefore $\xi^{(l)}$ is independent of m, if the phase $(-1)^m$ is taken into account. Taking these constraints into account leads to the form of Eq. (5.20). Note that $\xi^{(l)}$ can be viewed as a block-diagonal matrix, where the blocks are labeled by l. This block-diagonal structure also carries over to G and F, for which we use similar notation. Concretely,

$$G^{(l)}_{k,k'} = \langle \hat{\beta}^\dagger_{klm}\hat{\beta}_{klm}\rangle, \tag{5.21}$$
$$F^{(l)}_{k,k'} = (-1)^m \langle \hat{\beta}_{klm}\hat{\beta}_{kl-m}\rangle. \tag{5.22}$$

Eqs. (3.38) and (3.42) hold now separately for each block.

Computing expectation values with the Hamiltonian has now become rather straightforward. It turns out that even the expectation value of the quartic Lee-Low-Pines term

hugely simplifies. Indeed, it is given by

$$\langle \mathrm{GS}|\hat{\mathcal{H}}_{\mathrm{QLLP}}|\mathrm{GS}\rangle = \frac{1}{2M}\int_k\int_{k'} k\ k'\Big[(\phi_k^* G^{(1)}_{k,k'}\phi_{k'} - \phi_k^* F^{(1)}_{k,k'}\phi^*_{k'} + h.c.) + \sum_l (l+1)(2G^{(l+1)}_{k,k'}G^{(l)}_{k',k} - F^{(l+1)*}_{k,k'}F^{(l)}_{k',k} - F^{(l+1)}_{k,k'}F^{(l)*}_{k',k})\Big]. \quad (5.23)$$

Importantly, the expectation value of this term with respect to a coherent state is zero. That is because the coherent state has only angular-momentum zero components. We see furthermore that there are only couplings in the Hamiltonian between subsequent l-components.

In this parameterization one needs to numerically discretize the parameters and integrals to obtain workable equations in matrix form. Due to the large separation of length scales in the polaron problem it is most efficient to do this on a logarithmic grid. When one includes the numerical discretization of the integrals into the approach, this however means that the calculation is not variational any more in the strictest sense.

To optimize the parameters we find that iterated Bogoliubov theory (see Sec. 3.4.1) is particularly efficient. This is mostly the case because the coherent-state equation of motion is quadratic, and can therefore very simply be solved by diagonalization.

5.3 Cooperative binding effect

We have now formulated the problem of an impurity in a homogeneous BEC, which in principle has an infinite number of particles. However, before moving on to such true many-body physics it is important to answer some key questions on the few-body aspects. Which kind of bound states can be formed in this model? Does the heteronuclear Efimov effect also extend beyond the three-body case?

5.3.1 The two- and three-body problem

Let us start from the basics, and study first the two- and three-body problem in the reference frame of the impurity (i.e., the case of one or two bosons plus the impurity). For now, we set the background density n_0 in Eq. (5.14) to zero. Moreover, we consider non-interacting bosons ($a_B = 0$), yielding the Hamiltonian

$$\hat{\mathcal{H}} = \sum_{lm}\int_k \frac{k^2}{2\mu_r}\hat{b}^\dagger_{klm}\hat{b}_{klm} + \hat{\mathcal{H}}_{QLLP} + \frac{g}{2\pi^2}\int_{k_1}\int_{k_2} k_1 k_2\ \hat{b}^\dagger_{k_100}\hat{b}_{k_200}. \quad (5.24)$$

For the two- and three-body problem, the wave function can be exactly parameterized as

$$|\psi_{2b}\rangle = \int_k \beta_k \hat{b}^\dagger_{k00}|0\rangle, \quad (5.25)$$

$$|\psi_{3b}\rangle = \frac{1}{\sqrt{2}}\sum_{lm}\int_{k_1}\int_{k_2}(-1)^m \alpha_{k_1k_2l}\hat{b}^\dagger_{k_1lm}\hat{b}^\dagger_{k_2l-m}|0\rangle. \quad (5.26)$$

Here angular-momentum conservation has been taken into account and the total angular momentum has been set to zero. This has similar consequences as in the Gaussian-state case. In the two-body problem (Eq. (5.25)), the single boson always has angular momentum zero, whereas in the three-body problem (Eq. (5.26)), the two bosons always have opposite angular momenta in the frame of the impurity. Moreover, the wave function α depends only on m via the sign $(-1)^m$, reflecting spherical symmetry.

In the few-body case the eigenenergies, and in particular the ground-state energy, can be readily obtained by the direct diagonalization of the equations of motion instead of using imaginary-time evolution. These (real-time) equations of motion are given by

$$i\partial_t \beta_k = \frac{k^2 \beta_k}{2\mu_r} + \frac{gk}{2\pi^2} \int_{k'} k' \beta'_k, \tag{5.27}$$

$$\begin{aligned} i\partial_t \alpha_{k_1 k_2 l} = {} & \alpha_{k_1 k_2 l} \frac{k_1^2 + k_2^2}{2\mu_r} + \frac{g\delta_{l,0}}{2\pi^2} \int_k k(k_2 \alpha_{k_1 k 0} + k_1 \alpha_{k k_2 0}) \\ & - \frac{k_1 k_2}{M(2l+1)} [(l+1)\alpha_{k_1 k_2 (l+1)} + l\alpha_{k_1 k_2 (l-1)}], \end{aligned} \tag{5.28}$$

and can be diagonalized using standard numerical techniques.

The non-interacting problem

First, we consider the non-interacting problem ($g = 0$). In this case the momentum of each particle is a good quantum number. As a result, the two-body problem is trivial. Since the total momentum is fixed to zero, the impurity and the boson will always have opposite momenta. This directly yields the energy $\frac{k^2}{2\mu_r}$. The $\hat{\mathcal{H}}_{QLLP}$-term vanishes in the two-body problem and thus plays no role.

In contrast, for the three-body problem, the equations of motion *in the impurity frame* (Eq. (5.28)) are non-trivial, since the $\hat{\mathcal{H}}_{QLLP}$ term couples the different angular momentum modes. This coupling is indeed crucial since the lowest energy for total momentum $\boldsymbol{P} = 0$ and fixed absolute momenta of the two bosons k_1 and k_2 occurs when the two particles move in opposite directions. This means that the direction of motion of the bosons in the impurity frame needs to be correlated.

To proceed in this case, one may note that the non-interacting equations of motion of the three-body problem can be mapped to the problem of two coupled harmonic oscillators. This in turn can exactly be solved using a Bogoliubov rotation. For fixed absolute momenta k_1 and k_2 (leaving their direction free) one finds a minimum energy of $\frac{k_1^2+k_2^2}{2m} + \frac{(k_1-k_2)^2}{2M}$. This corresponds to an impurity momentum of $k_1 - k_2$, which shows that, as expected, the minimal energy is found when the bosons move in opposite directions. In the corresponding wave function every angular momentum mode is equally populated. This implies that an infinite number of modes is required to solve the usually trivial non-interacting problem in this framework. Fortunately, for finite $g < 0$, as considered below, lower angular momentum modes are favored since only the zeroth angular momentum mode has a (attractive) coupling with the impurity. In case of bound-state formation, this means that in practice convergence can be achieved with a small number of angular modes.

Including interactions

Next, we consider the case of a finite, negative g. In the two-body problem, a bound state is formed for positive scattering lengths which vanishes into the scattering continuum at unitarity, where $a \to \infty$. However, for three particles, due to the Efimov effect, a bound state can be formed for finite negative scattering lengths [76, 77]. Since this three-body bound state forms when the two-body bound state is not yet possible, this can already be regarded as an instance of cooperative binding, which is driven by the $\hat{\mathcal{H}}_{QLLP}$-term of the Hamiltonian. Indeed, when $\hat{\mathcal{H}}_{QLLP}$ is not included (i.e., omitting the second line of Eq. (5.28)), the equations of motion become separable and the equations of motion for the two-body problem are retrieved. This demonstrates that the $\hat{\mathcal{H}}_{QLLP}$-term must be crucial

species	^{168}Er	^{133}Cs	^{87}Rb	^{41}K	^{23}Na	^{7}Li
$a_-\Lambda$	-5.20	-5.69	-6.91	-11.1	-19.0	-135

Table 5.1: Scattering lengths a_- where the lowest energy three-body Efimov states cross the scattering threshold for ^{6}Li interacting with different species of bosons, using a regularized contact interaction in units of the three-body parameter Λ.

for the Efimov effect. Since this term originates from the kinetic energy of the impurity, it becomes evident that reducing the kinetic energy of the impurity is the driving force of the Efimov effect.

The full three-body problem can be solved numerically using sparse matrix diagonalization either employing linear or, more efficiently, logarithmic grids in k. In this way, the ground and low-lying excited Efimov states can be studied. While the method can be generalized relatively easily to arbitrary interaction potentials, including boson-boson interactions in this framework leads to involved expressions for the relevant matrix elements and removes the sparsity of the matrices representing the equations of motion, greatly increasing numerical complexity. In Chapter 6 we develop techniques to deal with these issues.

Focusing on the ground state, we calculate the Efimov scattering length a_- following from our model for ^{6}Li-atoms interacting with several types of bosons. The results are shown in Table 5.1. We find that a_- is smallest for light impurities, meaning that the cooperative binding is the strongest in that case. This can easily be understood from the underlying mechanism: the reduction of the kinetic energy of the impurity compared to the interaction energy. Because the kinetic energy of the impurity for a given momentum is larger for light than for heavy impurities, the reduction of this energy can have a larger impact. This is directly reflected in the $\hat{\mathcal{H}}_{QLLP}$-term of the Hamiltonian, which scales inversely with the mass of the impurity. As a result, a_- quickly grows as the mass ratio m/M decreases. Hence, observing Efimov physics experimentally can most easily be achieved by immersing a light impurity in a bath of heavy bosons. Motivated by this fact, we will focus in this Chapter on the mass ratio of the experimentally available system of a ^{6}Li impurity immersed in a BEC of ^{133}Cs atoms [86, 87].

5.3.2 Many-body Efimov effect

We now move on to demonstrate that the cooperative binding effect driving the Efimov effect also persists for larger particle numbers. To this end, we need to show that the binding energy per boson $E_{\text{bind}}/N = |E/N|$ increases monotonically with the number N of bound particles.

In order to study N-body bound states, the methods used in the previous subsection need to be extended to higher particle numbers. However, pursuing the same route of exactly solving the N-body problem rapidly becomes computationally intractable. Instead, we adopt a different approach, based on a variational Gaussian-state wave function that is not a particle number eigenstate, but rather a superposition of states with different particle numbers. In this Ansatz pairwise correlations between the bosons are fully taken into account in the frame of the impurity. This translates to fully including the three-body correlations between two bosons and the impurity in the laboratory frame.

We emphasize that the functional form of the correlations in a Gaussian state is different from the correlation functions in the Jastrow-formalism [156], often used in condensed-matter physics, which was, for example, also employed to describe Bose polarons in

Ref. [151, 157]. In our case, the covariance matrix, which characterizes the correlations, is optimized variationally without restrictions on the functional form of the correlations.

In the following we will now highlight our various findings.

Gaussian states incorporate 2- and 3-body physics

First, we demonstrate that a Gaussian state combined with the Lee-Low-Pines transformation captures the Efimov effect. To this end, we show that the equations of motion of the two- and three-body problem can be retrieved exactly by linearizing the equations of motion for Gaussian states around the vacuum.

For the real-time evolution of $\delta\xi$, up to linear order we find

$$i\partial_t \delta\xi = \Delta + \mathcal{E}\delta\xi + \delta\xi\mathcal{E}^*. \tag{5.29}$$

We can now plug in the values for η, Δ and $\mathcal{E}$:

$$\eta_k = \frac{k^2}{2\mu_r}\phi_k + \frac{gk}{2\pi^2}\int_q q\phi_q + \frac{k}{M}\int_q (G^{(1)}_{kq}\phi_q - F^{(1)}_{kq}\phi^*_q), \tag{5.30}$$

$$\mathcal{E}^{(l)}_{kk'} = \delta_{kk'}\frac{k^2}{2\mu_r} + \delta_{l,0}\frac{gkk'}{2\pi^2} + \frac{(l+1)kk'}{(2l+1)M}G^{(l+1)}_{kk'} + \frac{lkk'}{(2l+1)M}[\delta_{l,1}\phi_k\phi^*_{k'} + G^{(l-1)}_{kk'}], \tag{5.31}$$

$$\Delta^{(l)}_{kk'} = -\frac{(l+1)kk'}{(2l+1)M}F^{(l+1)}_{kk'} - \frac{lkk'}{(2l+1)M}[\delta_{l,1}\phi_k\phi_{k'} + F^{(l-1)}_{kk'}]. \tag{5.32}$$

Expanding the equation to first order in $\delta\phi$ and $\delta\xi$ gives

$$i\partial_t\delta\phi_k = \frac{k^2\delta\phi_k}{2\mu_r} + \frac{gk}{2\pi^2}\int_q q\delta\phi_q, \tag{5.33}$$

$$i\partial_t\delta\xi^{(l)}_{kk'} = \delta\xi^{(l)}_{kk'}\frac{k^2+k'^2}{2\mu_r} + \frac{g}{2\pi^2}\delta_{l,0}\int_q q[k'\delta\xi^{(0)}_{kq} + k\delta\xi^{(0)}_{qk'}] + \frac{kk'\big[(l+1)\delta F^{(l+1)}_{kk'} + l\delta F^{(l-1)}_{kk'}\big]}{M(2l+1)}. \tag{5.34}$$

Since $\delta F = \delta\xi$ after linearizing around the vacuum, it is evident that these equations exactly correspond to the equations of motion for the two- and three-body problem: Eq. (5.27) and (5.28). This shows that Gaussian states indeed fully capture the Efimov effect.

Cooperative binding with Gaussian states

We now turn to demonstrating the cooperative binding effect. Since a Gaussian state is not a particle number eigenstate, but a superposition of those, we cannot fix the particle number N. Instead we fix its expectation value $\langle\hat{N}\rangle$, given by

$$\langle GS|\hat{N}|GS\rangle = |\boldsymbol{\phi}|^2 + \mathrm{Tr}(G). \tag{5.35}$$

For the imaginary-time evolution this is achieved by adding a chemical potential term $\mu_N\hat{N}$ to the Hamiltonian, where $\hat{N}$ is the particle number operator. Using the relation [158]

$$\mu_N = \frac{\langle\hat{N}\hat{\mathcal{H}}\rangle - \langle\hat{N}\rangle\langle\hat{\mathcal{H}}\rangle}{\langle\hat{N}^2\rangle - \langle\hat{N}\rangle^2}, \tag{5.36}$$

the chemical potential μ_N is dynamically adjusted to keep the particle number fixed during the time evolution.

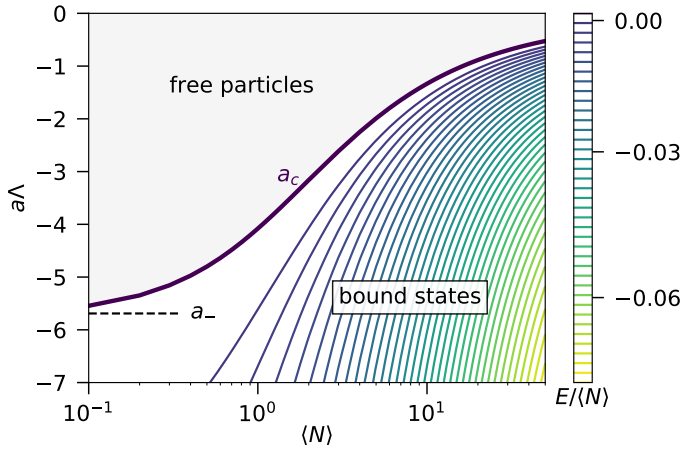

Figure 5.2: The energy per particle $E/\langle N \rangle$ as a contour plot as a function of the number of particles $\langle N \rangle$ and the scattering length a in terms of the three-body parameter Λ, for $M/m = 6/133$. The energy is given in units of Λ^2/M. The bold line indicates the critical scattering length at which a bound state first appears.

We aim to show that $E_{\text{bind}}/\langle \hat{N} \rangle$ grows monotonically with $\langle \hat{N} \rangle$, which is a strong indication that also E_{bind}/N grows with N. We find that during the optimization with fixed average particle number, the coherent part of the wave function approaches zero, leaving only the Gaussian part of the state. This is not surprising since this allows for the maximum amount of correlation between the particles.

In Fig. 5.2 we show a contour plot of the energy per particle as a function of $\langle \hat{N} \rangle$ and a. The bold line indicates the scattering length a_c where the energy per particle becomes negative and bound-state formation sets in. Note that since the Hamiltonian conserves particle number, a_c is a smooth line only due to a classical average over different particle number sectors. As discussed above, in the limit of $\langle \hat{N} \rangle$ going to zero, we recover the three-body Efimov effect. We therefore observe that in this limit, $a_c \to a_-$.

As $\langle \hat{N} \rangle$ is increased, a_c monotonically decreases in magnitude. Importantly, at fixed scattering length the energy $E_{\text{bind}}/\langle \hat{N} \rangle$ monotonically increases with $\langle \hat{N} \rangle$, as soon as $\langle \hat{N} \rangle$ is sufficient to lead to bound state formation. This clearly demonstrates cooperative binding, i.e., the ability of the bosons to support each other's binding to the impurity. This result is in good correspondence with recent work based on a stochastic variational approach by Blume [159], that also shows a strongly increasing energy as a function of particle number for an impurity immersed in a Bose gas.

As discussed above, it is important to emphasize that our method is variational not for fixed N, but for fixed $\langle \hat{N} \rangle$. This means that the ground-state energy we find for a given average $N = \langle \hat{N} \rangle$ may be lower than the lowest particle-number eigenstate of N particles. In fact, exactly because of the property that E_{bind}/N increases with N, it is beneficial in the optimization of the energy to have a larger spread in the particle number. The Gaussian form of the wave function does, however, restrict the particle-number statistics, meaning not arbitrary superpositions of particle-number eigenstates are allowed. The standard deviation of the particle number for the Gaussian states scales with $\langle \hat{N} \rangle$. This means that the particle-number fluctuations do not become relatively small for large $\langle \hat{N} \rangle$, such as often the case in statistical physics and, e.g., for coherent states. Thus, even for large $N = \langle \hat{N} \rangle$, the energy found with Gaussian states may be significantly lower than the particle-number eigenstate of N particles. Altogether, even though there are subtleties to be aware of, none of them discount our evidence for the cooperative binding effect.

One obvious question is whether a_c goes to zero if $\langle \hat{N} \rangle$ goes to infinity; i.e., will already an infinitely weak attraction enable bound-state formation? A hint of to the answer to this question is provided by the insight that the cooperative binding effect is fully driven by the $\hat{\mathcal{H}}_{QLLP}$-term originating from the kinetic energy of the impurity. A lower bound on $|a_c|$, that is quite general and in particular independent of the variational method, can therefore be derived by setting the kinetic energy of the impurity to zero. In this case the Hamiltonian becomes:

$$\hat{\mathcal{H}} = \sum_{lm} \int_k \frac{k^2}{2m} \hat{b}^\dagger_{klm} \hat{b}_{klm} + \frac{g}{2\pi^2} \int_{k_1} \int_{k_2} k_1 k_2 \hat{b}^\dagger_{k_1 00} \hat{b}_{k_2 00}. \tag{5.37}$$

While this formally corresponds to a Hamiltonian of bosons interacting with an infinitely heavy impurity, there is an important subtlety. Namely, the relation between the scattering length and the coupling constant is determined by the reduced mass of the problem. By solving the two-body problem corresponding to Eq. (5.37), where the reduced mass is m, one finds an expression for the scattering length a_{eff} in this effective model,

$$g^{-1} = \frac{m}{2\pi a_{eff}} - \frac{m\Lambda}{\pi^2}. \tag{5.38}$$

In the spectrum of the Hamiltonian (5.37) a bound state appears precisely when $a_{eff} = -\infty$. Inserting this condition into Eq. (5.38) and comparing with Eq. (5.9) immediately yields a limiting scattering length in the original model

$$a_{c,\mathrm{lim}} = -\frac{\pi M}{2m\Lambda}. \tag{5.39}$$

This is a bound for the smallest possible scattering length for which a bound state can appear. For the Li-Cs mass ratio, this value is given by $a_{c,\mathrm{lim}} = -0.07\Lambda^{-1}$. As can be seen in Fig. 5.2, this limit is only approached extremely slowly, and might in fact not be reached by a Gaussian-state Ansatz. In other words, the scattering length at which the most deeply bound Efimov state can form fulfills $a_-^{(min)} \leq a_{c,lim}$. We again emphasize that this limit is fundamental and independent of the variational method. With more advanced Ansätze the limit can only be approached faster or more closely. In contrast, the limit will depend on the form of the interaction potential. The fact that we find $|a_c| < \Lambda^{-1}$, with Λ^{-1} on the order of the van der Waals length, indicates that non-universal physics will become relevant in the description of a_c. From comparison with Table 5.1, it is evident that $a_{c,\mathrm{lim}}$ is approximately two orders of magnitude smaller than a_-. Note that such a minimal required scattering length to form an Efimov cluster does not exist for the homonuclear case, since there the pairwise interactions between all of the participating particles drive the cluster formation.

The increase in binding energy as a function of particle number and scattering length shown in Fig. 5.2 is accompanied by a decrease in the spatial extent of the Efimov clusters, which we define as

$$R = \sqrt{\frac{\langle \hat{N} \rangle}{\langle \int d\boldsymbol{k} \boldsymbol{k}^2 \hat{b}^\dagger_{\boldsymbol{k}} \hat{b}_{\boldsymbol{k}} \rangle}}. \tag{5.40}$$

As shown in Fig. 5.3, the size of the Efimov clusters monotonically decreases as a function of a and $\langle \hat{N} \rangle$. It is evident that these cooperative Efimov clusters are tightly bound, with $R\Lambda$ being of order 1. Note that R parameterizes the average distance of the bosons to the impurity, and not the distance of the particle furthest away. This means that the

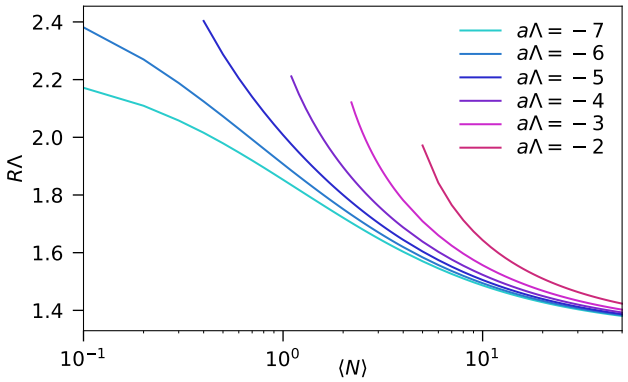

Figure 5.3: Spatial extent R, defined by Eq. (5.40), of an Efimov cluster as a function of the number of particles $\langle \hat{N} \rangle$ for different scattering lengths $a\Lambda$ (indicated by color). The lines terminate when the bound states disappear into the continuum (see Fig. 5.2). The mass ratio is $M/m = 6/133$.

total extent of the Efimov cluster wave function can be much larger than described by R, especially close to a_c.

Finally we corroborate our qualitative explanation of the mechanism underlying cooperative binding with quantitative numerical results. We have explained before that the impurity-mediated interaction between the bosons, described by the $\hat{\mathcal{H}}_{QLLP}$-term in the Hamiltonian, follows from a reduction of the kinetic energy of the impurity. In Fig. 5.4 we plot the relative values of the energetic contributions to the problem: the kinetic energy of the bosons $E_{\text{kin}}^{(\text{bos})}$, the kinetic energy of the impurity $E_{\text{kin}}^{(\text{imp})}$, and the interaction energy E_{int}, as a function of the scattering length for various particle numbers $\langle N \rangle$. Whereas the ratio between the bosonic kinetic energy and the interaction energy only changes marginally when the number of particles is increased, the kinetic energy of the impurity relative to the interaction energy can decrease by more than a factor two. Thus, it becomes apparent that the reduction of the kinetic energy of the impurity compared to the interaction energy, is indeed the driving force of the cooperative binding mechanism. Note that the kinetic energy of the impurity decreases in relative but not in absolute terms when more bosons are added. Indeed, adding more bosons leads to tighter binding and therefore larger kinetic zero-point energy. Furthermore, the ratio between the kinetic and interaction energy is not universal: it will depend on the shape of the potential. However, we believe that the general trend of the decreasing relative impurity kinetic energy for increasing particle number is a universal phenomenon.

The cooperative binding mechanism can also be interpreted in terms of an increase of the reduced mass of the system. For example, if a boson scatters on an impurity-boson bound state, this system has a larger reduced mass than the system of a boson scattering with a free impurity. However, the interaction potential remains the same, meaning that forming a bound state in the former system is easier than in the latter. This is clearly related to our explanation in terms of the impurity kinetic energy. Where in the case of a dimer state the impurity needs to completely compensate for the momentum of the boson it is bound to, in a trimer the bosons partially compensate for each other's momentum. This means that the impurity kinetic energy per boson is decreased.

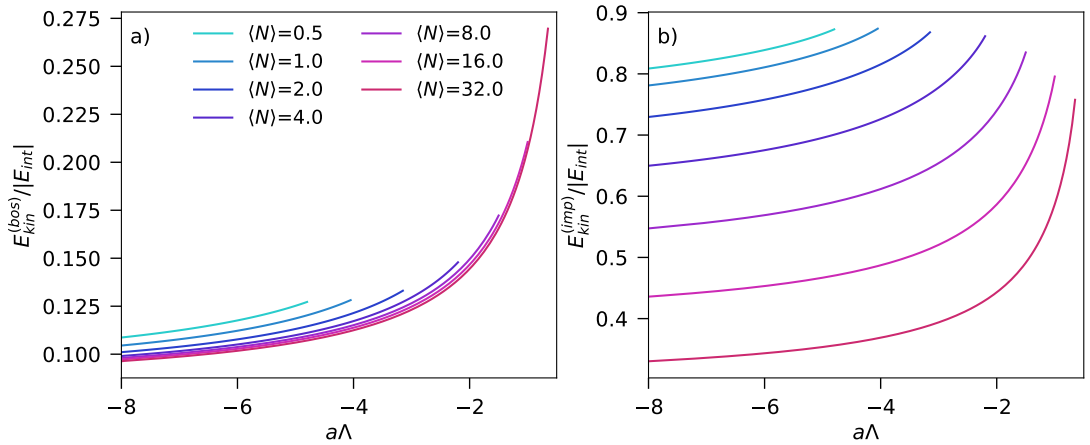

Figure 5.4: The kinetic energy of the bosons (a) and the impurity (b) compared to the total interaction energy, as a function of the scattering length a (in terms of Λ), for several values of $\langle N \rangle$ and $M/m = 6/133$. The lines terminate when the bound states disappear into the continuum (see Fig. 2). The legend displayed in figure (a), also corresponds to figure (b).

Further aspects

The Efimov clusters are inherently unstable due to recombination into deeply bound molecular states that are not included in our model. Because of this rapid recombination, the specific structure of these clusters is not relevant for experiments, which is why we refrained from discussing it in detail. Instead the main interest of this work is to show that the polaron, as discussed in the next section, can decay into Efimov clusters, a process independent of their microscopic structure. For this polaronic instability the cooperative binding effect is essential and this has hence been our main focus here.

The bound states that are formed for $N \gg 1$ are very tightly bound (as shown in Fig. 5.3) and the results we obtain in Figs. 5.2, 5.3 and 5.4 are therefore not universal. Indeed, universality breaks down due to the piling up of bosons around the impurity. The cooperative binding mechanism ultimately leading to this breakdown is universal though, since the driving $\hat{\mathcal{H}}_{QLLP}$-term is independent of the interaction potential.

The accumulation of bosons on the impurity can be prevented or limited by interboson repulsion. Due to the tightly-bound nature of the bound states not only the interboson scattering length but also the range of the interboson interactions will play an important role. As a result, a simple contact interaction will not be sufficient to describe this effect and more realistic potentials will need to be employed. Whether ultimately Van der Waals universality [79–83, 160, 161] persists even for deeply bound states and states with more particles [162], remains an interesting open question.

Furthermore, also using a two-channel model, where the interaction between the impurity and the bosons is modeled by a coupling to a closed molecular channel, may modify the results. Especially in the closed-channel dominated limit only a single boson can interact with the impurity at a time, resulting in an effective three-body repulsion [149]. Similar to a direct interboson repulsion, this may limit the size of Efimov clusters.

Finally we note that the coherent part of the Gaussian state may also contribute to cooperative binding, although more weakly than the Gaussian part. This is due to the mixing between the coherent and the Gaussian term in the expectation value of $\hat{\mathcal{H}}_{QLLP}$. In the next section this will become important, because only the coherent state term couples

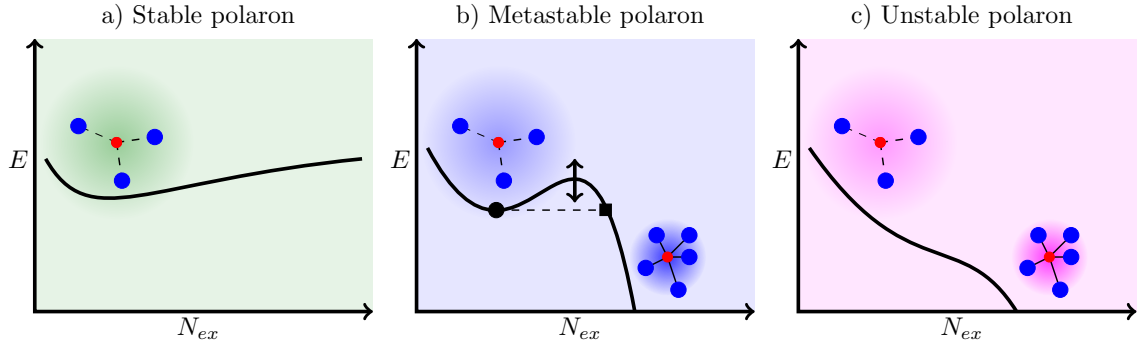

Figure 5.5: Illustration of the energy landscape of the extended Fröhlich model (5.10) as a function of the number of excitations N_{ex} surrounding the impurity at a fixed density and scattering length in the a) stable, b) metastable and c) unstable regime, which correspond to the regimes shown in Fig. 5.1. In the stable polaron regime, there are no Efimov clusters to decay into, in the metastable regime there is a barrier protecting the polaron from this decay, whereas in the unstable regime this barrier has completely disappeared. The black circle and square in b), connected by the dashed line, are of relevance for Fig. 5.7.

to the linear Fröhlich term in the Hamiltonian, crucial for polaron formation.

5.4 The Efimov effect and the Bose polaron

We have shown that large and strongly bound Efimov clusters already form at small negative scattering lengths. The ground state in our system is therefore not the Bose polaron, but a state where all particles are bound to the impurity. This immediately raises questions concerning the fate of the polaron. Does a polaron state still exist and if yes, will it still be stable? Can it decay into the cooperative Efimov clusters? Finding answers to these questions is the aim of this section.

5.4.1 Stable and metastable polaron

We are now in the position to discuss the spectrum shown in Fig. 5.1 in more detail. Starting at the left of this figure, as discussed below Eq. (5.39) in the previous section, there is a minimum scattering length $a_-^{(min)} \leq a_{c,\mathrm{lim}} < 0$ required to form any Efimov cluster. As a result, for $a > a_-^{(min)}$ the polaron remains the ground state of the Hamiltonian. However, $a_-^{(min)}$ can be very small for light impurities, yielding only a small region where the polaron is truly stable.

The first clusters that form at $a_-^{(min)}$ contain an exceedingly large number of particles. Since smaller clusters can not yet be formed, all particles required for the bound-state formation need to come together without the possibility to cascade through long-lived intermediate states. Since cold atomic gases are dilute, the rate of the required N-body scattering processes is extremely small. Therefore the polaron state, which at small scattering lengths is accompanied only by a relatively small and long-ranged deformation of the condensate, will not experience rapid decay into these clusters, and remain long-lived even far beyond $a_-^{(min)}$.

It can also be understood in a formal way from the Hamiltonian why the polaron should remain a stable state for weak interactions. For small scattering lengths and a small number of excitations in the polaron cloud, the contribution of the $\hat{\mathcal{H}}_{QLLP}$ term

in the Hamiltonian is negligible. Moreover, at negative scattering lengths no two-body bound states can be formed yet. This implies that the quadratic kinetic energy term in Eq. (5.10) dominates over the quadratic interaction terms. The remaining model thus closely resembles the original Fröhlich model (1.6) where a linear term drives polaron formation and a quadratic kinetic energy term counteracts this process. This model has a minimum of the energy as a function of particle number, as graphically illustrated in Fig. 5.5, where the energy landscape of the Hamiltonian is plotted as a function of the number of excitations around the impurity for fixed background density.

For $0 > a > a_-^{(min)}$ (Fig. 5.5a)), the polaron is the global minimum of the energy landscape and hence stable. When $a_-^{(min)}$ is crossed, the local minimum is not immediately affected, since the barrier protecting it is still large and a bound state can be formed only for a very large number of excitations. The correspondence to the original Fröhlich model persists as long as the particle number corresponding to the local minimum is sufficiently small for the quartic term to remain of minor importance. This changes, however, for large scattering lengths or densities. In this case the particle number at the polaron minimum found from the simplified model, is so large that the quartic term can no longer be neglected. When this occurs (as depicted in Fig. 5.5b)), the barrier protecting the polaron from decaying into Efimov clusters starts to disappear. Eventually, at the critical scattering length a^* the barrier completely disappears, resulting in the breakdown of the polaron, and one enters the regime illustrated in Fig. 5.5c).

5.4.2 The breakdown of the polaron

Now we will discuss in more detail the process leading to the breakdown of the polaron. At the critical scattering length a^* where the instability occurs, the polaron state is a saddle point on the variational manifold. Therefore, the polaron state is no longer stable against a specific type of perturbations. These perturbations can be identified by computing the tangent vectors [104, 106] on the variational manifold. The resulting processes represent single and double excitations on top of the Gaussian state. Thus, the polaron becomes unstable when a single or double excitation (or a linear combination thereof) can result in the formation of a bound state. Once a bound state is formed, the cooperative binding effect drives a cascade into more deeply bound states of ever increasing particle number. In a medium this is possible, since there is a coupling between the different particle number sectors: the polaron can draw particles from the medium. Eventually, this leads to the collapse of the system onto the impurity.

The value of the scattering length a^* can be calculated numerically as a function of the density. To this end, we use the following procedure: we start at small scattering lengths where the local minimum corresponding to the polaron can easily be identified. We then incrementally increase the coupling strength. In every step the polaron energy and wave function are calculated with iterated Bogoliubov theory (see Sec. 3.4.1), using the polaron wave function at the previous scattering length as a starting point. As the critical scattering length a^* is reached, the barrier preventing the polaron from decaying into many-body bound states disappears, leading to the breakdown of the impurity.

Polaronic instability and shift of the Efimov resonance

In Fig. 5.6 we show a^* as a solid black line as a function of the interparticle distance $n_0^{-1/3}\Lambda$ for two values of the interboson scattering length $a_B\Lambda = 0.01$ and $a_B\Lambda = 0.1$. Additionally, we show the spectral weight Z of the polaron as a colormap. It is given by the overlap of the wave function with the unperturbed state, which for a Gaussian state

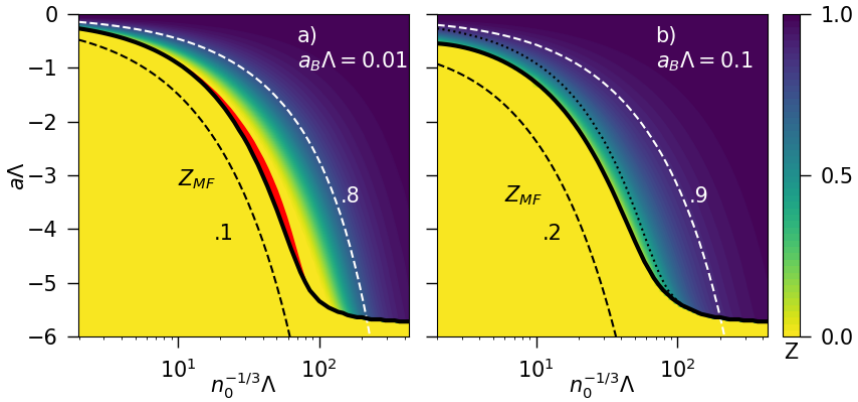

Figure 5.6: Polaron quasiparticle weight Z as a function of the interparticle distance $n_0^{-1/3}\Lambda$ and scattering length a for mass ratio $M/m = 6/133$. Two different interboson scattering lengths are chosen: a) $a_B\Lambda = 0.01$ and b) $a_B\Lambda = 0.1$. The black solid line indicates the critical scattering length a^* at which the polaron breaks down. The dotted line in b) is a guide to highlight the difference between figure a) and b), and corresponds to the solid line in a). The red region close to the solid line in figure a) is a region of dynamic instability. The dashed lines indicate contours of the quasiparticle weight Z_{MF} obtained from mean-field theory.

can be written using Eq. (3.46) as

$$Z = \frac{\exp[-|\phi|^2 + \frac{1}{2}(\phi^*\xi\phi^* + h.c.)]}{[\det(\mathbb{I} - \xi\xi^*)]^{1/2}}, \tag{5.41}$$

where I is the identity matrix. Experimentally, Z can be measured using injection rf-spectroscopy [144, 145].

First we consider the low-density limit. Here we find that $a^* \to a_-$, i.e., the polaron ceases to exist exactly at the three-body Efimov scattering length. This finding can be understood as follows. For small densities, the polaron cloud is extremely dilute, meaning the impurity is practically free. A bound state for a free impurity plus two excitations from the background can be formed when the first three-body bound state crosses the continuum, which precisely happens at a_-. This transition from a free impurity to a three-body Efimov state is accompanied by a sharp drop of the quasiparticle weight from 1 to 0.

As the density is increased, the polaron cloud surrounding the impurity is established containing excitations from the BEC. The formation of this polaron cloud has multiple consequences. First, as can be seen from Fig. 5.6, it leads to a reduction of the quasiparticle weight for increasing density. Second, due to the increased density around the impurity, scattering of two particles on the polaron can lead to the formation of clusters of more than three particles. Importantly, due to the cooperative binding effect these larger clusters can already be formed at scattering lengths smaller than a_-. Therefore, $|a^*|$ shifts to smaller scattering lengths as the density increases. This argument suggests the interpretation of the polaronic instability as a many-body shifted Efimov resonance, where the polaron takes over the role of the free impurity as a collision partner of two *additional* bosons. This reasoning also implies that the time-scale associated with this instability is on the same order as the time scale associated with three-body recombination.

One fascinating aspect of this finding is that the shift of a^* is continuous. While the average over particle number sectors in our discussion of cooperative binding in Section 5.3

and Fig. 5.2 was purely classical, here the Hamiltonian coherently couples different particle number sectors. This means that instead of obtaining a classical average over three-, four- and five-body Efimov states, clusters formed in presence of a background BEC contain a quantum mechanical superposition of different particle states. This originates from the quantum coherent nature of the BEC giving rise to the linear Fröhlich term in the Hamiltonian, and highlights an intriguing aspect of chemistry in a medium of a quantum nature. We will see an explicit experimental demonstration of this effect in Chapter 7.

Mechanism of the polaronic instability

We now study the mechanism underlying the polaronic instability quantitatively. To this end, it is useful to introduce the relevant length scales of the problem:

- the size of the Efimov trimer, which is on the order of a_-,
- the average interparticle distance, parameterized by $n_0^{-1/3}$,
- the size of the polaron cloud, which is determined by the modified healing length of the BEC $\xi_B = (8\pi n_0 a_B \mu_r/m)^{-1/2}$ [163].

In Fig. 5.7 we show the number of excitations in the polaron cloud computed with a Gaussian (coherent) state Ansatz as a function of the scattering length as dashed (dotted) lines. As solid lines (color indicating various background densities) we show the critical particle number needed to form a bound state with an energy lower than the polaron energy at the given scattering length and background density. In terms of the illustration in Fig. 5.5b), we compare the number of particles contained in the polaronic excitation cloud (black circle) with the number of particles that is needed to form a bound state of at least the polaron energy (black square).

The crosses at the end of the dashed lines indicate the scattering length a^* of the polaronic instability. This instability is not captured by the coherent-state Ansatz. In between the crosses and the diamonds appearing on some lines, we find regions of dynamical instability, discussed in more detail below. The black line in this figure shows the critical scattering length for bound-state formation as a function of particle number in absence of a background BEC, such as shown in Fig. 5.2.

First we compare the results from the coherent- and Gaussian-state Ansätze (dotted and dashed lines). While they coincide for small a and $\langle \hat{N}_{ex} \rangle$, for larger a the particle number of the polaron calculated using Gaussian states grows much more rapidly. This leads to a difference of 1-2 orders of magnitude close to the critical scattering length. Next, we consider the solid lines, corresponding to the onset of bound-state formation. Based on the simplified illustration in Fig. 5.5b), one would expect that the polaron instability would occur precisely when the dashed lines cross the solid lines. However, this is not the case. In the low-density regime, the dashed lines in fact continue after crossing the solid lines, meaning that the polaron remains stable even when containing more than enough particles to form a bound state. The crucial insight to understand this behavior is that in this regime $\xi_B \gg a_-$. Thus, even though the particle number in the polaron cloud is very large, the cloud is so extended that the number of particles within a volume set by a_- is still too small to facilitate bound-state formation. In contrast, in the high-density regime we find that the instability exactly occurs when the dashed lines hit the solid lines. In this regime the healing length ξ_B that determines the size of the polaron cloud is comparable to, or smaller than the extent of the Efimov state. Therefore a bound state can be formed immediately when the polaron cloud contains the required number of particles. In the

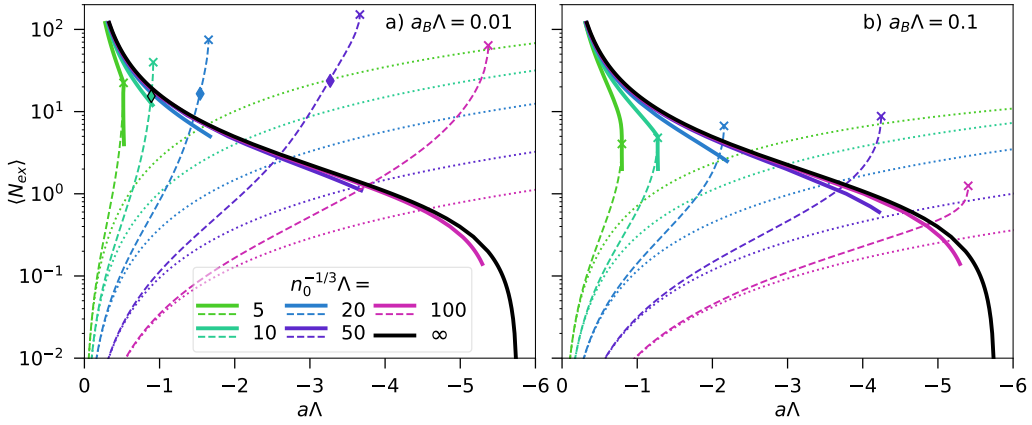

Figure 5.7: Quantitative analysis of the polaronic instability mechanism. The number of excitations $\langle \hat{N}_{ex} \rangle$ contained in the polaron cloud (Gaussian state: dashed, coherent state: dotted) compared to the critical number of particles needed for bound state formation (solid) in presence of a background BEC, plotted versus the scattering length $a\Lambda$. The interboson scattering length is given by a) $a_B\Lambda = 0.01$ and b) $a_B\Lambda = 0.1$. The black solid line indicates the critical particle number for bound state formation in absence of a background BEC, corresponding to the line of a_c displayed in Fig. 5.2. Crosses indicate where the polaron is destabilized in the Gaussian-state Ansatz. Diamonds indicate the position beyond which a dynamical instability occurs. The legend in subfigure a) also applies to b).

intermediate density regime, there is a crossover between these two regimes. Consistent with this interpretation, we find that the larger a_B, and thus the smaller ξ_B, the lower the density at which the transition occurs.

We see that the scattering length of the instability $|a^*|$ (indicated with the crosses in Fig. 5.7), shifts towards smaller values for larger densities. From Fig. 5.7 it appears that the main mechanism of this shift is an increase of the number of excitations in the polaron cloud as a function of background density (horizontal shift of dashed lines). Another contribution comes from the vertical shift of the solid lines. This shift is due to the linear Fröhlich term in the Hamiltonian, which leads to the stabilization of the coherent polaron cloud due to the background density. This coherent part of the wave function also participates in the cooperative binding, leading to a downward shift of the solid lines. This effect is in turn slightly counteracted by interbosonic repulsion and the associated modification of the Bogoliubov quasiparticle dispersion (compare Fig. 5.7 a) and b)), which plays the strongest role for large densities and a_B.

In contrast to the Gaussian-state approach, where a^* is shifted to *smaller* coupling strengths compared to a_-, in the coherent-state case the defined a_0 implies a shift to stronger coupling strengths (see Eqs. (5.1) and (5.11)). This highlights also the different mechanisms governing these shifts. For Gaussian states the shift is predominantly caused by the cooperative binding effect, whereas the interboson repulsion on the Bogoliubov level is responsible for the shift in the case of coherent states.

Using a renormalization-group approach [153], it was predicted that the polaron becomes unstable for a finite negative scattering length. This was attributed to phase and particle number fluctuations and no connection to the Efimov effect was made. Since the general picture of a polaronic instability at negative scattering lengths agrees with our results, it remains an interesting open question how these two pictures might be related.

We note that in our framework the most important role of a_B is to determine the

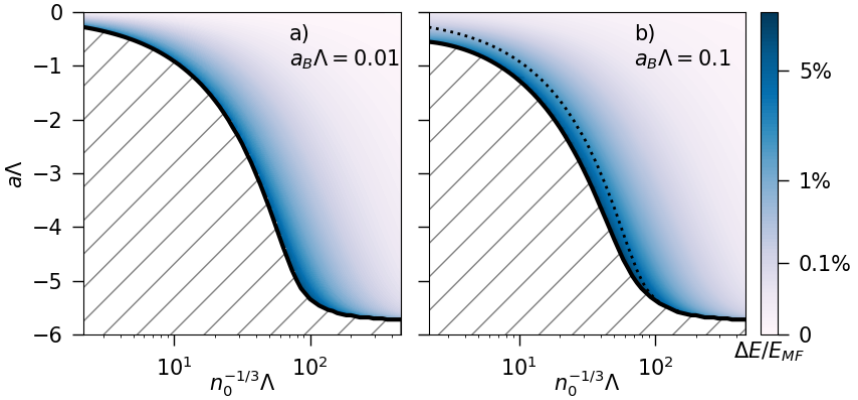

Figure 5.8: The relative energy difference $(E-E_{MF})/E_{MF}$ between the energy E obtained from the Gaussian state and mean-field theory E_{MF} as a function of the density n_0 and scattering length a for mass ratio $M/m = 6/133$. Two different interboson scattering lengths are chosen: a) $a_B\Lambda = 0.01$ and b) $a_B\Lambda = 0.1$. The black solid lines indicate a^*. The dotted line in figure b) corresponds to the solid line of figure a) and is shown to more clearly indicate the difference between figure a) and b). Note that the color scale is not linear, but cubic.

healing length. If we compare Figs. 5.7a) and b) we see that the healing length mainly determines the number of particles in the polaron cloud. This is also reflected in the quasiparticle weight Z in Fig. 5.6 a) and b).

5.4.3 Further aspects

Properties of the metastable polaron

Above we have focused on the instability of the polaron described by Gaussian states. Another interesting question is how much the properties of the polaron are altered compared to the coherent-state approach [152] in the regime where the polaron is metastable. In Fig. 5.8 we plot the energy difference $\Delta E = E - E_{MF}$ between the polaron energy calculated from Gaussian states E and coherent states E_{MF}, which is given in Eq. (5.1).

Remarkably, the effect on the energy appears to be very small. A significant correction to the polaron energy only appears close to the instability, although still limited to less than 10 %. Hence, while introducing correlations in the variational Ansatz leads to a decrease in spectral weight and destabilization at some point, the energy of the polaron is still very well described using mean-field theory. This reflects the general notion that while variational energies may be accurate, the same may not apply for the wave functions.

We have already seen by comparing the dashed and dotted lines in Fig. 5.7 that the number of excitations in the polaron cloud obtained from coherent or Gaussian states are very different. While they still coincide for small particle numbers and scattering lengths, where the quartic $\hat{\mathcal{H}}_{QLLP}$-term has only a small contribution, this term starts to be important for scattering lengths approaching a^*. As a result, the difference between Gaussian and coherent states rapidly increases. This finding is also directly associated with the much smaller Z-factor for the Gaussian State result (see Fig. 5.6).

Dynamical Instability

Our numerical results show a region of dynamical instability (red area in Fig. 5.6a)). A dynamical instability occurs when the variational parameters correspond to a minimum on the variational manifold, but to a saddle point with respect to its tangent space. To identify the presence of the dynamical instability we linearize the real-time equations of motion around the minimum found from iterated Bogoliubov theory. The system is stable when the symplectic diagonalization of the linearized time-evolution operator yields only positive real eigenvalues. However, in case of a dynamical instability, one finds imaginary eigenvalues corresponding to a negative direction in the Hessian. In the real-time evolution the imaginary eigenvalues manifest themselves as an instability with exponentially growing populations of the excitation modes.

Importantly, the dynamical instability indicates that the variational manifold is no longer suitable to describe the state of the system. Hence, to fully describe the dynamics in this regime, even higher order correlations would need to be incorporated in the model.

In Fig. 5.6 the dynamical instability occurs in the small red region attached to the solid line at intermediate densities for $a_B\Lambda = 0.01$. This is exactly the region where the polaron is very large in number of particles and extent, but where the density at the impurity is too small to lead to bound state formation. A dynamic instability was also found for the Bose polaron within the coherent-state description in Ref. [164]. Although the character and position of this instability is different from the one we find here, the origin may be related.

A dynamical instability can also be found when extending our plots to higher density. Here our results are, however, no longer valid, because when $n_0^{-1/3}\Lambda > 1$, one can no longer speak of universal long-range physics, and short-range physics will dominate the behavior of the system. This corresponds to interparticle distances comparable to the length scale of the interaction potentials. In gases of cold atoms the typical densities are orders of magnitude away from this limit.

5.5 Discussion and experimental proposal

5.5.1 Limitations of our approach

First, so far we have only considered light impurities and weak interboson repulsion. In the next Chapter we will find out what happens also for stronger repulsion and heavier impurities. Here, the repulsion can no longer be treated in the Bogoliubov approach, and the picture of the instability will break down. An elaborate comparison of our Gaussian-state approach to coherent-state and double-excitation methods including the repulsion will also be made in the next chapter.

Second, we have studied here the properties of local energy minima on our variational manifold only using imaginary-time evolution. For that reason we could in particular not go beyond a^* to study, e.g., higher-order Efimov states or the repulsive polaron. Furthermore, calculating spectral functions with a Gaussian-state variational manifold is challenging. Therefore the fate of the polaron branch in our model beyond the instability remains an important open direction of study. We consider it unlikely that the polaron branch will completely disappear and we hypothesize that it will be broadened due to the decay into the Efimov clusters. We expect that the resulting width of the spectral line will be inversely proportional to the timescale of the decay, likely determined by, and similar to, the time scale of three-body recombination.

Third, our approach considers up to three-body correlations between two bosons and the impurity. It is thus a natural question to ask how our results would generalize when including even higher order correlations. We expect that when up to N-body correlations are included, the value of a^* would asymptotically connect to the resonance of the N-body Efimov cluster. Due to the cooperative binding effect its absolute value would in turn be smaller than $|a^*|$ obtained in this work. As discussed before, however, we do not expect the polaron branch in the spectrum to suddenly disappear at the point of instability, but we rather expect it to be broadened by the time scale associated with its decay. Since cold atomic gases are typically very dilute, experimental time scales for N-body scattering in experiments are typically highly suppressed for $N > 3$ [90]. As a result, we expect that the inclusion of beyond three-body correlations should not have a strong effect on most observables.

Finally, we note that our results may not fully apply to closed-channel dominated Feshbach resonances, because we use a single-channel model. Effective repulsive three-body interactions present in such systems [149, 150] could counteract the cooperative binding, but are not included in our model.

5.5.2 Experimental implementation

Our predictions have not yet been tested experimentally [144–146]. In experiments performed so far the impurities were at least as heavy as the bosons of the BEC, leading to a strong suppression of the Efimov effect. As a result, any Efimov features would only have been observable at very large negative or positive scattering lengths. In this work we focus on the example of ^{6}Li impurities in a BEC of ^{133}Cs, but for Li in Rb or K BECs, as also available in experiments [165, 166], the results should be very similar.

The typical densities of BECs vary in the range of 10^{13}-10^{15} cm^{-3} [167]. Assuming the three-body parameter $\Lambda \approx l_{vdw}^{-1}$ and a Van der Waals-length of Li-Cs of $45a_0$ this gives a regime of $n_0^{-1/3}\Lambda \sim 40 - 200$. This implies that the low- and intermediate-density regimes of our results can readily be probed, and a clear shift of the Efimov resonance should be observable. In practice, tuning the density in the experiment for a given BEC may in be difficult. However, the resonance position in a BEC could be compared with the resonance position in a thermal gas. The latter could then serve as a reference that should give comparable results to our low-density predictions.

For the specific case of the Efimov resonances observed for Li-Cs at positive Cs-Cs scattering length [80, 168], an interesting subtlety comes into play. In this case the resonance corresponding to the lowest energy Efimov state is suppressed due to coupling to a shallow Cs_2 bound state. Therefore the first observed Efimov resonance actually corresponds to the second Efimov state and it appears at a scattering length of around $-2000a_0$. If we use this Efimov resonance as the lowest resonance in our model, we find a larger three-body parameter $\Lambda^{-1} = 8\ l_{vdw}$. By virtue of the larger size of the Efimov state, this implies that in fact the high-density regime of our results could be probed: $n_0^{-1/3}\Lambda \sim 5 - 25$. Moreover, for smaller mass ratios m/M such as ^{6}Li in a BEC of ^{23}Na, the value of a_- is naturally larger. As a result, $n_0^{-1/3}a_-$ is larger and higher dimensionless densities can be reached as well.

We propose combining two experimental approaches to test our predictions. The first approach would be to perform loss measurements such as regularly used to observe Efimov resonances [78, 80, 86, 87, 90, 91, 168]. In this case the magnetic field should adiabatically be ramped from weak to stronger interactions to form a polaron. Then, at a given final scattering length a, the magnetic field should be kept fixed and the loss arising from

recombination should be measured. As this final scattering length is varied, one should observe an enhancement of the loss when a^* is reached. Whether this appears as a resonant feature or as the onset of a regime where three-body recombination is enhanced, is an open question and subject of further study. Loss measurements may be more efficiently performed by using the recently introduced photoassociative ionization technique [169].

The second approach would be to perform rf-injection spectroscopy such as used in Refs. [144, 145] for lighter impurities. A clear drop in quasiparticle weight and a broadening of the polaron spectral line should be observable as the scattering length of the polaronic instability is approached and crossed. When doing ejection spectroscopy as in Ref. [146], the ground-state polaron is prepared in the initial state. In this case enhanced three-body loss due to Efimov cluster formation will be the most important observable. The formation of tightly bound Efimov clusters may also give rise to higher frequency tails in the rf-spectrum because of their large amount of kinetic energy.

In conclusion, observation of our theoretically predicted phenomena are in reach with current state-of-the-art experimental techniques.

5.6 Conclusion and Outlook

In this Chapter, we used a variational Gaussian-state Ansatz to describe the Bose polaron problem and the Efimov effect. We found that the cooperative binding caused by the Efimov effect leads to the formation of many-particle Efimov clusters. The cooperative binding is driven by the reduction of the kinetic energy of the impurity. Since the Efimov clusters are lower in energy than the Bose polaron, the polaron is not the ground state of the extended Fröhlich Hamiltonian but it rather exists as a metastable, excited state. This excited state loses its stability at a critical scattering length a^* that can be interpreted as a many-body shifted Efimov resonance.

We predict that while the mean-field energy of the polaron is reliable up to the point where the polaron becomes unstable, the inclusion of interboson correlations leads to a strong decrease in the spectral weight. Our results can be experimentally probed by a combination of rf-spectroscopy and three-body loss measurements of light impurities immersed in BECs. The parameter regimes discussed in our work are experimentally feasible, requiring systems that feature both a small interboson scattering length and a large boson-impurity scattering length. We expect our results to also hold, up to quantitative shifts, for slightly larger interboson scattering lengths.

Future interesting directions include the study of the real-time dynamics of the polaron [157, 164, 170] using Gaussian states. Certainly one aim should be to understand how Efimov cluster formation occurs in real-time and whether indeed resonant behavior can be observed at the scattering length a^*. Furthermore, the scope of our results can be extended to multi-channel models and finite polaron momentum [171]. This will respectively allow the study of closed-channel dominated resonances and the dispersion relation of the polaron. Our methods can also be extended to rotating impurities [172–174] or bipolarons [175–177] to study the effect of induced interboson correlations in those systems.

Finally, it would be fascinating to explore the connection to quenched BECs [92–100]. There is a similarity of the polaronic instability to the collapse of a BEC, since the impurity-mediated interactions lead to a net attraction between the bosons of the background gas. Furthermore, we have shown that the formation of a polaron cloud around an impurity can lead to a modification of Efimov physics. One natural question to ask is whether a similar effect occurs in BECs quenched to negative scattering lengths. While one can

certainly not employ the language of polarons or polaron clouds in this case, it is still two-body and higher-order correlations between the bosons that make them cluster together more closely, which is also the essence of polaron physics. Hence, it will be interesting to explore whether a shift of Efimov resonances can also be observed in said scenarios. One way to explore such effects could be the application of the cumulant expansion method as described in Ref. [99, 100] to negative scattering lengths. These connections highlight how the study of impurity physics can give new insights into the dynamics of quenched or collapsing BECs.

Chapter 6. Phase diagram for strong-coupling Bose polarons

This Chapter is based on the following work
[3] Arthur Christianen, J. Ignacio Cirac, R. Schmidt,
Phase diagram for strong coupling Bose polarons,
preprint (2023), arXiv:2306.09075 [cond-mat.quant-gas]

6.1 Introduction

In Chapter 5, we have predicted that the Efimov effect can give rise to an instability of the Bose polaron. Qualitatively, the reason why the polaron becomes unstable is simple: if the impurity can mediate attractive interactions between the bosons from the BEC, the BEC will become attractive, and attractive BECs are known to collapse [43]. The polaronic instability is therefore nothing else than a local, impurity-induced collapse of a part of the BEC.

It is intuitively clear that a sufficiently strong interboson repulsion would prevent this instability, because the accumulation of bosons becomes energetically costly. In this case it is more favorable for only few bosons to be tightly bound to the impurity to form a small molecule [147–149]. However, we find that for sufficiently weak repulsion, the instability still qualitatively persists, even though there is no longer a complete collapse. The lowest energy states in this case are deeply bound many-body clusters. The instability and crossover scenarios are contrasted in Fig. 6.1a), where we illustrate for both cases how the character of the attractive Bose polaron changes as the boson-impurity interactions are swept across a Feshbach resonance. Specifically, we show the energy of the polaron as a function of the inverse scattering length.

In this Chapter we unify the instability and crossover phenomena in a single theoretical picture. We achieve this by comparing the Gaussian-state and double-excitation approaches on equal footing, fully including the interboson repulsion. To this end, we use a quantum-chemistry inspired parameterization of our variational wave function. An important result is Fig. 6.1b), where we highlight which of the two scenarios occurs as a function of the impurity-boson mass ratio and the interboson interaction strength. The crossover occurs if the impurity is heavier or similar in mass to the bosons of the BEC, or if the interboson scattering length a_B is significantly larger than the van der Waals length. If both the impurity is light and the interboson repulsion is weak, we find the polaronic instability. The largest part of the parameter space corresponds to the crossover, and most experiments (see for example Chapter 7) without fine-tuning would therefore show this behavior. However, the instability regime should also be experimentally accessible.

Furthermore, we derive an analytical model using a simple Gaussian wave function, which qualitatively captures both the instability and crossover scenarios. We develop an interpretation of the phenomena in terms of the paradigmatic Landau model of first- and second-order phase transitions [178]. This shows that one can view the instability-to-crossover physics as an analog of the typical liquid-to-gas transition, but appearing at zero temperature.

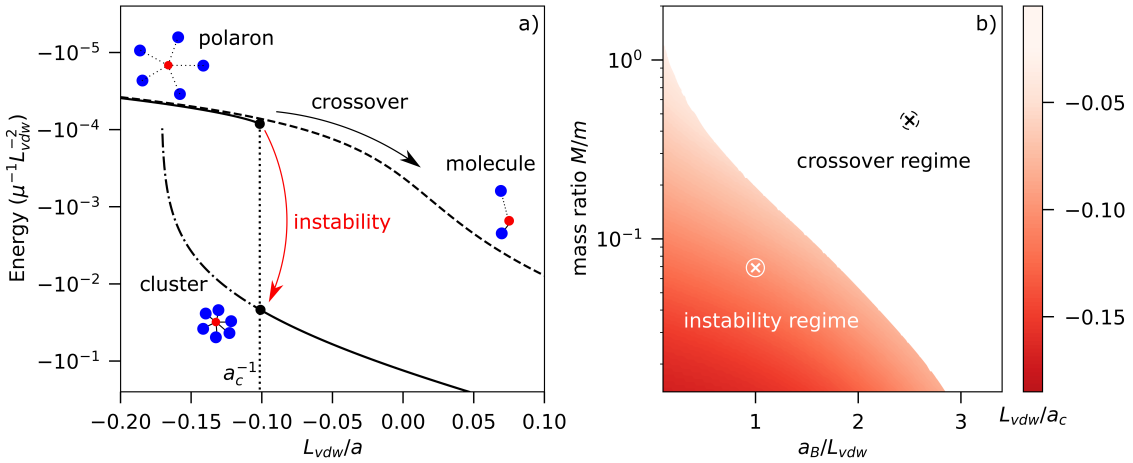

Figure 6.1: a) Energy of the Bose polaron as a function of the inverse impurity-boson scattering length $1/a$ in the regime where it undergoes an instability (bold) or crossover (dashed) as a function of the interaction strength. In the instability regime, the polaron state becomes unstable at the scattering length indicated by the dot. At this point the polaron decays into a cluster. The energy of the cluster before the instability is drawn with the dash-dotted line (only shown in the regime where it is lower than the polaron energy). The bold and dash-dotted lines are computed using a Gaussian-state Ansatz, and the dashed line using a double-excitation Ansatz (see Sec. 6.2). b) Stability diagram indicating whether an instability or crossover will occur as a function of the impurity-boson mass ratio M/m and the interboson repulsion scattering length a_B. In the lower left part of the diagram, the scattering length of the instability a_c is indicated by the colormap. The crosses indicate the parameters corresponding to the lines in subfigure a). For both a) and b), the scales characterizing the interaction ranges of the boson-impurity and boson-boson potential are chosen to be equal: $L_g = L_U = 2L_{vdw}$ (see Sec. 6.2.3). For the density of the BEC we have chosen a typical value of $n_0 = 10^{-5}L_g^{-3}$ (approximately 10^{14} cm^{-3}).

The structure of this Chapter is as follows. In Section 6.2 we highlight the novel features of the theoretical approach relative to the previous chapter. We then demonstrate how we include the renormalized interboson interactions with Gaussian states in Section 6.3. In section 6.4, we describe our numerical results showing the transition from the instability to the crossover regime, we discuss the validity of our approach and the possibility to probe this physics experimentally. The analytical model that captures this behavior is presented in Section 6.5. Finally, we conclude our work in Section 6.6 and we provide an outlook on future directions.

6.2 Theoretical and computational methods

6.2.1 Hamiltonian and variational methods

In this Chapter we do not take the Bogoliubov approximation, and we write our variational state as

$$|\psi\rangle = \hat{U}_{n_0}\hat{U}_{LLP}\hat{A}(\boldsymbol{x})|0\rangle, \tag{6.1}$$

where $\hat{A}(\boldsymbol{x})$ describes the variational wave function on top of the background BEC in the reference frame of the impurity. The vector $\boldsymbol{x}$ contains the variational parameters. If we

again set the total momentum of the system to zero, we find the transformed Hamiltonian

$$\begin{aligned}\hat{\mathcal{H}} &= \hat{U}_{LLP}^\dagger \hat{U}_{n_0}^\dagger \hat{\mathcal{H}}_0 \hat{U}_{n_0} \hat{U}_{LLP} \\ &= \int_{\boldsymbol{k}} \frac{k^2}{2\mu_r} \hat{b}_{\boldsymbol{k}}^\dagger \hat{b}_{\boldsymbol{k}} + \frac{1}{2M} \int_{\boldsymbol{k'}} \int_{\boldsymbol{k}} \boldsymbol{k'} \cdot \boldsymbol{k}\ \hat{b}_{\boldsymbol{k'}}^\dagger \hat{b}_{\boldsymbol{k}}^\dagger \hat{b}_{\boldsymbol{k'}} \hat{b}_{\boldsymbol{k}}, + \int_{\boldsymbol{r}} V_{IB}(\boldsymbol{r})(\hat{b}_{\boldsymbol{r}}^\dagger + \sqrt{n_0})(\hat{b}_{\boldsymbol{r}} + \sqrt{n_0}) + \\ &\int_{\boldsymbol{r'}} \int_{\boldsymbol{r}} V_{BB}(\boldsymbol{r'} - \boldsymbol{r}) \Big[\frac{n_0}{2} (2\hat{b}_{\boldsymbol{r'}}^\dagger \hat{b}_{\boldsymbol{r}} + \hat{b}_{\boldsymbol{r'}}^\dagger \hat{b}_{\boldsymbol{r}}^\dagger + \hat{b}_{\boldsymbol{r'}} \hat{b}_{\boldsymbol{r}}) + \sqrt{n_0} (\hat{b}_{\boldsymbol{r'}}^\dagger \hat{b}_{\boldsymbol{r}}^\dagger \hat{b}_{\boldsymbol{r}} + \hat{b}_{\boldsymbol{r}}^\dagger \hat{b}_{\boldsymbol{r'}} \hat{b}_{\boldsymbol{r}}) + \frac{1}{2} \hat{b}_{\boldsymbol{r'}}^\dagger \hat{b}_{\boldsymbol{r}}^\dagger \hat{b}_{\boldsymbol{r'}} \hat{b}_{\boldsymbol{r}} \Big].\end{aligned} \tag{6.2}$$

Aside from the Gaussian-state Ansatz, in this chapter we will also consider the double-excitation (DE) Ansatz, given by

$$\hat{A}_{\mathrm{DE}}[\beta_0, \beta(\boldsymbol{k}), \alpha(\boldsymbol{k}, \boldsymbol{k'})] = \beta_0 + \int_{\boldsymbol{k}} \beta(\boldsymbol{k}) \hat{b}_{\boldsymbol{k}}^\dagger + \frac{1}{\sqrt{2}} \int_{\boldsymbol{k}} \int_{\boldsymbol{k'}} \alpha(\boldsymbol{k}, \boldsymbol{k'}) \hat{b}_{\boldsymbol{k}}^\dagger \hat{b}_{\boldsymbol{k'}}^\dagger. \tag{6.3}$$

For the double-excitation Ansatz, the case where $\alpha = 0$ is often called the Chevy Ansatz, after Frédéric Chevy, who first introduced an Ansatz of this kind for the Fermi polaron problem [137].

6.2.2 Basis set and computations

We parameterize the variational wave functions in terms of a Gaussian basis set. This approach is inspired by quantum chemistry, where the use of Gaussian basis functions is common practice [179]. Concretely, in the Gaussian-state case, this parameterization corresponds to

$$\phi_{\boldsymbol{k}} = \sum_i \phi_i \chi_{00}(\sigma_i^{(\phi)}, \boldsymbol{k}), \tag{6.4}$$

$$\xi^{(l)} i_{\boldsymbol{k}\boldsymbol{k'}} = \sum_{ij} \xi_{ij}^{(l)} \chi_{lm}(\sigma_i^{(\xi,l)}, \boldsymbol{k}) \chi_{l-m}(\sigma_j^{(\xi,l)}, \boldsymbol{k}). \tag{6.5}$$

Here, $\chi_{lm}(\sigma, \boldsymbol{k})$ are spherical Gaussian basis functions,

$$\chi_{lm}(\sigma, \boldsymbol{k}) = (2\pi)^{3/2} Y_{lm}(\theta, \phi) i^{-l} k^l \exp(-\sigma k^2). \tag{6.6}$$

In Appendix 6.A we show how to compute the matrix elements of the Hamiltonian terms with the Gaussian basis functions.

Since the polaron cloud has a smooth shape and is localized around the impurity, this approach requires fewer variational parameters than the method applied in the previous Chapter, where the wave functions were parameterized by simply discretizing ϕ and ξ in a spherical-wave basis. The Gaussian basis functions are chosen over other types of basis functions which might more closely resemble the shape of the polaron cloud, because integrals over Gaussian functions give simple analytical expressions. Especially the matrix elements of the interboson interactions generally take a complicated form, whereas for Gaussian basis functions they can still be computed analytically, at least for Gaussian potentials.

For the calculations one can either choose to keep the exponents of the Gaussian basis functions fixed, or to also treat them as variational parameters. Here we leave them fixed. The size of the smallest σ is determined by the range of the potential, and the size of the largest σ by the extent of the polaron cloud. Since these length scales are orders of magnitude different, we choose the values of σ to be spaced logarithmically. The spacing of σ is then chosen to ensure convergence of the parameters of interest. For varying

calculations we typically use between five and twenty values of σ per angular-momentum mode, depending on the variational method, the observable, and the desired convergence.

To work with this Gaussian basis set in practice we need a few additional steps. Indeed, the basis functions are not orthonormal and we define the Hermitian overlap matrix S as

$$S_{ij}^{(l)} = \int_{\boldsymbol{k}} \chi_{lm}^*(\sigma_i^{(\xi,l)}, \boldsymbol{k})\chi_{lm}(\sigma_j^{(\xi,l)}, \boldsymbol{k}) = \frac{\sqrt{\pi}(2l+1)!!}{2^{l+2}(\sigma_i^{(\xi,l)} + \sigma_j^{(\xi,l)})^{3/2+l}}. \tag{6.7}$$

In a similar way, we define $S^{(\phi)}$, where $l, m = 0$ and the exponents correspond to $\sigma^{(\phi)}$, and

$$S_{ij}^{(mix)} = \int_{\boldsymbol{k}} \chi_{00}^*(\sigma_i^{(\phi)}, \boldsymbol{k})\chi_{00}(\sigma_j^{(\xi,0)}, \boldsymbol{k}). \tag{6.8}$$

Similar to ξ, S can be viewed as a block-diagonal matrix, where the blocks are labeled by (l).

Using these overlap matrices we can now also directly express F and G in terms of ξ. Taking G as an example, we write

$$G(\boldsymbol{k}, \boldsymbol{k'}) = \sum_l \sum_{m=-l}^{l} \boldsymbol{\chi}_{lm}^T(\boldsymbol{k}) G^{(l)} \boldsymbol{\chi}_{lm}^*(\boldsymbol{k'}), \tag{6.9}$$

where G is again a block diagonal matrix with blocks labeled by l, and $\boldsymbol{\chi}_{lm}$ is the vector of basis functions with angular-momentum labels l and m. With this notation, G can be cast into matrix form:

$$G = \sum_{n=1}^{N} (\xi S^T \xi^* S)^n S^{-1} = \left[[\mathbb{I} - (\xi S^T \xi^* S)]^{-1} - \mathbb{I}\right] S^{-1}, \tag{6.10}$$

$$\equiv X - S^{-1}. \tag{6.11}$$

Similarly for F,

$$F = XS\xi = \xi S^T X^T = \xi + GS\xi. \tag{6.12}$$

The overlap matrices now also appear in the equations of motion. Considering Eq. (3.69) and taking $x_j' = \phi_j$ we find

$$0 = \eta_j^* + \sum_i \partial_\tau \phi_i^* [S_{ij}^{(\phi)} + 2(S^{(mix)} G^{(0)} [S^{(mix)}]^T)_{ij}] - \sum_i \partial_\tau \phi_i [2(S^{(mix)} [F^{(0)}]^* [S^{(mix)}]^T)_{ij}], \tag{6.13}$$

where $\eta_j^* = \partial_{\phi_j} E$. Again, in practice taking a simplified equation for ϕ

$$\partial_\tau \boldsymbol{\phi} = -[S^{(\phi)}]^{-1} \boldsymbol{\eta}, \tag{6.14}$$

gives the same result with comparable computational efficiency. The equations of motion for ξ are also the same as in Eq. (3.78), except for the addition of the S-matrices,

$$\partial_\tau \xi^* = -[S^{-1}\Delta^* S^{-1} + S^{-1}\mathcal{E}^*\xi^* + \xi^*\mathcal{E}S^{-1} + \xi^*\Delta\xi^*]. \tag{6.15}$$

Since we now include the interboson repulsion fully, both the equations of motion for ϕ and ξ are non-linear. As a result of the stronger non-linearity, the direct imaginary-time evolution is now more stable and efficient than the iterated Bogoliubov theory we used in Chapter 5. We solve the imaginary-time evolution equations numerically with a solver based on backward-differentiation formulas [180, 181], which greatly outperforms standard

Runge-Kutta methods for this problem due to the stiffness of the differential equations. The stiffness originates from the interplay of the vastly different length scales of the range of the potential and the healing length of the BEC. We find that using the Gaussian basis set, qualitative and near-quantitative results can already be retrieved with a relatively small number of parameters. However, in the regimes with the strongest correlations the stiffness of the non-linear equations of motion can lead to problems for reaching strict convergence when increasing the number of parameters. In our implementation, it is the stiffness of the differential equation rather than the direct scaling with the number of parameters which limits the computational cost. When too many basis functions are included, the basis set comes close to creating linear dependencies. This slows down the numerical optimization and it sometimes leads to the solver getting stuck. In the regime of large repulsion, where the correlations are most important, this limits the convergence of our parameters of study to about five percent.

For the double-excitation Ansatz, most computation steps proceed analogously. Here one can also derive equations of motion for imaginary-time evolution. However, opposed to the Gaussian-state case, the equations of motion are linear and can be solved much more efficiently by direct diagonalization. Here the stiffness is no issue, and more rigorous convergence can be reached.

6.2.3 Interaction potentials

Instead of using contact interactions, in our framework with a Gaussian basis set, it is more convenient to use Gaussian model potentials,

$$V_{IB}(\boldsymbol{r}) = \frac{g}{2L_g^2} \exp\Big(-\frac{r^2}{L_g^2}\Big), \tag{6.16}$$

$$V_{BB}(\boldsymbol{r}) = \frac{U}{2L_U^2} \exp\Big(-\frac{r^2}{L_U^2}\Big). \tag{6.17}$$

Here L_g and L_U set the ranges of the potentials and g and U set the coupling strengths. The matrix elements over these interactions potentials and the spherical Gaussian basis functions are computed analytically and given in Appendix 6.A. Since these potentials have a proper real-space representation, they are also more physical than the separable contact interactions which obtain their range through a UV-cutoff.

We fix the coupling strengths g and U to give us the desired scattering lengths a and a_B, respectively. The scattering lengths corresponding to the Gaussian potentials can simply be determined by solving the two-body problem, or using the simple approximate formulas from Ref. [182]. There is no unique choice of U and g, but we take $U > 0$ and for g we take the smallest negative value that reproduces the desired scattering length.

The range of the boson-impurity Gaussian potential can be related to the range of the typical cold-atom van der Waals potential via the effective range r_{eff}. We do this at unitarity $a \to \infty$. There, $r_{eff} \approx 1.4 L_g$ for the Gaussian potential, whereas for a van der Waals potential $r_{eff} \approx 2.8 L_{vdw}$ [64, 183], meaning that $L_g \approx 2 L_{vdw}$. For modest positive scattering lengths, the results are less universal, and the repulsive interboson Gaussian potential we use here can generally not reproduce the effective range of a van der Waals potential. By fixing the absolute range relative to L_g, however, we believe we still obtain representative results. Note that having finite-range interactions is crucial for the description of the Efimov effect, since the range of the interactions sets the three-body parameter and therefore the scattering length of the first Efimov resonance a_- [77, 81, 82, 184].

6.3 Repulsion

6.3.1 Interboson repulsion energy functional

As a first step, we discuss how we describe the interboson interactions with the Gaussian-state Ansatz. The expectation value of the interboson repulsion term of the Hamiltonian is given by

$$\begin{aligned}E_U(\phi,\xi) = \langle GS|\hat{\mathcal{H}}_U|GS\rangle = \frac{U}{2L_U^2}\int_{\boldsymbol{r}}\int_{\boldsymbol{r'}} \exp\big[-\frac{(\boldsymbol{r'}-\boldsymbol{r})^2}{L_U^2}\big] \\ \Big\{\frac{n_0}{2}\Big[\phi^*(\boldsymbol{r})\phi(\boldsymbol{r'}) + \phi(\boldsymbol{r})\phi(\boldsymbol{r'}) + F(\boldsymbol{r'},\boldsymbol{r}) + G(\boldsymbol{r'},\boldsymbol{r}) + h.c.\Big] \\ + \sqrt{n_0}\Big[|\phi(\boldsymbol{r})|^2\phi(\boldsymbol{r'}) + G(\boldsymbol{r},\boldsymbol{r})\phi(\boldsymbol{r'}) + G(\boldsymbol{r'},\boldsymbol{r})\phi(\boldsymbol{r}) + F(\boldsymbol{r'},\boldsymbol{r})\phi^*(\boldsymbol{r}) + h.c.\Big] \\ + \frac{1}{2}\Big[|\phi(\boldsymbol{r})|^2|\phi(\boldsymbol{r'})|^2 + \big[|\phi(\boldsymbol{r'})|^2 + \frac{G(\boldsymbol{r'},\boldsymbol{r'})}{2}\big]G(\boldsymbol{r},\boldsymbol{r}) \\ + \big[\phi^*(\boldsymbol{r})\phi(\boldsymbol{r'}) + \frac{G(\boldsymbol{r'},\boldsymbol{r})}{2}\big]G(\boldsymbol{r},\boldsymbol{r'}) + \big[\phi^*(\boldsymbol{r})\phi^*(\boldsymbol{r'}) + \frac{F^*(\boldsymbol{r},\boldsymbol{r'})}{2}\big]F(\boldsymbol{r},\boldsymbol{r'}) + h.c.\Big]\Big\}.\end{aligned} \tag{6.18}$$

Since we approximate in Eq. (6.1) the background BEC with a coherent state, no interboson correlations are included, and the interactions are treated on the level of the Born approximation. If we now include interboson correlations close to the impurity, the interboson interactions will be renormalized, unphysically resulting in a weaker effective interboson repulsion close to the impurity than in the background BEC.

A natural way to overcome this issue is to also treat the background BEC on the level of a Gaussian state, as in Chapter 4. However, this would severely complicate the structure of the cubic and quartic terms of the polaron Hamiltonian in Eq. (6.2).

Instead, we choose a hybrid approach. Far from the impurity we take a coherent-state wave function and describe the interactions within the Born approximation, whereas close to the impurity we keep the bare coupling, which is renormalized by the Gaussian-state wave function. As we have seen in Chapter 4, the term predominantly responsible for renormalizing the interactions in the background BEC, is the n_0F-term. Removing this term ensures that the energy of the BEC cannot be lowered by our Ansatz in the case for which there are no boson-impurity interactions. We find that our approach works best when we also remove the $\sqrt{n_0}\phi F$ terms. Since we have now removed the renormalization mechanism for these terms, we replace in the quadratic and cubic terms the coupling constant U by $U_B = \frac{8a_B}{m\sqrt{\pi}L_U}$ which gives the same scattering length when applying the Born approximation. Hence, we obtain

$$\begin{aligned}E_U(\phi,\xi) \approx \frac{1}{2L_U^2}\int_{\boldsymbol{r}}\int_{\boldsymbol{r'}} \exp\big[-\frac{(\boldsymbol{r'}-\boldsymbol{r})^2}{L_U^2}\big]\Big\{\frac{n_0U_B}{2}\Big[\phi^*(\boldsymbol{r})\phi(\boldsymbol{r'}) + \phi(\boldsymbol{r})\phi(\boldsymbol{r'}) + G(\boldsymbol{r'},\boldsymbol{r}) + h.c.\Big]] \\ + \sqrt{n_0}U_B\Big[|\phi(\boldsymbol{r})|^2\phi(\boldsymbol{r'}) + G(\boldsymbol{r},\boldsymbol{r})\phi(\boldsymbol{r'}) + G(\boldsymbol{r'},\boldsymbol{r})\phi(\boldsymbol{r}) + h.c.\Big] \\ + \frac{U}{2}\Big[|\phi(\boldsymbol{r})|^2|\phi(\boldsymbol{r'})|^2 + \big[|\phi(\boldsymbol{r'})|^2 + \frac{G(\boldsymbol{r'},\boldsymbol{r'})}{2}\big]G(\boldsymbol{r},\boldsymbol{r}) + \big[\phi^*(\boldsymbol{r})\phi(\boldsymbol{r'}) + \frac{G(\boldsymbol{r'},\boldsymbol{r})}{2}\big]G(\boldsymbol{r},\boldsymbol{r'}) \\ + \big[\phi^*(\boldsymbol{r})\phi^*(\boldsymbol{r'}) + \frac{F^*(\boldsymbol{r},\boldsymbol{r'})}{2}\big]F(\boldsymbol{r},\boldsymbol{r'}) + h.c.\Big]\Big\}.\end{aligned} \tag{6.19}$$

Importantly, the quartic term, involving no bosons from the background condensate, is still treated fully within our Gaussian-state approach. This term is the most important for

Table 6.1: Explanation of lines and methods used for Fig. 6.2. Here U_2 and U_3 stand for the coupling constants in the quadratic and cubic terms of the interboson repulsion in Hamiltonian (6.2) and U_4 stands for the quartic term. The coupling constant U is the bare coupling and $U_B = \frac{8a_B}{m\sqrt{\pi}L_U}$, is the coupling giving the same scattering length on the level of the Born approximation.

label	line	Ansatz	U_2 and U_3	U_4
GS	solid	mod. Gaussian	U_B	U
CS1	dashed	coherent	U_B	U_B
CS2	dash-dotted	coherent	U_B	U
CS3	dotted	coherent	U	U

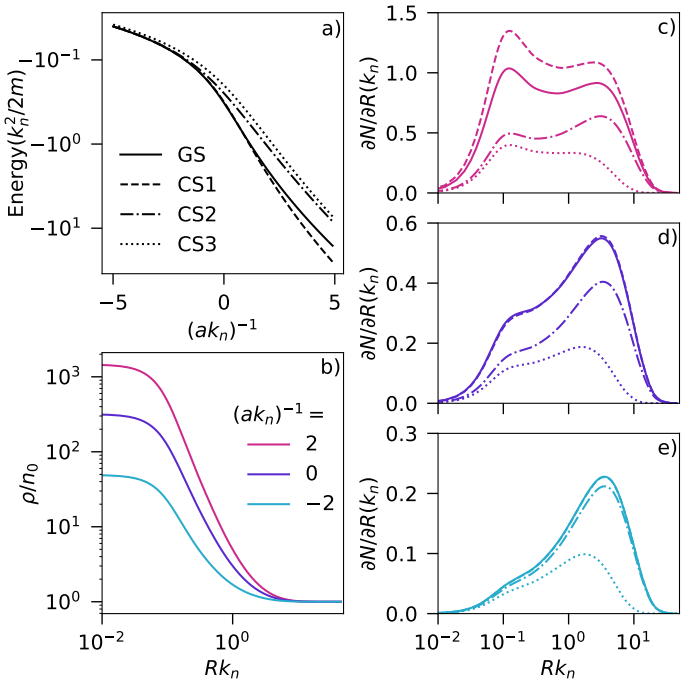

Figure 6.2: Properties of an infinite mass impurity immersed in an interacting BEC of density $n_0 = 10^{-5}L_g^{-3}$ and for $a_B = L_g = L_U$. a) Polaron energy as a function of the inverse boson-impurity scattering length. b) Bosonic density for three different scattering lengths from Gaussian states as a function of the distance to the impurity. c-e) Number of additional particles at distance R from the impurity (see Eq. (6.20)) for c) $(ak_n)^{-1} = 2$, d) $(ak_n)^{-1} = 0$, and e) $(ak_n)^{-1} = -2$. For the characterization of the computational approaches, see Tab. 6.1 and the main text. The legend for the line style and color in a) and b) also apply to c) ,d) and e).

the strong-coupling physics close to the impurity, since it describes the repulsion between the excitations from the BEC.

6.3.2 Infinitely heavy impurity

To test the validity of this hybrid approach we consider first the case of an infinite-mass impurity. This is a well-studied case [150, 163, 185, 186], for which there are no impurity-mediated interactions. For negative scattering lengths up to unitarity, the Born approximation for the interboson interactions is expected to hold well [185]. As a result, a

coherent-state approach should describe the repulsion quite accurately when the interactions are treated using the Born approximation.

In Fig. 6.2 we compare the Gaussian-state result using the hybrid Born description with coherent-state results using varying interboson coupling constants (see Table 6.1). In the approach denoted as CS1 we fully take the Born approximation, for CS2 we take the bare coupling for the quartic term, and for CS3 we take the bare coupling in all the terms. We set $L_g = L_U = a_B$ and consider a high density BEC, $n_0 = 10^{-5} L_g^{-3}$ (corresponding to a density of $\sim 10^{-14}$ cm^3). We show our results in units of the characteristic wave vector $k_n = (6\pi^2 n_0)^{1/3}$. In Fig. 6.2a) we plot the energies from these methods as a function of the inverse scattering length. In Fig. 6.2b) we plot the density of bosons as a function of the distance from the impurity. In Fig. 6.2c), d) and e) we show the number of excitations surrounding the impurity in a shell at a certain distance R:

$$\frac{\partial N}{\partial R}(R) = R^2 \int_{|\boldsymbol{r}|=R} d\Omega(\langle b_{\boldsymbol{r}}^\dagger b_{\boldsymbol{r}} \rangle - n_0), \tag{6.20}$$

for scattering lengths $(ak_n)^{-1} = 2$, $(ak_n)^{-1} = 0$, and $(ak_n)^{-1} = -2$, respectively.

In the weak-coupling regime, i.e., in the left of Fig. 6.2a), the quadratic interboson repulsion term is most important, and all approaches treating this term on the same footing (GS, CS1 and CS2) agree with each other within a percent. The result from CS3 already gives a difference in energy, and furthermore, in Fig. 6.2e) we see that this approach underestimates the extent of the polaron cloud. This is because the healing length of the BEC, which sets the extent of the polaron cloud, is too small with the unrenormalized coupling constant.

Going to stronger coupling, the short-range repulsion becomes more important. While the GS and CS1 results keep agreeing with each other within 3% up to unitarity, $(ak_n)^{-1} = 0$, the CS2 approach starts to strongly deviate from these results at $(ak_n)^{-1} \approx -1$. Indeed, Fig. 6.2d) shows that also the differences in the wave functions become larger.

For positive scattering lengths larger than $(ak_n)^{-1} \approx 1$ the Born approximation breaks down and the Gaussian-state result starts to deviate from the CS1 result. In this regime, the short-range repulsion is the dominant effect, since the density close to the impurity is more than a factor 1000 higher than the background density, see Fig. 6.2b).

Altogether, we now have the confidence that the Gaussian state with the hybrid Born approach properly renormalizes the interboson interactions. The Gaussian-state results namely agree with the coherent-state results with the Born approximation in the parameter regime where this approximation is valid. Without renormalization of the repulsion, the results would clearly be different, as shown via the CS2 and CS3 results. Furthermore, in the region where the Born approximation is expected to break down, indeed the Gaussian-state results are different from the coherent-state results.

6.3.3 Double-excitation Ansatz

Properly including the interboson interactions is more complicated for the single- and double-excitation Ansätze, since these are not mean-field approaches. Restricting the number of excitations namely implicitly leads to many-body correlations. To make the most fair comparison in the next section, we as far as possible treat the double-excitation Ansatz calculation on the same footing as the Gaussian-state calculation. The original

value of $E_U(\beta_0,\beta,\alpha) = \langle DE|\hat{\mathcal{H}}_U|DE\rangle$ is given by

$$E_U(\beta_0,\beta,\alpha) = \frac{U}{2L_U^2}\int_{\boldsymbol{r}}\int_{\boldsymbol{r'}} \exp\big[-\frac{(\boldsymbol{r'}-\boldsymbol{r})^2}{L_U^2}\big]\Big\{\frac{n_0}{2}\big[\beta^*(\boldsymbol{r})\beta(\boldsymbol{r'}) + \sqrt{2}\beta_0^*\alpha(\boldsymbol{r'},\boldsymbol{r}) + 2\int_{\boldsymbol{r''}}\alpha^*(\boldsymbol{r'},\boldsymbol{r''})\alpha(\boldsymbol{r''},\boldsymbol{r}) + h.c.\big] + \sqrt{2n_0}\big[\beta^*(\boldsymbol{r})\alpha(\boldsymbol{r},\boldsymbol{r'}) + h.c.\big] + |\alpha(\boldsymbol{r'},\boldsymbol{r})|^2\Big\}. \tag{6.21}$$

To be most consistent with the Gaussian-state case we choose to approximate this using the following energy functional

$$E_U(\beta_0,\beta,\alpha) \approx \frac{1}{2L_U^2}\int_{\boldsymbol{r}}\int_{\boldsymbol{r'}} \exp\big[-\frac{(\boldsymbol{r'}-\boldsymbol{r})^2}{L_U^2}\big]\Big\{\frac{n_0U_B}{2}\big[2\beta^*(\boldsymbol{r})\beta(\boldsymbol{r'}) + 4\int_{\boldsymbol{r''}}\alpha^*(\boldsymbol{r'},\boldsymbol{r''})\alpha(\boldsymbol{r''},\boldsymbol{r}) + h.c.\big] + \sqrt{2n_0}U_B\big[\beta^*(\boldsymbol{r})\alpha(\boldsymbol{r},\boldsymbol{r'}) + h.c.\big] + U|\alpha(\boldsymbol{r'},\boldsymbol{r})|^2\Big\}. \tag{6.22}$$

This energy functional is chosen to reproduce the mean-field result in the weak-coupling limit. The quartic term is still described exactly, which is most important for our work.

6.4 Results: Polaronic instability or smooth crossover?

We now move on to the case of a finite-mass impurity, where aside from the interboson and boson-impurity interactions, there are also *mediated* interactions between the bosons that are generated by the impurity. We will show that this new ingredient drastically changes the behavior of the polaron. It can lead to the previously discussed polaronic instability and induce physics akin to that of first-order phase transitions. In this section we explore the parameter space to determine under which conditions the polaronic instability occurs, and in which regimes it is suppressed.

6.4.1 Light impurities and the polaronic instability

For concreteness, we again consider a ^{6}Li-impurity in a BEC of ^{133}Cs atoms. We vary both the impurity-boson and the boson-boson scattering lengths. We take the ranges of the potentials, L_g and L_U, to be related via

$$\frac{L_U}{L_g} = \frac{L_{vdw,CsCs}}{L_{vdw,LiCs}}. \tag{6.23}$$

Here, $L_{vdw,CsCs(LiCs)}$ is the Van der Waals length for the Cs-Cs (Li-Cs) potential. This results in a value of $L_U \approx 2.3L_g$.

First we test what our variational approaches predict for the interboson scattering lengths $a_B = 1.5L_g$ and $2.7L_g$, at a density of $10^{-5}L_g^{-3}$. In a typical scenario this density approximately corresponds to 10^{14}cm^{-3}. We use the Gaussian-state and double-excitation approaches as discussed in the previous section. Moreover, we study a coherent-state approach using the Born approximation in all terms of the energy functional (CS1 in the nomenclature of the previous section). The results are shown in Fig. 6.3. Here we plot the energies of the various methods as a function of the inverse impurity-boson scattering length, in units of L_g. In Fig. 6.3a) the parameters lie in the instability regime and in Fig. 6.3b) in the crossover regime. Recognizing the logarithmic scale, one immediately sees

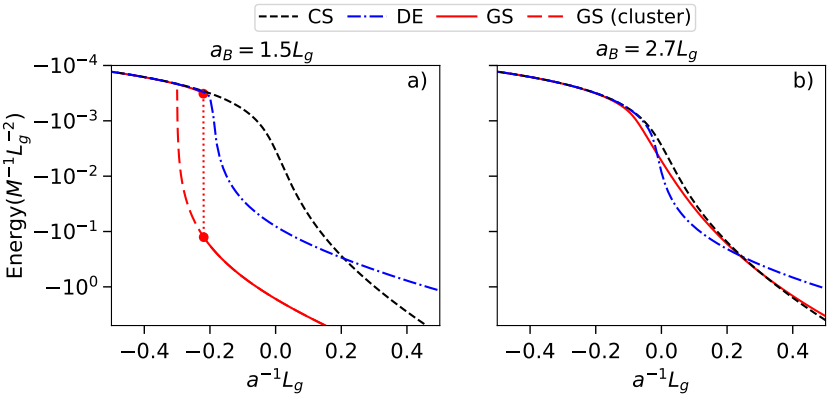

Figure 6.3: Polaron energies compared to cluster energies as a function of scattering length for a mass ratio $M/m = 6/133$, $n_0 = 10^{-5}L_g^{-3}$ and interboson scattering lengths of a) $a_B = 1.5L_g$ and b) $2.7L_g$, and $L_U = 2.3L_g$. The three lines correspond to the coherent-state, Gaussian-state and double-excitation Ansätze. In figure a) we observe the polaronic instability for the Gaussian-state Ansatz, where the energy jumps from a polaron state to a cluster state, indicated with the dots and the dotted line. The cluster state before the instability is indicated with the red dashed line, and is only shown for energies lower than the polaron energy.

that the curves in Fig. 6.3 are qualitatively different from those in Fig. 6.2a), and that the predictions of the three methods differ by *orders of magnitude*.

In Fig. 6.3a), the three approaches start to strongly differ around the Efimov resonance, since the three-body correlations introduced by the Efimov effect are treated in a widely varying manner. Before this point, in the far left of the figure, the boson-impurity coupling is weak, and all curves coincide. The coherent state does not capture three-body correlations at all, and continues describing the mean-field polaron. The double-excitation Ansatz predicts a relatively sharp crossover into the trimer state which appears at the Efimov resonance. Finally, the Gaussian-state Ansatz predicts a polaronic instability, marked in Fig. 6.3a) by the red dots, where the mean-field polaron ceases to be stable and decays into a many-particle cluster. The red dashed line indicates the energy of the many-body cluster before the polaron becomes unstable. In this regime the polaron is metastable and not the ground state. Since the polaronic instability corresponds to a many-body shifted Efimov resonance (see Chapter 5), it happens close to where the trimer crosses the continuum. Compared to the Efimov energy scale, the density is still relatively low and the resonance is therefore not shifted substantially (see also Fig. 6.6). Since all three approaches are variational, the lowest energy state best describes the ground state, and therefore the Gaussian-state approach is most appropriate.

In the crossover regime, such as in Fig. 6.3b), the story is different. Here the interboson repulsion is much larger and overcomes the mediated interactions, pushing the Efimov resonance towards unitarity. We therefore see that the mean-field regime, where the curves coincide, extends to stronger interactions. Around unitarity, now the double-excitation Ansatz gives the best description. In this regime, no large clusters can be formed, and the polaron experiences a crossover into a trimer-like state. As evident, this behavior cannot be captured well by the Gaussian- or coherent-state methods, whose curves lie relatively close together. Only when the attractive impurity-boson interaction is increased further, more particles can bind to the impurity, and the Gaussian- and coherent-state methods outperform the double-excitation approach, as signified by their resulting energies. Note,

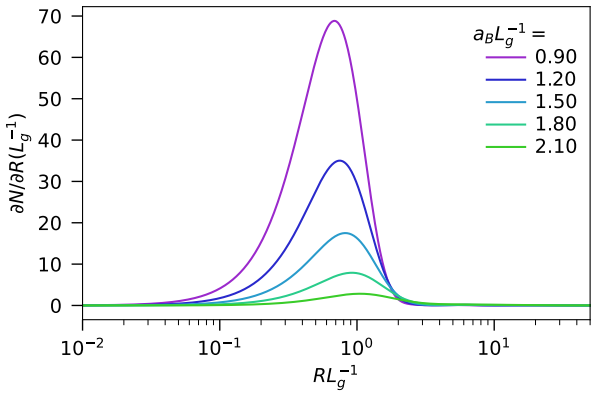

Figure 6.4: The wave function of the deepest bound clusters at unitarity (i.e., $a^{-1} = 0$) found from Gaussian states for the mass ratio $M/m = 6/133$ and for $n_0 = 0$. The colors of the lines indicate the value of the interboson repulsion.

however, that this occurs relatively far outside the universal regime.

The character of the clusters that form in the instability regime in Fig. 6.3a) is quite distinct from the polaron. Example wave functions of the clusters are shown in Fig. 6.4 for increasing interboson repulsion in absence of a background BEC ($n_0 = 0$) and for unitary boson-impurity interactions. We see in Fig. 6.4 that many particles come together within the range of the potential. A polaron cloud can also host many particles, but for a polaron state most particles are far away from the impurity, at a distance set by the healing length (see Fig. 6.2c-e)).

For increasing repulsion, the number of particles in the cluster rapidly decreases. At some point the bound state contains only a few particles. Here the Gaussian-state description (as the coherent-state approach) fails since it is bound to represent a superposition of states with different particle numbers, with limited control over the weights of their contributions. This is especially detrimental for the description of a bound state with exactly one or two particles. Therefore, a double-excitation Ansatz is more suitable in this regime.

As a technical side note, numerically, we find not just one, but in fact two types of stable cluster states from the Gaussian-state approach. The clusters shown so far contain both a coherent and a Gaussian contribution to the wave function, but another local minimum on the variational landscape arises when there is solely a Gaussian contribution to the wave function ($\phi = 0$). This second type of clusters is generally higher in energy, but the real-space wave functions such as in Fig. 6.4 are qualitatively similar. There is one regime where the second type of cluster is lower in energy than the first type: when the particle number in the cluster goes to zero. In this case the Gaussian state just describes a superposition of the free impurity and a trimer.

6.4.2 Emergent "phase diagram"

We now discuss the behavior of the polaron as predicted from the variational methods, for varying densities of the background BEC. In Fig. 6.5 we show the energy of the polaron as a function of the inverse scattering length for several densities (indicated by the colors). We have also added the energies of the dimer (black dashed), trimer (black dashed with triangles) and the two types of cluster discussed before (thin and thick black solid) as a function of the inverse scattering length in absence of a background BEC. The different panels correspond to Gaussian-state results (Fig. 6.5a) and b)) and double-excitation results (Fig. 6.5c) and d)) for different values of the interboson repulsion. Note that the

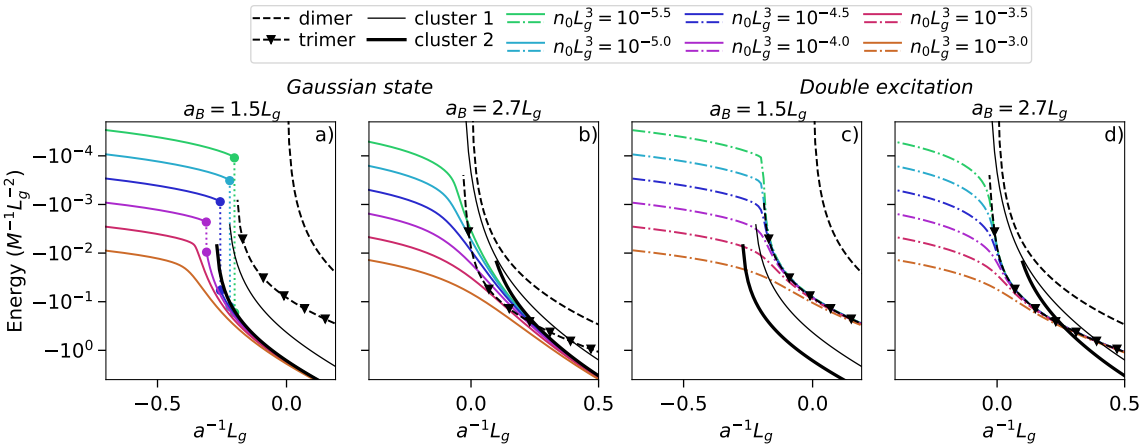

Figure 6.5: Polaron energies (colored lines) as a function of the inverse boson-impurity scattering length for a light impurity ($M/m = 6/133$), calculated using a,b) the Gaussian-state Ansatz, c,d) the double-excitation Ansatz. In panels a) and c) $a_B = 1.5L_g$, in panels b) and d) $a_B = 2.7L_g$. The color of the lines indicates their corresponding background density. In all panels the black dashed lines indicate the dimer and trimer (with triangles) energies. The black solid lines indicate the energies from the two types of cluster from the Gaussian-state approach at $n_0 = 0$. In figure a) the point of polaronic instability is indicated with the pairs of dots and dotted lines.

scale of the x-axis is different in the left and right panels.

For weak impurity-boson attraction, on the left side of all four panels, the polaron is in the mean-field regime, and the energy should depend approximately linearly on the density (see Eq. (5.1)). Since the colored lines are spaced linearly on the logarithmic energy grid and the corresponding densities are also spaced logarithmically, we indeed recover this expected result. The energy scale of the polaron is much smaller than the scale of the bound states, except for the highest densities.

In Fig. 6.5a) we again note the presence of the polaronic instability, but interestingly, this instability disappears for large densities. The transition from a polaronic instability to a crossover can therefore happen both as a function of density, and as a function of the interboson repulsion. The point where the instability disappears is the point where the gap between the polaron energy and the cluster energy closes. In the case of Fig. 6.5a), this gap is closed by increasing the polaron energy through an increase in the density. The character of the cluster is largely unaffected by the increase of the density, meaning that the formed clusters can still contain many particles even in the crossover regime.

In Fig. 6.5b), the repulsion is large enough that there is a crossover for all densities. For all but the largest densities, the Gaussian state does not describe this crossover well around unitary interactions (compare to Fig. 6.5d)) since the Gaussian-state energy actually lies above the trimer energy.

In the lower two panels (Fig. 6.5c) and d)), we see that the double-excitation Ansatz behaves qualitatively the same for all densities and for both values of the interboson repulsion: it gives a smooth crossover between the polaron and the trimer state, irrespective of the presence of larger clusters, which cannot be captured by this approach. It is interesting to notice that for increasing density, the crossover happens over a broader range of interaction strengths, and that the interaction strength where the polaron energy merges with the trimer line becomes larger. This is the opposite trend compared to the instability in Fig. 6.5a), where the polaronic instability happens for decreasing interaction strengths

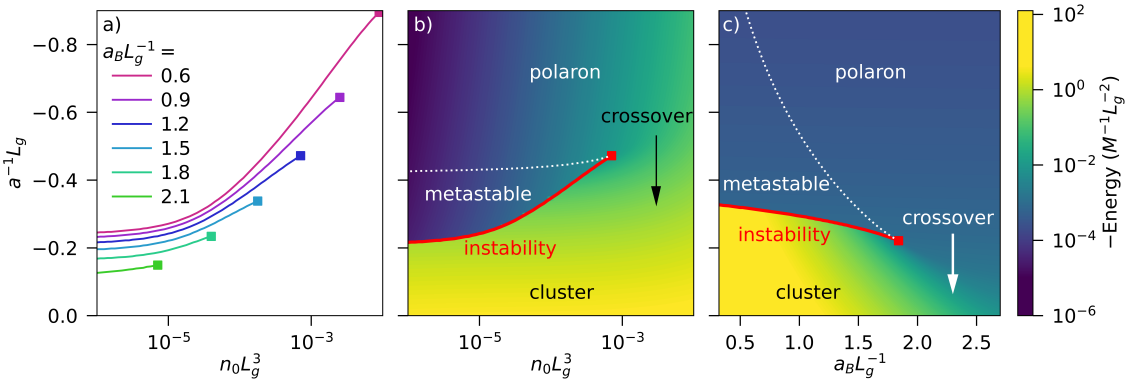

Figure 6.6: a) Critical scattering length a_c of the polaronic instability as a function of the density n_0, for various values of the interboson scattering length a_B. At the square endpoints of the line the gap between the polaron and cluster states has closed, and the instability turns into a crossover. b,c) Polaron energy as a function of scattering length for b) varying density and fixed $a_B = 1.2L_g$ and c) varying a_B and fixed density $n_0 L_g^3 = 10^{-4.5}$. The red lines indicate the critical scattering length of instability, such as in figure a). The white dotted line indicates the scattering length where the energy of the cluster crosses the polaron energy. Between the dotted and dashed lines the polaron is thus metastable. The mass ratio is chosen to be $M/m = 6/133$ and $L_U = 2.3L_g$.

as the background density is increased. This difference can be explained as follows. For the Gaussian state, a larger particle number in the polaron cloud means that it is easier to decay into a cluster. Hence, at larger densities smaller interaction strengths are needed. For the double-excitation Ansatz, there is a competition between the polaron energy, which increases with the density, and the trimer energy, which is not strongly affected by the density. Therefore, the regime of the crossover is shifted towards larger interaction strengths as the density increases.

Next, we examine in more detail the density dependence of the critical scattering length of the polaronic instability. In Fig. 6.5a) we can already see that the point of instability shifts to smaller scattering length as the density increases. In Fig. 6.6a), this critical scattering length is plotted as a function of the density for various values of the interboson repulsion, increasing from top to bottom.

For low densities, on the left hand side of Fig. 6.6a), the lines of critical scattering length approach the value of the Efimov scattering length. This scattering length already gives a dependence on the interboson repulsion, reflecting that also the value of the Efimov scattering length depends strongly on the interboson repulsion.

When moving to higher density, the critical interaction strength (at fixed repulsion) decreases and at some critical density the gap between the polaron and cluster energies closes. This is also visualized in Fig. 6.6b), where the underlying energy landscape (computed using Gaussian states) is shown as a colormap for $a_B = 1.2L_g$. Here the instability is marked with the red line. The point where the gap between polaron and cluster closes, marks the end point of the transition from the polaron to the cluster states. Beyond this density a crossover occurs. Considering again Fig. 6.6a), we find that the density where the instability terminates increases rapidly with the interboson repulsion. This is because the cluster binding energy decreases with the repulsion. Therefore the gap closes already at smaller polaron energies and thus smaller densities.

Aside from the red line marking the instability, Fig. 6.6b) also shows (white dotted line)

the scattering length where the cluster energy first crosses the polaron energy. This line therefore marks the point where the ground state of the model truly switches character. In between the white dotted and red lines we find the regime of metastability, where the polaron is not the ground state, but where there is no decay process included in our Ansatz from the polaron state into the cluster state. In Fig 6.3 this is the region before the instability where the dashed line lies below the solid line. Note that the white dotted line is almost horizontal in this figure. That is because the cluster energies are on a different scale than the polaron energy, and changing the polaron energy via the density therefore does not strongly affect the crossing point of the polaron and cluster energies.

In Fig. 6.6c) we show a similar graph, but here we fix the density $n_0 L_g^3 = 10^{-4.5}$ and vary instead the interboson repulsion. While as a function of the density, the polaron energy changes and the cluster energy is approximately constant, the opposite is true when varying the interboson repulsion, which has a much larger impact on the cluster state than the polaron. Therefore in this case the gap between the polaron and cluster energies is closed by decreasing the cluster energy. However, qualitatively the picture is the same. There is still a transition terminating in a critical point, beyond which there is a crossover. As we saw in Fig. 6.6a), the point of instability shifts to larger interaction strengths for increasing repulsion, following the trend of the position of the Efimov resonance.

In contrast to Fig. 6.6b), where the white dotted line is almost flat, here the white dotted line varies much more with the interboson repulsion than the line of instability. This is because the line of instability is determined by the smallest cluster into which the polaron can initially decay, and the line of metastability by the many-particle cluster which is lowest in energy. Since the more particles there are in the cluster, the more important their repulsion, it is not surprising that the metastability line depends more strongly on the repulsion than the instability line.

Altogether, we see that a remarkable picture emerges of a first-order transition between a polaron and a cluster, which terminates at a critical point. This is strongly reminiscent of classical first-order phase transitions, such as the phase transition of condensation of a gas into a liquid. We discuss this analogy in more detail in Section 6.5 where we develop an analytical model for the Bose polaron that qualitatively recovers this behavior.

6.4.3 Mass dependence

So far we have considered the scenario of a light impurity in a BEC, where the impurity-mediated interactions are particularly strong. Now we explore in more detail how the phenomena we observe manifest themselves for a wider range of impurity masses.

In Fig. 6.7, diagrams are shown that indicate for which values of the mass ratio and interboson repulsion the polaronic instability appears. The color code indicates the corresponding critical scattering length. The background density n_0 is fixed within both panels, and given by a) $10^{-6} L_g^{-3}$ and b) $10^{-4} L_g^{-3}$ (approximately 10^{13} and 10^{15} cm^{-3}, respectively). In Fig. 6.1b) another such colormap is shown for the density $10^{-5} L_g^{-3}$. Note that on the x-axis the interboson scattering length is given in units of L_U. We have chosen these units, because varying L_U while keeping a_B/L_U fixed only gives rise to minor changes in the plots. This indicates that also the range of the interboson repulsion matters, and not just its scattering length. This is not surprising, since the range of the potentials is known to be important for the Efimov effect.

We see that the region of instability appears for light impurities and weak interboson repulsion, in the lower left of both panels. Here, the impurity-mediated interactions are the strongest and dominate over the interboson repulsion. For equal mass or heavy impurities the regime where an instability appears shrinks drastically. Furthermore, no instability

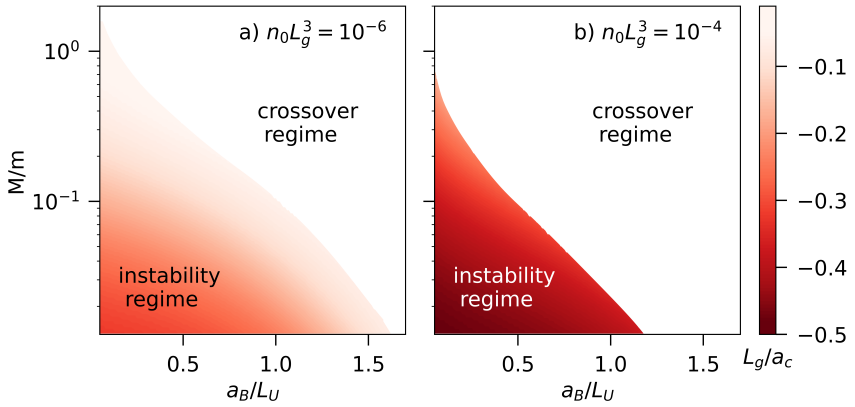

Figure 6.7: Stability diagrams of the polaron for densities a) $n_0 L_g^3 = 10^{-6}$ and b) $n_0 L_g^3 = 10^{-6}$ as a function of the impurity-boson mass ratio M/m and the interboson repulsion scattering length a_B. In the lower left part of the diagram, when the boson impurity scattering length is swept across the Feshbach resonance, the polaron will experience an instability at scattering length a_c indicated by the colormap. In the upper right part the polaron will smoothly cross over into a small cluster. For this plot $L_g = L_U = 1$.

appears if a_B is significantly larger than L_U.

Comparing Figs. 6.7a) and b), we observe that the regime of instability shrinks as the density is increased. This is because the larger the density, the larger the polaron energy, and hence the smaller the energy gap between polaron and cluster. From the change of color one sees that the critical scattering length at which the instability occurs also becomes smaller (as also visible in Figs. 6.5a) and 6.6).

6.4.4 Comparison of Gaussian-state and double-excitation Ansatz

Having discussed the qualitative distinction between the regimes of the instability and the crossover, we now systematically compare the Gaussian-state and double-excitation methods. The main aim of this comparison is to demonstrate in which parameter regime which method works best. In Fig. 6.8 we show the polaron energies from the Gaussian-state Ansatz (first column), the double-excitation Ansatz (second column), and their ratio, as a function of the mass ratio and the interboson repulsion. The different rows correspond to different boson-impurity scattering lengths. Comparing to Fig. 6.7, the y-axis extends to larger mass ratios.

In the lower left of the plots, again the region of polaronic instability appears. Here the energy found from Gaussian states is obviously lower than the energy from the double-excitation Ansatz, as evident from the right column and the results we have shown before. The region in parameter space where a many-particle cluster is found with Gaussian states is more or less similar to the regime where a trimer is formed with much lower energy than the energy scale of the mean-field polaron, as seen from the double-excitation results.

For system parameters in the crossover regime, the Gaussian-state and double-excitation results appear more similar, because here at least the energy scale is the same: the scale of the mean-field polaron energy, set by the density of the BEC. For heavy impurities and $a = -0.05 L_g^{-1}$, in the blue region of Fig. 6.8a) and b), the system is truly in the polaron regime, and bound state physics does not play a crucial role. Here the ground-state energy (which is already rescaled by the reduced mass) is only mildly dependent on the mass ratio and the interboson repulsion. Despite being in the polaron regime, in the far left

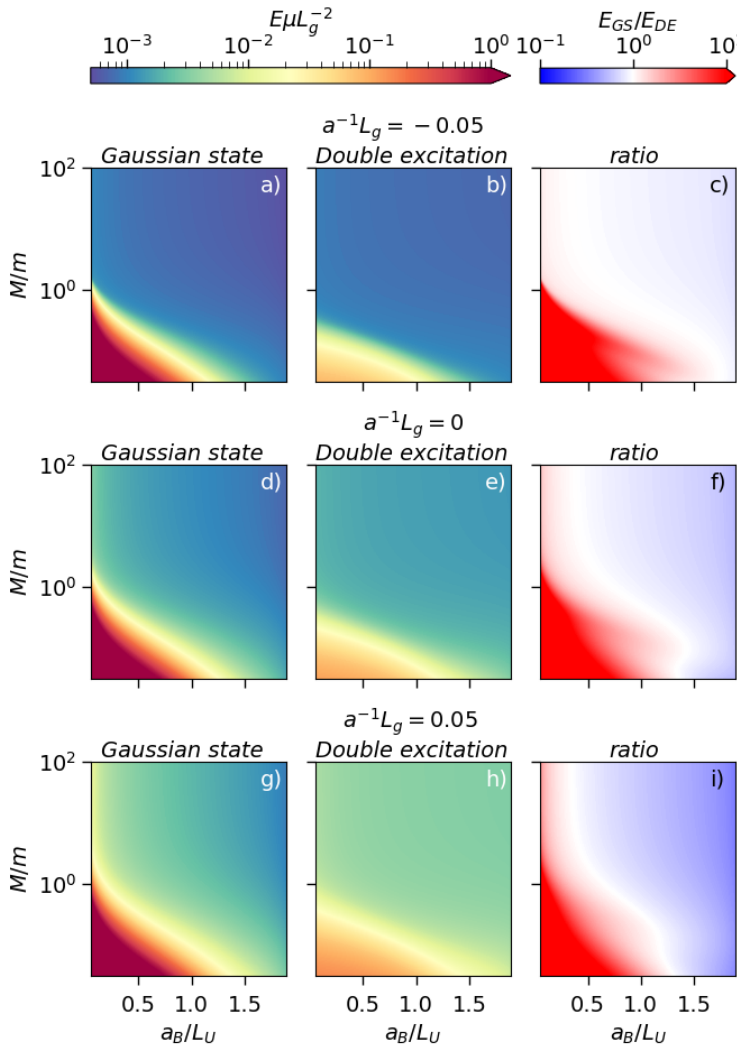

Figure 6.8: Colormaps of the polaron energy as a function of the mass ratio M/m and interboson scattering length a_B from the Gaussian-state Ansatz (first column) and double-excitation Ansatz (second column). In the third column the ratio of the energies from these approaches is shown. The different rows correspond to different inverse boson-impurity scattering lengths, given by a-c) $-0.05L_g^{-1}$, d-f) $0L_g^{-1}$, f-i) $0.05L_g^{-1}$. Here $L_g = L_U$ and the density is given by $n_0 = 10^{-5}L_g^{-3}$.

and far right of the plot there is a significant energy difference of up to 30 % between the Gaussian-state and double-excitation results. For low interboson repulsion the Gaussian state performs better, because here many excitations can come close to the impurity. In contrast, in the regime of large repulsion the double-excitation Ansatz works better. Here the number of excitations is limited, and having more correlations between these few excitations and the bath is therefore more effective. Note that this argument even holds for the infinitely heavy impurity. Thus, our results show that merely the Born approximation being satisfied is not sufficient to show that a coherent or Gaussian state accurately describes the ground state. This has the important implication that also the Gross-Pitaevskii equation, which is equivalent to a coherent-state approach, loses its validity. This confirms the analysis of Ref. [150].

When moving from the upper row of Fig. 6.8 to the lower rows, i.e., to stronger boson-

impurity interaction strengths, we see that the differences between the Gaussian-state and double-excitation results become progressively larger. This is because here bound-state physics starts to play a larger role. In the right-hand side of the plots a bound state containing only one or two particles is more favorable than a true polaron state. This is reflected in the much lower energy of the double-excitation result compared to the Gaussian-state result. However, towards the left-hand side of these plots the number of particles close to the impurity grows significantly, rendering, in turn, the double-excitation Ansatz insufficient.

In the strong-coupling regime where Gaussian states and the double-excitation Ansatz give similar energies (white regions in figures f) and i)), we expect that actually neither of them work very well. While the double-excitation Ansatz does not have enough excitations, the Gaussian-state Ansatz does not give enough independent control over the different particle number sectors. We identify this as the most challenging regime, which requires going beyond the double-excitation Ansatz [149] or using Quantum Monte Carlo.

6.4.5 Experimental implementation

Now we turn to a discussion of the feasibility of realizing the physics predicted in this Chapter in experiments. First, let us discuss the density of the BEC. The density range of 10^{-6}-$10^{-4} L_g^{-3}$, corresponds via $L_g \approx 2L_{vdw}$ and a typical value of $L_{vdw} \approx 50a_0$ [64] to densities of $7 \cdot 10^{12}$-10^{14} cm^{-3}. Such densities are readily available experimentally.

Next, we turn to the interboson repulsion. With the usual magnetic-field controlled Feshbach resonances, the boson-impurity and boson-boson scattering lengths cannot be tuned independently. This limits experiments to the background scattering lengths in the BEC at the magnetic fields of the boson-impurity resonances. Far away from Feshbach resonances and for a stable BEC, typically $a_B \sim L_{vdw}$. As a result, most experiments without large mass imbalance naturally operate relatively deep in the crossover regime (see Figs. 6.1 and 6.7).

There are other mechanisms to change the scattering lengths, which could be used in combination with the magnetic-field approach to be able to tune multiple scattering lengths simultaneously [187]. Optical control of the scattering length has already been observed [188, 189], and Feshbach resonances tuned via radiofrequency or microwave fields [187, 190] have been proposed theoretically. Even though these schemes usually lead to losses, in the Bose polaron context it might help that the interboson scattering length needs to be decreased instead of increased, and that experiments would only need to run for a short time.

From the Bose polaron experiments carried out so far, the experiments using ^{39}K [145, 191] incidentally have a very small interboson scattering length of $a_B \approx 9a_0$. While these experiments are still most likely not in the regime of instability, they are relatively close, and therefore the formation of large clusters could be expected. However, to populate such deeply bound states one needs to go beyond the standard injection spectroscopy, because starting with a non-interacting state will give only very small overlap with such deep, many-particle bound states.

Concerning the realization of varying mass ratios between the impurity and the bosons, there are setups realizing a large mass imbalance with light impurities. Prominent examples are the Li-Cs mixtures used to study heteronuclear Efimov physics [80, 86, 87, 168]. Unfortunately, for ^{133}Cs the background scattering length is usually very large, so this would most likely prevent the presence of the polaronic instability.

Another issue which arises in systems of large mass imbalance is very fast three-body loss at strong coupling. This loss arises precisely from the same mediated interactions

between bosons which also lead to the polaronic instability. While this highlights another interesting connection between the field of polarons and conventional few-body physics, this may also make preparing such mixtures in a stable way at ultracold temperatures difficult.

Altogether, the physics which would be observed could differ tremendously between the different mixtures and even for different Feshbach resonances in the same mixture, see below. This gives the exciting opportunity to explore the different types of behavior. However, this also implies that caution is required when comparing different experiments, since seemingly small differences in the experimental parameters might lead to drastically different behavior. This gives a unique opportunity to explore the rich interplay between few- and many-body physics.

6.4.6 Discussion

We now discuss some limitations of the theoretical approaches employed in this work.

Description of the clusters

A Gaussian state is not very suitable to accurately describe the structure and energies of the deeply bound clusters formed in the instability regime. There are several reasons for that. First, in absence of a background condensate, the true cluster states are particle number eigenstates and Gaussian states are not. In fact, the spread in the particle number of a Gaussian state is of the order of the number of particles. Second, higher-order correlations will most likely become important in the microscopic description of many-body clusters. Even though three-body correlations between the bosons and the impurity are included, this will generally not be sufficient for bound states of more than three particles. Third, the properties of deep many-particle bound states cannot be expected to be universal. Therefore the properties of these states will depend on the details of the interactions potentials and the use of simple model potentials is not warranted.

However, the structures of these clusters are unlikely to be important for experimental observables. Experimentally, once such a deeply bound cluster is formed, this would immediately lead to fast recombination losses. Furthermore, in the density regime reachable in cold-atom experiments, the qualitative mechanism of the polaronic instability should not be very sensitive to the detailed structure of the underlying clusters. In fact, unlike the wave function of the deeply bound clusters, the mechanism of the instability itself and the mediated interactions should be universal. The mediated interactions namely originate from the Lee-Low-Pines term in the Hamiltonian, which is independent of the potential. Furthermore, the first clusters into which the polaron decays will contain only few particles, and only after the formation of these small intermediate clusters, will the system cascade into the deeply bound ground state. When the background density of the BEC becomes very high this picture might break down, however, and here the point where the instability terminates will depend on the actual energy of the cluster.

The double-excitation Ansatz

In the crossover regime of Figs. 6.1 and 6.7, far enough away from the polaronic instability, we believe that the ground-state energy is well described by the double-excitation Ansatz. Possible corrections can be accounted for by an extension to the triple-excitation Ansatz [149]. Therefore, we believe that regarding the ground-state energies, the picture sketched for equal mass and heavy impurities is accurate in Refs. [149, 150].

However, whether the *wave function* of the resulting state is also well described, remains an open point of discussion [152]. For example, in the regime where the ground state of the system is a trimer, the double-excitation Ansatz will "invest" its excitations to describe this trimer state. However, it is not unlikely that in reality this molecule will again induce its own polaron cloud. The double-excitation Ansatz is not capable of describing this behavior, since its excitations are already used up in the description of the bound state itself. While for the ground-state energy this may not have a significant effect, for the wave function and the description of the full excitation spectrum it can certainly be of importance.

Another shortcoming of the double-excitation Ansatz is its description of the weak-coupling Bose polaron in presence of interboson repulsion. For the weak coupling case, it is most natural to describe the polaron cloud on the same footing as the background BEC. This is naturally achieved using a coherent- or Gaussian-state Ansatz. In these approaches it is also more clear how to describe the interboson interactions correctly. Consistently doing this with the double-excitation Ansatz is more difficult, because this would require an accurate description of the interactions in the background BEC.

Moreover, the double-excitation Ansatz brings with it the subtle problem of how to count the number of particles in the polaron cloud. One would expect that the double-excitation Ansatz gives rise to at most two excitations. This is indeed true if one does not allow the double-excitation Ansatz to have a component in the mode of the BEC. However, with a coherent-state or Gross-Pitaevskii approach, one does not have this restriction. If indeed the double-excitation Ansatz is also allowed a component in the mode of the BEC, then the cross-terms with the BEC will give rise to equally large particle numbers in the polaron cloud as in the coherent-state case. This could potentially explain the qualitative difference between the large number of particles the coherent-state approaches predict in the polaron cloud [163, 185, 186] and the apparent success of variational approaches with only few excitations [147, 149, 150].

Narrow Feshbach resonances

In this work we use a single-channel model for the boson-impurity interactions, which is best suited to describe broad and isolated Feshbach resonances [64]. In Refs. [147, 149] a two-channel model has been used, which is also applicable to narrow resonances. In this case, the multi-channel nature of the interactions can lead to an effective three-body repulsion. This will have a similar effect as the intrinsic interboson repulsion and therefore help to suppress the instability. This may therefore lead to a shift of the boundary of the instability region in Figs. 6.1 and 6.7.

6.5 Analytical model

The form of Fig. 6.6b) and c), with its first-order transition ending in a critical point, followed by a smooth crossover, is remarkably similar to well-known diagrams of first-order phase transitions such as the liquid-gas phase transition. To strengthen this connection we attempt to understand the Bose polaron phenomenology in simpler terms. To this end, we develop an analytical model to qualitatively reproduce the key features of Fig. 6.1 and Fig. 6.6. Surprisingly, we find that we can achieve this with a much simplified Gaussian-state Ansatz. As we will see, even when restricting the variational Ansatz to only $l = 0$ and $l = 1$ angular momentum modes, and only a *single* Gaussian basis function per angular-momentum mode, the model already qualitatively reproduces the essential physics.

We thus start the derivation of the analytical model by writing

$$\phi(\boldsymbol{k}) = \phi\chi_{00}(\sigma_\phi, \boldsymbol{k}), \tag{6.24}$$

$$\xi(\boldsymbol{k}, \boldsymbol{q}) = \xi_0\chi_{00}(\sigma_\phi, \boldsymbol{k})\chi_{00}(\sigma_\phi, \boldsymbol{q}) + \xi_1 \sum_m (-1)^m \chi_{1m}(\sigma_1, \boldsymbol{k})\chi_{1-m}(\sigma_1, \boldsymbol{q}). \tag{6.25}$$

6.5.1 Coherent states and effective scattering length

To build our understanding, we start by first considering a coherent-state Ansatz and omitting the interboson interactions in the Hamiltonian. We replace the real-space Gaussian boson-impurity potential by a short-range separable interaction with a Gaussian cutoff function in momentum space,

$$\hat{\mathcal{H}}_{\text{int}} = g\Big[\int_{\boldsymbol{k}} e^{-\sigma_g k^2}(\hat{b}^\dagger_{\boldsymbol{k}} + \sqrt{n_0}\delta(\boldsymbol{k}))\Big] \times \Big[\int_{\boldsymbol{k}} e^{-\sigma_g k^2}(\hat{b}_{\boldsymbol{k}} + \sqrt{n_0}\delta(\boldsymbol{k}))\Big]. \tag{6.26}$$

The scattering length a for this potential is related to the coupling constant g as

$$g^{-1} = \frac{\mu_r}{2\pi a} - \frac{\mu_r}{\sqrt{(2\pi)^3\sigma_g}}. \tag{6.27}$$

Using only the coherent-state part of our Ansatz (i.e. $\xi = 0$), one finds the energy as a function of ϕ and σ_ϕ to be given by

$$E(\phi, \sigma_\phi) = gn_0 + T_\phi\phi^2 + 2gV_\phi\sqrt{n_0}\phi + gV_\phi^2\phi^2, \tag{6.28}$$

where T_ϕ and V_ϕ are the expectation values of the kinetic and interaction energies

$$T_\phi = \int_{\boldsymbol{k}} \frac{k^2}{2\mu_r}|\chi_{00}(\sigma_\phi, \boldsymbol{k})|^2 = \frac{3\sqrt{\pi}}{16\mu_r(2\sigma_\phi)^{5/2}}, \tag{6.29}$$

$$V_\phi = \int_{\boldsymbol{k}} e^{-\sigma_g k^2}\chi_{00}(\sigma_\phi, \boldsymbol{k}) = \frac{1}{4\sqrt{2\pi(\sigma_g + \sigma_\phi)^3}}. \tag{6.30}$$

Eq. (6.28) can be trivially minimized with respect to ϕ and σ_ϕ. The resulting value of $\sigma_\phi = 5\sigma_g$ is independent of any of the other parameters. This leads to

$$E = \frac{n_0}{g^{-1} + \frac{V_\phi^2}{T_\phi}} = \frac{2\pi n_0}{\mu_r(a^{-1} - a^{-1}_{\text{shift}})}, \tag{6.31}$$

where

$$a^{-1}_{\text{shift}} = (2\pi\sigma_g)^{-1/2} - \frac{2\pi V_\phi^2}{\mu_r T_\phi} = \frac{1 - \frac{5^{5/2}}{3^4}}{\sqrt{2\pi\sigma_g}}. \tag{6.32}$$

Note that this expression of the energy is remarkably similar to the energy found from mean-field theory assuming a weakly repulsive BEC within the Bogoliubov approximation [152]. In the case of Eq. (5.1) from Ref. [152], the origin of the shift a_0 of the scattering length in the denominator can be traced back to the interboson repulsion limiting the size of the polaron cloud. In our case it is the exponent of the Gaussian basis function that limits the size of the cloud.

If we want to compare our analytical result with the full model we can define an effective scattering length

$$a^{-1}_{\text{eff}} = a^{-1} - a^{-1}_{\text{shift}}. \tag{6.33}$$

This effective scattering length diverges when a bound state appears in our model. We can also express g in terms of a_{eff} as

$$g^{-1} = \frac{\mu_r}{2\pi a_{\text{eff}}} - \frac{V_\phi^2}{T_\phi}. \tag{6.34}$$

With this replacement, the coherent-state energy for the polaron without background repulsion is perfectly recovered.

6.5.2 Gaussian states and the polaronic instability

Having considered the coherent-state case, we now include also the Gaussian part as in Eq. (6.25) into the wave function; still without including the interboson repulsion. The additional variational parameters are ξ_0, ξ_1, σ_0 and σ_1. We keep $\sigma_\phi = 5\sigma_g$ fixed, since the coherent part is the dominant part in the polaron regime. Expanding the energy functional up to quadratic order in ϕ^2, ξ_0 and ξ_1, we find

$$E(\phi, \xi_0, \sigma_0, \xi_1, \sigma_1) = gn_0 + T_\phi\phi^2 + (T_0 + gV_0^2)S_0\xi_0^2 + 3T_1S_1\xi_1^2 + 2gV_\phi\sqrt{n_0}\phi + gV_\phi^2\phi^2 - 3T_{L\phi}\phi^2\xi_1 - 3T_{L0}\xi_0\xi_1. \tag{6.35}$$

In this expression, the quantities T_1 and $T_{L\phi}$ are given by

$$T_1 = \int_{\boldsymbol{k}} \frac{k^2}{2\mu_r}|\chi_{1m}(\sigma_\phi, \boldsymbol{k})|^2 = \frac{15\sqrt{\pi}}{32\mu_r(2\sigma_1)^{7/2}}, \tag{6.36}$$

$$T_{L\phi} = -\frac{1}{M}\left[\int_{\boldsymbol{k}} \boldsymbol{k}\chi_{1m}^*(\sigma_1, \boldsymbol{k})\chi_{00}(\sigma_\phi, \boldsymbol{k})\right]^2 = \frac{3\pi}{64M(\sigma_\phi + \sigma_1)^5}. \tag{6.37}$$

The quantities T_0, V_0 and T_{L0} are defined similarly to T_ϕ, V_ϕ, and $T_{L\phi}$ by substituting σ_ϕ by σ_0. The $T_{L\phi}$ and T_{L0} terms originate from the Lee-Low-Pines term in the Hamiltonian.

The terms S_0 and S_1 are overlap integrals, given by

$$S_0 = \int_{\boldsymbol{k}} |\chi_{00}(\sigma_0, \boldsymbol{k})|^2 = \frac{\sqrt{\pi}}{4(2\sigma_0)^{3/2}}, \tag{6.38}$$

$$S_1 = \int_{\boldsymbol{k}} |\chi_{1m}(\sigma_0, \boldsymbol{k})|^2 = \frac{3\sqrt{\pi}}{8(2\sigma_1)^{5/2}}. \tag{6.39}$$

Minimizing the energy functional (6.35) with respect to σ_0, σ_1, ξ_0 and ξ_1 now yields $\sigma_0 = \sigma_\phi = 5\sigma_g$ and $\sigma_1 = \frac{15}{2}\sigma_g$. This implies $T_\phi = T_0$ and $T_{L\phi} = T_{L0} = T_L$. For ξ_0 and ξ_1 one then finds

$$\xi_0 = \frac{3T_L}{2S_0(T_0 + gV_0^2)}\xi_1, \tag{6.40}$$

$$\xi_1 = \frac{T_L\phi^2}{2S_1T_1 - \frac{3T_L^2}{2S_0(T_0+gV_0^2)}}. \tag{6.41}$$

The parameters ξ_i characterize the Gaussian part of the wave function. Thus, already from Eqs. (6.40) and (6.41) we can see a sign of the instability, which will occur when the denominator of ξ_1 vanishes and hence ξ_0 and ξ_1 diverge. From Refs. [1, 2] we know that in the low-density limit this happens at the Efimov scattering length a_-, where the three-body Efimov bound state arises. Hence, if we derive the value of a_{eff} where the divergence

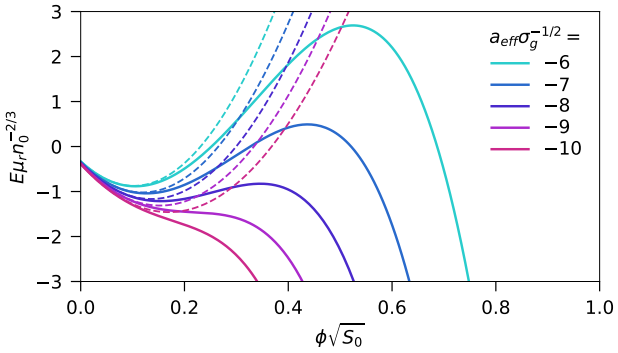

Figure 6.9: Energy functional of Eq. (6.31) (dashed) and Eq. (6.44) (solid), where the energy is plotted in units of $\mu_r n_0^{-2/3}$ as a function of the normalized "order parameter" ϕ for several effective scattering lengths. The magnitude of the scattering length increases from top to bottom. The mass ratio here corresponds to Li-Cs and $n_0\sigma_g^{3/2} = 1.25\ 10^{-5}$.

occurs, we can extract the value of $a_{\text{eff},-}$ in our model with the simplified wave function. This is given by:

$$a_{\text{eff},-} = \frac{T_0\mu}{V_0^2 2\pi}\left(1 - \frac{4S_1T_1S_0T_0}{3T_L^2}\right), \tag{6.42}$$

$$= \frac{3^4\sqrt{2\pi\sigma_g}}{5^{5/2}}\left(1 - \frac{M^2 5^{11}}{\mu_r^2 2^{14}3^6}\right) \approx 3.6\sqrt{\sigma_g}\left(1 - 4.1\frac{M^2}{\mu_r^2}\right). \tag{6.43}$$

The scattering length $a_{\text{eff},-}$ is negative. We thus see that even in our simple model a three-body bound state appears from the continuum in a Borromean way, i.e., it arises before a two-body bound state is possible. Furthermore, the linear scaling of $a_{\text{eff},-}$ with the length scale of the potential $\sqrt{\sigma_g}$, matches the expectations of van der Waals universality [81, 82, 184]. Finally, note that for a light impurity $\frac{M^2}{\mu_r^2} \to 1$ and for a heavy impurity $\frac{M^2}{\mu_r^2} \to \infty$. This implies that $a_{\text{eff},-} \to -11.2\sqrt{\sigma_g}$ for light impurities and $a_{\text{eff},-} \to -\infty$ for heavy impurities. The limits of the mass-dependence of $a_{\text{eff},-}$ are therefore also physical. Quantitatively, however, one should note that the realistic mass dependence of a_- is stronger than found here.

Now we can plug in the expressions for ξ_0 and ξ_1 to obtain an energy functional in terms of only ϕ:

$$E(\phi) = gn_0 + 2gV_0\sqrt{n_0}\phi + (T_0 + gV_0^2)\phi^2 - \frac{\mu_r S_0 T_0^2 \phi^4}{2\pi V_0^2(a_{\text{eff}} - a_{\text{eff},-})}. \tag{6.44}$$

The structure of this equation with linear, quadratic and quartic terms in ϕ is reminiscent of the paradigmatic Landau model for phase transitions, where ϕ would correspond to the order parameter. Our scenario, with a positive quadratic term and a negative quartic term, corresponds to the case of a *first-order* phase transition. Here the linear term, which depends on the density of the background BEC, adds an effective external field to the description (similar to an external magnetic field in the theory of phase transitions in magnetic materials). Note that all the terms depend explicitly on the boson-impurity interaction strength.

The energy functional (6.44) is plotted in Fig. 6.9 for different values of a_{eff}. Here $\sqrt{S_0}$, as defined in Eq. (6.38), serves to normalize the Gaussian basis function. The dashed lines indicate the combined contribution of the linear and quadratic parts, while the solid lines

show the full result from Eq. (6.44). Note the remarkable similarity of this figure to the qualitative picture we sketched in Fig. 5.5.

For small a_{eff}, the function has a minimum at small ϕ corresponding to the polaron state. In this regime, the quartic term plays no significant role. For increasing a_{eff}, the value of ϕ at the polaron minimum increases. Therefore the quartic term becomes more and more important. As evident from Eq. (6.44), the quartic term is also directly dependent on a_{eff}, further enhancing its importance for increasing a_{eff}.

At some point the quartic term overcomes the quadratic term and the polaron minimum disappears: the polaron becomes unstable. Because no interboson repulsion is included to stabilize the energy functional, ϕ will grow indefinitely beyond this point. Our model breaks down in this limit since ξ_0 and ξ_1 cease to be small parameters, and higher-order terms in ξ will be important in Eq. (6.35).

The point of polaronic instability does *not* correspond to the point of a phase transition in the Landau model, because a phase transition in the thermodynamic sense happens when the ground state of the system changes its character. This would be at the point where any cluster becomes lower in energy than the polaron for the first time. The metastability of the polaron can instead be interpreted as a form of hysteresis. The point of the true phase transition is not properly described in the energy functional (6.44) and requires to improve the model further as we will discuss in the following.

At the point of instability, both the first and second derivative of the energy with respect to ϕ vanish and we can use this to find the density and scattering length determining the "stability boundary" of the polaron state. This critical density, as a function of the scattering length, is given by

$$n_{0,c} = \frac{T_0 \mu_r (a_{\text{eff}} - a_{\text{eff},-})}{27\pi S_0 a_{\text{eff}}^2 (1 - \frac{2\pi V_0^2 a_{\text{eff}}}{\mu_r T_0})} = \frac{a_{\text{eff}} - a_{\text{eff},-}}{360\pi a_{\text{eff}}^2 \sigma_g (1 - \frac{5^{5/2} a_{\text{eff}}}{3^4 \sqrt{2\pi\sigma_g}})}. \tag{6.45}$$

Finding the inverse equation for a_{eff} as a function of n_0 can be done by solving a third-order polynomial, yielding an analytical, but lengthy expression. Remarkably, the only dependence on the mass in equation Eq. (6.45) is via $a_{\text{eff},-}$, see Eq. (6.42).

6.5.3 Including interboson repulsion

To obtain an even stronger analogy to the theory of phase transitions, we now include the interboson repulsion to stabilize the cluster states. The only interboson-repulsion term which qualitatively matters for the description of the behavior at strong coupling is the quartic term in the Hamiltonian of Eq. (6.2). The quadratic and cubic term are mostly important to determine the shape of the polaron cloud at long distances, which we do not attempt to describe in this simplified model. Therefore, we only keep the quartic term. Note that this is the opposite approach compared to what is usually done in the Bogoliubov approximation.

To see all the relevant effects we need to expand the energy functional to the third instead of only second order in ϕ^2, ξ_0, and ξ_1. At this point we do not optimize the exponents of the Gaussian basis functions again, but simply use the optimized exponents obtained in the previous step. This yields the energy functional

$$\begin{aligned} E(\phi, \xi_0, \xi_1) = {} & g n_0 + 2 g V_0 \sqrt{n_0}\phi + (T_0 + g V_0^2)\phi^2 + \frac{U_{00}}{2}\phi^4 + \big(\frac{Y_0}{2} + 2 S_0 U_{00}\phi^2\big)\xi_0^2 \\ & + \big[\frac{3Y_1}{2} + 3 S_1 (U_{10}'\phi^2 + T_L^2 \phi^2)\big]\xi_1^2 + U_{00}\phi^2\xi_0 - 3 Y_L \phi^2 \xi_1 - 3 Y_L \xi_0 \xi_1. \end{aligned} \tag{6.46}$$

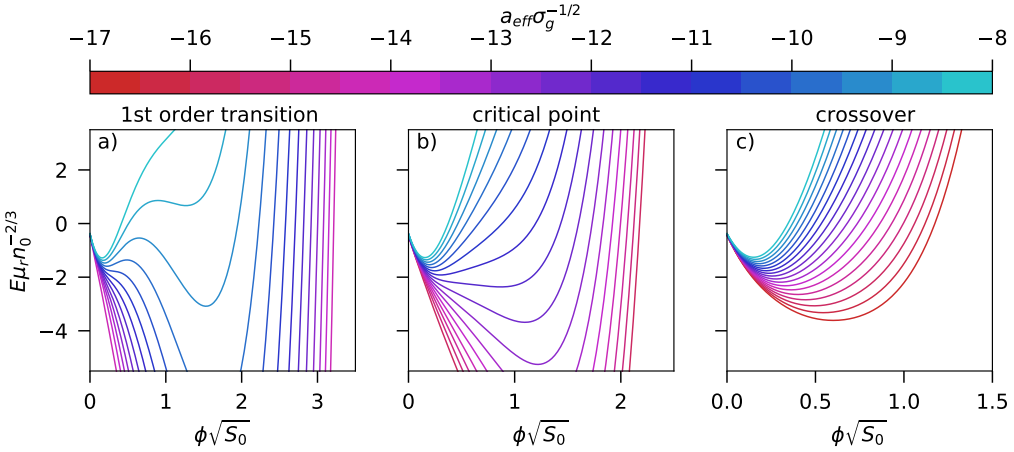

Figure 6.10: Energy functional of Eq. (6.53), where the energy is plotted in units of $\mu_r n_0^{-2/3}$ as a function of the normalized ϕ for several scattering lengths. The magnitude of the scattering length is indicated by the colorbar and it increases for the graphs from top to bottom. The mass ratio chosen here corresponds to Li-Cs and $n_0\sigma_g^{3/2} = 1.25\ 10^{-5}$. The three subfigures correspond to three different values of the interboson scattering length from left to right given by $a_B = 0.7$, 0.9 and 1.1 L_U, respectively. Here $L_U = 4.5\sqrt{\sigma_g}$.

Here we have defined

$$Y_0 = 2S_0(T_0 + gV_0^2) + U_{00}, \tag{6.47}$$
$$Y_1 = 2S_1T_1 + 3U_{11}, \tag{6.48}$$
$$Y_L = T_L^2 - U_{10}. \tag{6.49}$$

The numbers U_{00}, U_{10}, U'_{10} and U_{11} are defined in the Appendix in Eqs. (6.80- 6.83).

Minimizing Eq. (6.46) with respect to ξ_0 and ξ_1 gives

$$\xi_0 = \frac{\left[3Y_L^2 - [Y_1 + 2S_1(U'_{10} + T_L^2)\phi^2]U_{00}\right]\phi^2}{[Y_0 + 4S_0U_{00}\phi^2][Y_1 + 2S_1(U'_{10} + T_L^2)\phi^2] - 3Y_L^2}, \tag{6.50}$$
$$\xi_1 = \frac{[Y_0 + 4S_0U_{00}\phi^2]\xi_0 + U_{00}\phi^2}{3Y_L}. \tag{6.51}$$

Taking the limit $\phi \to 0$, we can find a new value for $a_{\text{eff},-}$ as a function of U,

$$a_{\text{eff},-}(U) = \frac{T_0\mu}{V_0^2 2\pi}\left(1 - \frac{2S_0T_0Y_1}{3Y_L^2 - Y_1U_{00}}\right). \tag{6.52}$$

When we again expand the energy functional up to quartic order in ϕ we retrieve Eq. (6.44) but with $a_{\text{eff},-}$ replaced by $a_{\text{eff},-}(U)$. To recover the effect of the stabilization of the polaronic collapse, we need to go to higher order in ϕ. We find

$$E(\phi) = gn_0 + 2gV_0\sqrt{n_0}\phi + (T_0 + gV_0^2)\phi^2 - (T_0 + gV_0^2 + 2U_{00}\phi^2)\xi_0\phi^2. \tag{6.53}$$

Since ξ_0 has ϕ^2 in multiple arguments of the denominator and the numerator, this does not allow a simple expression in terms of $a_{\text{eff},-}(U)$. Note further, that the quartic interboson repulsion term $\frac{U_{00}\phi^4}{2}$ from Eq. (6.46) has been absorbed into the quartic term originating from the Gaussian part of the state.

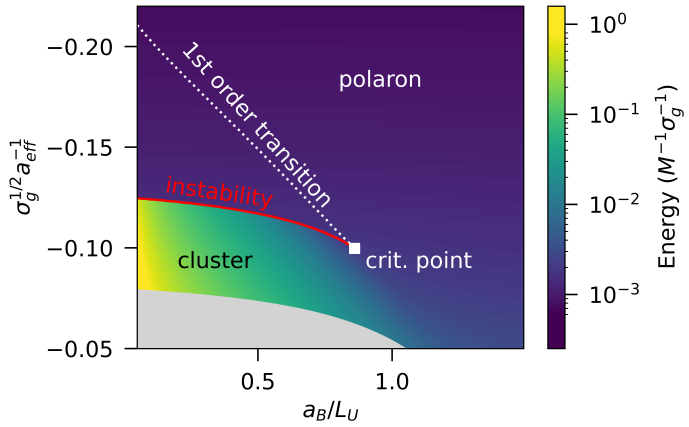

Figure 6.11: Colormap of the energy of the polaron as a function of the effective impurity-boson scattering length a_{eff} and the interboson repulsion scattering length a_B as obtained from our analytical model. The density $n_0\sigma_g^{3/2} = 2.5\ 10^{-5}$ and $L_U = 2\sigma_g^{1/2}$. The red line indicates the polaronic instability and the white dashed line indicates the point where the first-order phase transition happens, where the cluster energy crosses below the polaron energy. Both of these lines end at the critical point. In the gray region in the bottom left, our analytical model is not applicable.

In Fig. 6.10 the value of the energy functional of Eq. (6.53) is plotted as a function of the order parameter $\phi\sqrt{S_0}$ for several boson-impurity (indicated via the color of the lines) and interboson scattering lengths. For weak repulsion (Fig. 6.10a)) we find a double well picture of a shallow well corresponding to the polaron and a deeper well corresponding to the Efimov cluster. Quantitatively, the cluster has a much weaker binding energy than in the original model, mainly because the exponents of the Gaussian basis functions are optimized for the polaron and not the clusters.

Qualitatively, however, the physics is very similar to the full model. In Fig. 6.10a), the first-order transition is clearly apparent. It occurs when the well corresponding to the cluster on the right becomes lower in energy than the well associated with the polaron state. However, the polaron first remains a metastable local minimum, even though the cluster state is lower in energy. Then, at some critical scattering length, the barrier protecting the polaron disappears and there is a sudden transition from the polaron into the cluster state. This can still be interpreted as a form of polaronic instability.

If the interboson repulsion is increased, the double-well picture no longer applies. In Fig. 6.10b) the energy functional is shown close to the critical point. Here we see that there is no first-order transition or polaronic instability any more, but still the ground state changes rapidly in character for some critical scattering length. Finally, for even stronger repulsion, in Fig. 6.10c), no sign of a transition remains, and we are deeply in the smooth crossover regime.

In Fig. 6.11 we capture this behavior in a single figure, by showing the polaron energy as a function of the boson-impurity and boson-boson scattering length. Indeed, the figure is remarkably similar to Fig. 6.6c), showing how well our analytical model captures this behavior. Note that in the gray area in the bottom left, $a_{\text{eff}} < a_{\text{eff},-}(U)$. Here our model breaks down. In particular, in this figure we clearly see the line of first-order transition, where the polaron ceases to be the ground state, and the line of instability, where the polaron becomes completely unstable. These two points merge in the critical point, where the energy functional takes the form as shown in Fig. 6.10b). At this critical point, where

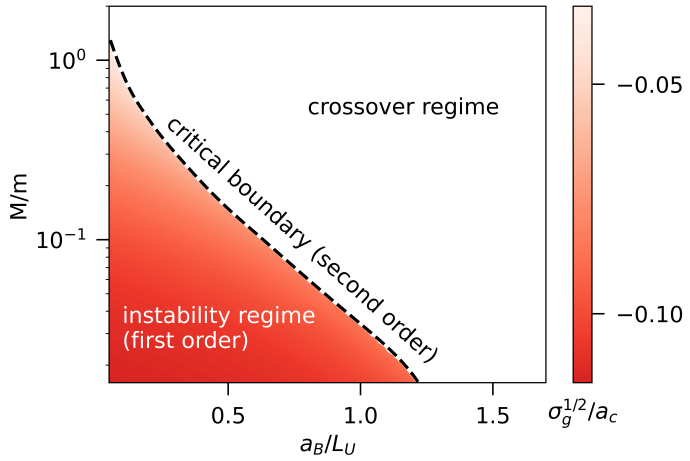

Figure 6.12: Stability diagram of the polaron as a function of the impurity-boson mass ratio M/m and the interboson repulsive scattering length a_B, as obtained from our analytical model. The density $n_0\sigma_g^{3/2} = 1.25\ 10^{-5}$ and $L_U = 2\sigma_g^{1/2}$. In the red area of the diagram the polaron undergoes an instability as the boson-impurity interaction strength is swept across a Feshbach resonance. The critical scattering length a_c of the instability is indicated by the colormap. In the white regime the polaron instead undergoes a smooth crossover.

the line of first-order transition terminates, the phase transition turns second order.

Fig. 6.11 as a whole, as well as Fig. 6.6b) and c), are strikingly similar to the phase diagram corresponding to the gas-liquid phase transition. In this analogy the polaron state corresponds to the gaseous state and the cluster state to the liquid state. The gas-liquid transition is also a first-order phase transition, up to a critical point, after which the state is called a supercritical fluid. In the regime where the polaron state is metastable, this would be analogous to a supercooled gas: a gas cooled below its condensation point. Note, however, that in the polaron case, this phase diagram is realized in the quantum regime at zero temperature.

As a final result, in Fig. 6.12 we plot the "Bose polaron phase diagram" as a function of the mass ratio and the interboson repulsion, based on our analytical model Eq. (6.53). We see that the stability diagram is very similar to Figs. 6.1 and 6.7, even on a quantitative level [1]. This shows that the form of the Bose-polaron phase diagram is remarkably robust.

6.6 Conclusion and Outlook

We have characterized the behavior of the attractive Bose polaron, i.e., the ground state of a mobile impurity interacting with a Bose-Einstein condensate, across a large parameter regime of boson-impurity and boson-boson scattering lengths, BEC densities and impurity-to-boson mass ratios. Thus, we have brought together qualitatively different results from several studies into a single, unified theoretical picture. To this end, we have compared two state-of-the-art variational methods: the Gaussian-state and double-excitation approaches. We developed a computationally efficient technique by expressing the variational functions in terms of a set of spherical Gaussian basis functions.

We confirmed that the polaron instability predicted in the previous Chapter persists in

[1] Note for direct comparison that the potential in the analytical model is best compared to the Gaussian potential with $L_g = 2\sigma_g^{1/2}$. This means that the density of Fig. 6.12 is best compared to the case of Fig. 6.7a) (note also the difference in the scale of the colormap)

presence of interboson repulsion, as long as the impurity is light and this repulsion is weak. This instability turns into a smooth crossover for larger repulsion or heavier impurities. Most of the experiments will naturally be in the crossover regime, but the instability regime should be experimentally accessible with light impurities in BECs with a small interboson scattering length.

We developed a simple analytical model capturing the phenomenology of the instability and crossover. From this model it becomes apparent that the physics of attractive Bose polarons can be understood in the language of the Landau model of first-order phase transitions. It is in fact strongly reminiscent of the gas-liquid phase transition, where the polaron state is analogous to the gaseous phase and the cluster state represents the liquid phase. Clearly, in the case of a single impurity we cannot truly speak of a phase transition in the thermodynamic sense. However, it is likely that the observed physics will turn into a proper quantum phase transition when considering a finite density of impurities. We have furthermore shown that the stability diagram of the polaron is reproduced surprisingly well by the simple analytical model. A topic inviting further study would be a more detailed characterization of the critical behavior at the critical point where the phase transition turns second order.

Given that the properties of the ground state differ strongly across the parameter space, an interesting question remains how these effects would manifest themselves in the dynamics and the excitation spectrum of the polaron. Especially interesting would be to see whether some resonant behavior occurs at the onset of the polaronic instability, in analogy to the Efimov resonance. Dynamical calculations have so far been carried out mostly using (extended) Gross-Pitaevskii equations [157] or equivalently, with a coherent-state approach [152, 164, 171]. To see the effects mentioned above one would need to explicitly allow for the correlations between the bosons induced by the impurity. In principle, the Gaussian-state approach can also be applied for real-time evolution, but this is computationally more challenging due to the more oscillatory nature of the wave function. For this reason, the parameterization of the variational functions used here in terms of Gaussian basis functions, is likely not optimal for real-time evolution.

Furthermore, interesting effects are predicted to also appear in the finite-temperature behavior of the Bose polaron [192–195], for which several approaches have again found conflicting results. Therefore, it would be a promising avenue of study to see whether a unified model can also be developed capturing the finite-temperature properties for varying mass ratios and background repulsion.

In the context of Bose-Fermi mixtures, mediated interactions by fermions in Bose Einstein condensates have been studied already both theoretically [196–198] and experimentally [199, 200] in a regime of finite fermion density. However, in our work the fermion-mediated interactions are caused by a different mechanism. Namely, they arise from the Efimov effect, instead of the many-body effects originating from the Fermi surface of the fermions. Since we show that the impurity-mediated interactions play a profound role in the Bose polaron model, it can be expected it will also be important in the general description of finite-density mixtures at strong interactions. We hope our work can provide a starting point for fruitful studies in this direction. In particular, we hope that further inspiration can be drawn from quantum chemistry to also tackle the bipolaron problem.

Bose polarons have recently been observed for the first time in two-dimensional semiconductors coupled to a microcavity [201]. Even though the standard Efimov effect does not exist in two dimensions, it is still possible that in certain conditions bound states with more than two particles can form. Therefore, similar phenomena as we have predicted here in the context of cold atomic gases might well be found in these solid-state platforms.

Appendices

6.A Computation of Gaussian integrals

The expectation values with respect to the kinetic, boson-impurity interaction and LLP-terms yield relatively simple expressions.

For the kinetic energy we find

$$T_{l,ij} = \int_{\boldsymbol{k}} \frac{k^2}{2\mu_r} \chi^*_{lm}(\sigma_i, \boldsymbol{k}) \chi_{lm}(\sigma_j, \boldsymbol{k}) = \frac{\sqrt{\pi}(2l+3)!!}{2^{l+4}\mu_r(\sigma_{l,i}+\sigma_{l,j})^{5/2+l}}. \tag{6.54}$$

For the Gaussian-state expectation values of the LLP-term we find terms of the form

$$T_{L,l,ijpq} = \frac{1}{M}\sum_{m'} \int_{\boldsymbol{k}}\int_{\boldsymbol{k'}} \boldsymbol{k}\cdot\boldsymbol{k'}\ \chi^*_{(l+1)m'}(\sigma_i,\boldsymbol{k})\chi_{lm}(\sigma_j,\boldsymbol{k})\chi^*_{lm}(\sigma_q,\boldsymbol{k'})\chi_{(l+1)m'}(\sigma_p,\boldsymbol{k'}), \tag{6.55}$$

$$= -\sum_{m'} \frac{(-1)^{m+m'}}{M} \int_{\boldsymbol{k}}\int_{\boldsymbol{k'}} \boldsymbol{k}\cdot\boldsymbol{k'}\ \chi^*_{(l+1)m'}(\sigma_i,\boldsymbol{k})\chi_{lm}(\sigma_j,\boldsymbol{k})\chi^*_{(l+1)-m'}(\sigma_p,\boldsymbol{k'})\chi_{l-m}(\sigma_q,\boldsymbol{k'}), \tag{6.56}$$

$$= \frac{\pi(l+1)[(2l+3)!!]^2}{(2l+1)M2^{2l+6}(\sigma_{l+1,i}+\sigma_{l,j})^{5/2+l}(\sigma_{l+1,p}+\sigma_{l,q})^{5/2+l}}. \tag{6.57}$$

For the interaction term with the Gaussian boson-impurity interaction potential (6.16) it is most convenient to carry out the integral in real space, and define the Fourier transform $\tilde{\chi}$ of the Gaussian orbitals. Then we find

$$\tilde{\chi}_{lm}(\sigma,\boldsymbol{r}) = \frac{1}{(2\sigma)^{l+3/2}} Y_{lm}(\theta,\phi)\exp(-\frac{r^2}{4\sigma}), \tag{6.58}$$

$$V^{(1)}_{l,i} = \frac{1}{2L_g^2}\int_{\boldsymbol{r}} \exp(-\frac{r^2}{L_g^2})\tilde{\chi}_{lm}(\sigma_i,\boldsymbol{r}) = \delta_{l,0}\frac{\pi L_g}{2^{1/2}(L_g^2+4\sigma_i)^{3/2}}, \tag{6.59}$$

$$V^{(2)}_{l,ij} = \frac{1}{2L_g^2}\int_{\boldsymbol{r}} \exp(-\frac{r^2}{L_g^2})\tilde{\chi}^*_{lm}(\sigma_i,\boldsymbol{r})\tilde{\chi}_{lm}(\sigma_j,\boldsymbol{r}) = \frac{\sqrt{\pi}(2l+1)!!L_g^{2l+1}}{2^{l+3}[L_g^2(\sigma_i+\sigma_j)+4\sigma_i\sigma_j]^{l+3/2}}. \tag{6.60}$$

For the separable Gaussian potential used in Section 6.5 one has

$$V_{l,i} = \int_{\boldsymbol{k}} \exp(-\sigma_g k^2)\chi_{lm}(\sigma_i,\boldsymbol{k}) = \frac{1}{4\sqrt{2\pi}(\sigma_i+\sigma_g)^{3/2}}. \tag{6.61}$$

Computing the expectation values of the interboson repulsion term is more complex. In this case, we need to calculate integrals of the form (where $\boldsymbol{j} = (n,l,m)$):

$$I_{\boldsymbol{j_1},\boldsymbol{j_2},\boldsymbol{j_3},\boldsymbol{j_4}} = \int_{\boldsymbol{r}_1}\int_{\boldsymbol{r}_2} r_1^{l_1+l_3} r_2^{l_2+l_4} Y^*_{l_1m_1}(\boldsymbol{\Omega}_1) Y_{l_3m_3}(\boldsymbol{\Omega}_1) Y^*_{l_2m_2}(\boldsymbol{\Omega}_2) Y_{l_4m_4}(\boldsymbol{\Omega}_2)$$
$$\exp(-\alpha_1 r_1^2)\exp(-\alpha_3 r_1^2)\exp(-\alpha_2 r_2^2)\exp(-\alpha_4 r_2^2)\exp\big[-(\boldsymbol{r}_1-\boldsymbol{r}_2)^2/L_U^2\big]. \tag{6.62}$$

Here we use the combined indices $\boldsymbol{j_1} = (j_1 l_1 m_1)$, where the first index labels the exponent α_{j_1}, for which $\alpha_i = \frac{1}{4\sigma_i}$. The integral is nontrivial because the interaction potential depends

on the distance between the bosons $(\boldsymbol{r}_1 - \boldsymbol{r}_2)$. To perform the angular and radial integrals we need to write this in a different form. Indeed, following Ref. [202] we can decompose the term according to

$$\exp\left[-\alpha_U(\boldsymbol{r_1} - \boldsymbol{r_2})^2\right] = \sum_L (2L+1) i_L(2\alpha_U r_1 r_2) \exp[-\alpha_U(r_1^2 + r_2^2)] P_L(\cos(\theta_{12})), \quad (6.63)$$

$$= 4\pi \sum_L \sum_M i_L(2\alpha_U r_1 r_2) \exp[-\alpha_U(r_1^2 + r_2^2)] Y^*_{LM}(\boldsymbol{\Omega}_1) Y_{LM}(\boldsymbol{\Omega}_2), \quad (6.64)$$

where we defined $\alpha_U = 1/L_U^2$. Here i_l is the modified spherical Bessel function

$$i_L(x) = i^l j_L(ix). \quad (6.65)$$

Now we can write the integral (6.62) as

$$I_{\boldsymbol{j}_1,..,\boldsymbol{j}_4} = \sum_{LM} \int d\boldsymbol{\Omega}_1 Y^*_{l_1 m_1}(\boldsymbol{\Omega}_1) Y_{l_3 m_3}(\boldsymbol{\Omega}_1) Y^*_{LM}(\boldsymbol{\Omega}_1) \int dr_1 r_1^{2+l_1+l_3} \exp[-(\alpha_1 + \alpha_3 + \alpha_U) r_1^2]$$
$$\int d\boldsymbol{\Omega}_2 Y^*_{l_2 m_2}(\boldsymbol{\Omega}_2) Y_{l_4 m_4}(\boldsymbol{\Omega}_2) Y_{LM}(\boldsymbol{\Omega}_2) \int dr_2 \; r_2^{2+l_2+l_4} \exp[-(\alpha_2 + \alpha_4 + \alpha_U) r_2^2] i_L(2\alpha_U r_1 r_2). \quad (6.66)$$

To simplify the following expressions, we define $\gamma_1 = (\alpha_1 + \alpha_3 + \alpha_U)$, $\gamma_2 = (\alpha_2 + \alpha_4 + \alpha_U)$, $L_1 = l_1 + l_3 + 3$, and $L_2 = l_2 + l_4 + 3$.

For the angular integrals we use the identity

$$\int d\boldsymbol{\Omega} Y_{l_1 m_1}(\boldsymbol{\Omega}) Y_{l_2 m_2}(\boldsymbol{\Omega}) Y^*_{l_3 m_3}(\boldsymbol{\Omega}) =$$
$$(-1)^{m_3} \sqrt{\frac{(2l_1+1)(2l_2+1)(2l_3+1)}{4\pi}} \begin{pmatrix} l_1 & l_2 & l_3 \\ 0 & 0 & 0 \end{pmatrix} \begin{pmatrix} l_1 & l_2 & l_3 \\ m_1 & m_2 & -m_3 \end{pmatrix}. \quad (6.67)$$

Without using the symmetries of the problem, these expressions cannot be simplified further.

The radial integrals need to be carried out in two steps, since the Bessel function i_L contains both r_1 and r_2. In the first step we carry out the following integral

$$\int dr_2 \; r_2^{2+l_2+l_4} \exp[-\gamma_2 r_2^2] i_L(2\alpha_U r_1 r_2) =$$
$$\frac{\sqrt{\pi}(2\alpha_U r_1)^L \Gamma(\frac{L+L_2}{2})}{2^{L+2}\gamma_2^{\frac{(L+L_2)}{2}} \Gamma(L+\frac{3}{2})} \; {}_1F_1\big(\frac{L+L_2}{2}; L+\frac{3}{2}; \frac{\alpha_U^2 r_1^2}{\gamma_2}\big). \quad (6.68)$$

Here we used from Ref. [203]

$$\int_0^\infty x^\mu e^{-\alpha x^2} J_\nu(\beta(x)) dx = \frac{\beta^\nu \Gamma(\frac{\nu+\mu+1}{2})}{2^{\nu+1}\alpha^{\frac{1}{2}(\mu+\nu+1)}\Gamma(\nu+1)} \; {}_1F_1\big(\frac{\nu+\mu+1}{2}; \nu+1; -\frac{\beta^2}{4\alpha}\big), \quad (6.69)$$

where J_ν is the standard (non-spherical) Bessel function and ${}_1F_1$ is the confluent hypergeometric function. Now the integral that remains is

$$\int dr_1 \; r_1^{2+l_1+l_3+L} \exp[-\gamma_1 r_1^2] {}_1F_1\big(\frac{L+L_2}{2}; L+\frac{3}{2}; \frac{\alpha_U^2 r_1^2}{\gamma_2}\big). \quad (6.70)$$

After replacing the integration variable: $t = r_1^2$ we use another equation from Ref. [203]:

$$\int_0^\infty e^{-st} t^{b-1}\ {}_1F_1(a;c;kt)dt = \Gamma(b)s^{-b}F(a,b;c;ks^{-1}). \tag{6.71}$$

Here $F(a,b;c;z)$ is the hypergeometric function (sometimes also denoted as ${}_2F_1$). Using this identity gives

$$\begin{aligned}\frac{1}{2}\int dt\ t^{\frac{1+l_1+l_3+L}{2}} \exp[-\gamma_1 t]{}_1F_1(\frac{L+L_2}{2}; L+\frac{3}{2}; \frac{\alpha_U^2 t}{\gamma_2}) \\ = \frac{1}{2}\frac{\Gamma(\frac{L+L_1}{2})}{\gamma_1^{\frac{L+L_1}{2}}} F\big(\frac{L+L_2}{2}, \frac{L+L_1}{2}; L+\frac{3}{2}; \frac{\alpha_U^2}{\gamma_1\gamma_2}\big).\end{aligned} \tag{6.72}$$

Combining this with the prefactor of Eq. (6.68) and the integral over the angular parts (Eq. (6.67)) gives

$$\begin{aligned}I_{\boldsymbol{j}_1,\boldsymbol{j}_2,\boldsymbol{j}_3,\boldsymbol{j}_4} = \frac{\sqrt{\pi}}{8}\sum_{LM}(2L+1)(-1)^{m_2+m_3}\sqrt{(2l_1+1)(2l_2+1)(2l_3+1)(2l_4+1)} \\ \begin{pmatrix} l_3 & l_1 & L \\ 0 & 0 & 0\end{pmatrix}\begin{pmatrix} l_3 & l_1 & L \\ -m_3 & m_1 & M\end{pmatrix}\begin{pmatrix} l_2 & l_4 & L \\ 0 & 0 & 0\end{pmatrix}\begin{pmatrix} l_2 & l_4 & L \\ -m_2 & m_4 & M\end{pmatrix} \\ \frac{\Gamma(\frac{L+L_2}{2})\Gamma(\frac{L+L_1}{2})}{\Gamma(L+\frac{3}{2})}\frac{\alpha_U^L}{\gamma_1^{\frac{L+L_1}{2}}\gamma_2^{\frac{L+L_2}{2}}} F\big(\frac{L+L_2}{2}, \frac{L+L_1}{2}; L+\frac{3}{2}; \frac{\alpha_U^2}{\gamma_1\gamma_2}\big).\end{aligned} \tag{6.73}$$

The expression can be simplified when taking our symmetries into account. For the coherent part for example, $l_1 = l_2 = l_3 = l_4 = 0$. In this case we find

$$I_{\phi^4} = \frac{\sqrt{\pi}\Gamma(\frac{3}{2})}{8}\frac{F\big(\frac{3}{2},\frac{3}{2};\frac{3}{2};\frac{\alpha_U^2}{(\alpha_1+\alpha_3+\alpha_U)(\alpha_2+\alpha_4+\alpha_U)}\big)}{(\alpha_1+\alpha_3+\alpha_U)^{\frac{3}{2}}(\alpha_2+\alpha_4+\alpha_U)^{\frac{3}{2}}}. \tag{6.74}$$

Now we can use that $F(a,b;b,z) = (1-z)^{-a}$ and that $\Gamma(\frac{3}{2}) = \frac{\sqrt{\pi}}{2}$. This finally yields

$$I_{\phi^4} = \frac{\pi}{16}[(\alpha_1+\alpha_3+\alpha_U)(\alpha_2+\alpha_4+\alpha_U) - \alpha_U^2]^{-\frac{3}{2}}. \tag{6.75}$$

Of course, this matrix element containing only the angular-momentum zero modes, could also have been obtained in simpler ways.

For the terms in Eq. (6.19) containing F and ϕ^2 we have that $l_1 = l_2$, $m_1 = -m_2 = m$ and $l_3 = l_4 = 0$. This leads to

$$I_{F\phi^2} = (-1)^m\frac{\pi(2l+1)!!}{2^{l+4}}\alpha_U^l[(\alpha_1+\alpha_3+\alpha_U)(\alpha_2+\alpha_4+\alpha_U) - \alpha_U^2]^{-(l+\frac{3}{2})} \tag{6.76}$$

We find the same contribution, except for the $(-1)^m$ term, for the terms in Eq. (6.19) containing G and ϕ^2, in the case where $l_1 = l_4$, $m_1 = m_4 = m$ and $l_2 = l_3 = 0$. There are also G-ϕ^2 contributions with $l_1 = l_3$, $m_1 = m_3 = m$ and $l_2 = l_4 = 0$, for which we find

$$I_{G\phi^2} = \frac{\pi(2l+1)!!}{2^{l+4}}(\alpha_2+\alpha_4+\alpha_U)^l[(\alpha_1+\alpha_3+\alpha_U)(\alpha_2+\alpha_4+\alpha_U) - \alpha_U^2]^{-(l+\frac{3}{2})}. \tag{6.77}$$

In case of the F^2 terms, we have that $l_1 = l_2 = l$, $m_1 = -m_2 = m$, $l_3 = l_4 = l'$ and $m_3 = -m_4 = m'$, so that

$$\sum_{m,m'} (-1)^{m+m'} I_{FF} =$$
$$\frac{\sqrt{\pi}}{8}(2l+1)(2l'+1)\sum_L \Big[\begin{pmatrix} l' & l & L \\ 0 & 0 & 0 \end{pmatrix}\Big]^2 \frac{(2L+1)\Gamma(\frac{L+l+l'+3}{2})^2 \alpha_U^L}{\Gamma(L+\frac{3}{2})[(\alpha_1+\alpha_3+\alpha_U)(\alpha_2+\alpha_4+\alpha_U)]^{\frac{(l+l'+L+3)}{2}}}$$
$$F(\frac{L+l+l'+3}{2}, \frac{L+l+l'+3}{2}; L+\frac{3}{2}; \frac{\alpha_U^2}{(\alpha_1+\alpha_3+\alpha_U)(\alpha_2+\alpha_4+\alpha_U)}). \quad (6.78)$$

For the G^2 terms, we again find an identical result to Eq. (6.78) if $l_1 = l_4$, $m_1 = m_4 = m$, $l_2 = l_3$ and $m_2 = m_3 = m'$. If instead $l_1 = l_3$, $m_1 = m_3 = m$, $l_2 = l_4$ and $m_2 = m_4 = m'$, we find that

$$\sum_{m,m'} I_{GG} = \frac{\sqrt{\pi}}{8}(2l+1)(2l'+1)\frac{\Gamma(l+\frac{3}{2})\Gamma(l'+\frac{3}{2})}{\Gamma(\frac{3}{2})(\alpha_1+\alpha_3+\alpha_U)^{l+\frac{3}{2}}(\alpha_2+\alpha_4+\alpha_U)^{l'+\frac{3}{2}}}$$
$$F(l+\frac{3}{2}, l'+\frac{3}{2}; \frac{3}{2}; \frac{\alpha_U^2}{(\alpha_1+\alpha_3+\alpha_U)(\alpha_2+\alpha_4+\alpha_U)}). \quad (6.79)$$

Now we have all we need to find the expressions for U_{00}, U_{10}, U'_{10} and U_{11} from Eq. (6.46). For this, the integrals need to be multiplied by the prefactor $\frac{U}{2L_U^2}$. Furthermore, we need to add the prefactors following the Fourier transform to real space, see Eq. (6.58). Using this, we can employ the equations above for the case of our analytical model:

$$U_{00} = \frac{U\pi L_U}{256\sigma_0^3}[L_U^2 + 4\sigma_0]^{-\frac{3}{2}}, \quad (6.80)$$
$$U_{10} = \frac{3U\pi L_U}{16\sigma_0^2}[L_U^2(\sigma_0+\sigma_1)^2 + 8\sigma_0\sigma_1^2 + 8\sigma_1\sigma_0^2]^{-\frac{5}{2}}, \quad (6.81)$$
$$U'_{10} = \frac{3U\pi L_U}{1024\sigma_0^{3/2}\sigma_1^{5/2}}(L_U^2 + 2\sigma_0)[L_U^2 + 2\sigma_0 + 2\sigma_1]^{-\frac{5}{2}}, \quad (6.82)$$
$$U_{11} = \frac{3U\pi L_U}{256\sigma_1^5}(L_U^2 + 4\sigma_1)^{-7/2}[\sigma_1^2 + \frac{(L_U^2 + 2\sigma_1)^2)}{16}]. \quad (6.83)$$

Chapter 7. Dimer-trimer superpositions from Bose polarons

The content of this chapter is based on

[4] Carsten Robens*, Arthur Christianen*, Alex Y. Chuang, Yiqi Ni, Richard Schmidt, Martin W. Zwierlein,
Superpositions of dimers and trimers formed from Bose polarons,
in preparation, *: equal contributions

7.1 Introduction

In Chapter 6 we have described in detail what happens to the attractive Bose polaron as the scattering length is swept across a Feshbach resonance. One either finds an instability, where the polaron suddenly becomes unstable and decays into large bound clusters, or a smooth crossover into a few-body bound state. The focus of the previous Chapters has mostly been on the instability regime. Now we discuss in more detail the crossover case.

An interesting aspect in the crossover regime is that the energy scales of the many-body dressing and the molecular binding can be similar. Hence, one can expect that the molecules which are formed in this regime are not just bare molecules, as one would find in a thermal gas, but molecules whose properties are severely influenced by the surrounding degenerate medium. The process of molecule formation in a BEC is therefore again an excellent example of *chemistry in a quantum medium*.

For this study we work together with the experimental group of Martin Zwierlein at the Massachusetts Institute of Technology (MIT). In their experiments they prepare a BEC of ^{23}Na in which they immerse a ^{40}K-impurity. They perform a variation of *radiofrequency injection spectroscopy*. In the traditional protocol, one would start with a non-interacting impurity state, and drive an rf-transition to an interacting final state [144, 145]. By measuring the transferred fraction of impurities as a function of the transition frequency, one can then map out the spectrum of the final-state Hamiltonian, including the overlap of the final states with the initial state, according to Fermi's golden rule. A problem of this approach is that it does not work so well to study the attractive-polaron branch for large positive scattering lengths, because the wave-function overlap between the non-interacting initial state and the final states with a molecular character is small.

In our study, we do not start with a non-interacting initial state, but with a *preformed polaron state*. We make use of the overlapping Feshbach resonances in the Na-K system (see Fig. 2.3) to prepare attractive polarons in the initial state. Due to the increased density of bosons around the impurity, there is now an enhanced overlap with the final states with a molecular character. Note that the injection spectroscopy protocol for positive final-state scattering lengths, is very similar to the rf-association procedure to make Feshbach molecules and measure their binding energy [204–206]. The polaron spectroscopy can therefore be viewed as driving the chemical reaction of rf-association, but in a degenerate background medium.

We will show that the main spectral features can well be described with a conceptually

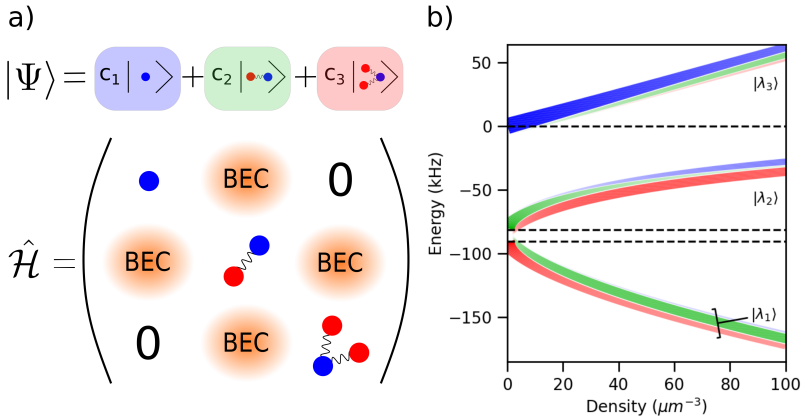

Figure 7.1: a) The wave function of a single impurity in a BEC forming a superposition of a free impurity, a dimer, and a trimer, and the effective Hamiltonian in the basis of these three states. On the diagonal are the energies of these states and the off-diagonal contributions are due to the exchange of particles with the BEC. b) The energies (in kHz) and structure of the three eigenstates $|\lambda\rangle$ of the Hamiltonian as a function of the density of the BEC in μm^{-3}. The widths and opacities of the colored sub-lines indicate the size of the coefficients (as shown in a)) $|c_1|^2$ (blue), $|c_2|^2$ (green) and $|c_3|^2$ (red) for each of the eigenstates. The horizontal dashed lines indicate the energies of the three basis states in absence of a background BEC.

simple three-level model as shown in Fig. 7.1a) and b). The three levels are the free-impurity state, the dimer state, but also a trimer state. Since the impurity is heavier than the bosons, and the bosons have repulsive interactions among each other, the Efimov effect is strongly suppressed. Nevertheless, shallow trimer states can form with a slightly larger binding energy than the dimer. Because this splitting is so small, it turns out that for the densities typically realized in experiments, the coupling with the medium is larger than the splitting between the free dimer and trimer energies. This implies that the eigenstates of the in-medium Hamiltonian are strongly mixed, and correspond to coherent dimer-trimer superpositions for which the dimer and trimer contributions have approximately equal weights.

In the rest of this Chapter we will first outline in Section 7.2 how we implement the experimental parameters into the theoretical model, and how we describe these dimer-trimer superpositions. Then we will show the experimental and theoretical results in Section 7.4. We conclude and give an outlook in Section 7.5.

7.2 Theoretical description

7.2.1 Potential calibration

To check whether the theoretical parameterization matches the experimental conditions, we start by comparing the dimer energies. Experimentally, the dimer energy is measured in the dilute wings of the BEC and in a separate experiment where only a dilute thermal gas is prepared. Theoretically we compute the dimer energies from the universal formulas of Eqs. (2.17) and (2.18). The scattering length and effective range as a function of magnetic field are computed employing the coupled channels approach (see Sec. 2.5) using the potentials from Ref. [70].

The experimental and theoretical dimer energies are plotted together in Fig. 7.2. We

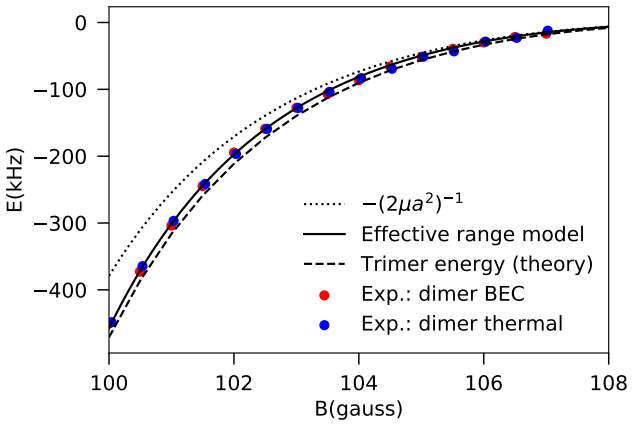

Figure 7.2: NaK dimer energy as a function of magnetic field measured from experiment (red and blue dots) compared to the universal theoretical predictions (dotted and solid lines). We also show the theoretically computed trimer energies.

find that the experimentally measured dimer energies agree remarkably well with the theoretical results, showcasing the high quality of the potentials from Ref. [70]. In the experimentally probed regime of magnetic fields, the dimer energy deviates from Eq. (2.17) in terms of only the scattering length, but if we take the next-order approximation in terms of the effective range (Eq. (2.18)) we find almost perfect agreement. Note here that it is important to take explicitly into account the substantial magnetic-field dependence of the effective range. The root-mean-square discrepancy between the theoretical and experimental results is approximately 3 kHz, and the same for both experimental datasets. There is a region between 103 and 106 G, where the experimental data lie systematically around 4 kHz below the theory curve.

For the polaron calculations we replace the physical interaction potential between the Na and K-atoms by a single-channel Gaussian model potential as in Eq. (6.16) with the same scattering length and effective range. We do this separately for every magnetic field. The dimer energy computed using this potential has negligible deviations from the universal curve and the same holds true for the dimer energies computed from the realistic potentials from Ref. [70]. The same procedure of extracting the scattering length and effective range from the coupled-channels calculation and then using them to construct Gaussian model potentials, is also used for the initial state of the spectroscopic protocol.

Similarly, we compute the scattering length and effective range for the Na-Na collisions, using potentials from Ref. [207]. Over the magnetic-field range of interest we find that the scattering length is approximately $56.5a_0$ with variation of only $0.2a_0$, which we neglect. In this case there does not exist a single Gaussian potential without bound states with the correct combination of scattering length and effective range. Therefore, we use a sum of two Gaussian potentials

$$V_{BB}(\boldsymbol{r}) = \frac{U_1}{2L_{U1}^2}\exp(-\frac{r^2}{L_{U1}^2}) + \frac{U_2}{2L_{U2}^2}\exp(-\frac{r^2}{L_{U2}^2}). \tag{7.1}$$

When L_{U1}, L_{U2}, U_1 and U_2 are all left as variable parameters, there are multiple sets of parameters having the correct combination of scattering length and effective range. We take $U_1 > 0$, $U_2 < 0$, $|U_2| \ll |U_1|$ and $2L_{U1} \leq L_{U2}$ to mimic the shape of the van der Waals potential. To choose optimal values of these coefficients we compute the energy-dependent phase shift for collision energies from 0 to 80 MHz (up to 4 mK) for the model potentials

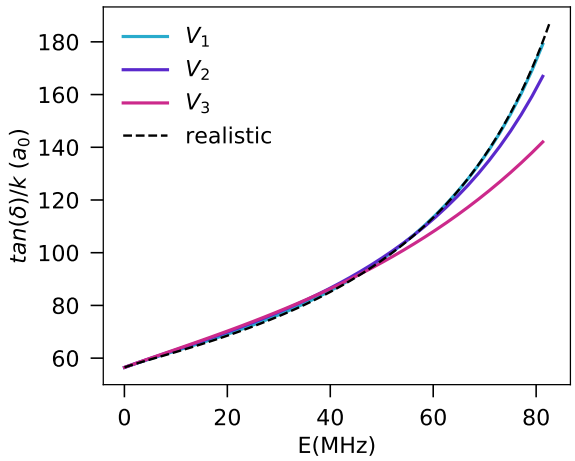

Figure 7.3: Energy dependent phase shifts for collisions of two ^{23}Na atoms in the $|F = 1, m_F = 1\rangle$ state at 105 G, for the realistic scattering including the full hyperfine structure, and for three single-channel model potentials of the form Eq. (7.1).

Table 7.1: Parameters of the interboson potentials from Fig. 7.3 in atomic units.

potential	LU_1	LU_2	$m_{\mathrm{Na}}U_1$	$m_{\mathrm{Na}}U_2$	$m_{\mathrm{Na}}U_{B1}$	$m_{\mathrm{Na}}U_{B2}$
V_1	39.19	195.93	102.12	-0.163	6.56	-0.0105
V_2	52.45	157.35	30.51	-0.458	5.09	-0.0763
V_3	65.15	130.29	18.93	-1.363	4.57	-0.329

and compare them with the real potentials. We chose this energy range since 80 MHz is approximately the well depth of the deepest boson-impurity model potential we consider.

We test three different potentials V_1, V_2, and V_3 for which the phase shift matches qualitatively with the momentum-dependent phase shift of the realistic model. These phase shift curves are all plotted in Fig. 7.3. We on purpose compare these potentials with visibly different phase shifts to test the sensitivity of our results to these differences. The parameters corresponding to these potentials are given in Table 7.1. We see that potential V_1 gives the closest match to the realistic phase-shift curve, indicating that the real potential is best approximated by a very hard core and a shallow attractive long range. However, this is more challenging to take into account into the calculations, and softer-core potentials V_2 and V_3 still also give qualitative agreement with the realistic phase shifts. We will see below that all of these potentials give rise to similar trimer energies.

For completeness, we have also given the parameters U_{B1} and U_{B2} which give rise to the same scattering length on the level of the Born approximation. Note the order of magnitude differences between U_1 and U_{B1}, which indicate that these potentials are far from the Born approximation and that including the interboson correlations is thus crucial.

Furthermore, for the boson impurity potential, L_g varies between 70-100 a_0 in the experimental magnetic-field range, and the coupling constant $m_{\mathrm{Na}}g$ varies between -4.9 and -4.2 a_0^{-2}. Note that the interboson coupling constants are thus much larger than the boson-impurity coupling constants, even though the boson-impurity scattering length is an order of magnitude larger. This shows again the importance of taking into account the interboson interactions, even though the scattering length is much smaller compared to the boson-impurity scattering length.

In principle the match of the calculations to the experiment could be improved further by also choosing more complex boson-impurity potentials to better match the realistic

phase-shifts. However, over the same energy range the main features in these phase shifts follow from multichannel effects and are affected by the proximity of the other scattering resonances (see Fig. 2.3). These features can not be incorporated well in a single-channel picture. How much the trimer energy is affected by this remains a topic for further research. Note that some of these multichannel features are already incorporated via their effect on the scattering length and the effective range.

7.2.2 Variational treatment

For the variational three-body and polaron calculations, we use the theoretical framework of Chapter 6. Since the parameters lie deep into the crossover regime, we choose to use the double-excitation approach, where we again parameterize our wave function in terms of a Gaussian basis set. We also use a very similar treatment of the interboson repulsion.

To improve the accuracy of our calculations for very shallow three-body bound states we make one further approximation. The problem here is that a very high resolution in the wave function in the spherical basis is needed to describe the interboson interactions far from the impurity. To resolve this, we treat the quartic interboson interaction term as a three-body interaction between the bosons and the impurity, which reduces to the full interboson interaction close to the impurity, and the interaction on the Born approximation far from the impurity. The modified interboson repulsion Hamiltonian (in the frame of the impurity) then corresponds to

$$\hat{\mathcal{H}}_U = \sum_{i=1,2} \frac{1}{2L_{Ui}^2} \int_{\boldsymbol{r}} \int_{\boldsymbol{r'}} U_i^{(B)} \exp[-\frac{(\boldsymbol{r'}-\boldsymbol{r})^2}{L_{Ui}^2}][2n_0 \hat{b}_{\boldsymbol{r'}}^\dagger \hat{b}_{\boldsymbol{r}} + \sqrt{n_0}(\hat{b}_{\boldsymbol{r'}}^\dagger \hat{b}_{\boldsymbol{r}}^\dagger \hat{b}_{\boldsymbol{r}} + h.c.) + \frac{1}{2}\hat{b}_{\boldsymbol{r'}}^\dagger \hat{b}_{\boldsymbol{r}}^\dagger \hat{b}_{\boldsymbol{r'}} \hat{b}_{\boldsymbol{r}}]$$
$$+ \frac{(U_i - U_i^{(B)})}{2} \exp[-\frac{(\boldsymbol{r'}-\boldsymbol{r})^2}{L_{Ui}^2} - \frac{\boldsymbol{r'}^2 + \boldsymbol{r}^2}{L_W^2}] \hat{b}_{\boldsymbol{r'}}^\dagger \hat{b}_{\boldsymbol{r}}^\dagger \hat{b}_{\boldsymbol{r'}} \hat{b}_{\boldsymbol{r}}. \quad (7.2)$$

Note that in the last term, the interboson interaction potential is dependent on the distance from the impurity. The idea is that we do not renormalize the interboson scattering far from the impurity so that the coupling constant reduces to U_B, while we keep the bare coupling U close to the impurity. The length scale L_W sets the distance from the impurity at which we switch between U_B and U.

7.2.3 Three-body problem

For consistency and for calibration of the L_W parameter, we first check the performance of the wave-function parameterization for the three-body problem. For comparison, we compute accurate trimer energies for our model potentials using the adiabatic hyperspherical approach [101, 102]. We plot the difference between the dimer and trimer energies for the different approaches and potentials in Fig. 7.4.

We observe that the accurate trimer energies from the hyperspherical calculations, indicated by crosses, coincide for the three model potentials. The relative differences are of the order of 0.1 kHz, so on the order of 1% of the dimer-trimer difference and 0.1% of the total trimer energy.

We find that also the results of our simplified calculations (dashed lines) coincide with these accurate trimer results if we include the single free L_W parameter for every interboson potential. The fact that a single L_W value can lead to a agreement over the full magnetic-field range, shows that this approximation is justified. If we do not include this L_W parameter, we find much larger differences between the theoretical results for the different model potentials. By increasing the basis-set size, these lines will eventually

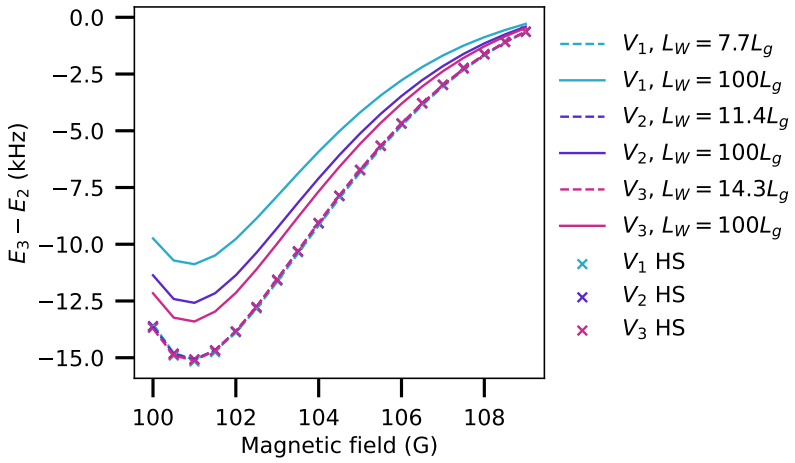

Figure 7.4: Difference between the theoretical trimer and dimer energy in the magnetic field range of 100-109 Gauss. The different colors indicate the different interboson model potentials, the dashed lines indicate the model results with the effective three-body interaction for the fitted L_W indicated in the legend, whereas the solid lines show the result for large $L_W = 100L_g$. The crosses show the results from accurate hyperspherical calculations.

converge, but this requires a large number of parameters. We see that the value of L_W found for the various potentials differs. This is because the repulsive core increases in radius subsequently for V_1, V_2, and V_3. Hence, for a fixed basis set, the distance from the impurity at which the required resolution can be reached is also increased. This explains the variation in the L_W parameter, which follows approximately linearly the trend in L_{U1}. Note furthermore that L_W is an order of magnitude larger than L_g, so that the interboson scattering close to the impurity is still well described.

7.2.4 Three-level model

For our effective three-level model, we first minimize the energy using the double-excitation approach, see Eq. (6.3). Then we take our three levels to be (up to normalization)

$$|1\rangle = |0\rangle, \tag{7.3}$$

$$|2\rangle = \int d^3r \beta(\boldsymbol{r}) \hat{b}^\dagger_{\boldsymbol{r}} |0\rangle, \tag{7.4}$$

$$|3\rangle = \frac{1}{\sqrt{2}} \int\int d^3r d^3r' \alpha(\boldsymbol{r}, \boldsymbol{r}') \hat{b}^\dagger_{\boldsymbol{r}} \hat{b}^\dagger_{\boldsymbol{r}'} |0\rangle. \tag{7.5}$$

As obvious, the three levels correspond respectively to free-impurity, dimer, and trimer states. The dimer and trimer states are not the same as the free dimer and trimer states, but the wave functions are optimized to give the minimum energy in the double-excitation approach in presence of the background BEC. The three-level Hamiltonian is found by computing the matrix elements of the Hamiltonian with respect to these three states. By construction, the ground-state energy in this three-level model is the ground-state energy also found from the variational minimization of the double-excitation Ansatz.

7.3 Experimental details

The experiment starts with a Bose-Fermi mixture of ^{23}Na and ^{40}K at $\approx 100\,$nK, trapped in an optical dipole trap with trapping frequencies $2\pi \times (108, 112, 9)$. The BEC has a

typical peak density of $n_B \approx 40\mu m^{-3}$ and the Fermi gas is two orders of magnitude more dilute. We perform rf-injection spectroscopy by driving ^{40}K from its initial spin state, which we denote as $|\downarrow\rangle$, into a final spin state $|\uparrow\rangle$ for which the impurity-boson interatomic potential supports a shallow bound state. By measuring the number of transferred atoms we can extract information about the presence of final states at the probed energy, and importantly, the overlap with these final states and the initial state.

An essential feature of our experiment is that the impurity is strongly interacting with the bath already in the initial state $|\downarrow\rangle$, with approximately constant $(k_n a)^{-1} \sim -1$, where $k_n = (6\pi n_B)^{1/3}$ is the inverse interboson distance. This is possible due to the proximity of a broad initial-state Feshbach resonance to the magnetic field range of $100-120$G containing the final-state resonance, see Fig. 2.3. Indeed, we allow the impurity to form a strongly interacting attractive Bose polaron by letting it thermalize with the bath for 25ms before performing spectroscopy. This boosts the wavefunction overlap with the bound states of interest in the final many-body Hamiltonian, as the BEC density is already strongly enhanced near the impurity. This allows us to drive the rf-transition to final bound states faster than the decay of the short-lived final states. Key here is to vary the pulse time with the impurity-bath interaction strength, such that $\sim$50% of the initial polaron $|\downarrow\rangle$ population is injected into the manifold of bound states. This is necessary as the coupling strength between the initial attractive polaron and bound states changes dramatically near the Feshbach resonance. With this procedure we are able to both deplete the initial population as well as witness the production and arrival of novel molecular states in our experiment.

7.4 Results

We naturally observe the effect of the background BEC on the impurity atoms by spatially resolving the rf-signal at different positions in the atomic cloud, as shown in Fig. 7.5a) for the magnetic field of B=102.5G. In Fig. 7.5b) we show a few cuts from Fig. 7.5a), but as a function of the density. The frequency shown is the frequency shift compared to the bare hyperfine transition. The solid lines show the fitting-parameter-free theoretical predictions using the three-level model described before.

At low density in the edge of our cloud, we observe the bare free-to-free and free-to-bound hyperfine transitions. Here we already recognize our first key result: in Fig. 7.5b), we see a clear double peak emerging in the free-to-bound spectrum, which we attribute to the dimer and the trimer states. The experimentally fitted dimer and trimer energies are marked by the dashed and dash-dotted lines. This marks the first observation of such a weakly-bound trimer state in the Efimov-unfavorable regime. The weights of the two contributions are approximately equal because the transition is saturated.

When the density is increased towards the middle of the cloud, the narrow peaks at low density broaden immensely due to the coupling with the medium. The upper peak shifts upward in energy, due to the formation of a *repulsive polaron*. The lower peak on average shifts to lower energies, due to *attractive polaron* effects. The coupling with the medium is so strong that the lowest energy at which we observe significant signal lies approximately 50 kHz below both the dimer and the trimer energies, that is about a third of the binding energy. We are therefore clearly in the strong-coupling regime where the many-body correlations with the medium are equally important as the binding leading to molecule formation.

A key indication that the admixing of both dimer and trimer states is required to explain these results, is the fact that a theoretical description admitting only a single

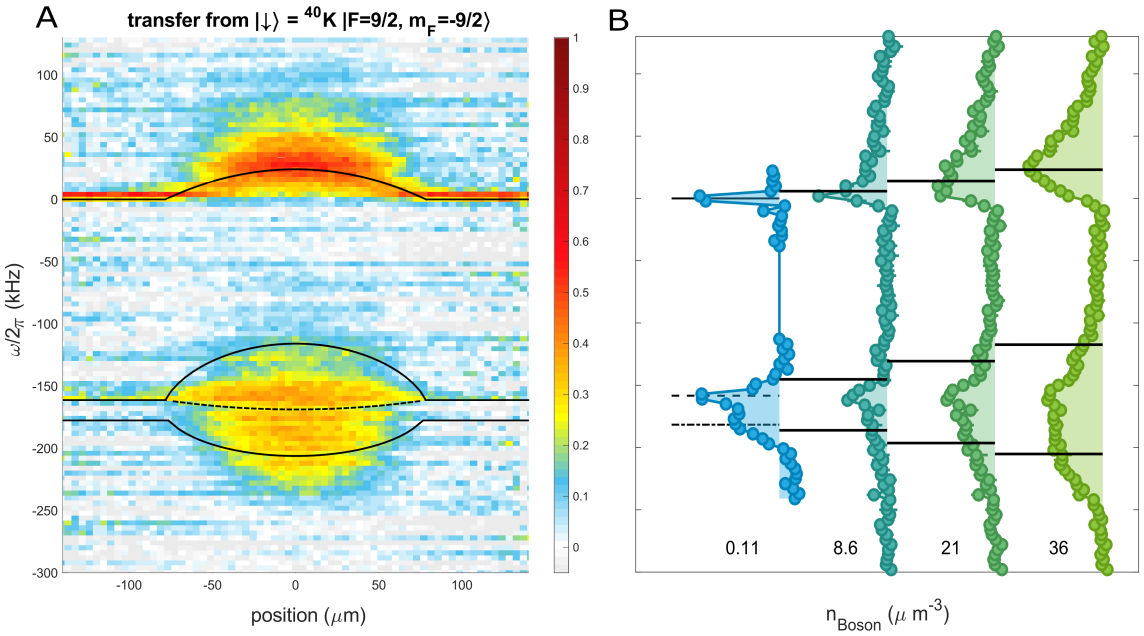

Figure 7.5: (A) The population transfer fraction from impurity spin state $|\downarrow\rangle$ depends strongly on its position within the BEC. We show spatially resolved spectra at $B = 102.5$G measuring the remaining population in $|\downarrow\rangle$ as a function of displacement along the long axis of the cigar shaped trap and the rf-frequency detuning from the bare hyperfine transition. In (B) cuts of Fig. (A) are shown for some densities. The solid lines indicate the theory predictions from the three-level model, whereas the dashed line in (A) shows the theory result with at most one excitation from the BEC. In (B) the dashed and dashed-dotted lines indicate the experimentally fitted dimer and trimer energies.

excitation from the medium (indicated by the dashed line) does not capture at all the lowest attractive polaron energy. Our theoretical three-level model captures the width of the rf-spectrum much better, showing that the qualitative picture is correct. Still, the lowest attractive polaron energy is underestimated. This is likely due to the admixture of states with even higher number of excitations from the medium, and broadening due to three-body loss. We also see by comparing the theory lines in (A) and the experimentally fitted dimer and trimer energies in (B), that the dimer-trimer gap measured in experiment is larger than in theory. The reason is subject to further investigation, but might be multichannel effects due to the proximity of other resonances. The middle line of the three-level model captures well the upper edge of the experimental attractive polaron signal. This shows that the strength of the many-body splitting due to the coupling with the condensate matches well the experimental picture.

In Fig. 7.6 we see the polaron rf-spectrum as a function of the magnetic field, studying our system over a broad range of impurity-bath final interaction strengths. Focusing first on Fig. 7.6A, we show the spectrum obtained from measuring the atoms transferred from the initial state, and we see again the repulsive and attractive polaron branches. The black horizontal bars in Fig. 7.6A mark the deepest binding energies where we see spectral response, and the threshold behavior we observe on the low-energy flank of the spectra strongly suggests that we indeed observe the ground state of the final-state Hamiltonian. The full width at half maximum (FWHM) of the attractive branch is indicated by the triangles, and the theory curves (opaque lines) are computed using the three-level model

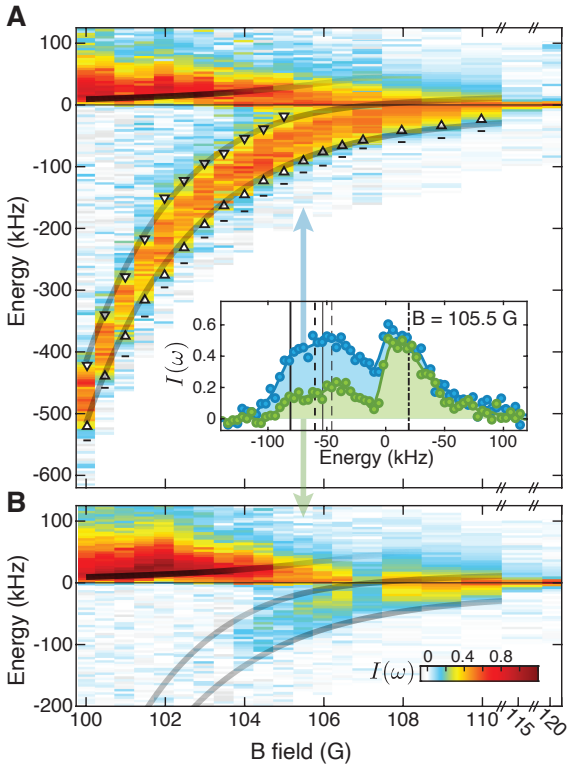

Figure 7.6: Measurement of the RF transfer fraction in the center of the BEC via (A) depletion of $|\downarrow\rangle$ and (B) arrival of $|\uparrow\rangle$. Spectra are taken at various magnetic fields and plotted versus the energy of the final state with respect to the bare impurity state. In the inset a cut is shown of the obtained signal at 105.5G. In (A) the full width at half maximum of the signal is indicated by the triangles. The theory results from the three-level model are indicated via the solid lines, of which the opacity is set by the overlap of the states with the initial polaron state, weighted by the duration of the RF pulse. The horizontal black markers in (A) denote the lowest energies for which nonzero rf transfer was measured in our experiment.

discussed before. The opacity of the theory curves is given by the overlap of the initial state and weighted by the rf-pulse length T_{rf}, which is proportional to the transferred population for pulses within linear response. We additionally note that for B =115, 120G, the interspecies scattering length of initial and final spin states are approximately equal, so despite strong interactions, both branches collapse into a single feature given by the spectral resolution of our probe.

We find that the two lowest energies of the theoretical three-level model reliably describe the FWHM frequencies of the attractive polaron branch over the wide range of interaction strengths explored. Thus, the models accounting for the many-body correlations due to the BEC are sufficient to predict the spectral location and width. However, the accurate computation of the full spectral lineshape is beyond current theoretical approaches. Our experiment provides an excellent testbed for developing theory that also includes the mechanisms of three-body loss and adding phononic excitations on top of the molecular states.

We remark that the peaks of the repulsive polaron branch of the spectra deviate from its theoretical repulsion energy, as shown by the upper opaque line in Fig.7.6A. The repulsive polaron corresponds to a broad continuum of scattering states, which are shifted upward in

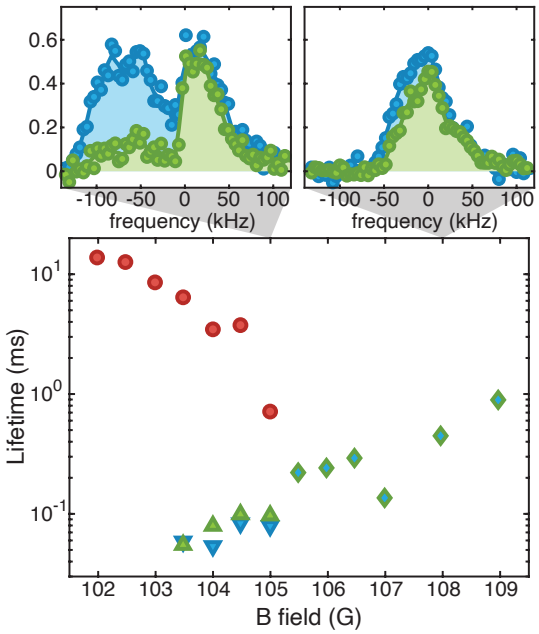

Figure 7.7: The lifetimes of the states created by rf-injection are inferred from the ratio of population depleted from $|\downarrow\rangle$ to population observed in $|\uparrow\rangle$, as shown in Fig. 7.6. Population transferred to $|\uparrow\rangle$ during the rf-pulse can decay rapidly due to three-body recombination. For data taken at $B \leq 105$G, we are able to resolve the attractive and repulsive branches of the spectrum, whereas for larger magnetic fields the two features merge. This can be seen in the exemplary spectra shown in the top row. The lifetime of the bound states (triangles) decreases at deeper binding energy (away from the Feshbach resonance), whereas the lifetime of the repulsive polaron branch (circles) increases. At sufficiently deep binding energies, we do not observe any population in $|\downarrow\rangle$.

energy due to the need for the quantum-mechanical wave function to be orthogonal to the attractive polaron states. The experimentally determined spectral weights not only depend on the available density of states, but also on the wave-function overlap with the initial state. The intricacies of the repulsive polaron lineshape cannot be expected to be captured by the single repulsive polaron line following from our three-level model. However, what is still captured is the decrease in the repulsive polaron spectral weight for increasing positive impurity-boson scattering length.

Fig. 7.6B we show the number of arrived atoms in the final state. Comparing this signal to the depletion signal from Fig. 7.6A allows us quantitatively estimate the decay lifetimes $1/\Gamma$ of the states prepared during the rf-injection pulse time. These lifetimes are shown in Fig. 7.7. We model transfer between populations $P_\downarrow, P_\uparrow$ as $dP_\downarrow \propto -\Omega_R(t)^2 P_\downarrow dt$, where the Rabi frequency Ω_R is time-dependent due to pulse shaping, and the loss in $|\uparrow\rangle$ as $dP_\uparrow + dP_\downarrow = -\Gamma P_\uparrow dt$. We first are able to observe the arrival of the upper repulsive polaron branch, where losses are weak. However, in the attractive branch the arrival signal is much weaker. The origin of this effect is the final state being short-lived compared to the rf-pulse duration. Their short lifetimes can be explained by a significant trimer admixture, and trimers have a short lifetime due to three-body recombination. We find that the lifetime decreases substantially with increasing binding energy. Qualitatively this is to be expected, since the probability that the three particles meet each other at short distance and undergo the recombination reaction increases along with the binding energy.

At the magnetic fields where we are able to detect nonzero population in $|\downarrow\rangle$ in the attractive branch, we observe decay lifetimes $1/\Gamma$ of greater than 50μs. Up to factors order unity, this contributes to a lifetime broadening of $\Gamma/(2\pi) \approx 3$ kHz, whereas the typical spectral widths measured (> 50 kHz, e.g., Fig. 7.7 top left) is at least an order of magnitude greater. This serves as an additional confirmation that the broad spectra we observe cannot simply be attributed to loss and gives further credence for the many-body interpretation presented above.

7.5 Conclusion/Outlook

Our study provides experimental observation of conceptually novel molecular states in a superposition of two- and three-body bound states, induced by coupling to a degenerate bosonic bath. We find that the mixing induced by the background field causes strong level repulsion, setting one of the dominant energy scales in our spectra. We show that by preparing an initial metastable polaronic state, we are able to probe the unexplored crossover between few- and many-body physics of fermions immersed in a BEC within experimentally meaningful timescales. Furthermore, our measurements provide an excellent testing ground for both existing and developing theories of polaron systems.

Our work opens the door into several new directions, spanning from fundamental questions on the role of quantum coherence in polaron physics to the present challenges in ultracold atomic and molecular gases. There are conflicting theoretical results on the finite-temperature properties of the Bose polaron [192–195], and it remains to be explored to which degree the coherence that accompanies the high density and low temperature of the bosonic bath is essential to observing the hybridization effects. Such experiments could be implemented cleanly in homogeneous trapping potentials [208], where the spatial density is decoupled from temperature. We separately raise the experimental question of whether the existence and proximity of few-body bound states is a fundamentally limiting loss mechanism on the road to efficient creation and quantum degeneracy of molecular gases, when starting from degenerate atomic quantum mixtures near a Feshbach resonance [209, 210]. We shed light on this process with spectroscopic precision by revealing many-body correlations and finite final-state lifetimes of impurities immersed in a quantum bath.

Part C. Ultracold molecules

Abstract

Ultracold gases of ground-state molecules provide many exciting prospects, such as cold and controlled chemistry, quantum simulation and quantum computing. However, the chemical properties of ultracold molecules have so far remained mysterious. Collisions of the ground-state molecules namely appear to lead to loss, even in cases when the molecules are not supposed to be reactive. It has been proposed that ultracold molecules can stick together when they collide, forming collision complexes which may even live on the order of micro- or milliseconds.

In our previous work we have suggested that these collision complexes can get electronically excited by the trapping laser, leading to photoinduced loss. Some recent experiments have indeed observed this loss mechanism, with rates close to the theoretical predictions. However, other experiments, for instance at the Max Planck Institute of Quantum Optics (MPQ), have not observed any loss reduction when turning off the trapping laser, implying a deviation from the theoretical predictions by two orders of magnitude.

In this Chapter we discuss these recent experiments, in particular the MPQ experiment, and provide potential theoretical arguments to partially explain the results. We show that in case of fermionic molecules, the p-wave barrier leads to an orders of magnitude increased sticking time, and we propose a new mechanism to explain the absence of any resonances in the scattering rate due to the broadening of the resonances caused by the loss.

Chapter 8. Sticky collisions of ultracold molecules

This chapter is based on the following works

[5] Roman Bause, Andreas Schindewolf, Renhao Tao, Marcel Duda, Xing-Yan Chen, Goulven Quéméner, Tijs Karman, Arthur Christianen, Immanuel Bloch, Xin-Yu Luo,
Collisions of ultracold molecules in bright and dark optical dipole traps,
Physical Review Research 3, 033013 (2021)

[6] Arthur Christianen and Gerrit C. Groenenboom and Tijs Karman,
Lossy quantum defect theory of ultracold molecular collisions,
Physical Review A 104, 043327 (2021)

[7] Roman Bause, Arthur Christianen, Andreas Schindewolf, Immanuel Bloch, Xin-Yu Luo,
Ultracold Sticky Collisions: Theoretical and Experimental Status,
Reprinted with permission from The Journal of Physical Chemistry A 127, 729-741 (2023).

Note that the introductory part of this chapter (Secs. 8.1 and 8.2) also summarizes the main results of the following works completed before starting my PhD.

[10] Arthur Christianen, Tijs Karman, Gerrit C. Groenenboom,
Quasiclassical method for calculating the density of states of ultracold collision complexes,
Physical Review A 100, 032708 (2019)

[11] Arthur Christianen, Martin W. Zwierlein, Gerrit C. Groenenboom, Tijs Karman,
Photoinduced Two-Body Loss of Ultracold Molecules,
Physical Review Letters 123, 123402 (2019)

8.1 Introduction

We have seen so far that an impurity atom immersed in an atomic BEC can undergo interesting chemical processes involving the background medium. However, in most chemical processes in the world around us, the involved particles are much more complex. Hence, it would be very interesting to consider the case where our medium and/or impurities would consist of ultracold molecules instead of atoms. The most popular applications for ultracold molecules are metrology [27, 28, 211], quantum simulation with dipolar interactions [212–219] and quantum computation [220, 221]. From the chemistry perspective, ultracold molecules give unique opportunities to control and observe the outcomes of reactions in a quantum-state selective way [39, 40, 50, 51, 222].

[1] Accessible via: https://pubs.acs.org/articlesonrequest/AOR-4ZVM8MPYMVPTRPPDG7RM

Because laser cooling of ultracold molecules is extremely hard [223], the most successful route to make ultracold molecules so far has been to create them from mixtures of ultracold atoms. The first step in this procedure we have already discussed before: association of ultracold atoms into Feshbach molecules. The second step is then to turn these Feshbach molecules into ground-state molecules via stimulated Raman adiabatic passage (STIRAP) [224, 225]. Even though this step is not trivial, by now this is routinely done in many experiments.

The first ultracold molecules (^{40}K ^{87}Rb) in their absolute ground state were realized in 2008 [226]. Here they already witnessed chemistry at ultracold temperatures, because KRb turned out to be reactive [52, 227] towards the formation of K_2 and Rb_2. Indeed, they found that every time the KRb molecules collided with each other, these collisions led to loss. Therefore this loss was called "universal". For many applications it is beneficial to have stable molecules, however. Hence, other groups have focused on realizing other bialkali molecules for which the equivalent rearrangement reactions are endoergic [228–231]. These include NaK, NaRb and RbCs [52]. Surprisingly, in all of these cases, loss rates compatible with universal loss were observed as well.

A partial explanation was offered by Mayle *et al.* [53, 54], who suggested that the collisions are "sticky": that the molecules stick together for a long time when they collide. This hypothesis was supported by Hu *et al.* [232], who directly detected these long-lived collision complexes. This is by itself remarkable, since it is highly unusual in chemistry that intermediate complexes in collisions and reactions can be directly detected. The anomalously long lifetimes of these complexes are therefore a unique feature of these ultracold molecular collisions.

However, collisional sticking is not sufficient to explain the loss. Indeed, something needs to happen to the collision complexes to prevent the molecules from dissociating again. In 2019, we predicted that the complexes can be destroyed due to photo-excitation by the trapping laser of the optical dipole trap [11]. Based on improved calculations of the sticking time [10] using realistic interaction potentials [9], we estimated that the photo-excitation rate is one order of magnitude higher than the complex dissociation rate, meaning that the complexes are destroyed practically every time they are formed.

The hypothesis that the trap laser light can excite the collision complexes was confirmed within a year in two different experiments [233, 234], and the mystery had seemingly been solved. In Ref. [233] the authors demonstrated using reactive ^{40}K^{87}Rb molecules, that they could use the laser intensity to determine the branching ratio between the photo-excitation process and the reaction mentioned before [233]. They also measured the lifetime and photo-excitation rate of the complexes to be consistent with theoretical predictions. In another experiment [234], the optical dipole trap was periodically modulated so that the laser light was completely off in some time-intervals. For dark times longer than the collisional sticking time, the collision complexes can survive and dissociate again, and the loss should be reduced. This effect was indeed observed, and by tuning the modulation frequency the authors also extracted sticking times and photo-excitation rates, which again turned out to be consistent with theory.

Assuming that photo-excitation by the trapping laser causes the loss, one should be able to avoid this loss by trapping the molecules in absence of light. As we will discuss in this Chapter, experiments at MPQ [5] show that, surprisingly, for the fermionic ^{23}Na^{40}K molecules of study, the loss persists even when the laser intensity is suppressed by orders of magnitude. Similar results were found in Ref. [235] for bosonic ^{23}Na^{39}K and ^{23}Na^{87}Rb molecules. In this Chapter we will introduce the topic of sticky collisions and photo-induced loss, and work out some of the missing ingredients to explain the experimental

results [6]. Still the main mystery remains unresolved, however, and we identify future directions to resolve this puzzle.

The Chapter has the following structure. In Section 8.2, we explain the phenomenon of sticky collisions, show how to compute the loss rates with quantum defect theory, and introduce the photo-induced loss mechanism. In Section 8.3, we briefly describe experimental methods to probe this photo-induced loss, and discuss the MPQ experiment [5] in this direction. Section 8.4 addresses the validity of assumptions in Section 8.2 and contains a discussion of possible effects which were not considered in previous models. In particular the results from Ref. [6] are highlighted. Finally, in Section 8.5, we suggest research directions which we believe to be promising in order to resolve the "sticky mystery".

8.2 Theory framework

Some basics of the scattering of ultracold molecules were already discussed in Chapter 2.3.3, but we did not yet elaborate on how these scattering processes are usually described theoretically. As we will explain below, the number of internal states which need to be accounted for is so immense that the standard scattering approaches such as introduced in Chapter 2.5 break down. However, in order to still make theoretical predictions, the model can be simplified. This is typically done using quantum defect theory (QDT) [236–238]. In the long range the molecules still occupy their internal ground state, and exhibit their quantum mechanical wave-like character in their translational motion. In this regime a quantum mechanical description is still feasible. However, at short range, too many internal states become available and a full theoretical description becomes computationally intractable. One can still obtain qualitative, and in some cases quantitative results by choosing an intermediate range threshold. The result of the short-range dynamics is now to provide a certain boundary condition for the long-range wave function at this threshold. Given this boundary condition, the long-range problem can be solved exactly. We will discuss this procedure in more detail below, in Section 8.2.2. First, we will discuss the effective model we apply to understand the short-range problem, and explain why ultracold collisions are so "sticky".

8.2.1 Complex lifetime from RRKM theory

The main concepts of sticky collisions are illustrated in Fig. 8.1. When two bialkali molecules collide, they enter the large phase space of the collision complex. Due to their strong and anisotropic interactions, the molecules move chaotically through the available configurations [53, 54, 239–241] before eventually dissociating when they by chance go back to their respective initial states. The "sticking time" is in this picture naturally related to the size of the available phase space divided by the size of the "opening" through which the particles can leave.

These ideas are more precisely formulated in a quantum-mechanical way in the statistical Rice-Ramsperger-Kassel-Marcus (RRKM) theory [242–244]. In this formalism the lifetime of the complex, τ_{RRKM}, follows from a simple relation between the density of states ρ and the number of outgoing states N_{out} [53]:

$$\tau_{\mathrm{RKKM}} = \frac{2\pi\hbar\rho}{N_{\mathrm{out}}}. \tag{8.1}$$

Quantum mechanically, the notion of chaos implies that (almost) every eigenstate is delocalized over the entire accessible phase space [245]. When these eigenstates couple

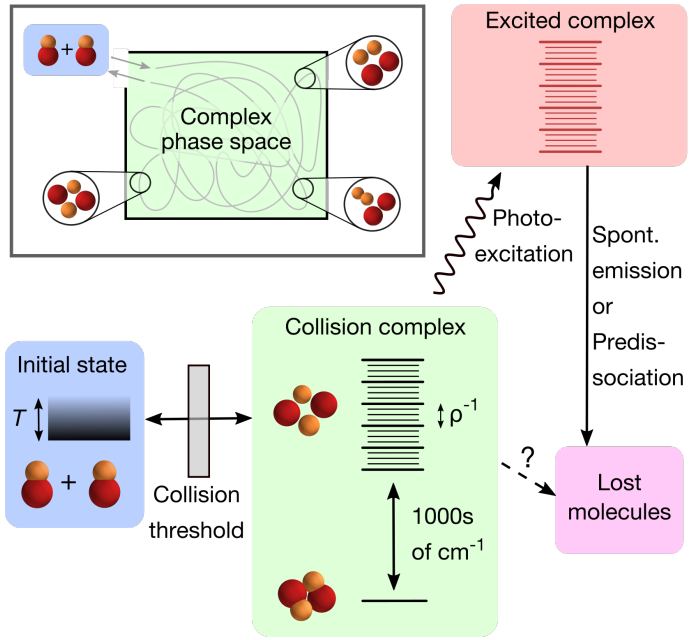

Figure 8.1: Schematic diagram of sticky collisions of nonreactive molecules. The box on the top left shows a classical picture. When molecules collide and enter the complex phase space, the path they follow is assumed to be random. The rest of the figure shows the possible pathways of sticky collisions. The kinetic-energy distribution of the initial ground-state molecules is set by the temperature. When they collide, they need to pass the threshold before they enter the short-range potential and form a complex. The number of available states in the complex may be increased depending on which quantum numbers are conserved (illustrated by additional smaller lines). The complex can be electronically excited by photons from the trapping laser and subsequently decay to other states. Otherwise, it can dissociate into ground-state molecules, or another hypothetical loss mechanism may occur.

into the scattering continuum, they give rise to scattering resonances which in turn lead to sticky collisions. Since the RRKM model is statistical, the experimental interval of collision energies needs to contain multiple resonances for the model to be predictive.

Applying this model to ultracold bialkali molecules yields sticking times which are very long compared to molecular timescales. This is because N_{out} is small and ρ is very large. The reason that N_{out} is small is simple: if molecules are in their absolute ground state and are sufficiently cold, no inelastic collision channels are energetically accessible, thus $N_{\mathrm{out}} = 1$. For reactive collisions N_{out} is larger, but for bialkali molecules the value is typically still modest. For example, for KRb+KRb it is approximately 100 [233]. The available phase space is very large because of the strong chemical interaction, e.g., the interaction energy of two NaK molecules is $\sim 4500\,\mathrm{cm}^{-1}$ [9]. The rotational and vibrational constants for NaK are $0.095\,\mathrm{cm}^{-1}$ and $124\,\mathrm{cm}^{-1}$, so if the interaction energy is turned into kinetic energy, up to 200 rotational levels and 35 vibrational levels can be occupied (assuming a harmonic vibrational potential). Taking into account the degeneracies of the rotations, this leads to ∼20000 rotational states for a single molecule. Since the degrees of freedom of two molecules plus their relative motion need to be considered, the number of involved states becomes huge. It can grow even orders of magnitude further in the presence of external fields breaking angular momentum conservation or when the hyperfine state can change during the collision.

Table 8.1: The estimated DOS [10], in μK^{-1} (RRKM lifetime, in μs) for all singlet polar bialkali molecules ($J = 0$) in a single hyperfine state. The star indicates the NaK-NaK lifetime has been determined accurately, without extrapolation.

	^{23}Na	^{39}K	^{87}Rb	^{133}Cs
^{7}Li	0.0051 (0.25)	0.014 (0.67)	0.024 (1.17)	0.068 (3.3)
^{23}Na	.	0.124(6.0)*	0.27 (12.9)	0.83 (40)
^{39}K	.	.	0.48 (23.0)	1.50 (72)
^{87}Rb	.	.	.	5.3 (253)

The large number of quantum states is exactly the reason why one needs to resort to statistical models in the first place, as it makes rigorous quantum mechanical calculations computationally intractable. Some of the most computationally demanding scattering calculations to date were carried out for alkali atom-diatom collisions [240, 241], which have three fewer motional degrees of freedom. This shows that moving to a full quantum description of molecule-molecule bialkali collisions will probably not be possible in at least the next decade, especially for the heavier species, for which ρ is generally larger. Even if these calculations were tractable, they are sensitive to the details of the interaction potential, which is hard to calculate with sufficient precision. This means that only qualitative conclusions could be drawn from this kind of calculation.

Exactly computing the density of states is equally difficult as solving the scattering problem. However, here one can resort to quasiclassical approximations, which are believed to be accurate because the involved rovibrational quantum numbers are high. In Ref. [10] such a quasiclassical method was proposed to estimate ρ for realistic interaction potentials [9]. The result is shown in Table 8.1. In the absence of external fields and when the nuclear spin states of the atoms are conserved, Eq. (8.1) typically yields τ_{RKKM} ranging from few to hundreds of microseconds for collisions between bialkali molecules.

Note that this discussion is specific to bialkali dimers. For example, many other molecules have much weaker interactions and would therefore not be expected to be sticky. This especially holds for typical chemically stable molecules naturally occurring in the gas phase. Even the triplet LiNa molecule [246] is in this sense different from the other investigated bialkalis because it is very light and the interaction potential is comparatively shallow. Also in the case of very strong interactions, sticky collisions are not guaranteed. For example, CaF is highly reactive [15], leading to a large value of N_{out}.

8.2.2 Quantum defect theory

We now move to the quantum-defect-theory description of the long-range part of the collision, which will allow us to estimate scattering cross sections [6, 236–238, 247]. Here we summarize the essential points. Let us define an intermediate range R_c beyond which the coupling between the different asymptotic collision channels is negligible. Furthermore, we assume that we can find analytical solutions of the wave function in the long-range part of the potential, which we call here f and g. These functions asymptotically take the form

$$f(R) \to kR\sqrt{2\mu_r/\pi\hbar}[j_l(kR)\cos\eta - y_l(kR)\sin\eta], \tag{8.2}$$

$$g(R) \to kR\sqrt{2\mu_r/\pi\hbar}[j_l(kR)\sin\eta - y_l(kR)\cos\eta], \tag{8.3}$$

when $R \to \infty$. Similar to Eq. (2.37) we can now define a K-matrix at the matching point R_c, so that

$$\psi(R) = f(R) + Kg(R). \tag{8.4}$$

Note that the difference in sign compared to Eq. (2.37) follows from the different definition of f and g. In this approach, a general background phase shift η_l is already included in the definition of the asymptotic functions. Therefore this K-matrix only describes the resonant part of the short-range scattering. For simplicity we assume there is only a single open channel for distances larger than R_c.

It turns out that this K-matrix generally depends strongly on the collision energy due to the long-range part of the scattering process. However, this energy dependence is well-understood and can be absorbed into the asymptotic wave functions by defining $\tilde{f}$ and $\tilde{g}$

$$\begin{pmatrix} \tilde{f}(R) \\ \tilde{g}(R) \end{pmatrix} = \begin{pmatrix} C(E) & 0 \\ -C(E)\tan\lambda(E) & C^{-1}(E) \end{pmatrix} \begin{pmatrix} f(R) \\ g(R) \end{pmatrix}. \tag{8.5}$$

Importantly, the parameters $\lambda(E)$, $\eta(E)$ and $C(E)$ are only dependent on the properties of the long-range potential, and can therefore be determined without any knowledge of the short-range physics. We can define a new K_{SR} matrix based on these modified $\tilde{f}$ and $\tilde{g}$

$$\psi(R) = \tilde{f}(R) + K_{SR}\tilde{g}(R). \tag{8.6}$$

In this case the energy dependence of K_{SR} stems purely from the short-range dynamics of the scattering process. One can now relate the two K-matrices by inserting Eq. (8.5) in Eq. (8.6) to find

$$K = C^{-2}(K_{SR}^{-1} - \tan\lambda)^{-1}. \tag{8.7}$$

It turns out that C^{-2} represents the transmission rate through the long range of the potential, and that if $C^{-2} \to 0$ the wave function is simply not reaching the short range. Therefore, we see from Eq. (8.7) that the contribution of K_{SR} disappears for $C^{-2} \to 0$.

Via Eq. (2.42), the S-matrix can be obtained from the K-matrix using

$$S = \exp(2i\eta)\frac{1 + iC^{-2}(K_{SR}^{-1} - \tan\lambda)^{-1}}{1 - iC^{-2}(K_{SR}^{-1} - \tan\lambda)^{-1}}. \tag{8.8}$$

Note that the additional factor $\exp(2i\eta)$ appears compared to Eq. (2.42), because we have included the additional phase shift η in the definition of f and g. The collision cross sections for elastic collisions and loss of identical particles are given by

$$\sigma_{\text{el}} = \frac{2\pi}{k^2}[1 - S^2], \tag{8.9}$$

$$\sigma_{\text{loss}} = \frac{2\pi}{k^2}(1 - |S|^2). \tag{8.10}$$

If one takes all the possible collision processes into account, the S-matrix has to be unitary, and the loss cross section is automatically zero. However, here we make an effective model where we include some unknown loss process by allowing S to be non-unitary. In this case the sub-unitarity of S describes the loss cross section. The simplest case is that of universal loss, where all particles going into the short range disappear, leading to $S_{SR} = 0$ and therefore $K_{SR} = i$. If we plug this into Eqs. (8.8) and(8.10) we find

$$\sigma_{\text{univ}} = \frac{2\pi}{k^2}\frac{4C^{-2}}{\tan^2\lambda + (C^{-2}+1)^2}. \tag{8.11}$$

For s-wave collisions with a van der Waals potentials, the QDT coefficients are given by

$$\tan\eta = -ka, \tag{8.12}$$

$$\tan\lambda = 1 - \frac{a}{\bar{a}}, \tag{8.13}$$

$$C^{-2} = k\bar{a}[1 + \tan^2\lambda]. \tag{8.14}$$

Inserting these in Eq. (8.11) and assuming that $ka, k\bar{a} \to 0$, we see that

$$1 - |S|^2 = 4k\bar{a}. \tag{8.15}$$

The loss is therefore independent of the actual scattering length a; it only depends on $\bar{a}$, which is a simple function of the reduced mass and the C_6 coefficient (see Sec. 2.3).

What remains to be done is to find K_{SR} for the case of sticky collisions. Actually computing this matrix is a hopeless task, but if we assume that the short-range dynamics is completely chaotic, K_{SR} can be qualitatively represented via random matrix theory [53, 54, 248]. In this case K_{SR} can be described by the sum of the contributions of resonances at energies E_ν and widths γ_ν, drawn from a statistical distribution:

$$K_{SR} = -\frac{1}{2}\sum_\nu \frac{\gamma_\nu}{E - E_\nu}. \tag{8.16}$$

The energies E_ν are distributed according to the Wigner-Dyson distribution with mean spacing ρ^{-1}, for the density of states computed previously. The expectation value of the width from the so-called Weisskopf estimate is given by $\bar{\gamma} = (2\pi\rho)^{-1}$.

Mayle *et al.* [53, 54] now assumed that the interval of collision energies is sufficiently large, so that many of these scattering resonances are included. Furthermore, they assumed that resonant scattering is dominant over non-resonant scattering. In this case one finds for the elastic cross section [6]

$$\langle |1 - S|^2 \rangle = C^{-2} = k\bar{a}[1 + \tan^2 \lambda]. \tag{8.17}$$

Aside from the universal factor $k\bar{a}$ this also contains the non-universal factor $1 + \tan^2 \lambda$ and compared to the universal loss, a factor 4 is missing. Since $1 + \tan^2 \lambda$ will be of order one in most cases, the collision cross section is therefore comparable to the universal loss cross section. Even though this partially explains why near-universal loss was found in these experiments, no loss is actually included in this model, since K_{SR} is real and S_{SR} is therefore unitary. So still it remains an open question at this point where the loss of the complexes comes from.

8.2.3 Complex-mediated loss via photoexcitation

Several loss processes have been suggested, such as collisions with a third molecule [54] and excitation by the trapping laser [11] (see Fig. 8.1). In typical experiments, where molecules are held in optical dipole traps, the latter mechanism is predicted to be strong enough to excite almost every complex which is formed [10, 11].

Why can the trapping laser electronically excite the collision complexes? For the free molecules the trapping laser is detuned from any electronic transition so that the molecules cannot be photoexcited. However, as the geometry of the complex is continuously evolving, the gap between its electronic ground and excited states changes, sometimes matching the trap-laser frequency. Again one can take a classical approximation and assume that the geometry of the complex does not change upon electronic excitation. This way, the photoexcitation rate can be computed statistically as an average over phase space [11]. At typical intensities, the resulting rate is one to two orders of magnitude higher than the expected dissociation rate of the complexes [11]. Once a complex has been excited, it can decay in multiple ways, such as spontaneous emission or dissociation into various asymptotic states. This makes it very unlikely that the colliding molecules go back to their original states, causing them to be effectively lost.

Given this mechanism, the rate equations for the molecule and complex populations (n and n_c) take the form

$$\dot{n} = -k_2 n^2 + \frac{2C^{-2}n_c}{\tau_{\mathrm{RRKM}}}, \tag{8.18}$$

$$\dot{n}_c = \frac{k_2 n^2}{2} - \frac{C^{-2}n_c}{\tau_{\mathrm{RRKM}}} - k_I I n_c. \tag{8.19}$$

Here k_2 is the molecular scattering rate coefficient, k_I is the laser-excitation rate coefficient, I is the laser intensity and the C^{-2} factor from QDT. The factor C^{-2} [6, 249] plays an important role here, and is implicitly also included in k_2. We will discuss this in more detail in Sec. 8.4. To accurately describe experimental data, it is often necessary to also model effects resulting from inhomogeneous density distribution, one-body loss, and evaporation [5, 250].

Other loss processes, such as three-body collisions, non-excited complexes falling out of the trap, spontaneous decay into stable four-atom states, or excitation by black-body radiation, seem to be orders of magnitude too slow compared to τ_{RRKM} [10, 251]. Therefore, trapping ground-state molecules in the absence of intense laser light should lead to a suppression of the loss.

8.3 Experimental verification

How to check experimentally whether such complexes can indeed be destroyed by the laser light? The idea is simple: just turn off the light! However, the light from the optical dipole trap is also trapping the molecules, and turning it off permanently is therefore no option.

One way to resolve this, is to use a chopped dipole trap, i.e., a trap whose intensity is periodically modulated in a square-wave pattern. Due to the inertia of the molecules, they experience a time-averaged potential and remain trapped if the modulation frequency is much higher than the harmonic trap frequency. During the periods where the trap is on, complexes are still likely to scatter at least one photon and are thus lost. However, if the off-times are at least comparable to the complex lifetime against dissociation into ground-state molecules, and the intensity is low enough, the time-averaged two-body loss rate should be reduced. Because the intensity modulation can cause loss in itself, it is difficult to directly compare lifetimes measured in modulated and non-modulated traps. This can be fixed by adding a continuous laser, a "kill beam", to the modulated trap, and comparing the results with this kill beam on or off. By varying the kill-beam power, one can probe the necessary intensity to excite a complex during its lifetime.

Indeed, a reduction of loss in such an experiment was observed with ^{87}Rb^{133}Cs-molecules [234, 252]. This proved for the first time that the laser of the optical dipole trap can indeed photo-excite the formed complexes. Furthermore, the authors also measured the complex lifetime and the photo-excitation rate by varying the chopping frequency and the intensity of the kill-beam. Both of these quantities were in qualitative agreement with the theoretical results.

An entirely different approach to probe the photo-induced loss is used in Refs. [232, 253], where they use an apparatus allowing direct detection of the molecules present in their experiment. Aside from the reactive ^{40}K^{87}Rb molecules they used and the reaction products K_2 and Rb_2, they were also able to directly detect the collision complexes and to measure their lifetime. This was spectacular since it is very rare in chemistry that intermediate complexes in a reaction are so long-lived that they can be detected. Furthermore, they

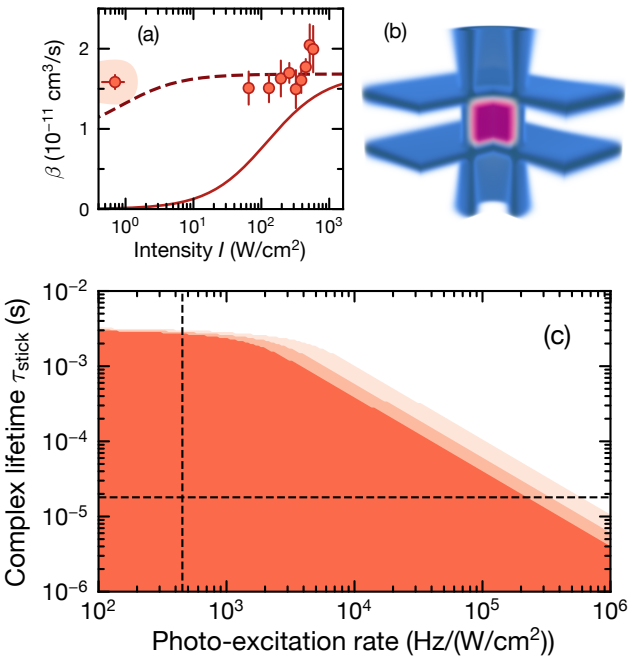

Figure 8.2: Complex loss of ^{23}Na^{40}K in a repulsive box-shaped trap. (a) Two-body loss coefficient β versus 1064-nm-light intensity. The solid line indicates the predictions from Ref. [10], the dashed line is calculated for the shortest complex lifetime which is consistent with the experimental data within 3σ. (b) Sketch of the box trap used to confine molecules at low light intensity. The molecule cloud is shown in purple. One quadrant is cut out for visibility. (c) Parameter space excluded by the data under the assumption that complexes can only be lost by photoexcitation or by leaving the trap. The three shaded areas are excluded with 1σ, 2σ, and 3σ confidence, respectively. The dashed lines indicate the predictions from Ref. [10].

showed that the photo-induced loss mechanism competes with the reaction to the homonuclear molecules. In fact, they observe that the number of formed reaction products, as well as the number of collision complexes, decreases as a function of the trap-laser intensity. The sticking times and photoexcitation rates they measure in their experiments, are shown to be in good agreement with the theoretical predictions.

However, neither of these experiments offer solutions which would allow to trap molecules permanently, which is important for applications. Our MPQ experimental team has realized a way to permanently trap the molecules at low light intensity. Indeed, this is achieved by loading ^{23}Na^{40}K into a repulsive, box-shaped potential with sharp edges and very low residual intensity on its inside [5]. This is illustrated in Fig. 8.2b). Repulsive interactions between the atoms and the light can be realized by blue-detuning the laser from an electronic transition, instead of the red-detuning which is used for standard optical dipole traps. In our work the trapping laser is blue-detuned 300 MHz from a narrow optical transition at 866.1428(3) nm. By working at small detuning from the transition, the polarizability is large, and the required laser intensity to realize a certain trap depth is reduced. Furthermore, masks in the beam path are employed to minimize the laser power that the molecules experience in the center. Small electric fields gradients are applied to levitate the molecules. In total, the average laser power the molecules experience in the center of the trap is given by 0.7 W/cm^2. This is a factor 6000 lower than the laser intensity in the trapping region of typical red-detuned optical dipole traps and according

to theoretical predictions [11] this should be more than enough to very strongly suppress the photo-induced loss.

Surprisingly, we do not detect any suppression of the loss. We consider the box trap, to which we add an additional kill beam just as in the chopped trap experiments. The observed loss rate as a function of the kill-beam intensity is shown in Fig. 8.2a). From this graph it is clear that there is no dependence of the loss on the kill-beam intensity.

If we assume that the loss is still determined by laser excitation, we can put joint bounds on the sticking time and the photo-excitation rate. Either the sticking time needs to be much longer than predicted, or the photo-excitation rate needs to be much larger. The bounds we can extract from experiment are given in Fig. 8.2c). Here the red regions indicate the parameter regimes which can be excluded. The theoretically predicted parameters are indicated by the dashed lines. We see that the experimental results exclude a region of parameters more than two orders of magnitude around the theoretically predicted results. This shows very clearly that the current theory predictions are inconsistent with the experimental results. Furthermore, if we assume that the theoretical photo-excitation rate is roughly correct, the sticking time of milliseconds should be long enough for other mechanisms to become relevant. For example, on such timescales the complexes can no longer be assumed to be trapped by the optical dipole trap, and they might thus simply leave the trap.

We perform a number of further experiments to exclude potential explanations. To avoid enhanced sticking times due to electric fields, we repeat the experiment with the levitation electric field turned off. Again, the loss shows no dependence on the laser intensity. To test whether s-wave or p-wave collisions lead to different outcomes, we also repeat the experiment with an incoherent hyperfine mixture of the molecules. Also in this case, the loss is independent of the kill beam intensity. Finally, to exclude problems with the blue-detuned optical dipole trap, we perform experiments in a chopped dipole trap. No dependence on the kill beam intensity was found here either.

At the same time as our experiments, chopped-trap experiments were performed on bosonic ^{23}Na^{40}K and ^{23}Na^{87}Rb [235]. They did not find any suppression of the loss in absence of the trapping laser either, and their experiments also violate the theoretical predictions by two orders of magnitude. See Ref. [7] for a comprehensive overview of all the experimental results.

8.4 Testing the theoretical assumptions

We have now arrived at a major puzzle. How can it be that some bialkali species behave according to the theoretical predictions, whereas others behave totally differently? We will revisit the assumptions in the theoretical models and discuss their (in)validity.

8.4.1 The validity of RRKM theory

The assumption of chaoticity

First we discuss the validity of the assumption of chaotic dynamics, which is central in RRKM theory and which underlies Eq. (8.1). Hamiltonians which exhibit quantum chaos have a special structure in their spectrum, where the energy level spacings are distributed according to a Wigner–Dyson distribution, as opposed to a regular Poisson distribution. Also the distribution of resonance widths in case of quantum chaos is known. It was shown in explicit quantum scattering calculations by Croft *et al.* [240, 241] that such distributions according to quantum chaos are recovered relatively well for ultracold atom-diatom

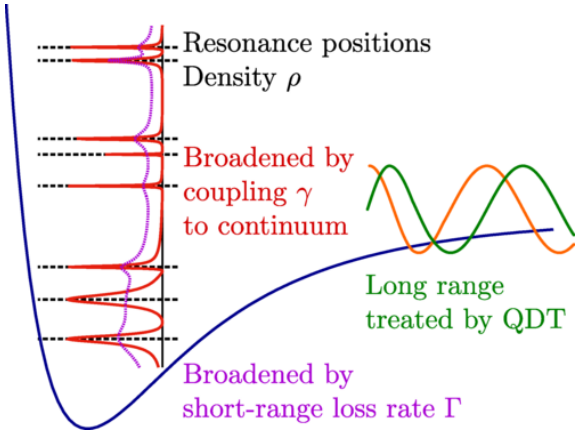

Figure 8.3: The short-range physics is dominated by a set of classically chaotic resonance states, with density ρ, described statistically. The short-range states are broadened by coupling with strength γ to the continuum, which is described by quantum defect theory. Furthermore, the short-range states undergo losses described by a decay rate Γ, which leads to further intrinsic broadening.

collisions of alkali atoms. Furthermore, in recent work by Man *et al.* [251], the statistical assumption for atom-diatom and diatom-diatom collisions was tested with classical trajectory simulations, and found to be valid. Hence, the assumption of chaotic dynamics is be well-justified.

How predictive is the statistical model?

Next, we discuss whether one indeed averages over many scattering resonances under experimental conditions, as required to get reliable predictions from the statistical model. As indicated in Fig. 8.1, the range of probed collision energies is set by the temperature, whereas the spacing of the resonances is set by the density of states ρ. The typical temperature is on the order of a microkelvin, and the density of states ranges from 0.005 to 5 $\mu\mathrm{K}^{-1}$ for different bialkalis, see Table 8.1. Comparing these numbers, one may notice that only very few, if any, resonances are expected to be probed under experimental conditions. The original idea [54] that many isolated narrow resonances would be included in the experimental window of collision energies, is therefore clearly not true. The applicability of the statistical model thus seems questionable.

The natural question then arises: if only a single or a few resonances are included in a typical experimental window of collision energies, then why are these not resolved? The key insight here is that the width of the resonances is set by the lifetime of the formed complexes. Indeed, if the complex lifetime is according to the RRKM prediction, then the spacing between the resonances is larger than their width. However, in presence of loss, the lifetime is much shorter, and as a result, the resonances become broader! This is illustrated in Fig. 8.3. If the loss is sufficiently strong, the resonances will become overlapping, and the loss rate should not be strongly dependent on the collision energy any more, as observed experimentally.

We can introduce the loss processes in the QDT description as follows [6]. We can take the K_{SR} matrix of Eq. (8.16) as a starting point, but give every resonance an additional

decay width Γ_ν due to the loss. This gives us

$$K_{SR} = -\sum_\nu \frac{\gamma_\nu/2}{E - E_\nu + i\Gamma_\nu/2}. \tag{8.20}$$

Indeed, if the mean decay width $\bar{\Gamma}$ is much larger than the spacing between the resonances ρ^{-1}, then one averages over many broadened resonances at every single collision energy, instead of averaging over many isolated resonances in a range of collision energies.

This model is also more consistent than Eq. (8.16), because the actual loss is included, allowing one to compute loss cross sections instead of just elastic cross sections. If we consider now the loss by averaging over an isolated representative resonance, we find

$$1 - |S|^2 = C^{-2}\frac{\bar{\Gamma}}{\bar{\gamma}C^{-2} + \bar{\Gamma}}. \tag{8.21}$$

Interestingly if the loss is fast compared to the sticking time, i.e. $\bar{\Gamma} \gg \bar{\gamma}C^{-2}$, we find that the rate of loss is the same as the rate of elastic collisions found by the Mayle-approach, as in Eq. (8.17). If we assume the resonances overlap, we also find a loss rate on the order of universal loss. In this case there are energy-dependent fluctuations because of the inhomogeneity of the resonances: the resonances are not all the same, but are drawn from a statistical distribution.

In conclusion, the statistical model cannot be justified by claiming that many isolated resonances are included in the experimental window of collision energies. However, due to the substantial broadening of the resonances in presence of loss, one will already average over the contributions of multiple resonances even at a single collision energy. As a result, a loss rate on the order of universal loss is recovered, as has been observed in experiments.

Threshold effects

Another point made in Refs. [6, 249] is that RRKM theory does not take into account threshold effects, and it turns out that for fermionic molecules, the p-wave barrier plays a substantial role. We have already discussed in Chapter 2 that fermions need to tunnel through the centrifugal barrier when they are colliding, leading to a reduced collision rate in the low-temperature regime. However, what was not realized before, is that the molecules forming a collision complex also need to tunnel through this barrier again to *leave* the collision complex. If this tunneling probability C^{-2} is therefore low, this can lead to orders of magnitude longer sticking times.

We can see this effect clearly in Eq. (8.21), where C^{-2} shows up in the prefactor and in the denominator. The C^{-2} in the prefactor gives us the effect that a centrifugal barrier at low temperatures suppresses the collision cross section. In the denominator, we see the competition between the $\bar{\gamma}C^{-2}$ term, which sets the complex dissociation rate, and the $\bar{\Gamma}$ term, the loss rate. Important here is the appearance of C^{-2} in the complex dissociation rate, instead of only having $\bar{\gamma}$. As a result, one should not directly compare $\bar{\Gamma}$ to $\bar{\gamma}$, which would correspond to comparing the loss rate to the RRKM lifetime, but to $\bar{\gamma}C^{-2}$, the prolonged lifetime in presence of the "recollisions" following from reflecting off the centrifugal barrier on the way out of the collision complex.

The tunneling probability C^{-2} decreases with lower temperature, making the effect more pronounced for very cold samples. Indeed, if we set $a = \bar{a}$, then for s-wave collisions $C^{-2} = k\bar{a}$, whereas for p-wave collisions $C^{-2} \approx 1.064k^3\bar{a}^3$. For fermionic ^{23}Na^{40}K, in the experimental conditions of Ref. [5], the tunneling probability is only about 1%. Complexes formed in these p-wave collisions should thus live 100 times longer than the RRKM lifetime.

This can explain the sticking-time measurements on identical fermionic NaK molecules shown in Fig. 8.2. For the experiments probing s-wave collisions [5, 235], the factor is of order 1, so threshold effects cannot explain the observations for bosonic or distinguishable molecules.

8.4.2 Coupling to hyperfine degrees of freedom and external electric fields

Even if RRKM theory is valid, there could still be large uncertainties in the calculation of the density of states. In the estimation of the sticking times in Ref. [10] and comparison to photoexcitation rates [9], it is assumed that the motional angular momentum of the molecules is conserved during the collision. However, coupling to external electric fields or to hyperfine states of the molecules can break this angular-momentum conservation, potentially enlarging the explored phase space and the sticking time by up to four orders of magnitude[2]. If the sticking times are really enhanced by this additional factor, the magnetic field could also break the total angular momentum conservation, enlarging the phase space even more.

Using classical trajectory simulations, Man *et al.* [251] estimated that electric fields on the order of 10 V/cm are already sufficient to break angular-momentum conservation. Such electric fields are larger than the stray fields typically present in experiments, but at least one order of magnitude smaller than those needed to polarize the molecules.

For nuclear spins, the strongest effect is the coupling of the dynamically changing electric-field gradient at the nuclear positions to the nuclear quadrupole moments [251, 254]. Using the couplings of the free molecules, Man *et al.* [251] estimated that nuclear-spin flips are unlikely to happen. However, Jachymski *et al.* [254] showed that the couplings are strongly geometry-dependent, and therefore nuclear-spin-changing collisions can currently not be ruled out. If nuclear-spin changes can occur during a collision, this can have the additional effect that molecules entering the collision in excited hyperfine states can leave the collision in a lower hyperfine state, hence increasing N_{out} as well.

Even though nuclear-spin changes could be the cause for the enhanced sticking time, it is very difficult to explain why this enhancement would happen for the light bialkalis NaK and NaRb, but not for the heavier RbCs. One would actually expect the opposite scenario, since both the hyperfine couplings and τ_{RRKM} are smaller for lighter bialkalis. Hence, if nuclear-spin changes in the complex are responsible for longer sticking times, there must be some yet unknown ingredient to bring this explanation into agreement with the experimental observations.

8.4.3 Loss processes

In addition to the sticking time, the complex loss rate is also of crucial importance to assess whether the molecules will survive a collision. As explained in Section 8.2.3, the computation of the photoinduced loss rate, just like RRKM theory, is based on a quasiclassical statistical model. The validity of this model has not yet been explicitly tested theoretically. In a quantum-mechanical picture, in the case of quantum chaos, all eigenstates are delocalized throughout phase space in both the ground and excited state. Therefore,

[2]To get to four orders of magnitude for the electric field case, we assume that the projection of the angular momentum is conserved [10] and that the entire phase space is explored. For the hyperfine case we assume the total angular momentum (including the nuclear spin) during the collision is conserved, but still that the entire accessible phase space is probed. The exact numbers depend on the sizes of the nuclear spins of the atoms. For example, for ^{23}Na^{39}K and ^{23}Na^{87}Rb, the enhancement factor will be $\sim 10^3$, and for ^{23}Na^{40}K, for ^{87}Rb^{133}Cs it will be $\sim 10^4$.

every state has a small but usually nonzero Franck–Condon overlap with all the states in the excited potential. If the width of the electronic transitions is then larger than the rovibrational spacing, this means that there are no photoexcitation resonances and that the complex can be excited by a continuum of laser frequencies. Since the linewidth of the typical trapping lasers is very small, the observed linewidth of the transition is limited by the lifetime of the electronic state.

Let us briefly consider the loss pathways from this electronically excited state. The simplest possibility is spontaneous emission back to some rovibrational level in the electronic ground state. Because this would be similar to an electronic transition of one of the constituent diatoms, the rate of such a process can be assumed to be on the order of 10 MHz [255]. Other processes include dissociation into a trimer and a free atom, or into a singlet and a triplet dimer via spin-orbit coupling. How fast these processes are depends on the details of the interaction potential, and the specific state where the complex ends up after photoexcitation. A more detailed theoretical investigation of the complex dynamics in the excited state would definitely be interesting. This could be experimentally relevant, to know in which scenarios one would expect to find resolved photoexcitation lines as opposed to a continuum. For most diatom-diatom collisions, spontaneous emission would already be fast enough to lead to a continuum of excited states, but for atom-diatom collisions individual lines would be observable if this was the only or the fastest decay process.

One can also imagine loss processes other than photoexcitation playing a role. The original proposal was that this could be three-body loss [54], but in Ref. [10] the three-body rate was estimated to be too small. Furthermore, the complexes might escape from optical dipole traps as they are not trapped by the trapping laser. This is especially likely for repulsive traps such as the one used in Ref. [5]. For this process to be relevant, the sticking time typically needs to be on the scale of milliseconds. Estimation of rovibrational transition rates of non-excited complexes due to spontaneous emission and black-body coupling are given in Ref. [251]. Both processes are far too slow to occur in the τ_{RKKM} timescale and require sticking times of approximately tens of seconds.

Another potential explanation for the loss is the presence of special features in the potentials such as conical intersections. Conical intersections are known to occur and have an influence on the collision dynamics for alkali atom-diatom collisions [256]. We do not expect that such features destroy the validity of RRKM models, but they might enhance the probability of nuclear-spin flips or lead to the population of electronically excited states. In Ref. [11] it was estimated that for NaK-NaK there are conical intersections close to, but still outside, the classically-allowed region. However, this might need to be revisited with more accurate methods to give a clearer judgment. Then one would need to find and characterize the loss processes that could happen around such a conical intersection. What makes this explanation attractive is that the presence of a conical intersection could strongly depend on the species, and therefore explain the seemingly arbitrary differences between the bialkalis.

8.5 Conclusion and outlook

Molecular collisions at ultracold temperatures give rise to remarkable chemical effects, such as long-lived collision complexes and tunable reaction rates, but for quantum-science applications it would be better eliminate these chemical processes so that the ultracold molecules are actually stable.

In presence of laser light, photoinduced loss is probably the dominant loss mechanism of ultracold molecules. However, we have shown with the box-trap experiments [5] that our

understanding of the sticky collisions is far from complete. Theoretically, we have resolved inconsistencies in the statistical approach to compute the collisional loss rates and we have found that threshold effects can strongly enhance the collisional sticking times [6]. These effects are insufficient, though, to explain all the experimental results for the lighter bialkalis in the dark.

The most important open question from the theory side is how the nuclear-spin degrees of freedom are involved in the collision. Experiments with RbCs in other hyperfine states have shown that the hyperfine state can make a difference [252], so the possibility of nuclear spin changes should definitely be further explored.

Alternatively, it is possible that the experimental results can be explained by a combination of threshold effects and external electric fields. Specifically, for the case of the hyperfine-pure samples of fermionic ^{23}Na^{40}K, the p-wave barrier might be the cause of the much longer sticking times. If the electric fields in the experiments with (bosonic) ^{23}Na^{39}K and ^{23}Na^{87}Rb were large enough to break angular-momentum conservation, this problem would be solved as well. To confirm this hypothesis, the sticking time should be measured as a function of electric field strength.

Further experimental and theoretical work is going to be needed to find an explanation for the sticky-collision mystery. From the experimental side, it will be necessary to gather data from more species and under a wider range of conditions. Second, valuable information can be gained from atom-molecule collisions, where also surprising results have been obtained (see for example Refs. [250, 257–259]). Theoretically, aside from a more detailed study of hyperfine changing processes, it would be interesting to develop a more complete description of the photoexcitation process.

In the meantime mechanisms were proposed to avoid this loss, by preventing short-range collisions in the first place. All of these mechanisms involve the dipolar interactions between the molecules, which are manipulated to give rise to a long-range repulsive potential barrier. This can be done by confining the molecules to two dimensions in presence of strong electric fields [260], so that molecules only have side-to-side collisions in a repulsive geometry. Alternatively, an energy barrier can be engineered by creating an avoided crossing between rotationally excited states using strong electric fields [261] or microwave dressing [262–264]. These methods have proven to be promising, and many exciting results on ultracold molecules can therefore be expected in the near future.

Part D. Quantum Computing

Abstract

Simulating the full dynamics of complex quantum systems in a scalable way, is generally impossible on classical computers. There is rapid progress in the development of quantum computers, but the current devices are plagued by decoherence and noise, limiting the number of qubits and the circuit depths for which reliable computations are possible. One of the key problems where quantum computers are desired, is the prediction of phase diagrams and thermal properties of strongly correlated materials.

In this Chapter we propose a protocol to study thermalization on near-term digital quantum devices. The two key problems to address are the imperfect implementation of the time-evolution operator in terms of digital gates, and the noise. We show that the trotterization of the time-evolution can be understood as a periodic driving. At long times this generally leads to heating to an infinite temperature state, but if the Trotter step is sufficiently small, there is an intermediate regime where the initial state prethermalizes. In the prethermal plateau, expectation values of operators can be extracted which approximate the thermal observables of the underlying Hamiltonian. Importantly, this regime is already reached even for a relatively coarse Trotter decomposition, making it accessible for modest circuit depths. To reach the prethermal plateaus in presence of noise, we develop an error-mitigation scheme based on measurement and rescaling of survival probabilities, which is applicable to time-evolution problems in general. We demonstrate the effectiveness of the entire protocol by applying it to the two-dimensional XY model and we numerically verify its performance with realistic noise parameters for superconducting quantum devices. Our proposal thus provides a route to achieving quantum advantage for relevant problems in condensed-matter physics.

Chapter 9. Prethermalization on near-term digital quantum computers

This Chapter is based on the following work
[8] Yilun Yang, Arthur Christianen, Sandra Coll-Vinent, Vadim Smelyanskiy, Mari Carmen Bañuls, Thomas E. O'Brien, Dominik S. Wild, J. Ignacio Cirac,
Simulating Prethermalization Using Near-Term Quantum Computers,
PRX Quantum 4, 030320 (2023)

9.1 Introduction

Simulating quantum systems on classical computers is difficult, as we have already seen in this thesis. Indeed, we have discussed in Chapter 8 that even the seemingly simple scattering problem of two molecules can be too computationally difficult for the current generation of computers. In Part B, where we studied the case of an impurity in a weakly interacting BEC, computational studies were still tractable up to some degree, because the BEC itself was only weakly correlated. If instead a strongly interacting BEC is considered, theoretical approaches become extremely challenging, and it becomes almost impossible to simulate the dynamics beyond short times [96, 98, 99]. Formally, if one wants to exactly simulate the dynamics of a quantum system on a classical computer, the computational cost, both in memory and time, scales exponentially with the system size [56, 265].

A natural solution to this was proposed by Feynman: make a computer which itself is based on the principles of quantum mechanics [55, 56]. Indeed, in recent years the development of such quantum computers has seen tremendous progress, and the first claims of "quantum supremacy" have been made [266–269], where a quantum computer outperforms the best classical computers for a certain task. Even though these claims of supremacy have so far seemingly been debunked [270–273], it seems a matter of time before quantum supremacy is truly within reach.

A natural task one might try to solve with a quantum computer is to discover the phase diagrams of strongly-correlated materials [265, 274]. A possible way to achieve this, is to prepare a relatively simple quantum state, followed by time-evolution under the Hamiltonian of interest. Under some assumptions this leads to thermalization, implying that at long times, equilibrium states are reached which have properties similar to the eigenstates of the Hamiltonian [275–278]. If the initial states then span the spectral width of the Hamiltonian, one can try to extract a phase diagram.

Unfortunately, with current-day (digital) quantum devices, the number of operations that can be carried out before the system decoheres is very limited [58]. Thus, long simulation times are not accessible and it seems out of reach to let systems fully thermalize. A second problem is that the time-evolution operator can usually not exactly be represented on a digital quantum computer. If the Hamiltonian is non-trivial, it will contain multiple non-commuting terms acting on the same qubit, which can not be implemented in the same layer of a digital quantum circuit. Hence, the time-evolution circuit is typically approximated by dividing it into layers that each contain only commuting terms. This

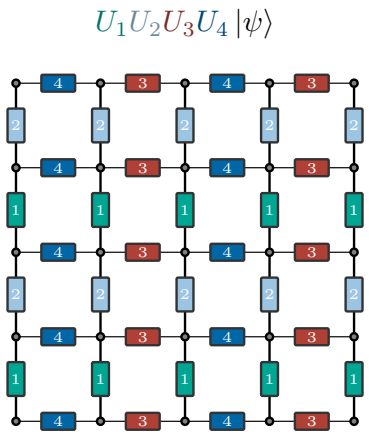

Figure 9.1: Trotterization of a spin model on a square lattice with nearest-neighbor interactions. The circles represent qubits and the rectangles on the links represent unitaries acting on two neighboring qubits. The different colors indicate the layers of the quantum circuit into which the gates are divided.

process is called trotterization, and it is illustrated in Fig. 9.1. Here we show how a spin model on a square lattice with nearest-neighbor interactions can be trotterized. All the gates with the same color can be implemented in the same layer. If the time step goes to zero, trotterization becomes exact, but for a fixed evolution time this then automatically leads to very large circuit depths. Therefore, it is typically not possible to operate in the regime where the Trotter error is guaranteed to be small, while still going to long enough times to see interesting physics.

Nevertheless, we demonstrate in this Chapter that thermalization can already be observed for much larger Trotter steps than needed to guarantee a bounded Trotter error, making it feasible to study this phenomenon on near-term quantum devices. In this regime, the system may be viewed as subject to a periodic Floquet drive [279–281], where one Trotter step corresponds to one period. The fate of Floquet systems at late times has been a subject of recent interest [282–284]. Even though the system generally heats up to infinite temperatures [285, 286], the heating time may be very long if the driving frequency is large compared to all local energy scales [287]. The system then *prethermalizes* [288–296]: before it heats up, its dynamics mirror the equilibration of a closed system. The prethermal regime is relatively easy to access in practice because the Floquet heating time increases exponentially with the driving frequency or, equivalently, the inverse Trotter step size (see Fig. 9.2).

With this in mind, we define the *prethermalized expectation value problem* (PEVP): given a Floquet unitary and a product initial state, what value does a local observable reach in the prethermal plateau? We find that this problem can be solved even in presence of realistic noise. Following a small circuit adjustment, the PEVP turns out to be amenable to a simple but highly effective error-mitigation scheme based on rescaling survival probabilities. Using this strategy, the error-mitigated PEVP reproduces the equilibrium properties of a model that is closely related to the Hamiltonian underlying the Trotterization. More precisely, the prethermal expectation values describe the diagonal ensemble of this model, which is equivalent to the microcanonical ensemble assuming that the eigenstate thermalization hypothesis (ETH) [275–278] is valid. Besides its application to the study of thermalization, the PEVP may be viewed as a problem of independent com-

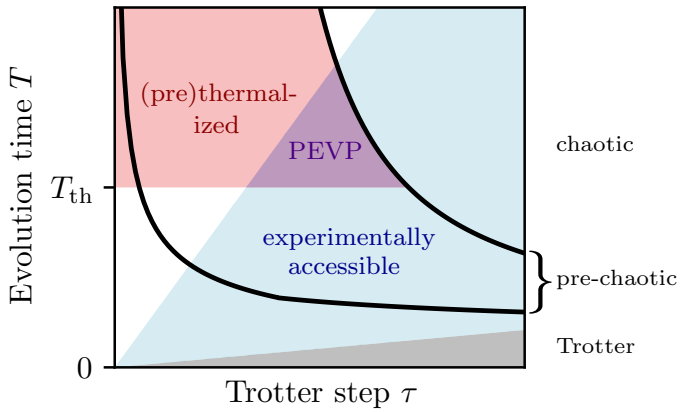

Figure 9.2: Different regimes of the dynamics of local observables depending on the Trotter step τ and the evolution time T. The black lines separate three regimes: bounded Trotter error (bottom), Floquet prethermalization (middle), and chaotic dynamics (top). The lower line scales as $\mathcal{O}\left(\max\left\{\tau^{-p/(d+1)}, N^{-1}\tau^{-p}\right\}\right)$, following error bounds for the p^{th}-order Trotter decomposition with system size N. The upper line is determined by the Floquet heating time and scales as $e^{\mathcal{O}(1/\tau)}$. The blue shaded area indicates constant maximum circuit depth, relevant for noisy quantum computers. The gray area is excluded due to the constraint that $T \geq \tau$. The red shading highlights where the total time T exceeds a system-dependent (pre)thermalization time scale T_{th}. The prethermalized expectation value problem is experimentally accessible in the purple intersection.

putational interest, for which noisy quantum computers can outperform state-of-the-art classical computational methods.

The rest of the Chapter is structured as follows. In Section 9.2, we discuss thermalization in Floquet systems and present simulation results for the two-dimensional XY model as an example. We introduce our error-mitigation strategy based on the rescaling of survival probabilities in Section 9.3, where we also provide a thorough numerical analysis of its performance. Equipped with that, we demonstrate the suitability of the PEVP for near-term devices by simulating it with realistic noise parameters of superconducting quantum computers. We conclude in Section 9.4.

9.2 The prethermalized expectation value problem

9.2.1 Time evolution on digital quantum computers

Let us first formulate more precisely how the time evolution under a Hamiltonian H can be reproduced on a digital quantum computer using the Suzuki–Trotter decomposition. In its simplest, first-order form, the decomposition approximates the time-evolution unitary $\hat{U}(\tau) = e^{-i\hat{H}\tau}$ by

$$\hat{U}_{\text{Trotter}}(\tau) = \prod_{j=1}^{\Gamma} e^{-i\hat{H}_j\tau}, \tag{9.1}$$

where $\hat{H} = \sum_{j=1}^{\Gamma} \hat{H}_j$. Each $\hat{H}_j$ is a sum of mutually commuting local terms, such that $e^{-i\hat{H}_j\tau}$ can be efficiently implemented using local gates. The smaller the Trotter step τ,

the more accurate the Trotter decomposition. For the p-th order Trotter decomposition [297], which generalizes the previous simple formula, the error of $\hat{U}_{\text{Trotter}}(\tau)$ with respect to the desired unitary $\hat{U}(\tau)$ is bounded from above by $\mathcal{O}(N\tau^{p+1})$, where N is the system size [298]. The dependence on N can be eliminated if all quantities of interest are local observables. According to the Lieb–Robinson bound, only a light cone with a radius proportional to the total evolution time T is relevant [299]. Therefore, the system size N can be replaced with the size of the light cone $\sim T^d$ before it reaches the edges of the system, where d is the spatial dimension. We hence require that the Trotter step τ be less than $\mathcal{O}(\max\left\{T^{-(d+1)/p}, (NT)^{-1/p}\right\})$ for the Trotterized time evolution of local observables to converge to the continuous evolution under H.

We can now define the following computational problem.

Problem 1 (The Trotter time-average problem) *Given a unitary $\hat{U}_{\text{Trotter}}(\tau)$, a state $|\psi\rangle$, a local observable $\hat{A}$ and a time $t = m\tau$ for positive integer m, and a small positive constant ϵ, compute the time-averaged observable*

$$\langle \hat{A} \rangle_t = \frac{1}{m+1} \sum_{n=0}^{m} \langle \psi | \hat{U}^\dagger_{\text{Trotter}}(\tau)^n \hat{A} \hat{U}_{\text{Trotter}}(\tau)^n | \psi \rangle \tag{9.2}$$

within additive error $\epsilon \|\hat{A}\|$, where $\|\cdot\|$ is the operator norm.

Note that the Trotterization is not uniquely defined by the Hamiltonian and $\hat{U}_{\text{Trotter}}$ must be specified explicitly. The cost of solving this problem on a classical computer generically scales exponentially with either the number of Trotter steps m or the system size N [1], whereas on a fault-tolerant quantum computer, the effort increases at most polynomially with both. The hardness of the problem is further supported by the fact that it becomes BQP-complete at times $t = \text{poly}(n)$ if the Trotter error is negligible [300]. In Section 9.3, we present evidence that the problem is solvable on noisy quantum computers up to a maximum number of Trotter steps, which is independent of system size. We then show in Section 9.3.3 that noisy quantum devices may reach a classically intractable regime with realistic noise parameters, even when taking into account the overhead of our error-mitigation strategy.

9.2.2 Prethermalization

Problem 1 is not only interesting from the perspective of dynamics but it can also yield insight into equilibrium properties. In condensed matter or statistical physics, one would typically describe a system in equilibrium in terms of its temperature, or in case of the microcanonical ensemble, its internal energy. Under ETH, the microcanonical ensemble at the mean energy of the state $|\psi\rangle$ can be approximated by solving Problem 1.

More precisely, in the limit of continuous time evolution, the long-time average of an observable is described by the diagonal ensemble. For a given initial state $|\psi\rangle$ and an observable $\hat{A}$,

$$\lim_{T\to\infty} \frac{1}{T} \int_0^T \langle \psi(t) | \hat{A} | \psi(t) \rangle \, \mathrm{d}t = \sum_k |\langle k|\psi\rangle|^2 \langle k|\hat{A}|k\rangle , \tag{9.3}$$

[1] For example, a state vector simulation scales linearly in the number of Trotter steps but exponentially with the system size. While a tensor network simulation scales polynomially in system size but exponentially with the number of Trotter steps.

where $\hat{H} = \sum_k E_k |k\rangle \langle k|$ is the spectral decomposition of a non-degenerate Hamiltonian [2]. Assuming ETH, the expectation value $\langle k|\hat{A}|k\rangle$ is a smooth function of the energy E_k up to a small, state-dependent correction [275]. The diagonal ensemble is then equivalent to the microcanonical ensemble at energy $\langle\psi|\hat{H}|\psi\rangle$ provided the energy variance of $|\psi\rangle$ is sufficiently small. For observables that are an average of an extensive number of local terms, e.g., the total magnetization per site, we expect the microcanonical ensemble to vary significantly only on an extensive energy scale. It is thus possible to estimate expectation values in the microcanonical ensemble from the diagonal ensemble of states whose width in energy is subextensive. Product states satisfy this condition as their widths in energy are (under weak assumptions) proportional to $\sqrt{N}$ [301].

The above discussion shows that it is possible to probe the microcanonical ensemble by solving Problem 1 with product initial states at different mean energies. This is, however, challenging with current quantum devices for two reasons. First, the maximum number of Trotter steps T/τ is limited by the maximum circuit depth in the presence of noise, while the total time T required to reach equilibrium may be large. Therefore, noisy quantum devices are usually unable to reach long enough times with bounded Trotter error. Secondly, the finite calibration precision renders it challenging to reach high relative precision in the angle of rotation for gates that are very close to the identity, bounding from below the size of τ.

We will now argue that it is nevertheless possible to study equilibrium phenomena. Using larger, experimentally feasible Trotter steps can be viewed as applying a periodic Floquet drive. The system can be described by the Floquet Hamiltonian $\hat{H}_F$, which is implicitly defined by

$$\hat{U}_{\text{Trotter}}(\tau) = e^{-i\hat{H}_F\tau}. \tag{9.4}$$

The Floquet Hamiltonian is not unique as its eigenvalues are only defined modulo $\omega = 2\pi/\tau$, the effective driving frequency. For large τ, (small ω), i.e., outside the Trotter limit, the Floquet Hamiltonian is highly non-local and will cause a generic initial state to heat up to infinite temperature [285, 286]. Despite this, it is possible to observe (approximate) equilibration if the heating time scale is much greater than the equilibration time scale. This is known as Floquet prethermalization [288, 294, 302].

For local Hamiltonians and local observables, Floquet prethermalization is relatively easy to access because Floquet heating occurs on a time scale $t_F \propto e^{\mathcal{O}(1/kJ\tau)}$, where k is the interaction range and J is the local energy scale, assuming $kJ\tau \lesssim \mathcal{O}(1)$ [289]. We highlight the favorable exponential dependence of t_F on $1/kJ\tau$. Moreover, kJ is independent of the system size N such that slow heating can be accomplished by a constant value of τ.

For times much less than t_F, the system evolves approximately according to an effective Hamiltonian which is close to, but not the same as, the original Hamiltonian H. More precisely, the effective Hamiltonian is local and it is given by the n_0-th order Magnus expansion [303, 304] of the Floquet Hamiltonian, where $n_0 = \mathcal{O}(1/kJ\tau)$ (see Appendix 9.B for details). Observables start to equilibrate under the effective Hamiltonian before eventually heating up. If the equilibration time t_0 is much shorter than t_F, then there exists a prethermal plateau $t_0 \leq t \ll t_F$, during which the expectation value of the observable is approximately constant. We provide a formal definition of a plateau in Appendix 9.A.

In the prethermal plateau, we expect that the expectation values of local observables give a good approximation of their thermal expectation values of the original Hamiltonian. The correction term to the Hamiltonian in case of the truncated Magnus expansion

[2] In the case of degenerate Hamiltonian spectrum, one can still diagonalize the observable projected onto each subspace of Hamiltonian eigenvalue to define the diagonal ensemble as long time average

can be viewed as a local perturbation of strength $\mathcal{O}(kJ\tau)$. Assuming the phase of the system is robust with respect to this perturbation, the difference between the expectation values of local observables at the prethermal plateau and their equilibrium values for the initial Hamiltonian can therefore also be expected to be of order $\mathcal{O}(kJ\tau)$. Even though this deviation might be too large for calculations where high accuracy is required, in many models already qualitative physical understanding is valuable yet unattainable with classical techniques.

The above observations motivate the definition of the PEVP:

Problem 2 (Prethermalized expectation value problem) *Given a unitary $\hat{U}_{\mathrm{Trotter}}(\tau)$, a state $|\psi\rangle$, and a local observable $\hat{A}$, assume that a prethermal plateau exists between times t_1 to t_2, such that $\max_{t\in[t_1,t_2)}\langle\hat{A}\rangle_t - \min_{t\in[t_1,t_2)}\langle\hat{A}\rangle_t \leq \epsilon\|\hat{A}\|$ for some positive constant ϵ. Find the value of $\langle\hat{A}\rangle_t$ to within additive error $2\epsilon\|\hat{A}\|$ for any $t \in [t_1, t_2)$.*

This problem reduces to solving Problem 1 at time $t = t_1$. In the following sections, we show using the example of the two-dimensional XY model that the prethermal plateau is indeed accessible and that the properties of the effective Hamiltonian closely resemble those of the initial Hamiltonian. We further demonstrate that the PEVP can be solved on a noisy quantum device with realistic parameters up to system sizes for which classical simulation of the dynamics is intractable.

9.2.3 PEVP with the XY model

We focus on the two-dimensional quantum XY model on a square lattice for the remainder of this work. We emphasize, however, that the approach can be readily applied to many other models. The Hamiltonian of the XY model is given by

$$\hat{H}_{\mathrm{XY}} = -J\sum_{\langle ij\rangle}\left(\hat{S}_i^x\hat{S}_j^x + \hat{S}_i^y\hat{S}_j^y\right), \tag{9.5}$$

where J is the interaction strenth, S_i^α ($\alpha \in \{x, y, z\}$) are spin-1/2 operators on site i, and the sum runs over all pairs of nearest neighbors. The two-site interaction of the model generates a partial iSWAP gate,

$$e^{-iJ(\hat{S}_i^x\hat{S}_j^x+\hat{S}_i^y\hat{S}_j^y)\tau} = \mathrm{iSWAP}_{ij}^{-J\tau/\pi}, \tag{9.6}$$

which is also called the fSim gate [305]. It can be natively implemented on superconducting qubits with a tunable angle $\theta = J\tau/2$. A single Trotter step in a first-order decomposition consists of applying a partial iSWAP gate to each nearest-neighbor pair of qubits. As non-overlapping gates can be performed in parallel, these operations can be carried out in a circuit whose depth is equal to the number of nearest neighbors (4 in the case of the square lattice).

The XY model in two dimensions can be solved with quantum Monte Carlo algorithms [306, 307] and thus serves as a good benchmark to our method. It is known to undergo the Kosterlitz–Thouless (KT) transition [307, 308] at nonzero temperature. This phase transition can be characterized by the mean-squared in-plane magnetization per site,

$$m_x^2 + m_y^2 = 4\cdot\frac{\left(\sum_i\hat{S}_i^x\right)^2 + \left(\sum_i\hat{S}_i^y\right)^2}{N^2}, \tag{9.7}$$

which is an approximation to the in-plane susceptibility [307]. The mean-squared magnetization can be written as the sum of two-site correlators, which decay exponentially with

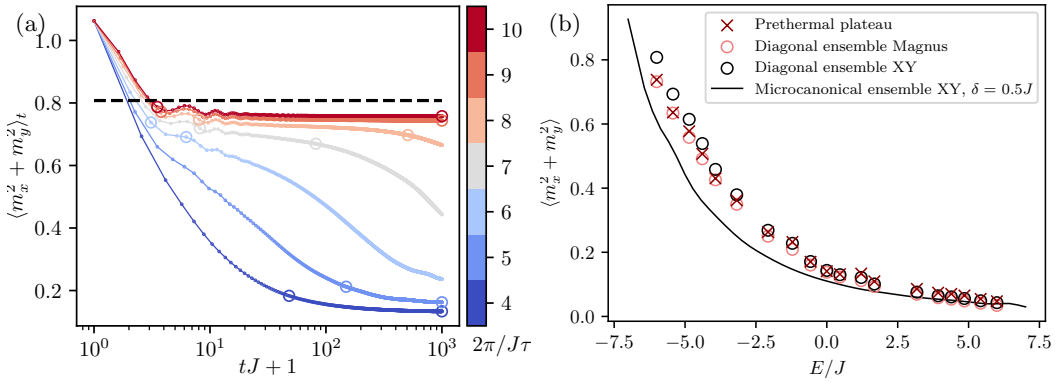

Figure 9.3: (a) Prethermal plateau of the 2D XY model for system size $N = 4 \times 4$. The initial state is $|X+\rangle$. The colored lines show the time averages of the mean-squared in-plane magnetization for different Trotter step sizes τ, corresponding to different driving frequencies $\omega = 2\pi/\tau$, ranging from $4J$ to $10J$. The large circles stand for the starting and end points of the plateaus according to Definition 4 with tolerance $\epsilon = 0.05$ and a maximum value of $t_2 J$ of 10^3. The black dashed line represents the value in the diagonal ensemble of the initial Hamiltonian. (b) Comparison of the value at the prethermal plateau with the values in the microcanonical and diagonal ensemble values of the initial XY Hamiltonian and in the diagonal ensemble of the first-order Magnus expansion. The energy on the x-axis is given by the expectation value of the XY Hamiltonian with regard to initial states. The system size is 4×4. The driving frequency is as $\omega = 8J$ and the plateau value is taken from the time average at $t = 20/J$, which is on the prethermal plateau for all computed initial states with tolerance $\epsilon = 0.05$. For the microcanonical ensemble, we average over an energy window of width $\delta = 0.5J$ in the $m_z = 0$ subspace (see Appendix 9.A).

the distance between the two sites at high temperature. Hence, $m_x^2 + m_y^2$ decreases with the system size as $1/N$ in the thermodynamic limit. Below the critical temperature, the system exhibits quasi long-range order. The mean-squared magnetization decays only as $1/N^{1/8}$ and its value remains non-negligible for moderately large systems [307].

In analogy to the long-time average that gives rise to the diagonal ensemble, we probe the prethermal plateaus using the Floquet time average as in Definition 1, where the Trotterization is shown in Fig. 9.1. We explore this quantity using exact diagonalization on a square lattice with $N = 4 \times 4$ spins and open boundary conditions. Figure 9.3a) shows the values of the mean-squared in-plane magnetization for the initial state $|\psi\rangle = |X+\rangle = \left[\frac{1}{\sqrt{2}}(|0\rangle + |1\rangle)\right]^{\otimes N}$. The different colors indicate the Trotter step size τ or, equivalently, the driving frequency $\omega = 2\pi/\tau$. The initial state is close to the ground state of the XY Hamiltonian. We therefore expect the in-plane magnetization to remain high in the prethermal plateau, provided the effective Hamiltonian does not differ too much from the XY model.

We indeed observe prethermal plateaus for large driving frequencies ($\omega \geq 8J$, or $\tau \leq \pi/4J$), and these last for $t > 10^3/J$ when $\omega \geq 9J$. The plateau values approach the diagonal ensemble value (black dashed line) with increasing driving frequencies. They deviate only slightly due to the correction in the Magnus expansion, which will be discussed later in this subsection. This confirms that the dynamics with fast Floquet drive are similar to the dynamics of the original Hamiltonian in this prethermal regime. By contrast, no plateaus are observed at low driving frequencies, where the time average of the mean-squared magnetization quickly drops to expected value at infinite temperature, $2/N$. We

note that the expectation value of the initial Hamiltonian exhibits a similar behavior as shown in Fig. 9.B.1b) in the appendix. This further confirms that the Floquet heating happens only on a time scale t_F that is exponential in $1/\tau$. Moreover, the change of energy with regard to initial Hamiltonian at early times is small such that its use for the horizontal axis in Fig. 9.3b) is justified. Concretely, the energy of the $|X+\rangle$ state (leftmost point in Fig. 9.3b)) changes by approximately $0.5J$ for $\tau = \pi/4J$ ($\omega = 8J$).

We may perform the same analysis for different initial states. We choose product states in which the spins on the two sublattices of the square lattice are in the respective states $|\theta, 0\rangle$ and $|\pi - \theta, \phi\rangle$, where $|\theta, \phi\rangle = \cos(\theta/2)\,|0\rangle + \sin(\theta/2)e^{i\phi}\,|1\rangle$ parameterizes an arbitrary state of a qubit (spin-1/2). This choice of states allows us to cover a wide range of the spectrum while ensuring that the total magnetization in the z-direction vanishes. The latter constraint is convenient because the XY Hamiltonian conserves the total z-magnetization, $m_z = \sum_{i=1}^{N} \sigma_i^z/N$. This is still true after Trotterization, since we only apply (partial) iSWAP operators [3]. Thermalization therefore occurs in the eigenspaces of m_z. Low-energy product states however are not eigenstates of m_z. By choosing the expectation value of m_z to be zero, we maximize the overlap of the product state with the sectors of low z-magnetization, for which we expect similar equilibration dynamics.

We find that all product states of the above form exhibit prethermal plateaus at similar driving frequencies and evolution times. We evaluate the prethermal values of the in-plane magnetization by performing the Floquet time average up to time $t = 20/J$ with driving frequency $\omega = 8J$. The result is shown for various initial states as a function of their mean energy in Fig. 9.3b). For comparison, we also show the diagonal and microcanonical ensemble values of the initial XY model, as well as the diagonal ensemble one of the first-order Magnus expansion of Floquet Hamiltonian, given by

$$\begin{aligned}\hat{H}^{(1)}_{\text{Magnus}} =& \frac{1}{\tau}\int_0^\tau \mathrm{d}t_1 \hat{H}(t_1) \\ &+ \frac{1}{2i\tau}\int_0^\tau \mathrm{d}t_1 \int_0^{t_1} \mathrm{d}t_2 \left[\hat{H}(t_1), \hat{H}(t_2)\right].\end{aligned} \tag{9.8}$$

Here, $H(t)$ is the piecewise constant Hamiltonian corresponding to the different terms of the Trotter expansion Eq. (9.1):

$$\hat{H}(t) = \Gamma \hat{H}_j \text{ for } (j-1)\tau/\Gamma \leq t < j\tau/\Gamma, \tag{9.9}$$

where $1 \leq j \leq \Gamma$. Definitions of the different ensembles and higher orders of the Magnus expansion can be found in Appendix 9.A and Appendix 9.B, respectively.

The values at the prethermal plateau are close to those of the diagonal ensemble $H^{(1)}_{\text{Magnus}}$, indicating that the first-order truncation already serves as a good approximation for Floquet Hamiltonian in the prethermal regime. In Appendix 9.B, we show that the higher orders lead to no significant improvement for $\omega = 8J$. The thermal equilibrium values of the initial XY Hamiltonian, in both the diagonal and the microcanonical ensemble, deviate slightly from the Floquet values. We attribute the deviation to the perturbation from the Magnus expansion as well as to finite-size effects. The latter are evident from the fact that the diagonal ensemble of the XY model differs significantly from the microcanonical ensemble even though they are expected to agree in the thermodynamic limit. The reason for this is that a product initial state $|\psi\rangle$ spans a range of energies

[3] In principle the Trotterization may break symmetries of the initial Hamiltonian and this can have an important effect on the thermalization. In our case the z-magnetization is conserved, but the translational symmetry on the lattice is partially broken by the Trotterization, which results in larger unit cells. For our small system with open boundary conditions we do not expect this to have a large effect.

of width $\sigma_\psi = \mathcal{O}(\sqrt{N})$. In the thermodynamic limit σ_ψ represents a vanishingly small fraction of the entire spectrum, which is of width $\mathcal{O}(N)$. For our system sizes, however, the energy spread σ_ψ is not negligible. Nevertheless, the comparison indicates that the prethermal properties of the Floquet system reveals nontrivial thermal properties of the XY Hamiltonian.

9.3 Error mitigation

9.3.1 Rescaling of survival probabilities

Without mitigation, noise will frustrate any naive attempts to observe prethermal plateaus on current quantum hardware. Noise provides an additional heating source to the Floquet driving already discussed; one that we expect to be far stronger with today's error rates, and one without favorable scaling in the system size. It is therefore desirable to develop an error-mitigation technique to estimate the result of a noiseless quantum circuit from multiple measurements in a noisy circuit [309–311]. However, we do not see a reliable method for extracting the desired noiseless results from measurements of the noisy state as this would imply the ability of inferring low-temperature results from high-temperature ones.

To circumvent this issue, we avoid direct tomography of the time-evolved observables on the noisy state. Instead, we convert observable estimation into a survival probability circuit, in a manner similar to that used in out-of-time-order correlators (OTOC) [312] or echo verification circuits [313, 314]. After forward evolution, we *apply* the observable and then evolve backwards in time, followed by a projection onto the initial state (see Fig. 9.4a)). This yields a survival probability of the form

$$L_{A,\psi}(t) = \left|\langle\psi|e^{i\hat{H}t}\hat{A}e^{-i\hat{H}t}|\psi\rangle\right|^2 = \langle\psi|\hat{A}(t)|\psi\rangle^2 . \tag{9.10}$$

In the following, we drop the label ψ for notational simplicity. For this procedure to work, A must be a (local) unitary. For spin systems, it is possible to write any observable as a sum of products of unitary Pauli operators and to measure each Pauli operator separately. Although $L_A(t)$ only gives the expectation value of an observable up to a sign, one can infer the sign by tracking it from the known initial value, assuming $\langle\psi|\hat{A}(t)|\psi\rangle$ is a smooth function [315]. This simplifies previous Loschmidt-echo style methods for learning $\langle\psi|\hat{A}(t)|\psi\rangle$, which require ancilla qubits, the preparation of large Greenberger-Horne-Zeilinger (GHZ) states [313] or intermediate re-preparation and measurement of qubits [314].

As we will now demonstrate, a simple rescaling is remarkably effective at mitigating errors in the estimation of the survival probability. The strategy is based on the observation that the survival probability is approximately proportional to the probability of no error occurring. The reason is that the state becomes highly entangled during the evolution, at which point a single-qubit error results in an orthogonal state with high probability. To be more concrete, consider a single Pauli error σ_i^μ occurring at time $t' < t$ at site i and set the observable A to be identity. The survival probability is then given by $[\mathrm{Tr}\ (\rho_i(t')\sigma_i^\mu)]^2$, where $\rho_i(t')$ is the reduced density matrix of $|\psi(t')\rangle$ at site i. If this site is entangled with the other parts of the system, the reduced density matrix will be close to the identity (completely mixed) and the survival probability will be close to zero.

The above discussion suggests that the survival probability with noise is related to the noiseless value, times the probability that no error has occurred. For concreteness, we consider error models in which a single-qubit noise channel $\mathcal{N}_p$ is applied to each qubit after every layer of unitary gates. Here, p is the probability that the channel causes an error on

the qubit. The state-of-the-art gate error rate is around 0.5% for two-qubit gates [316, 317], motivating our choice of $p = 0.3\%$ per qubit per gate as the reference value in our model [4].

Denoting the survival probability in the presence of noise by $L_A^{\mathcal{N}_p}(t)$, we expect that

$$L_A^{\mathcal{N}_p}(t)/L_A(t) \approx (1-p)^{ND}, \tag{9.11}$$

where N is the number of qubits and D is the circuit depth including both forward and backward evolutions. Crucially, no independent knowledge of the noise channel is required to estimate $L_A(t)$. By setting $A = \mathbb{1}$, we obtain $L_{\mathbb{1}}^{\mathcal{N}_p}(t) \approx (1-p)^{ND}$ since the noiseless survival probability satisfies $L_{\mathbb{1}}(t) = 1$. Hence,

$$L_A(t) \approx L_A^{\mathcal{N}_p}(t)/L_{\mathbb{1}}^{\mathcal{N}_p}(t), \tag{9.12}$$

where the right-hand side can be obtained from measurements on the noisy quantum device.

We can make this argument more rigorous for channels that can be represented in terms of unitary Kraus operators. For such channels, the probability that a particular error occurs is independent of the state. This class of channels includes depolarizing and dephasing noise as well as all other Pauli channels. Even though amplitude damping error is not included in this class of channels, we find that the conclusions of this section nevertheless hold to a good approximation for this noise model as well (see Appendix 9.C). Furthermore, it is always possible to turn the Kraus operators into unitary ones by means of Pauli twirling [318–321].

The survival probability after the noisy circuit can be expressed as

$$L_A^{\mathcal{N}_p}(t) = \mathrm{Tr}\ \left[\left(\hat{A}\rho_\psi^{\mathcal{N}_p}(t)\right)^2\right], \tag{9.13}$$

where $\rho_\psi^{\mathcal{N}_p}(t)$ is the mixed state after the noisy forward evolution [5]. We write the state $\rho_\psi^{\mathcal{N}_p}(t)$ as

$$\rho_\psi^{\mathcal{N}_p}(t) = q\,|\psi_t\rangle\langle\psi_t| + (1-q)\tilde{\rho}, \tag{9.14}$$

where $|\psi_t\rangle = U_{\mathrm{Trotter}}^{t/\tau}(\tau)\,|\psi\rangle$ is the state after noiseless forward evolution and $q = (1-p)^{ND/2}$ is the probability that no error occurred during the forward evolution. The density matrix $\tilde{\rho}$ is the state conditioned on at least one error having occurred. The survival probability in noisy simulation then becomes

$$\begin{aligned} L_A^{\mathcal{N}_p}(t) =& q^2|\langle\psi_t|\hat{A}|\psi_t\rangle|^2 + (1-q)^2\mathrm{Tr}\ \left[(\tilde{\rho}\hat{A})^2\right] \\ &+ 2q(1-q)\langle\psi_t|\hat{A}\tilde{\rho}\hat{A}|\psi_t\rangle\,. \end{aligned} \tag{9.15}$$

The trace of the product of two matrices $\mathrm{Tr}\ \left(A^\dagger B\right)$ can be viewed as an inner product, and thus the Cauchy-Schwarz inequality applies:

$$\left|\mathrm{Tr}\ \left(A^\dagger B\right)\right| \leq \sqrt{\mathrm{Tr}\ (A^\dagger A)\cdot \mathrm{Tr}\ (B^\dagger B)}. \tag{9.16}$$

[4] In experiments, XY rotations are sometimes compiled into more than one two-qubit gate. The value of p should then be increased accordingly.

[5] To obtain this equation, the circuit in Fig. 9.4a) has to be slightly modified: during backward evolution, the error gates occur before each evolution unitary gate instead of after it.

Defining $r = \sqrt{\text{Tr } [\tilde{\rho}^2]}$, and using that $\hat{A}$ is hermitian and unitary so that $\hat{A}^2 = \mathbb{1}$, the first perturbation term in Eq. (9.15) can be bounded by

$$\left|\text{Tr } \left[(\tilde{\rho}\hat{A})^2\right]\right| \leq \sqrt{\text{Tr } \left[(\hat{A}\tilde{\rho}\hat{A})^2\right] \cdot \text{Tr } [\tilde{\rho}^2]} = r^2. \tag{9.17}$$

Similarly, for the other term,

$$|\langle\psi_t|\hat{A}\tilde{\rho}\hat{A}|\psi_t\rangle| = \left|\text{Tr } \left(\hat{A}\tilde{\rho}\hat{A}\,|\psi_t\rangle\langle\psi_t|\right)\right| \leq \sqrt{\text{Tr } \left[(\hat{A}\tilde{\rho}\hat{A})^2\right]} = r. \tag{9.18}$$

Combining these inequalities, we get

$$\left|\frac{L_A^{\mathcal{N}_p}(t)}{q^2} - L_A(t)\right| \leq (1-q)^2\left(\frac{r}{q}\right)^2 + 2(1-q)\frac{r}{q}. \tag{9.19}$$

Since $0 < q, r \leq 1$, $L_A^{\mathcal{N}_p}(t)/q^2$ serves as a good approximation of $L_A(t)$ when $q \gg r$. This condition can be satisfied over a broad range of parameters because r typically decays with the system size. In the most extreme case of global depolarizing noise, $\tilde{\rho}$ is a completely mixed state, for which $r^2 = 2^{-N}$. The condition $q \gg r$ then gives rise to

$$(1-p)^{ND} > \frac{C}{2^N} \Rightarrow ND < \frac{N\log 2 - \log C}{\log[1/(1-p)]} \tag{9.20}$$

for some constant C. For $p = 0.3\%$, this evaluates to $D < 230$ in the thermodynamic limit. For more general types of noise, we similarly expect the scaling with q^2 to hold up to some constant circuit depth in the thermodynamic limit. The noisy survival probability at this constant circuit depth will, however, decay exponentially when increasing the system size such that exponentially many measurements are required to resolve the signal. Nevertheless, we will show below that the number of measurements remains experimentally feasible in superconducting quantum devices for moderately sized systems with realistic error rates.

Two situations where Eq. (9.12) fails directly follow from our argument. One is the case when q approaches r, as already discussed. The other is when the initial state does not thermalize. For example, the product state $|Z+\rangle = |0\rangle^{\otimes N}$ is invariant under the (Floquet) XY Hamiltonian and thus will not get entangled. However, even in this case Eq. (9.12) works well for many practical channels because two independent errors are unlikely to cancel each other.

9.3.2 Numerical results

We now numerically verify these considerations for the Floquet evolution of the XY model described in Sec. 9.2.3 in the presence of local depolarizing noise. For each qubit, the noise channel is given by

$$\mathcal{N}_p(\rho) = (1-p)\rho + \sum_{\mu=1}^{3}\frac{p}{3}\hat{\sigma}^\mu\rho\hat{\sigma}^\mu. \tag{9.21}$$

Other types of noise are discussed in the Appendix 9.C. In Fig. 9.4b) and c), we respectively show $L_{\mathbb{1}}^{\mathcal{N}_p}(t)$ and $L_A^{\mathcal{N}_p}(t)$ for the initial state $|\psi\rangle = |X+\rangle$ for different system sizes. The computations were performed using the Monte Carlo wave function method with the Cirq library [322]. Each data point in the figure corresponds to an average over 2000 quantum trajectories. This number of trajectories is sufficient to observe convergence of the mean

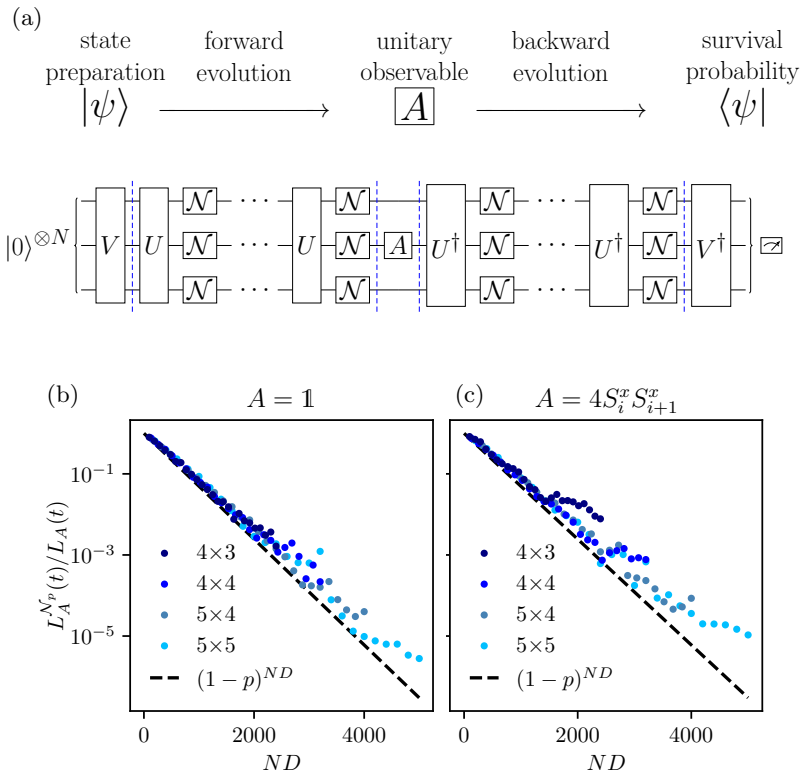

Figure 9.4: (a) Quantum circuit to map the expectation value of a (unitary) observable onto a survival probability. The initial state is prepared with V, $U = U_1, U_2, U_3$ or U_4 is a single step in the Trotter decomposition, and $\mathcal{N}$ denotes a local noise channel. (b), (c) Dependence of $L_{\mathbb{1}}^{\mathcal{N}_p}(t)$ and $L_A^{\mathcal{N}_p}(t)$ on the circuit depth D and system size N in the presence of depolarizing noise with error probability $p = 0.3\%$. The initial state is $|\psi\rangle = |X+\rangle$. The observable $A = 4S_i^x S_{i+1}^x$ is a correlator in the center of the lattice. The black dashed lines represent the scaling predicted by Eq. (9.11).

value in the region of our interest. The results agree well with Eq. (9.11). This also holds for different types of noise as we show in Appendix 9.C. We note that the data points start to deviate from the estimated black dashed lines at ND approximately linear in N, in line with the expectation from Eq. (9.20).

To quantify the error of the mitigation strategy, we define

$$s_A^{\mathcal{N}_p}(t) = L_A^{\mathcal{N}_p}(t)/L_{\mathbb{1}}^{\mathcal{N}_p}(t) - L_A(t). \tag{9.22}$$

Figure 9.5a shows the distribution of s of the mitigated data from Fig. 9.4. The error remains small for depths up to $D \approx 100$. To compare different noise rates, we plot in Fig. 9.5b) the square root of the moving average of s^2 for different values of p. Similar plots for types of noise other than depolarizing noise are presented in Appendix 9.C. For reference, the typical value of $L_A(t)$ in the simulation is around 0.3, which indicates that for circuit depth $D = 80$, the relative error is around 10% for $p = 0.3\%$.

Although these results confirm the effectiveness of our error-mitigation strategy, we also observe a systematic shift of s towards positive values. This can be explained by the error terms in Eq. (9.15). Let us assume for simplicity that $\tilde{\rho} = \mathbb{1}/2^N$. It then follows that

$$\frac{L_A^{\mathcal{N}_p}(t)}{L_{\mathbb{1}}^{\mathcal{N}_p}(t)} = \frac{q^2 L_A(t) + (1-q^2)/2^N}{q^2 + (1-q^2)/2^N}, \tag{9.23}$$

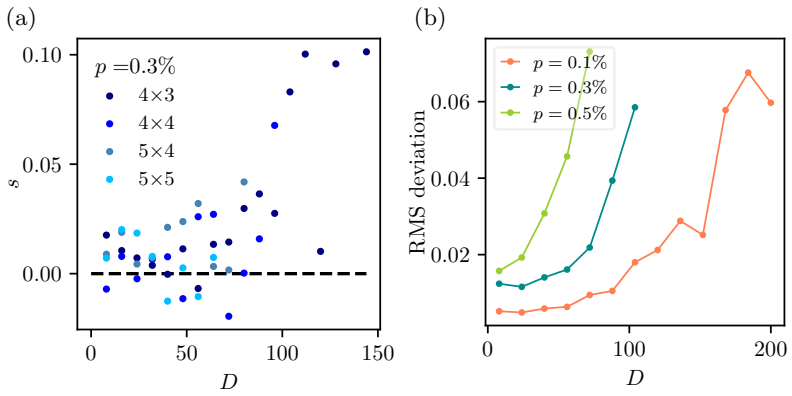

Figure 9.5: (a) The mitigation error $s_A^{\mathcal{N}_p}$ for the range of data in Fig. 9.4 where $L_{\mathbb{1}}^{\mathcal{N}_p}(t) > 0.01$. We choose this cutoff due to the limited number of trajectories in the simulation, which limits the significant digits. (b) The root-mean-square of s, $\sqrt{\sum_{\text{data}} s^2 / \sum_{\text{data}}}$, evaluated over the window of circuit depth $[D-16, D+16]$ in (a).

where we used the fact that $A^2 = \mathbb{1}$ since A is hermitian and unitary. Hence,

$$s_A^{\mathcal{N}_p}(t) = [1 - L_A(t)] \frac{(1-q^2)}{q^2 \cdot 2^N + (1-q^2)} > 0. \tag{9.24}$$

For certain error models, it may be possible to remove this systematic error by using a more complicated rescaling formula instead of (9.12). Nevertheless, the systematic error remains small as long as $q^2 \gg \text{Tr}\,(\tilde{\rho}^2)$.

We will now argue that our mitigation strategy enables the observation of prethermalization on current and near-term quantum devices. After Trotterization, the total required circuit depth D to simulate time evolution of the two-dimensional XY model up to time $t_{\max}$ is

$$D = 4 \cdot 2 \cdot t_{\max}/\tau, \tag{9.25}$$

which, from left to right, represents the number of layers per Trotter step, back and forward evolution, and the number of Trotter steps. To see prethermalization of the Floquet XY model, Fig. 9.3 indicates that $t_{\max}$ should be at least $8/J$ for $\omega = 8J$, which yields $D \approx 80$. The estimation is within the limit of the maximum circuit depth from Eq. (9.20) and Fig. 9.5 for $p = 0.3\%$, showing that our proposal is suitable for current and near-term quantum devices.

We have now gathered all the ingredients for the full simulation of the PEVP on a noisy quantum device. We consider the two-dimensional XY model on a 4×4 square lattice in the presence of depolarizing noise with noise rate $p = 0.3\%$. For the observable, we focus on the correlator $\hat{A} = 4\hat{S}_i^x \hat{S}_{i+1}^x$ of a pair of neighboring sites at the center of the lattice. In Fig. 9.6, we plot the time averages of $\langle \hat{A}(t) \rangle^2$ at driving frequency $\omega = 8J$ as a function of the initial-state energy E up to $t = 10\tau$, corresponding to circuit depth $D = 80$. The initial states were chosen from the same set as in Fig. 9.3b). The black crosses represent the noise-free results, whereas for the red points the experiment was simulated including noise and error mitigation. The error bars show statistical errors due to fluctuations of different Monte Carlo trajectories, propagated from the standard deviations of $L_A^{\mathcal{N}_p}(t)$ and $L_{\mathbb{1}}^{\mathcal{N}_p}(t)$. Note that the sign of $\langle \psi | \hat{A}(t) | \psi \rangle$ turns out to be constant during the Floquet time evolution in our range of simulations. In the long-time limit, the time average of the

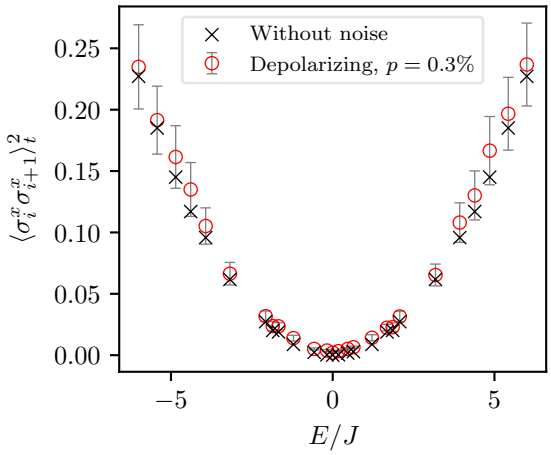

Figure 9.6: The time average of $L_{\sigma_i^x \sigma_{i+1}^x, \psi}(t)$ at $Jt \approx 7.85$ with $\omega = 8J$, or $\tau = \pi/4J$, corresponding to 10 Trotter steps. The black crosses show the noiseless result. The red points were obtained by applying our error-mitigation strategy to noisy simulations with a single-qubit depolarization rate $p = 0.3\%$. Error bars indicate the statistic errors due to fluctuations of different Monte Carlo trajectories, propagated from the standard deviations of $L_A^{\mathcal{N}_p}(t)$ and $L_{\mathbb{1}}^{\mathcal{N}_p}(t)$. The system size $N = 4 \times 4$.

square is therefore equivalent to the square of the time average, given that they converge to a constant. We further note that the deviation between the noisy and noise-free results is biased since the red points are systematically above the black crosses, consistent with the expectation from Eq. (9.24).

We find that the noise-free results lie within the error bars for all initial states and that the trend of the observable is well reproduced. Since the rescaling factor is about $q^2 = (1-p)^{ND} \approx 0.02$, the unmitigated points would be non-discernibly close to zero. This shows that our error-mitigation procedure is both viable and needed to solve the PEVP.

9.3.3 Implementation

The results of the previous section show that our error-mitigation strategy enables the solution of the PEVP for the XY model at a depolarizing noise rate of $p = 0.3\%$. One more step remains to assess the experimental viability: an estimate of the number of required measurements.

In experiments, the survival probabilities are estimated from binary outcomes (success / failure). This gives rise to shot noise, which in turn sets a lower bound on the necessary number of samples. To achieve a statistical uncertainty of ϵ, roughly $1/\epsilon^2$ samples are needed. For the error-mitigation scheme to work, the shot noise must be smaller than the survival probability. As the noisy survival probability is suppressed by the factor $(1-p)^{ND}$, it follows that the number of needed measurements scales as $(1-p)^{-2ND}$. We note that this number of samples is typically orders of magnitude larger than the number needed to suppress the fluctuations in Monte Carlo trajectories due to noisy dynamics.

Since the sample complexity scales exponentially with the number of qubits, this is an important limitation to the system size that can realistically be reached. Nevertheless, classically hard regimes are accessible with realistic parameters. For instance, setting $N = 50$ while keeping $p = 0.3\%$ and $D = 80$, we find that $(1-p)^{-2ND} \approx 3 \times 10^{10}$ samples

are needed. This is inconveniently large as current superconducting quantum devices can collect millions of samples on the time scale of minutes. However, a modest improvement in the error rate to $p = 0.2\%$ reduces the number of samples to a much more realistic value of 9×10^6.

We have so far neglected the role of measurement errors, which occur with probability $p_m \approx 1\% - 2\%$ for each single-qubit measurement in current devices [317, 323]. Fortunately, these errors are automatically remedied by our error-mitigation strategy. The measurement errors simply suppress the survival probability by another factor $(1 - p_m)^N$, which is independent of the circuit depth. For system sizes up to $N = 50$, this increases the required number of measurements by at most an order of magnitude.

9.4 Summary and outlook

We have proposed the prethermal expectation value problem as a way to study thermal observables on noisy, intermediate-scale quantum devices. Our approach relies on the observation that relatively large Trotter steps, which do not permit a rigorous bound on the Trotter error, can give rise to prethermalization. We showed that in the prethermal regime, the equilibration of observables is similar to the expected dynamics under the original Hamiltonian. It may be possible to approximate evolution under the original Hamiltonian even better by canceling higher-order terms of the Magnus expansion at the cost of more complex circuits. The range of energies at which the observables can be probed is set by the range of energies of the used initial states. In this work we restricted ourselves to product states, but the protocol can straightforwardly be extended to different initial states, which may increase the range of accessible energies.

We further demonstrated that the prethermal regime is experimentally accessible with noise rates of near-term devices using an error-mitigation scheme based on measuring and rescaling survival probabilities. This scheme is not limited to the PEVP but can be applied much more broadly in the context of quantum simulation. Our work provides all necessary ingredients to also study the approach to equilibrium and to extract, for instance, diffusion constants. Care should be taken, though, that the Trotterization does not break symmetries in the Hamiltonian which strongly affect the thermalization process. Alternatively, one could consider the quantum dynamics of models which do not thermalize, such as quantum scars [324, 325] or many-body localized systems [326, 327].

Our work creates a new avenue to exploring quantum many-body systems beyond those that can be classically simulated. Although the XY model studied here can be efficiently simulated on classical computers with quantum Monte Carlo methods [307], our approach can be readily adapted to more complex Hamiltonians. As a simple modification of the XY model, one might consider adding a site-dependent sign to the interaction strength J. This renders classical simulation of this model much harder since it causes a sign problem in quantum Monte Carlo methods [328–330]. The complexity of our proposed approach to quantum simulation however remains unaffected by this modification.

We highlight that our approach works up to a constant circuit depth that scales approximately as $D \sim \mathcal{O}(1/p)$. While for a fixed p this is not classically hard in the sense of computational complexity theory, the maximal circuit depth $D \sim 200$ corresponding to a realistic noise rate $p = 0.3\%$ is currently classically intractable for intermediate-size systems. Hence, beyond classical quantum simulation of dynamics and equilibrium properties is within reach.

Appendices

9.A Definition of problems

Setup

In this section we consider

- a local Hamiltonian $\hat{H}$ as considered in 9.2.1, with spectral decomposition

$$\hat{H} = \sum_k E_k \left|k\right\rangle \left\langle k\right|, \tag{9.26}$$

- the Trotterized time-evolution unitary $U_{\text{Trotter}}(\tau)$ (see Eq. (9.1)) with time step τ,
- an observable $\hat{A}$ with operator norm $\|\hat{A}\|$,
- and an initial state $|\psi\rangle$.

When also given a Trotter step τ, any time appearing in text will be stroboscopic, i.e., an integer multiple of τ.

Definition of thermal ensembles

Here we provide definitions of the microcanonical and diagonal ensembles in Fig. 9.3.

Definition 1 (The microcanonical ensemble) *Given an energy E and energy interval δ, the value of an observable A in the corresponding microcanonical ensemble is defined as*

$$\langle \hat{A} \rangle_{\text{micro},E} = \sum_{k \in I_{E,\delta}} \langle k|\hat{A}|k\rangle \, / |I_{E,\delta}|, \tag{9.27}$$

where $I_{E,\delta} = \{k | |E_k - E| < \delta/2\}$.

Alternatively, for the convenience of computation, the energy cutoff may be replaced by a Gaussian filter:

Definition 2 (The broadened microcanonical ensemble) *With the same setup as Definition 1, the broadened microcanonical ensemble is defined as*

$$\langle \hat{A} \rangle_{\text{micro}',E} = \sum_k \langle k|\hat{A}|k\rangle \, e^{-\frac{(E-E_k)^2}{2\delta^2}} \Big/ \sum_k e^{-\frac{(E-E_k)^2}{2\delta^2}}. \tag{9.28}$$

The two definitions are equivalent in the thermodynamic limit under the eigenstate thermalization hypothesis [315, 331]. In Fig. 9.3 we take the latter definition, which can be efficiently computed in 1D systems with classical computers using filtering algorithms for δ being a constant [331].

Definition 3 (The diagonal ensemble) *Given a state $|\psi\rangle$, the value of an observable $\hat{A}$ in the the diagonal ensemble is defined as*

$$A_{d,\psi} = \sum_k |\langle \psi|k\rangle|^2 \langle k|\hat{A}|k\rangle. \tag{9.29}$$

The diagonal-ensemble values are equivalent to the long-time average of the initial state $|\psi\rangle$ and observable $\hat{A}$ for non-degenerate Hamiltonians. It can be approximated again by filtering out the off-diagonal elements of an initial density matrix [332]. The entanglement entropy of the diagonal ensemble in operator space however obeys a volume-law scaling, which limits the system size reachable in classical simulations.

Definition of PEVP

To define the PEVP, we first need give a precise definition of a prethermal plateau. There is not a single accepted definition for a prethermal plateau in the literature. Here we formulate the practical definition we use. First we define what we consider to be a plateau.

Definition 4 (The plateau) *Given a tolerance $\epsilon \ll 1$, a plateau is a time interval $[t_1, t_2)$ with $t_1 < t_2 \leq \infty$ such that*

1. $\max_{t_1 \leq t < t_2} \langle \hat{A} \rangle_t - \min_{t_1 \leq t < t_2} \langle \hat{A} \rangle_t \leq \epsilon \|\hat{A}\|$, *where $\langle \hat{A} \rangle_t$ is defined in Eq. (9.2).*
2. *there exists no overlapping interval $[t_1', t_2')$ also satisfying 1 for which $t_2'/t_1' > t_2/t_1$.*

The second criterion ensures the plateau we find is locally the longest. Here we take the ratio t_2/t_1 as the measure of the length of the plateau to be more consistent with the ideas of prethermalization. A plateau can be identified as a prethermal plateau, if

- it is not connected to the final Floquet thermalization plateau at infinite time and temperature [291],
- the ratio t_2/t_1 grows exponentially with $1/\tau$ and
- in the small τ limit, t_1 converges to a positive number.

It is in general hard to identify a prethermal plateau, due to the difficulty of reaching the exponentially growing t_2 in simulations. Nevertheless, assuming its existence, it is relatively easy to find the plateau and compute the plateau value. Now let us restate Problem 2 in the main text:

Definition 5 (The prethermalized expectation value problem) *Given a unitary $\hat{U}_{\text{Trotter}}(\tau)$, a state $|\psi\rangle$, and a local observable $\hat{A}$, assume that a prethermal plateau exists between times t_1 to t_2, such that $\max_{t \in [t_1, t_2)} \langle \hat{A} \rangle_t - \min_{t \in [t_1, t_2)} \langle \hat{A} \rangle_t \leq \epsilon \|\hat{A}\|$. Find the value of $\langle \hat{A} \rangle_t$ to within additive error $2\epsilon \|\hat{A}\|$ for any $t \in [t_1, t_2)$.*

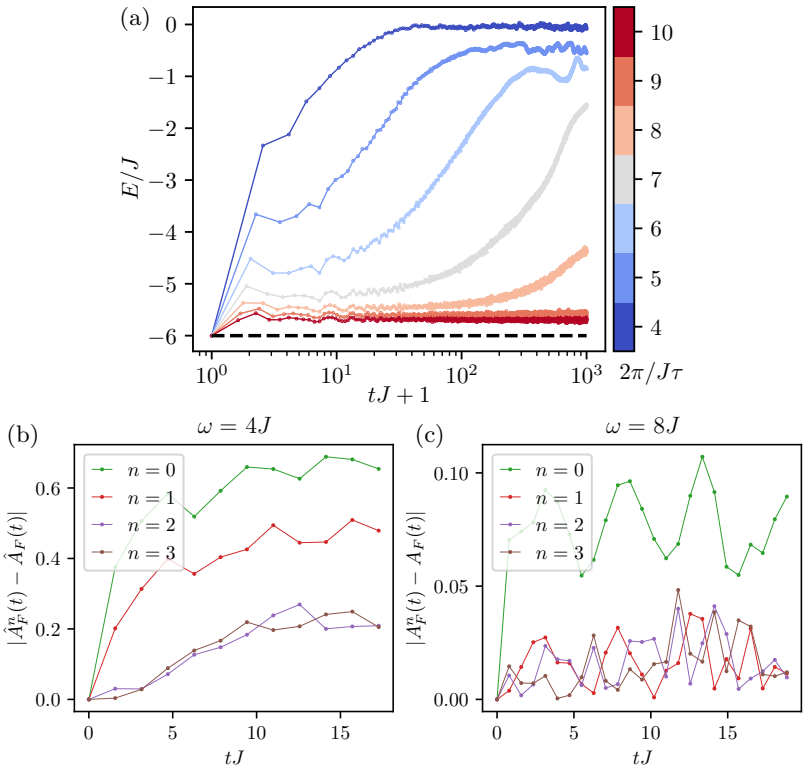

Figure 9.B.1: (a): Expectation value of the initial Hamiltonian during the Floquet evolution for the initial state $|X+\rangle$ evolved. The parameters are the same as Fig. 9.3a). (b)-(c): Simulation of evolving Floquet XY model with the Magnus expansion truncated to n-th order. Their differences from Floquet evolution are plotted. The initial state is $|X+\rangle$ and $A = m_x^2 + m_y^2$. The system size is $N = 4 \times 3$. (b): $\omega = 4J$, (d): $\omega = 8J$. Note the difference in scale on the y-axis.

9.B The Magnus expansion

The Magnus expansion serves as a high-frequency expansion for the effective Hamiltonian of a Floquet driving $\hat{H}(t)$ with period τ:

$$
\begin{aligned}
\hat{U}_F(\tau) =& \mathcal{T}\left(e^{-i\int_0^\tau \hat{H}(t)\mathrm{d}t}\right) = e^{-i\tau\sum_{k=1}^{\infty}\Omega_k}, \\
\hat{\Omega}_0 =& \frac{1}{\tau}\int_0^\tau \mathrm{d}t_1 \hat{H}(t_1), \\
\hat{\Omega}_1 =& \frac{1}{2i\tau}\int_0^\tau \mathrm{d}t_1 \int_0^{t_1} \mathrm{d}t_2 \left[\hat{H}(t_1), \hat{H}(t_2)\right], \\
\hat{\Omega}_2 =& -\frac{1}{6\tau}\int_0^\tau \mathrm{d}t_1 \int_0^{t_1} \mathrm{d}t_2 \int_0^{t_2} \mathrm{d}t_3 \\
& ([\hat{H}(t_1), [\hat{H}(t_2), \hat{H}(t_3)]] + [\hat{H}(t_3), [\hat{H}(t_2), \hat{H}(t_1)]]), \\
& \vdots
\end{aligned}
\tag{9.30}
$$

In general, the Magnus expansion is not convergent [280, 304] and thus higher-order contributions are not negligible for finite driving frequencies. Nevertheless, its finite truncation is still expected to approximate the quasi-stationary prethermal plateau [288]. To

be more precise, let $\hat{H}^{(n)}_{\text{Magnus}} = \sum_{j=0}^{n} \hat{\Omega}_j$ denote the n-th order truncated effective Hamiltonian, then there exists $n_0 = \mathcal{O}(\omega/kJ)$ such that

$$\|\hat{U}_F(\tau)^m - e^{-i\hat{H}^{(n_0)}_{\text{Magnus}} m\tau}\| \lesssim Nm\tau 2^{-n_0}. \tag{9.31}$$

The general estimation Eq. (9.31) for the unitary evolution operators has a linear dependence on system size, which does not imply prethermalization for $N \gtrsim \exp(\mathcal{O}(\omega/kJ))$. When considering local observables acting on a subsystem L and short-range interacting Hamiltonians, however, the bound can be tightened for the reduced density matrix ρ_L:

$$\|(\rho_L)_F(m\tau) - (\rho_L)^{(n_0)}_{\text{Magnus}}(m\tau)\|_1 \lesssim |L| m\tau e^{-\mathcal{O}(\omega)} \tag{9.32}$$

for the same n_0, where the system-size dependence is erased [288].

For the proof of this relation to hold rigorously, the required driving frequency is $\omega \geq 16\pi kJ \approx 100J$ for nearest-neighbor-interacting Hamiltonians, while in our numerical simulation in Fig. 9.3, prethermalization has occurred for $\omega \sim 8J$. For all of our numerical simulations of the XY-model, we use the Trotterization shown in Fig. 9.1a). In Fig. 9.B.1a), we plot the expectation value of the initial Hamiltonian during the Floquet evolution for the initial state $|X+\rangle$, where the parameters are the same as Fig. 9.3b). The figure shows that the expectation value quickly reaches a new quasi-equilibrium due to the evolution under the effective Floquet Hamiltonian. The expectation value then remains approximately constant up to the Floquet time scale t_F. We highlight that the initial increase in energy is small for the driving frequency $\omega = 8J$ used in the main text.

In Fig. 9.B.1b) and c) the differences between Floquet evolution and its Magnus expansions up to the third order are plotted. Note that the zeroth-order Magnus expansion is just the original non-Floquet Hamiltonian. For $\omega = 8J$, it turns out that the $n = 1$ case already gives a good approximation of the Floquet Hamiltonian.

9.C Phase- and amplitude-damping noise

In the main text, we focused on depolarizing noise. In this appendix, we show that the effects of phase damping and amplitude damping noise are qualitatively similar. The relevant noise channels are given by [333]:

- the phase-damping channel

$$\mathcal{N}_p^P(\rho) = (1-p)\rho + p\sigma_i^z \rho \sigma_i^z, \tag{9.33}$$

- and the amplitude-damping channel

$$\mathcal{N}_p^A(\rho) = M_0 \rho M_0^\dagger + M_1 \rho M_1^\dagger, \tag{9.34}$$

where $M_0 = \begin{pmatrix} 1 & 0 \\ 0 & \sqrt{1-p} \end{pmatrix}$ and $M_1 = \begin{pmatrix} 0 & \sqrt{p} \\ 0 & 0 \end{pmatrix}$.

In Fig. 9.C.1 we plot the simulation results for these two types of noise in the same fashion as in Fig. 9.4 and Fig. 9.5. From top to bottom, they are the scaling of survival probability without (left) and with (right) applying the observable, the error s of the mitigation strategy and the moving quadratic average of s. The scalings also fit well with Eq.(9.11). Interestingly, the error after rescaling is much smaller for phase-damping noise than for the other two noise types.

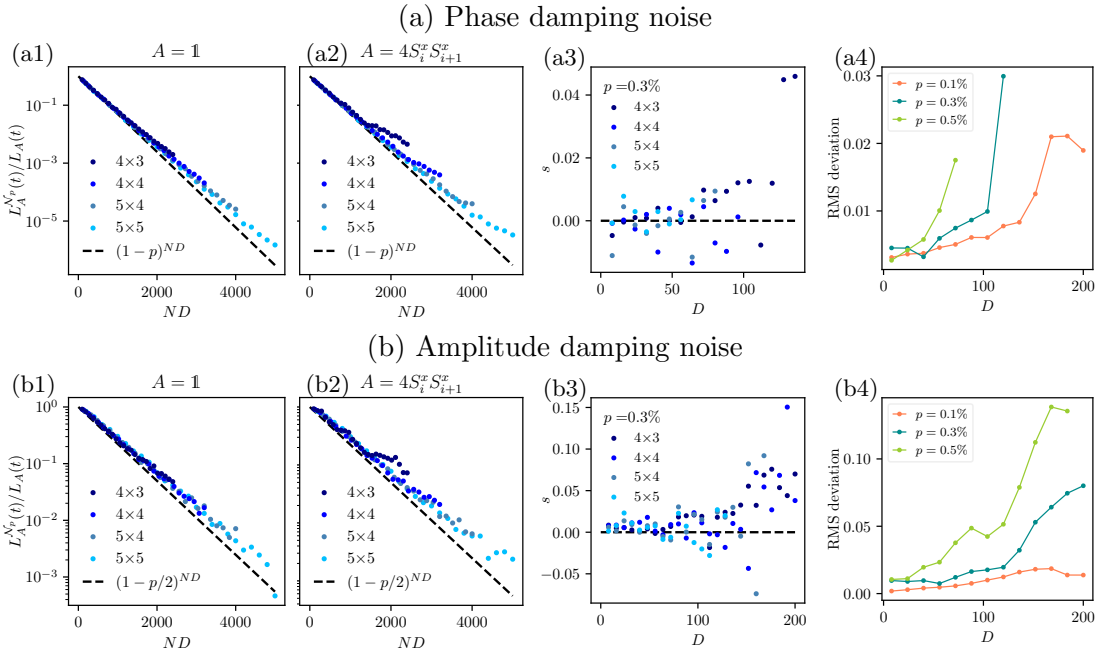

Figure 9.C.1: Simulation results for phase-damping (a1-a4) and amplitude-damping (b1-b4) noise and $p = 0.3\%$. The plotted quantities are the same as shown in Fig. 9.4 and Fig. 9.5.

Note that amplitude-damping noise involves non-unitary Kraus operators, and thus the performance of the rescaling strategy is a priori unclear. The above numerical results, however, indicate that rescaling still works with an effective noise rate $p/2$. Pauli twirling can be useful as a formal tool to explain the effective noise rate, as it converts non-unitary Kraus operators into unitary depolarizing ones. A possible set of Pauli twirling operators for the amplitude-damping channel is $W = \{\mathbb{1}, \sigma^x, \sigma^y, \sigma^z\}$ so that the conjugated noise channel becomes

$$\begin{aligned}\tilde{\mathcal{N}}_p^A(\rho) =& \frac{1}{|W|}\sum_{w\in W}\sum_{k=0,1} wM_k w^\dagger \rho w M_k^\dagger w^\dagger, \\ =& \left(\frac{1+\sqrt{1-p}}{2}\right)^2 \rho + \frac{p}{4}\sigma^x\rho\sigma^x + \frac{p}{4}\sigma^y\rho\sigma^y \\ &+ \left(\frac{1-\sqrt{1-p}}{2}\right)^2 \sigma^z\rho\sigma^z.\end{aligned} \tag{9.35}$$

In the small-p limit, the effective noise rate of this asymmetric depolarizing noise is just $1 - \left(\frac{1+\sqrt{1-p}}{2}\right)^2 \approx p/2$, in agreement with the numerical result.

Outlook

For the final outlook of this thesis, let us go back to its core topic: chemistry in a quantum medium. The chemical processes we have considered involving the Bose-Einstein condensate as a medium, are of a completely different nature than typical reactions considered in chemistry. Of course, the energy scales are vastly different. At room temperature, and in liquid solvents such as water, the energy available in the system is similar to the energy involved in creating and breaking chemical bonds in organic molecules. Hence, these are the processes which traditional chemistry predominantly focuses on.

Nevertheless, we have shown that at ten orders of magnitude lower energy scales, still interesting molecule-formation processes take place with a profound influence of the surrounding medium, see also Ref. [334]. Key here is to consider such weakly bound molecules that there is again a true competition between the binding energy and the kinetic or thermal energy in the surrounding medium. The additional feature is that at such low temperatures, quantum effects are more prominent.

We will not claim there is a universal underlying model which can directly be mapped to problems in chemistry. Maps to other fields of science are more direct in other cold-atom studies, for example in the case of quantum simulation of the Fermi-Hubbard model [35]. Still, it is an interesting question whether things can be learned from this bottom-up approach to chemistry in a quantum medium which can also lead to an improved understanding of traditional chemistry in a medium, in particular in regard to possible quantum effects.

In the outlooks within the indivdual Chapters we have discussed natural follow-up steps to achieve a still better understanding of the models we considered. In this final outlook of my thesis, I will take one step back, and give a broader perspective on how the seemingly large gap between our research and traditional scenarios in chemistry can partially be bridged. We will focus in particular on how to increase the complexity in a controlled way, and how to introduce stronger interactions in our system of consideration. In this regard, I will also touch on some future research directions in the field of ultracold molecules and quantum computing.

Ultracold gases of dipolar atoms and ultracold molecules

Using our scenario of an impurity in a BEC as a starting point, one way to increase the complexity of the medium is to introduce long-range interactions, such as dipolar interactions. This can for example be realized by using strongly magnetic atoms such as chromium, erbium, or dysprosium [66], instead of alkali atoms. For these magnetic atoms the strength of the dipolar interactions is comparable to the strength of the contact interactions. This competition gives rise to interesting phenomena, such as the formation of self-bound quantum droplets [123, 124] and supersolids [335–337].

Mixtures of dipolar atoms have even richer phase diagrams [338, 339]. It has for example been proposed that already a relative small concentration of impurities in a dipolar gas can help to stabilize the supersolid phase [339]. Studying this from the polaron perspective therefore seems promising, and first studies on dipolar polarons have been carried out in Refs. [340–342]. Interesting questions concern the shape of the polaron cloud, whether a single impurity can be a catalyst for droplet or supersolid formation, and to which degree

the dipole moment of the impurity plays a role. Mixtures of different dipolar atoms have already been realized experimentally [343], and also mixtures of alkali atoms and dipolar atoms are being studied [344, 345].

To study polaron physics and molecule formation in dipolar gases, suitable Feshbach resonances are required. Magnetic atoms typically have a very dense set of narrow resonances due to their complicated internal structure [346, 347], and most of them are not practical for these purposes. However, broad and suitable resonances have still been found, and this has also led to the creation of homonuclear and heteronuclear Feshbach molecules [347–349]. Studying polaron physics and molecule formation in a dipolar quantum medium therefore seems within reach.

As a side note, there are interesting connections between the scattering properties of magnetic atoms and ultracold molecules. In fact, the distribution of Feshbach resonances for magnetic atoms shows signatures of quantum chaos [346, 350], as we have discussed for molecules in Chapter 8. Furthermore, Feshbach molecules formed from K and Dy have also shown photo-induced loss [349]. Whether the mechanism is similar to the case for molecules remains to be explored, but for the K-Dy molecules a clear dependence of the loss on the laser frequency and intensity has been observed.

Ultracold molecules can also be used to realize dipolar quantum media. Here the dipolar interactions are stronger, and different parameter regimes can be achieved, which can lead to the appearance of a diverse range of many-body phases [219, 351]. So far, achieving degenerate samples of ultracold molecules has been very challenging due to the loss discussed in Chapter 8, but there has been tremendous recent progress in the implementation of techniques preventing this loss [260–264, 352]. In particular microwave shielding is promising, and this has recently enabled the clear observation of evaporative cooling of ultracold molecules [264]. Because microwave shielding requires a fine-tuned set of parameters, it is not clear yet whether it will also be applicable to mixtures of different species or multiple internal states. Therefore polaron physics does not seem like the most natural direction of study in the near future.

However, microwave shielding does give other interesting opportunities in connection with few-body physics and chemistry. For example, it allows one to engineer a long-ranged attractive well in the potential, while still maintaining the protection from the lossy short range by a repulsive barrier [263]. This long-ranged potential well can host bound states, and these give rise to scattering resonances when they appear from the continuum. These so-called field-linked resonances [353], and the associated bound states of two molecules [354] have already been observed. Even though these tetramers themselves are not so long-lived, collisions between these tetramers appear to not lead to additional loss. This seems to indicate that microwave shielding also works for higher-order collision processes. If this is true, microwave-shielded molecules would provide an interesting platform to study three-body physics without recombination, or more excitingly, to extend this to even larger clusters. In principle, one could imagine forming large bound complexes in some sense similar to helium droplets, but with tunable interaction strengths.

Helium droplets

Having mentioned helium droplets, this is another platform where chemistry in a quantum medium is of great interest. Indeed, helium droplets can be viewed as an intermediate case between ultracold gases and everyday fluids. Studies of superfluid helium have a rich history [355, 356], and there are many overlapping topics of interest with the field of ultracold atoms. The density of liquid helium is only one order of magnitude smaller than the density of water, but helium atoms only have very weak van der Waals interactions:

the depth of the pairwise helium interaction potential is only 11 K [357] (compared to $\sim$ 2500 K for water [358] and $>$ 5000 K for alkali atoms). In fact, also because helium is light, this potential only hosts a single bound state, which is extremely shallow. In the gas phase, trimers of helium therefore show characteristics of Efimov states [101, 359]. The equilibrium temperature of (bosonic) helium droplets is 0.38 K [360], so the huge separation of energy scales that ultracold-atom systems have is not present in the case of helium. One advantage of helium droplets is that they truly form the ground state of the system. Therefore they do not share the problem of bosonic ultracold gases that strong interactions and higher-order correlations are difficult to study due to recombination.

In the last decades, droplets of helium have gained considerable interest from the chemistry perspective [360–362]. It has turned out that helium droplets can relatively easily pick-up and absorb gas-phase molecules. The molecules are subsequently cooled via the evaporation of the helium droplet, making helium droplets a great environment for spectroscopic studies of low-temperature molecules. From the chemistry perspective, superfluid helium is the most "gentle" solvent that one can find, which only affects the molecular properties in a minimal way. This is because the internal energy scales inside the molecules are typically still much larger than the temperature in helium. To observe medium effects where the helium acts as more than a cooling agent, it seems most interesting to look at the formation of weakly bound clusters [362–364], with binding energies similar to the many-body scale of the helium droplets.

One example of an interesting quantum effect of molecules in helium, is the case of molecular rotation. It has turned out that the helium environment can have a pronounced effect on the molecular rotational dynamics [365]. The spectroscopic line broadening is surprisingly small, but the rotational constant changes. It has been shown that a remarkably simple theoretical description can already capture this effect by interpreting this in a polaron-like scenario. Analogous to how the translation motion of the impurity is altered in the polaron case, here the rotational motion is affected by the medium. This led to the introduction of the "angulon" quasiparticle [172–174]. A surprising aspect of the angulon model is that already a description of the helium bath in terms of Bogoliubov theory is sufficient to capture the key effects and match experimental results [174]. This is remarkable, because the condensate fraction in helium was determined to be less than 10% [366, 367]. Including the interactions between the helium atoms more accurately would be an interesting but challenging problem. Furthermore, the translational motion of angulons remains a largely open topic of study [368].

Bipolarons

When referring to "chemistry in a medium", one would usually have in mind reactions between solutes rather than reactions in which the solvent molecules are also reactants. In our framework this would correspond to the study of interactions and reactions between polarons. This was not our starting point, since it is much more complicated than the problem of a single Bose polaron.

In ultracold-atom systems, it is challenging to clearly observe interactions between polarons [369]. In other platforms such as helium droplets or two-dimensional semiconductors [201, 370, 371] such phenomena arise more naturally. Theoretically, several studies in the one-dimensional case have appeared [372–374], and in three dimensions some aspects have been addressed, see e.g. Refs. [175–177, 375, 376]. However, in the three-dimensional case the level of theory used in this thesis still remains out of reach. The main challenge is that for more than one impurity the degrees of freedom of the impurities cannot be fully integrated out any more. Additionally, the problem has a lower symmetry. Therefore,

interesting steps along the way would be the finite-momentum Bose polaron [171], which already has a strongly reduced symmetry compared to the momentum-zero polaron, and the moving angulon [368], which introduces also the rotational degree of freedom. The quantum-chemistry inspired parameterization of the variational wave function developed in Chapter 6 appears to be a promising way to handle the increased complexity. We believe that this method can be further optimized, drawing inspiration from how calculations in quantum chemistry are extended from atoms to complex molecules.

Quantum computing

Problems in chemistry also form an important possible application for quantum computers [377]. Most focus has been on computing the electronic structure of molecules, but there are also proposals to simulate molecular dynamics [378] and scattering [379]. Simulating chemistry in a medium seems very challenging, however, since it is not such a clean problem which can be encoded easily on a quantum computer. Potentially, polaron systems such as considered in this thesis could be an interesting starting point for research in this direction.

Regarding our own quantum-computing project discussed in Chapter 9, a natural extension is the application of energy-filtering techniques [315]. In our approach we approximate expectation values in the diagonal ensemble, where we still average over the energy width of the initial state. This width can be reduced by the approach in Ref. [315], but at the cost of a more difficult implementation due to the need of measuring complex quantities. This is challenging on quantum computers, because the standard Hadamard approach [380] for this purpose requires controlled operations, which are difficult to implement without large overheads. In our recent work [17] we develop a novel approach to resolve this issue.

Acknowledgments

I am very grateful for the opportunity to work on my PhD in the fantastic scientific atmosphere of MPQ, and the MPQ theory group. I have greatly enjoyed all the collaborations and discussions underlying much of the work presented in this thesis and beyond. Here I will give a special thanks to the people who made all of this possible, and who contributed to making this PhD a pleasant and fulfilling experience.

First and foremost, let me thank my supervisors Richard Schmidt and Ignacio Cirac. Richard, I greatly appreciate your unlimited enthusiasm and your creativity, which always make discussions with you inspiring and motivating. Even though you had two children and moved twice during my PhD and this sometimes limited your available time, you still did your utmost best to help us and to give us plenty of opportunities to develop ourselves and advance our careers. For this I am very grateful. I further appreciate your eye for detail and your quality to make things sound more interesting, which greatly improved our joint manuscripts.

Ignacio, I can only imagine how taxing it must be to lead such a large research group and to be director of a Max-Planck-Institute. Nevertheless, you truly care about all of your group members, and would always make time for discussions, about science but also to give career advice. The one time where a 15 minute discussion with you solved a problem I had been struggling with for a month, taught me the valuable lesson that learning from others is sometimes more effective than doing things by myself.

Besides Richard and Ignacio, I had the opportunity to collaborate with many others inside and outside of our group and institute. Inside the theory group it has been a great pleasure to work with Yilun, Sandra, Dominik and Mari Carmen on our quantum-computing project. Sandra, I am glad to have had the chance to co-supervise you, as my first Master student. Our Zoom-discussions were one of my few sources of social interaction in the second year of the Covid pandemic, and for that I am really grateful. Yilun and Dominik, working on this project as a team was a very nice experience for me. Teamwork in this form, where we really brainstormed together to solve problems over a long period of time, was kind of new to me and l have really come to appreciate our collaboration. I would also like to thank Tom O'Brien from Google Quantum AI for his contributions and the interesting discussions.

I also enjoyed working on our Fermi polaron project with Oriana and Jonas. I am happy I was able to contribute to this project, and I enjoyed learning about Fermi polarons in our discussions.

Another great collaboration inside MPQ was with the ultracold-molecule team led by Xin-Yu Luo, where I worked particularly with Roman Bause and Andreas Schindewolf. Already when I was applying at MPQ we were discussing about testing our theoretical prediction that the trapping laser kills your ultracold molecules. I still feel kind of guilty that all of your efforts working on the box trap did not lead to stable molecules, although you assured me you were also content with the surprising negative results. I am very happy in the end you found another solution with the microwave shielding. Writing the review paper together with you was one of the most pleasant writing experiences I have had. I would also like to thank Tijs and Gerrit from my former university for the theory collaborations on the ultracold-molecule projects. It was already a great pleasure to work

with you during my Master research, and I really enjoyed the discussions we had in the last years, and the ideas we managed to generate.

Outside MPQ, I had the pleasure to work with the excellent experimental group of Martin Zwierlein, in particular with Carsten Robens, Alex Chuang and Martin himself. The vibrant discussions we had were very inspiring, and it was a great experience for me to theoretically predict and explain your experimental results.

During my PhD, I had the opportunity to visit JILA, in the beautiful Boulder, Colorado. I owe many thanks to John Bohn, Ana Maria Rey, and their groups for their kind hospitality and for inspiring discussions. It was great to meet Dibyendu in person, who I had already been corresponding with for a year. Thanks also to everyone involved in organizing my shorter research visits in Aarhus, Innsbruck, Zurich, Barcelona, Warsaw, and Heidelberg.

What remains is to thank my colleagues in the theory group who created the excellent atmosphere to work in. I am grateful to all of the group members over the past years, but let me single out a few people here. First, let me thank my office mates. When I first arrived at MPQ, I shared the office with the other newbies Irene and David, which I still feel has made a special connection between us. Later, I moved into another fabulous office, with Johannes, Christoph and Tommaso. Even though we were not in the office together a lot during the Covid-pandemic, I am still very grateful for the pleasant atmosphere. Special thanks to Tommaso for teaching me a lot about Gaussian states and variational approaches. After Johannes, Christoph, and Tommaso had one by one graduated, my role in the office changed from junior to nestor when Marta and Denise joined, and for a few months Paula. Again this resulted in a very nice atmosphere, and in particular we shared our liking of cookies and cake. When in the end Irene also joined, the circle was round, and I was ready to graduate.

Further I would like to thank everyone in the Schmidt group, among others Jonas, Oriana, the Marcels, Rafał, Félix, and Zied. Many thanks in particular to Rafał for our many discussions about dipolar systems and two-dimensional materials and helping to organize my visit in Warsaw. Zied, it was fun to work with you and supervise you!

I would like to thank Patrick, Marton, Miguel and Guillermo for the great collaboration in organizing the seminar, and Andrea, Andrea, Regina, and Elena for the administrative support. Special thanks to David, Bennet and Julian for giving feedback on my thesis. Thanks as well to Kristian and Denise Braun (TU Eindhoven), for their input on Chapter 4 of this thesis. I also greatly appreciate the efforts of IMPRS and MCQST to organize so many interesting activities which strongly enriched my academic experience, thanks for that in particular to Sonya Gzyl and Barbara Tautz. I would further like to thank Christoph Hohmann for designing the cover of my thesis, and Prof. Michael Knap and Prof. Jonathan Finley for being part of my doctoral committee.

Last but not least, I would like to thank my family and my girlfriend. Without my parents I would never have been able to do my PhD, and I am grateful for their unending support. This is not the only book I have written in these years; writing a fantasy book together with my brother Ruben was great fun (most of the credits go to him), and a nice way to keep occupied during the lockdowns. I still have hope that we will also complete the next five books in the series someday. Grite: you have been a wonderful girlfriend for me, and my home-office mate during the first Covid-lockdown. Without you it would have been extremely challenging to get through the difficult Covid-times. After such a long time of long-distance relationship, I am really looking forward to being together with you more.

Bibliography

[1] A. Christianen, J. I. Cirac, and R. Schmidt, Phys. Rev. Lett. **128**, 183401 (2022).

[2] A. Christianen, J. I. Cirac, and R. Schmidt, Phys. Rev. A **105**, 053302 (2022).

[3] A. Christianen, J. I. Cirac, and R. Schmidt, preprint (2023), arXiv:2306.09075 [cond-mat.quant-gas] .

[4] C. Robens, A. Christianen, A. Y. Chuang, Y. Ni, E. Wolf, R. Schmidt, and M. W. Zwierlein, in preparation (2023).

[5] R. Bause, A. Schindewolf, R. Tao, M. Duda, X.-Y. Chen, G. Quéméner, T. Karman, A. Christianen, I. Bloch, and X.-Y. Luo, Phys. Rev. Res. **3**, 033013 (2021).

[6] A. Christianen, G. C. Groenenboom, and T. Karman, Phys. Rev. A **104**, 043327 (2021).

[7] R. Bause, A. Christianen, A. Schindewolf, I. Bloch, and X.-Y. Luo, J. Phys. Chem. A **127**, 729 (2023).

[8] Y. Yang, A. Christianen, S. Coll-Vinent, V. Smelyanskiy, M. C. Bañuls, T. E. O'Brien, D. S. Wild, and J. I. Cirac, PRX Quantum **4**, 030320 (2023).

[9] A. Christianen, M. W. Zwierlein, G. C. Groenenboom, and T. Karman, Phys. Rev. Lett. **123**, 123402 (2019).

[10] A. Christianen, T. Karman, and G. C. Groenenboom, Phys. Rev. A **100**, 032708 (2019).

[11] A. Christianen, T. Karman, R. A. Vargas-Hernández, G. C. Groenenboom, and R. V. Krems, J. Chem. Phys. **150**, 064106 (2019).

[12] A. Christianen and J. Sous, Phys. Rev. A **101**, 063610 (2020).

[13] T. Selim, A. Christianen, A. van der Avoird, and G. C. Groenenboom, J. Chem. Phys. **155**, 034105 (2021).

[14] O. K. Diessel, J. von Milczewski, A. Christianen, and R. Schmidt, preprint (2022), arXiv:2209.11758 [cond-mat.quant-gas] .

[15] D. Sardar, A. Christianen, H. Li, and J. L. Bohn, Phys. Rev. A **107**, 032822 (2023).

[16] B. Margulis, K. P. Horn, D. M. Reich, M. Upadhyay, N. Kahn, A. Christianen, A. van der Avoird, G. C. Groenenboom, M. Meuwly, C. P. Koch, and E. Narevicius, Science **380**, 77 (2023).

[17] Y. Yang, A. Christianen, M. C. Bañuls, D. S. Wild, and J. I. Cirac, preprint (2023), arXiv:2308.10796 [quant-ph] .

[18] C. Reichardt, J. Org. Chem. **87**, 1616 (2021).

[19] C. J. Burrows, J. B. Harper, W. Sander, and D. J. Tantillo, J. Org. Chem. **87**, 1599 (2022).

[20] J. Bardeen, L. N. Cooper, and J. R. Schrieffer, Phys. Rev. **108**, 1175 (1957).

[21] H. Hosono, K. Tanabe, E. Takayama-Muromachi, H. Kageyama, S. Yamanaka, H. Kumakura, M. Nohara, H. Hiramatsu, and S. Fujitsu, Sci. Technol. Adv. Mater. **16**, 033503 (2015).

[22] The LHCb Collaboration, J. Instrum. **3**, S08005 (2008).

[23] ATLAS collaboration, Phys. Lett. B **716**, 1 (2012).

[24] P. Foka and M. A. Janik, Rev. Phys. **1**, 172 (2016).

[25] S. N. Vogels, T. Karman, J. Kłos, M. Besemer, J. Onvlee, A. van der Avoird, G. C. Groenenboom, and S. Y. van de Meerakker, Nat. Chem. **10**, 435 (2018).

[26] S. G. Karshenboim, Phys. Rep. **422**, 1 (2005).

[27] ACME collaboration, J. Baron, W. C. Campbell, D. DeMille, J. Doyle, G. Gabrielse, Y. Gurevich, P. Hess, N. R. Hutzler, E. Kirilov, *et al.*, Science **343**, 269 (2014).

[28] ACME Collaboration, V. Andreev, D. Ang, D. , DeMille, J. Doyle, G. Gabrielse, J. Haefner, N. Hutzler, Z. Lasner, C. Meisenhelder, B. O'Leary, C. Panda, A. West, E. West, and X. Wu, Nature **562**, 355 (2018).

[29] H. R. Pruppacher, J. D. Klett, and P. K. Wang, *Microphysics of clouds and precipitation* (Taylor & Francis, 1998).

[30] W. D. Phillips, Rev. Mod. Phys. **70**, 721 (1998).

[31] C. N. Cohen-Tannoudji, Rev. Mod. Phys. **70**, 707 (1998).

[32] T. W. Hänsch and A. L. Schawlow, Opt. Commun. **13**, 68 (1975).

[33] R. Grimm, M. Weidemüller, and Y. B. Ovchinnikov, in *Adv. At. Mol. Opt. Phys.*, Vol. 42 (Elsevier, 2000) pp. 95–170.

[34] D. Jaksch, C. Bruder, J. I. Cirac, C. W. Gardiner, and P. Zoller, Phys. Rev. Lett. **81**, 3108 (1998).

[35] C. Gross and I. Bloch, Science **357**, 995 (2017).

[36] W. Ketterle and N. Van Druten, in *Adv. At. Mol. Opt. Phys.*, Vol. 37 (Elsevier, 1996) pp. 181–236.

[37] C. Deppner, W. Herr, M. Cornelius, P. Stromberger, T. Sternke, C. Grzeschik, A. Grote, J. Rudolph, S. Herrmann, M. Krutzik, A. Wenzlawski, R. Corgier, E. Charron, D. Guéry-Odelin, N. Gaaloul, C. Lämmerzahl, A. Peters, P. Windpassinger, and E. M. Rasel, Phys. Rev. Lett. **127**, 100401 (2021).

[38] N. Gaaloul, M. Meister, R. Corgier, A. Pichery, P. Boegel, W. Herr, H. Ahlers, E. Charron, J. R. Williams, R. J. Thompson, *et al.*, Nat. Commun. **13**, 7889 (2022).

[39] R. V. Krems, Phys. Chem. Chem. Phys. **10**, 4079 (2008).

[40] N. Balakrishnan, J. Chem. Phys. **145**, 150901 (2016).

[41] M. H. Anderson, J. R. Ensher, M. R. Matthews, C. E. Wieman, and E. A. Cornell, Science **269**, 198 (1995).

[42] K. B. Davis, M.-O. Mewes, M. R. Andrews, N. J. van Druten, D. S. Durfee, D. Kurn, and W. Ketterle, Phys. Rev. Lett. **75**, 3969 (1995).

[43] F. Dalfovo, S. Giorgini, L. P. Pitaevskii, and S. Stringari, Rev. Mod. Phys. **71**, 463 (1999).

[44] A. J. Leggett, Rev. Mod. Phys. **73**, 307 (2001).

[45] S. N. Bose, Z. Phys. **26**, 178 (1924).

[46] L. Landau, Phys. Z. Sowjetunion **3**, 644 (1933).

[47] H. Fröhlich, Adv. Phys. **3**, 325 (1954).

[48] J. Tempere, W. Casteels, M. K. Oberthaler, S. Knoop, E. Timmermans, and J. T. Devreese, Phys. Rev. B **80**, 184504 (2009).

[49] S. P. Rath and R. Schmidt, Phys. Rev. A **88**, 053632 (2013).

[50] Y. Liu and K.-K. Ni, Annu. Rev. Phys. Chem. **73**, 73 (2022).

[51] B. Zhao and J.-W. Pan, Chem. Soc. Rev. **51**, 1685 (2022).

[52] P. S. Żuchowski and J. M. Hutson, Phys. Rev. A **81**, 060703(R) (2010).

[53] M. Mayle, B. P. Ruzic, and J. L. Bohn, Phys. Rev. A **85**, 062712 (2012).

[54] M. Mayle, G. Quéméner, B. P. Ruzic, and J. L. Bohn, Phys. Rev. A **87**, 012709 (2013).

[55] R. P. Feynman, Int. J. Theor. Phys **21**, 467 (1982).

[56] S. Lloyd, Science **273**, 1073 (1996).

[57] A. J. Daley, I. Bloch, C. Kokail, S. Flannigan, N. Pearson, M. Troyer, and P. Zoller, Nature **607**, 667 (2022).

[58] J. Preskill, Quantum **2**, 79 (2018).

[59] E. P. Wigner, Phys. Rev. **73**, 1002 (1948).

[60] H. Sadeghpour, J. Bohn, M. Cavagnero, B. Esry, I. Fabrikant, J. Macek, and A. Rau, J. Phys. B: At. Mol. Opt. Phys. **33**, R93 (2000).

[61] D. A. Steck, Report, Los Alamos National Laboratory, Los Alamos **124**, 74 (2000).

[62] T. Tiecke, *Feshbach resonances in ultracold mixtures of the fermionic quantum gases* (Ph. D. thesis, Universiteit van Amsterdam, 2009).

[63] A. Derevianko, J. F. Babb, and A. Dalgarno, Phys. Rev. A **63**, 052704 (2001).

[64] C. Chin, R. Grimm, P. Julienne, and E. Tiesinga, Rev. Mod. Phys. **82**, 1225 (2010).

[65] G. F. Gribakin and V. V. Flambaum, Phys. Rev. A **48**, 546 (1993).

[66] L. Chomaz, I. Ferrier-Barbut, F. Ferlaino, B. Laburthe-Tolra, B. L. Lev, and T. Pfau, Rep. Prog. Phys. **86**, 026401 (2022).

[67] A. Gerdes, M. Hobein, H. Knöckel, and E. Tiemann, Eur. Phys. J. D **49**, 67 (2008).

[68] I. Temelkov, H. Knöckel, A. Pashov, and E. Tiemann, Phys. Rev. A **91**, 032512 (2015).

[69] P. S. Julienne and J. M. Hutson, Phys. Rev. A **89**, 052715 (2014).

[70] T. Hartmann, T. A. Schulze, K. K. Voges, P. Gersema, M. W. Gempel, E. Tiemann, A. Zenesini, and S. Ospelkaus, Phys. Rev. A **99**, 032711 (2019).

[71] P. Żuchowski, M. Kosicki, M. Kodrycka, and P. Soldán, Phys. Rev. A **87**, 022706 (2013).

[72] E. Braaten and H.-W. Hammer, Phys. Rep. **428**, 259 (2006).

[73] E. A. Burt, R. W. Ghrist, C. J. Myatt, M. J. Holland, E. A. Cornell, and C. E. Wieman, Phys. Rev. Lett. **79**, 337 (1997).

[74] S. Liao and X. Li, Natl. Sci. Rev. **6**, 1070 (2019).

[75] L. H. Thomas, Phys. Rev. **47**, 903 (1935).

[76] V. Efimov, Phys. Lett. B **33**, 563 (1970).

[77] P. Naidon and S. Endo, Rep. Prog. Phys. **80**, 056001 (2017).

[78] T. Kraemer, M. Mark, P. Waldburger, J. G. Danzl, C. Chin, B. Engeser, A. D. Lange, K. Pilch, A. Jaakkola, H.-C. Nägerl, and R. Grimm, Nature **440**, 315–318 (2006).

[79] M. Berninger, A. Zenesini, B. Huang, W. Harm, H.-C. Nägerl, F. Ferlaino, R. Grimm, P. S. Julienne, and J. M. Hutson, Phys. Rev. Lett. **107**, 120401 (2011).

[80] J. Johansen, B. DeSalvo, K. Patel, and C. Chin, Nat. Phys. **13**, 731 (2017).

[81] R. Schmidt, S. P. Rath, and W. Zwerger, Eur. Phys. J. B **85**, 1 (2012).

[82] J. Wang, J. P. D'Incao, B. D. Esry, and C. H. Greene, Phys. Rev. Lett. **108**, 263001 (2012).

[83] P. Naidon, S. Endo, and M. Ueda, Phys. Rev. A **90**, 022106 (2014).

[84] J. P. D'Incao and B. D. Esry, Phys. Rev. A **73**, 030702 (2006).

[85] G. Barontini, C. Weber, F. Rabatti, J. Catani, G. Thalhammer, M. Inguscio, and F. Minardi, Phys. Rev. Lett. **103**, 043201 (2009).

[86] S.-K. Tung, K. Jiménez-García, J. Johansen, C. V. Parker, and C. Chin, Phys. Rev. Lett. **113**, 240402 (2014).

[87] R. Pires, J. Ulmanis, S. Häfner, M. Repp, A. Arias, E. D. Kuhnle, and M. Weidemüller, Phys. Rev. Lett. **112**, 250404 (2014).

[88] J. Von Stecher, J. Phys. B: At. Mol. Opt. Phys. **43**, 101002 (2010).

[89] J. von Stecher, Phys. Rev. Lett. **107**, 200402 (2011).

[90] F. Ferlaino, S. Knoop, M. Berninger, W. Harm, J. P. D'Incao, H.-C. Nägerl, and R. Grimm, Phys. Rev. Lett. **102**, 140401 (2009).

[91] A. Zenesini, B. Huang, M. Berninger, S. Besler, H.-C. Nägerl, F. Ferlaino, R. Grimm, C. H. Greene, and J. von Stecher, New J. Phys. **15**, 043040 (2013).

[92] P. Makotyn, C. E. Klauss, D. L. Goldberger, E. Cornell, and D. S. Jin, Nat. Phys. **10**, 116 (2014).

[93] S. Piatecki and W. Krauth, Nat. Commun. **5**, 1 (2014).

[94] U. Eismann, L. Khaykovich, S. Laurent, I. Ferrier-Barbut, B. S. Rem, A. T. Grier, M. Delehaye, F. Chevy, C. Salomon, L.-C. Ha, and C. Chin, Phys. Rev. X **6**, 021025 (2016).

[95] C. E. Klauss, X. Xie, C. Lopez-Abadia, J. P. D'Incao, Z. Hadzibabic, D. S. Jin, and E. A. Cornell, Phys. Rev. Lett. **119**, 143401 (2017).

[96] V. Colussi, J. P. Corson, and J. P. D'Incao, Phys. Rev. Lett. **120**, 100401 (2018).

[97] C. Eigen, J. A. Glidden, R. Lopes, E. A. Cornell, R. P. Smith, and Z. Hadzibabic, Nature **563**, 221 (2018).

[98] J. P. D'Incao, J. Wang, and V. E. Colussi, Phys. Rev. Lett. **121**, 023401 (2018).

[99] V. E. Colussi, H. Kurkjian, M. Van Regemortel, S. Musolino, J. van de Kraats, M. Wouters, and S. J. J. M. F. Kokkelmans, Phys. Rev. A **102**, 063314 (2020).

[100] S. Musolino, H. Kurkjian, M. Van Regemortel, M. Wouters, S. J. J. M. F. Kokkelmans, and V. E. Colussi, Phys. Rev. Lett. **128**, 020401 (2022).

[101] H. Suno and B. D. Esry, Phys. Rev. A **78**, 062701 (2008).

[102] J. Wang, J. P. D'Incao, and C. H. Greene, Phys. Rev. A **84**, 052721 (2011).

[103] B. R. Johnson, J. Chem. Phys. **69**, 4678 (1978).

[104] L. Hackl, T. Guaita, T. Shi, J. Haegeman, E. Demler, and J. I. Cirac, SciPost Phys. **9**, 48 (2020).

[105] L. Hackl and E. Bianchi, SciPost Phys. Core **4**, 025 (2021).

[106] T. Shi, E. Demler, and J. I. Cirac, Ann. Phys. **390**, 245 (2018).

[107] R. A. Fisher, M. M. Nieto, and V. D. Sandberg, Phys. Rev. D **29**, 1107 (1984).

[108] T. Shi, J. Pan, and S. Yi, arXiv:1909.02432 (2019), 10.48550/arXiv.1909.02432.

[109] T. Guaita, L. Hackl, T. Shi, C. Hubig, E. Demler, and J. I. Cirac, Phys. Rev. B **100**, 094529 (2019).

[110] M. A. De Gosson, *Symplectic methods in harmonic analysis and in mathematical physics*, Vol. 7 (Springer Science & Business Media, 2011).

[111] E. P. Gross, Il Nuovo Cimento (1955-1965) **20**, 454 (1961).

[112] L. P. Pitaevskii, Sov. Phys. JETP **13**, 451 (1961).

[113] T. D. Lee, K. Huang, and C. N. Yang, Phys. Rev. **106**, 1135 (1957).

[114] S. Beliaev, Sov. Phys. JETP **7**, 299 (1958).

[115] H. Shi and A. Griffin, Phys. Rep. **304**, 1 (1998).

[116] J. O. Andersen, Rev. Mod. Phys. **76**, 599 (2004).

[117] S. Cenatiempo, J. Math. Phys. **60**, 081901 (2019).

[118] C. Boccato, C. Brennecke, S. Cenatiempo, and B. Schlein, Commun. Math. Phys. **376**, 1311 (2020).

[119] D. S. Petrov, Phys. Rev. Lett. **115**, 155302 (2015).

[120] C. Cabrera, L. Tanzi, J. Sanz, B. Naylor, P. Thomas, P. Cheiney, and L. Tarruell, Science **359**, 301 (2018).

[121] P. Cheiney, C. Cabrera, J. Sanz, B. Naylor, L. Tanzi, and L. Tarruell, Phys. Rev. Lett. **120**, 135301 (2018).

[122] G. Semeghini, G. Ferioli, L. Masi, C. Mazzinghi, L. Wolswijk, F. Minardi, M. Modugno, G. Modugno, M. Inguscio, and M. Fattori, Phys. Rev. Lett. **120**, 235301 (2018).

[123] I. Ferrier-Barbut, H. Kadau, M. Schmitt, M. Wenzel, and T. Pfau, Phys. Rev. Lett. **116**, 215301 (2016).

[124] L. Chomaz, S. Baier, D. Petter, M. Mark, F. Wächtler, L. Santos, and F. Ferlaino, Phys. Rev. X **6**, 041039 (2016).

[125] N. Bogoliubov, J. Phys. **11**, 23 (1947).

[126] J. L. Bohn, M. Cavagnero, and C. Ticknor, New J. Phys. **11**, 055039 (2009).

[127] J. L. Bohn and D. S. Jin, Phys. Rev. A **89**, 022702 (2014).

[128] A. R. Lima and A. Pelster, Phys. Rev. A **84**, 041604 (2011).

[129] A. R. P. Lima and A. Pelster, Phys. Rev. A **86**, 063609 (2012).

[130] C. A. Regal, M. Greiner, and D. S. Jin, Phys. Rev. Lett. **92**, 040403 (2004).

[131] C. Chin, M. Bartenstein, A. Altmeyer, S. Riedl, S. Jochim, J. H. Denschlag, and R. Grimm, Science **305**, 1128 (2004).

[132] M. W. Zwierlein, C. A. Stan, C. H. Schunck, S. M. F. Raupach, A. J. Kerman, and W. Ketterle, Phys. Rev. Lett. **92**, 120403 (2004).

[133] T. Bourdel, L. Khaykovich, J. Cubizolles, J. Zhang, F. Chevy, M. Teichmann, L. Tarruell, S. J. J. M. F. Kokkelmans, and C. Salomon, Phys. Rev. Lett. **93**, 050401 (2004).

[134] W. Zwerger, *The BCS-BEC crossover and the unitary Fermi gas*, Vol. 836 (Springer Science & Business Media, 2011).

[135] G. C. Strinati, P. Pieri, G. Röpke, P. Schuck, and M. Urban, Phys. Rep. **738**, 1 (2018).

[136] D. M. Eagles, Phys. Rev. **186**, 456 (1969).

[137] F. Chevy, Phys. Rev. A **74**, 063628 (2006).

[138] N. Prokof'ev and B. Svistunov, Phys. Rev. B **77**, 020408 (2008).

[139] M. Punk, P. T. Dumitrescu, and W. Zwerger, Phys. Rev. A **80**, 053605 (2009).

[140] A. Schirotzek, C.-H. Wu, A. Sommer, and M. W. Zwierlein, Phys. Rev. Lett. **102**, 230402 (2009).

[141] C. Kohstall, M. Zaccanti, M. Jag, A. Trenkwalder, P. Massignan, G. M. Bruun, F. Schreck, and R. Grimm, Nature **485**, 615 (2012).

[142] G. Ness, C. Shkedrov, Y. Florshaim, O. K. Diessel, J. von Milczewski, R. Schmidt, and Y. Sagi, Phys. Rev. X **10**, 041019 (2020).

[143] C. J. M. Mathy, M. M. Parish, and D. A. Huse, Phys. Rev. Lett. **106**, 166404 (2011).

[144] M.-G. Hu, M. J. Van de Graaff, D. Kedar, J. P. Corson, E. A. Cornell, and D. S. Jin, Phys. Rev. Lett. **117**, 055301 (2016).

[145] N. B. Jørgensen, L. Wacker, K. T. Skalmstang, M. M. Parish, J. Levinsen, R. S. Christensen, G. M. Bruun, and J. J. Arlt, Phys. Rev. Lett. **117**, 055302 (2016).

[146] Z. Z. Yan, Y. Ni, C. Robens, and M. W. Zwierlein, Science **368**, 190 (2020).

[147] J. Levinsen, M. M. Parish, and G. M. Bruun, Phys. Rev. Lett. **115**, 125302 (2015).

[148] M. Sun and X. Cui, Phys. Rev. A **96**, 022707 (2017).

[149] S. M. Yoshida, S. Endo, J. Levinsen, and M. M. Parish, Phys. Rev. X **8**, 011024 (2018).

[150] J. Levinsen, L. A. P. Ardila, S. M. Yoshida, and M. M. Parish, Phys. Rev. Lett. **127**, 033401 (2021).

[151] L. A. P. Ardila and S. Giorgini, Phys. Rev. A **92**, 033612 (2015).

[152] Y. E. Shchadilova, R. Schmidt, F. Grusdt, and E. Demler, Phys. Rev. Lett. **117**, 113002 (2016).

[153] F. Grusdt, R. Schmidt, Y. E. Shchadilova, and E. Demler, Phys. Rev. A **96**, 013607 (2017).

[154] J. P. D'Incao and B. D. Esry, Phys. Rev. A **73**, 030703 (2006).

[155] T. D. Lee, F. E. Low, and D. Pines, Phys. Rev. **90**, 297 (1953).

[156] R. Jastrow, Phys. Rev. **98**, 1479 (1955).

[157] M. Drescher, M. Salmhofer, and T. Enss, Phys. Rev. Research **2**, 032011 (2020).

[158] T. Shi, E. Demler, and J. I. Cirac, Phys. Rev. Lett. **125**, 180602 (2020).

[159] D. Blume, Phys. Rev. A **99**, 013613 (2019).

[160] R. Chapurin, X. Xie, M. J. Van de Graaff, J. S. Popowski, J. P. D'Incao, P. S. Julienne, J. Ye, and E. A. Cornell, Phys. Rev. Lett. **123**, 233402 (2019).

[161] X. Xie, M. J. Van de Graaff, R. Chapurin, M. D. Frye, J. M. Hutson, J. P. D'Incao, P. S. Julienne, J. Ye, and E. A. Cornell, Phys. Rev. Lett. **125**, 243401 (2020).

[162] E. Hiyama and M. Kamimura, Phys. Rev. A **90**, 052514 (2014).

[163] N.-E. Guenther, R. Schmidt, G. M. Bruun, V. Gurarie, and P. Massignan, Phys. Rev. A **103**, 013317 (2021).

[164] M. Drescher, M. Salmhofer, and T. Enss, Phys. Rev. A **99**, 023601 (2019).

[165] R. A. W. Maier, M. Eisele, E. Tiemann, and C. Zimmermann, Phys. Rev. Lett. **115**, 043201 (2015).

[166] B. Huang, I. Fritsche, R. S. Lous, C. Baroni, J. T. M. Walraven, E. Kirilov, and R. Grimm, Phys. Rev. A **99**, 041602 (2019).

[167] C. J. Pethick and H. Smith, *Bose-Einstein condensation in dilute gases* (Cambridge university press, 2008).

[168] J. Ulmanis, S. Häfner, R. Pires, E. D. Kuhnle, Y. Wang, C. H. Greene, and M. Weidemüller, Phys. Rev. Lett. **117**, 153201 (2016).

[169] M. Eisele, R. A. W. Maier, and C. Zimmermann, Phys. Rev. Lett. **124**, 123401 (2020).

[170] M. Drescher, M. Salmhofer, and T. Enss, Phys. Rev. A **103**, 033317 (2021).

[171] K. Seetharam, Y. Shchadilova, F. Grusdt, M. B. Zvonarev, and E. Demler, Phys. Rev. Lett. **127**, 185302 (2021).

[172] R. Schmidt and M. Lemeshko, Phys. Rev. Lett. **114**, 203001 (2015).

[173] R. Schmidt and M. Lemeshko, Phys. Rev. X **6**, 011012 (2016).

[174] M. Lemeshko, Phys. Rev. Lett. **118**, 095301 (2017).

[175] A. Camacho-Guardian and G. M. Bruun, Phys. Rev. X **8**, 031042 (2018).

[176] P. Naidon, J. Phys. Soc. Japan **87**, 043002 (2018).

[177] G. Panochko and V. Pastukhov, J. Phys. A **54**, 085001 (2021).

[178] K. Huang, *Statistical Mechanics*, 2nd ed. (John Wiley & Sons, 1987).

[179] E. Perlt, *Basis Sets in Computational Chemistry* (Springer, 2021).

[180] G. D. Byrne and A. C. Hindmarsh, ACM Trans. Math. Softw. **1**, 71 (1975).

[181] P. Virtanen *et al.*, Nat. Methods **17**, 261 (2020).

[182] P. Jeszenszki, A. Y. Cherny, and J. Brand, Phys. Rev. A **97**, 042708 (2018).

[183] V. V. Flambaum, G. F. Gribakin, and C. Harabati, Phys. Rev. A **59**, 1998 (1999).

[184] M. Berninger, A. Zenesini, B. Huang, W. Harm, H.-C. Nägerl, F. Ferlaino, R. Grimm, P. S. Julienne, and J. M. Hutson, Phys. Rev. Lett. **107**, 120401 (2011).

[185] P. Massignan, N. Yegovtsev, and V. Gurarie, Phys. Rev. Lett. **126**, 123403 (2021).

[186] R. Schmidt and T. Enss, SciPost Phys. **13**, 054 (2022).

[187] P. Zhang, P. Naidon, and M. Ueda, Phys. Rev. Lett. **103**, 133202 (2009).

[188] F. K. Fatemi, K. M. Jones, and P. D. Lett, Phys. Rev. Lett. **85**, 4462 (2000).

[189] L. W. Clark, L.-C. Ha, C.-Y. Xu, and C. Chin, Phys. Rev. Lett. **115**, 155301 (2015).

[190] D. J. Papoular, G. V. Shlyapnikov, and J. Dalibard, Phys. Rev. A **81**, 041603 (2010).

[191] M. G. Skou, T. G. Skov, N. B. Jørgensen, K. K. Nielsen, A. Camacho-Guardian, T. Pohl, G. M. Bruun, and J. J. Arlt, Nat. Phys. **17**, 731 (2021).

[192] N.-E. Guenther, P. Massignan, M. Lewenstein, and G. M. Bruun, Phys. Rev. Lett. **120**, 050405 (2018).

[193] B. Field, J. Levinsen, and M. M. Parish, Phys. Rev. A **101**, 013623 (2020).

[194] D. Dzsotjan, R. Schmidt, and M. Fleischhauer, Phys. Rev. Lett. **124**, 223401 (2020).

[195] G. Pascual and J. Boronat, Phys. Rev. Lett. **127**, 205301 (2021).

[196] D. H. Santamore and E. Timmermans, Phys. Rev. A **78**, 013619 (2008).

[197] D. Ludwig, S. Floerchinger, S. Moroz, and C. Wetterich, Phys. Rev. A **84**, 033629 (2011).

[198] J. J. Kinnunen and G. M. Bruun, Phys. Rev. A **91**, 041605 (2015).

[199] B. J. DeSalvo, K. Patel, G. Cai, and C. Chin, Nature **568**, 61 (2019).

[200] X.-Y. Chen, M. Duda, A. Schindewolf, R. Bause, I. Bloch, and X.-Y. Luo, Phys. Rev. Lett. **128**, 153401 (2022).

[201] L. B. Tan, O. K. Diessel, A. Popert, R. Schmidt, A. Imamoğlu, and M. Kroner, preprint (2022), arXiv:2212.11145 [cond-mat.quant-gas] .

[202] R. Sack, J. Math. Phys. **5**, 245 (1964).

[203] I. S. Gradshteyn and I. M. Ryzhik, *Table of integrals, series, and products* (Academic press, 2014).

[204] C. Ospelkaus, S. Ospelkaus, L. Humbert, P. Ernst, K. Sengstock, and K. Bongs, Phys. Rev. Lett. **97**, 120402 (2006).

[205] C. Klempt, T. Henninger, O. Topic, M. Scherer, L. Kattner, E. Tiemann, W. Ertmer, and J. J. Arlt, Phys. Rev. A **78**, 061602 (2008).

[206] C.-H. Wu, J. W. Park, P. Ahmadi, S. Will, and M. W. Zwierlein, Phys. Rev. Lett. **109**, 085301 (2012).

[207] S. Knoop, T. Schuster, R. Scelle, A. Trautmann, J. Appmeier, M. K. Oberthaler, E. Tiesinga, and E. Tiemann, Phys. Rev. A **83**, 042704 (2011).

[208] N. Navon, R. P. Smith, and Z. Hadzibabic, Nat. Phys. **17**, 1334 (2021).

[209] L. De Marco, G. Valtolina, K. Matsuda, W. G. Tobias, J. P. Covey, and J. Ye, Science **363**, 853 (2019).

[210] M. Duda, X.-Y. Chen, A. Schindewolf, R. Bause, J. von Milczewski, R. Schmidt, I. Bloch, and X.-Y. Luo, Nat. Phys. **19**, 1 (2023).

[211] T. Zelevinsky, S. Kotochigova, and J. Ye, Phys. Rev. Lett. **100**, 043201 (2008).

[212] G. E. Astrakharchik, J. Boronat, I. L. Kurbakov, and Y. E. Lozovik, Phys. Rev. Lett. **98**, 060405 (2007).

[213] N. Matveeva and S. Giorgini, Phys. Rev. Lett. **109**, 200401 (2012).

[214] D. Peter, S. Müller, S. Wessel, and H. P. Büchler, Phys. Rev. Lett. **109**, 025303 (2012).

[215] M. A. Baranov, M. Dalmonte, G. Pupillo, and P. Zoller, Chem. Rev. **112**, 5012 (2012).

[216] T.-S. Zeng and L. Yin, Phys. Rev. B **89**, 174511 (2014).

[217] O. Dutta, M. Gajda, P. Hauke, M. Lewenstein, D.-S. Lühmann, B. A. Malomed, T. Sowiński, and J. Zakrzewski, Rep. Prog. Phys. **78**, 066001 (2015).

[218] Z. Wu, J. K. Block, and G. M. Bruun, Sci. Rep. **6**, 19038 (2016).

[219] M. Schmidt, L. Lassablière, G. Quéméner, and T. Langen, Phys. Rev. Res. **4**, 013235 (2022).

[220] D. DeMille, Phys. Rev. Lett. **88**, 067901 (2002).

[221] K.-K. Ni, T. Rosenband, and D. D. Grimes, Chem. Sci. **9**, 6830 (2018).

[222] M.-G. Hu, Y. Liu, M. A. Nichols, L. Zhu, G. Quéméner, O. Dulieu, and K.-K. Ni, Nat. Chem. **13**, 435 (2021).

[223] D. McCarron, J. Phys. B: At. Mol. Opt. Phys. **51**, 212001 (2018).

[224] K. Bergmann, H. Theuer, and B. W. Shore, Rev. Mod. Phys. **70**, 1003 (1998).

[225] N. V. Vitanov, A. A. Rangelov, B. W. Shore, and K. Bergmann, Rev. Mod. Phys. **89**, 015006 (2017).

[226] K.-K. Ni, S. Ospelkaus, M. De Miranda, A. Pe'Er, B. Neyenhuis, J. Zirbel, S. Kotochigova, P. Julienne, D. Jin, and J. Ye, Science **322**, 231 (2008).

[227] S. Ospelkaus, K.-K. Ni, D. Wang, M. De Miranda, B. Neyenhuis, . G. Quéméner, P. Julienne, J. Bohn, D. Jin, and J. Ye, Science **327**, 853 (2010).

[228] T. Takekoshi, L. Reichsöllner, A. Schindewolf, J. M. Hutson, C. R. L. Sueur, O. Dulieu, F. Ferlaino, R. Grimm, and H.-C. Nägerl, Phys. Rev. Lett. **113**, 205301 (2014).

[229] J. W. Park, S. A. Will, and M. W. Zwierlein, Phys. Rev. Lett. **114**, 205302 (2015).

[230] M. Guo, X. Ye, J. He, M. L. González-Martínez, R. Vexiau, G. Quéméner, and D. Wang, Phys. Rev. X **8**, 041044 (2018).

[231] X. Ye, M. Guo, M. L. González-Martínez, G. Quéméner, and D. Wang, Sci. Adv. **4**, eaaq0083 (2018).

[232] M.-G. Hu, Y. Liu, D. D. Grimes, Y.-W. Lin, A. H. Gheorghe, R. Vexiau, N. Bouloufa-Maafa, O. Dulieu, T. Rosenband, and K.-K. Ni, Science **366**, 1111 (2019).

[233] Y. Liu, M.-G. Hu, M. A. Nichols, D. D. Grimes, T. Karman, H. Guo, and K.-K. Ni, Nat. Phys. **16**, 1132–1136 (2020).

[234] P. D. Gregory, J. A. Blackmore, S. L. Bromley, and S. L. Cornish, Phys. Rev. Lett. **124**, 163402 (2020).

[235] P. Gersema, K. K. Voges, M. Meyer zum Alten Borgloh, L. Koch, T. Hartmann, A. Zenesini, S. Ospelkaus, J. Lin, J. He, and D. Wang, Phys. Rev. Lett. **127**, 163401 (2021).

[236] F. H. Mies, J. Chem. Phys. **80**, 2514 (1984).

[237] F. H. Mies and P. S. Julienne, J. Chem. Phys. **80**, 2526 (1984).

[238] J. P. Burke, C. H. Greene, and J. L. Bohn, Phys. Rev. Lett. **81**, 3355 (1998).

[239] J. F. E. Croft and J. L. Bohn, Phys. Rev. A **89**, 012714 (2014).

[240] J. F. E. Croft, C. Makrides, M. Li, A. Petrov, B. K. Kendrick, N. Balakrishnan, and S. Kotochigova, Nat. Commun. **8**, 15897 (2017).

[241] J. F. E. Croft, N. Balakrishnan, and B. K. Kendrick, Phys. Rev. A **96**, 062707 (2017).

[242] O. K. Rice and H. C. Ramsperger, J. Am. Chem. Soc. **49**, 1617 (1927).

[243] L. S. Kassel, J. Phys. Chem. **32**, 225 (1928).

[244] R. A. Marcus, J. Chem. Phys. **20**, 359 (1952).

[245] L. D'Alessio, Y. Kafri, A. Polkovnikov, and M. Rigol, Adv. Phys. **65**, 239 (2016).

[246] T. M. Rvachov, H. Son, A. T. Sommer, S. Ebadi, J. J. Park, M. W. Zwierlein, W. Ketterle, and A. O. Jamison, Phys. Rev. Lett. **119**, 143001 (2017).

[247] Z. Idziaszek and P. S. Julienne, Phys. Rev. Lett. **104**, 113202 (2010).

[248] G. E. Mitchell, A. Richter, and H. A. Weidenmüller, Rev. Mod. Phys. **82**, 2845 (2010).

[249] J. F. E. Croft, J. L. Bohn, and G. Quéméner, Phys. Rev. A **107**, 023304 (2023).

[250] K. K. Voges, P. Gersema, T. Hartmann, S. Ospelkaus, and A. Zenesini, Phys. Rev. Res. **4**, 023184 (2022).

[251] M. P. Man, G. C. Groenenboom, and T. Karman, Phys. Rev. Lett. **129**, 243401 (2022).

[252] P. D. Gregory, J. A. Blackmore, M. D. Frye, L. M. Fernley, S. L. Bromley, J. M. Hutson, and S. L. Cornish, New J. Phys. **23**, 125004 (2021).

[253] Y. Liu, D. D. Grimes, M.-G. Hu, and K.-K. Ni, Phys. Chem. Chem. Phys. **22**, 4861 (2020).

[254] K. Jachymski, M. Gronowski, and M. Tomza, Phys. Rev. A **106**, L041301 (2022).

[255] K. M. Jones, E. Tiesinga, P. D. Lett, and P. S. Julienne, Rev. Mod. Phys. **78**, 483 (2006).

[256] B. K. Kendrick, H. Li, M. Li, S. Kotochigova, J. F. E. Croft, and N. Balakrishnan, Phys. Chem. Chem. Phys. **23**, 5096 (2021).

[257] H. Yang, D.-C. Zhang, L. Liu, Y.-X. Liu, J. Nan, B. Zhao, and J.-W. Pan, Science **363**, 261 (2019).

[258] X.-Y. Wang, M. D. Frye, Z. Su, J. Cao, L. Liu, D.-C. Zhang, H. Yang, J. M. Hutson, B. Zhao, C.-L. Bai, and J.-W. Pan, New J. Phys. **23**, 115010 (2021).

[259] M. A. Nichols, Y.-X. Liu, L. Zhu, M.-G. Hu, Y. Liu, and K.-K. Ni, Phys. Rev. X **12**, 011049 (2022).

[260] M. De Miranda, A. Chotia, B. Neyenhuis, D. Wang, G. Quéméner, S. Ospelkaus, J. Bohn, J. Ye, and D. Jin, Nat. Phys. **7**, 502 (2011).

[261] K. Matsuda, L. De Marco, J.-R. Li, W. G. Tobias, G. Valtolina, G. Quéméner, and J. Ye, Science **370**, 1324 (2020).

[262] T. Karman and J. M. Hutson, Phys. Rev. Lett. **121**, 163401 (2018).

[263] L. Lassablière and G. Quéméner, Phys. Rev. Lett. **121**, 163402 (2018).

[264] A. Schindewolf, R. Bause, X.-Y. Chen, M. Duda, T. Karman, I. Bloch, and X.-Y. Luo, Nature **607**, 677 (2022).

[265] I. M. Georgescu, S. Ashhab, and F. Nori, Rev. Mod. Phys. **86**, 153 (2014).

[266] F. Arute, K. Arya, R. Babbush, D. Bacon, J. C. Bardin, R. Barends, R. Biswas, S. Boixo, F. G. Brandao, D. A. Buell, *et al.*, Nature **574**, 505 (2019).

[267] H.-S. Zhong, H. Wang, Y.-H. Deng, M.-C. Chen, L.-C. Peng, Y.-H. Luo, J. Qin, D. Wu, X. Ding, Y. Hu, *et al.*, Science **370**, 1460 (2020).

[268] L. S. Madsen, F. Laudenbach, M. F. Askarani, F. Rortais, T. Vincent, J. F. Bulmer, F. M. Miatto, L. Neuhaus, L. G. Helt, M. J. Collins, *et al.*, Nature **606**, 75 (2022).

[269] Y. Kim, A. Eddins, S. Anand, K. X. Wei, E. Van Den Berg, S. Rosenblatt, H. Nayfeh, Y. Wu, M. Zaletel, K. Temme, *et al.*, Nature **618**, 500 (2023).

[270] F. Pan, K. Chen, and P. Zhang, Phys. Rev. Lett. **129**, 090502 (2022).

[271] C. Oh, L. Jiang, and B. Fefferman, preprint (2023), arXiv:2301.11532 [quant-ph] .

[272] C. Oh, M. Liu, Y. Alexeev, B. Fefferman, and L. Jiang, preprint (2023), arXiv:2306.03709 [quant-ph] .

[273] J. Tindall, M. Fishman, M. Stoudenmire, and D. Sels, preprint (2023), arXiv:2306.14887 [quant-ph] .

[274] E. Altman *et al.*, PRX Quantum **2**, 1 (2021).

[275] M. Srednicki, J. Phys. A Math. Gen. **32**, 1163 (1999).

[276] M. Rigol, V. Dunjko, and M. Olshanii, Nature **452**, 854 (2008).

[277] L. D'Alessio, Y. Kafri, A. Polkovnikov, and M. Rigol, Adv. Phys. **65**, 239 (2016).

[278] J. M. Deutsch, Rep. Prog. in Phys. **81**, 082001 (2018).

[279] N. Goldman and J. Dalibard, Phys. Rev. X **4**, 031027 (2014).

[280] M. Bukov, L. D'Alessio, and A. Polkovnikov, Adv. Phys. **64**, 139 (2015).

[281] R. Moessner and S. L. Sondhi, Nat. Phys. **13**, 424 (2017).

[282] L. M. Sieberer, T. Olsacher, A. Elben, M. Heyl, P. Hauke, F. Haake, and P. Zoller, NPJ Quantum Inf. **5**, 1 (2019).

[283] C. Kargi, J. P. Dehollain, F. Henriques, L. M. Sieberer, T. Olsacher, P. Hauke, M. Heyl, P. Zoller, and N. K. Langford, preprint (2021), arXiv:2110.11113 [quant-ph] .

[284] A. Morningstar, D. A. Huse, and V. Khemani, preprint (2022), arXiv:2210.13444 [cond-mat.stat-mech] .

[285] A. Lazarides, A. Das, and R. Moessner, Phys. Rev. E **90**, 1 (2014).

[286] L. D'Alessio and M. Rigol, Phys. Rev. X **4**, 1 (2014).

[287] D. Abanin, W. De Roeck, and F. Huveneers, Phys. Rev. Lett. **115**, 256803 (2015).

[288] T. Kuwahara, T. Mori, and K. Saito, Ann. Phys. **367**, 96 (2016).

[289] T. Mori, T. Kuwahara, and K. Saito, Phys. Rev. Lett. **116**, 120401 (2016).

[290] D. V. Else, B. Bauer, and C. Nayak, Phys. Rev. X **7**, 011026 (2017).

[291] T. Mori, T. N. Ikeda, E. Kaminishi, and M. Ueda, J. Phys. C: Solid State Phys. **51**, 112001 (2018).

[292] A. Rubio-Abadal, M. Ippoliti, S. Hollerith, D. Wei, J. Rui, S. L. Sondhi, V. Khemani, C. Gross, and I. Bloch, Phys. Rev. X **10**, 021044 (2020).

[293] P. Peng, C. Yin, X. Huang, C. Ramanathan, and P. Cappellaro, Nat. Phys. **17**, 444 (2021).

[294] A. Morningstar, M. Hauru, J. Beall, M. Ganahl, A. G. Lewis, V. Khemani, and G. Vidal, PRX Quantum **3**, 020331 (2022).

[295] A. Pizzi, A. Nunnenkamp, and J. Knolle, Phys. Rev. Lett. **127**, 140602 (2021).

[296] B. Ye, F. Machado, and N. Y. Yao, Phys. Rev. Lett. **127**, 140603 (2021).

[297] N. Hatano and M. Suzuki, in *Quantum annealing and other optimization methods* (Springer, 2005) pp. 37–68.

[298] A. M. Childs, Y. Su, M. C. Tran, N. Wiebe, and S. Zhu, Phys. Rev. X **11**, 11020 (2021).

[299] E. H. Lieb and D. W. Robinson, Commun. Math. Phys. **28**, 251 (1972).

[300] D. Janzing and P. Wocjan, Quantum Inf. Process. **4**, 129 (2005).

[301] M. Hartmann, G. Mahler, and O. Hess, Lett. Math. Phys. **68**, 103 (2004).

[302] C. Fleckenstein and M. Bukov, Phys. Rev. B **103**, L140302 (2021).

[303] W. Magnus, Commun. Pure Appl. Math. **7**, 649 (1954).

[304] S. Blanes, F. Casas, J. A. Oteo, and J. Ros, Phys. Rep. **470**, 151 (2009).

[305] B. Foxen *et al.* (Google AI Quantum), Phys. Rev. Lett. **125**, 120504 (2020).

[306] E. Loh, D. J. Scalapino, and P. M. Grant, Phys. Scr. **32**, 327 (1985).

[307] H. Q. Ding, Phys. Rev. B **45**, 230 (1992).

[308] J. M. Kosterlitz and D. J. Thouless, J. Phys. C: Solid State Phys. **6**, 1181 (1973).

[309] K. Temme, S. Bravyi, and J. M. Gambetta, Phys. Rev. Lett. **119**, 1 (2017).

[310] S. Endo, S. C. Benjamin, and Y. Li, Phys. Rev.X **8**, 1 (2018).

[311] Z. Cai, R. Babbush, S. C. Benjamin, S. Endo, W. J. Huggins, Y. Li, J. R. McClean, and T. E. O'Brien, preprint (2022), arXiv:2210.00921 [quant-ph] .

[312] X. Mi *et al.*, Science **374**, 1479 (2021).

[313] T. E. O'Brien, S. Polla, N. C. Rubin, W. J. Huggins, S. McArdle, S. Boixo, J. R. McClean, and R. Babbush, PRX Quantum **2**, 020317 (2021).

[314] M. Huo and Y. Li, Phys. Rev. A **105**, 022427 (2022).

[315] S. Lu, M. C. Bañuls, and J. I. Cirac, PRX Quantum **2**, 020321 (2021).

[316] X. Mi *et al.*, Science **378**, 785 (2022).

[317] K. X. Wei *et al.*, Phys. Rev. Lett. **129**, 060501 (2022).

[318] E. Magesan, D. Puzzuoli, C. E. Granade, and D. G. Cory, Phys. Rev. A **87**, 1 (2013).

[319] M. Gutiérrez, L. Svec, A. Vargo, and K. R. Brown, Phys. Rev. A **87**, 1 (2013).

[320] M. R. Geller and Z. Zhou, Phys. Rev. A **88**, 1 (2013).

[321] Z. Cai and S. C. Benjamin, Sci. Rep. **9**, 11281 (2019).

[322] C. Developers, "Cirq," (2022), See full list of authors on Github: https://github.com/quantumlib/Cirq/graphs/contributors.

[323] K. J. Satzinger *et al.*, Science **374**, 1237 (2021).

[324] C. J. Turner, A. A. Michailidis, D. A. Abanin, M. Serbyn, and Z. Papić, Nat. Phys. **14**, 745 (2018).

[325] C.-J. Lin and O. I. Motrunich, Phys. Rev. Lett. **122**, 173401 (2019).

[326] A. Pal and D. A. Huse, Phys. Rev. B **82**, 174411 (2010).

[327] D. A. Abanin, E. Altman, I. Bloch, and M. Serbyn, Rev. Mod. Phys. **91**, 21001 (2018).

[328] E. Y. Loh, J. E. Gubernatis, R. T. Scalettar, S. R. White, D. J. Scalapino, and R. L. Sugar, Phys. Rev. B **41**, 9301 (1990).

[329] M. Takasu, S. Miyashita, and M. Suzuki, Prog. Theor. Phys. **75**, 1254 (1986).

[330] N. Hatano and M. Suzuki, Phys. Lett. A **163**, 246 (1992).

[331] Y. Yang, J. I. Cirac, and M. C. Bañuls, Phys. Rev. B **106**, 024307 (2022).

[332] A. Çakan, J. I. Cirac, and M. C. Bañuls, Phys. Rev. B **103**, 115113 (2021).

[333] M. A. Nielsen and I. L. Chuang, *Quantum Computation and Quantum Information: 10th Anniversary Edition* (Cambridge University Press, 2010) pp. 378–386.

[334] Z. Zhang, S. Nagata, K.-X. Yao, and C. Chin, Nat. Phys. (2023), 10.1038/s41567-023-02139-8.

[335] L. Tanzi, E. Lucioni, F. Famà, J. Catani, A. Fioretti, C. Gabbanini, R. N. Bisset, L. Santos, and G. Modugno, Phys. Rev. Lett. **122**, 130405 (2019).

[336] L. Chomaz, D. Petter, P. Ilzhöfer, G. Natale, A. Trautmann, C. Politi, G. Durastante, R. M. W. van Bijnen, A. Patscheider, M. Sohmen, M. J. Mark, and F. Ferlaino, Phys. Rev. X **9**, 021012 (2019).

[337] F. Böttcher, J.-N. Schmidt, M. Wenzel, J. Hertkorn, M. Guo, T. Langen, and T. Pfau, Phys. Rev. X **9**, 011051 (2019).

[338] R. N. Bisset, L. A. P. Ardila, and L. Santos, Phys. Rev. Lett. **126**, 025301 (2021).

[339] D. Scheiermann, L. A. P. Ardila, T. Bland, R. N. Bisset, and L. Santos, Phys. Rev. A **107**, L021302 (2023).

[340] B. Kain and H. Y. Ling, Phys. Rev. A **89**, 023612 (2014).

[341] L. A. P. Ardila and T. Pohl, J. Phys. B: At. Mol. Opt. Phys. **52**, 015004 (2018).

[342] A. G. Volosniev, G. Bighin, L. Santos, and L. A. P. Ardila, preprint (2023), arXiv:2305.17969 [cond-mat.quant-gas] .

[343] A. Trautmann, P. Ilzhöfer, G. Durastante, C. Politi, M. Sohmen, M. J. Mark, and F. Ferlaino, Phys. Rev. Lett. **121**, 213601 (2018).

[344] C. Ravensbergen, V. Corre, E. Soave, M. Kreyer, E. Kirilov, and R. Grimm, Phys. Rev. A **98**, 063624 (2018).

[345] A. Ciamei, S. Finelli, A. Trenkwalder, M. Inguscio, A. Simoni, and M. Zaccanti, Phys. Rev. Lett. **129**, 093402 (2022).

[346] A. Frisch, M. Mark, K. Aikawa, F. Ferlaino, J. L. Bohn, C. Makrides, A. Petrov, and S. Kotochigova, Nature **507**, 475 (2014).

[347] T. Maier, I. Ferrier-Barbut, H. Kadau, M. Schmitt, M. Wenzel, C. Wink, T. Pfau, K. Jachymski, and P. S. Julienne, Phys. Rev. A **92**, 060702 (2015).

[348] A. Frisch, M. Mark, K. Aikawa, S. Baier, R. Grimm, A. Petrov, S. Kotochigova, G. Quéméner, M. Lepers, O. Dulieu, and F. Ferlaino, Phys. Rev. Lett. **115**, 203201 (2015).

[349] E. Soave, A. Canali, Z.-X. Ye, M. Kreyer, E. Kirilov, and R. Grimm, preprint (2023), arXiv:2304.07921 [cond-mat.quant-gas] .

[350] G. Durastante, C. Politi, M. Sohmen, P. Ilzhöfer, M. J. Mark, M. A. Norcia, and F. Ferlaino, Phys. Rev. A **102**, 033330 (2020).

[351] F. Deng, X.-Y. Chen, X.-Y. Luo, W. Zhang, S. Yi, and T. Shi, Phys. Rev. Lett. **130**, 183001 (2023).

[352] L. Anderegg, S. Burchesky, Y. Bao, S. S. Yu, T. Karman, E. Chae, K.-K. Ni, W. Ketterle, and J. M. Doyle, Science **373**, 779 (2021).

[353] X.-Y. Chen, A. Schindewolf, S. Eppelt, R. Bause, M. Duda, S. Biswas, T. Karman, T. Hilker, I. Bloch, and X.-Y. Luo, arXiv preprint , arXiv:2210.13324 (2022), accessed 25 October 2022.

[354] X.-Y. Chen, S. Biswas, S. Eppelt, A. Schindewolf, F. Deng, T. Shi, S. Yi, T. A. Hilker, I. Bloch, and X.-Y. Luo, preprint (2023), arXiv:2306.00962 [cond-mat.quant-gas] .

[355] A. J. Leggett, Rev. Mod. Phys. **71**, S318 (1999).

[356] M. Barranco, R. Guardiola, S. Hernández, R. Mayol, J. Navarro, and M. Pi, J. Low Temp. Phys. **142**, 1 (2006).

[357] R. A. Aziz and M. J. Slaman, J. Chem. Phys. **94**, 8047 (1991).

[358] A. Mukhopadhyay, S. S. Xantheas, and R. J. Saykally, Chem. Phys. Lett. **700**, 163 (2018).

[359] M. Kunitski, S. Zeller, J. Voigtsberger, A. Kalinin, L. P. H. Schmidt, M. Schöffler, A. Czasch, W. Schöllkopf, R. E. Grisenti, T. Jahnke, D. Blume, and R. Dörner, Science **348**, 551 (2015).

[360] A. Slenczka and J. P. Toennies, *Molecules in Superfluid Helium Nanodroplets: Spectroscopy, Structure, and Dynamics* (Springer Nature, 2022).

[361] J. P. Toennies and A. F. Vilesov, Angew. Chem. Int. Ed. **43**, 2622 (2004).

[362] S. Yang and A. M. Ellis, Chem. Soc. Rev. **42**, 472 (2013).

[363] E.-M. Lottner and A. Slenczka, J. Phys. Chem. A **124**, 311 (2019).

[364] E. García-Alfonso, M. Barranco, D. A. Bonhommeau, N. Halberstadt, M. Pi, and F. Calvo, J. Chem. Phys. **157**, 014106 (2022).

[365] D. Pentlehner, J. H. Nielsen, A. Slenczka, K. Mølmer, and H. Stapelfeldt, Phys. Rev. Lett. **110**, 093002 (2013).

[366] H. R. Glyde, R. T. Azuah, and W. G. Stirling, Phys. Rev. B **62**, 14337 (2000).

[367] S. Moroni and M. Boninsegni, J. Low Temp. Phys. **136**, 129 (2004).

[368] E. Yakaboylu, B. Midya, A. Deuchert, N. Leopold, and M. Lemeshko, Phys. Rev. B **98**, 224506 (2018).

[369] C. Baroni, B. Huang, I. Fritsche, E. Dobler, G. Anich, E. Kirilov, R. Grimm, M. A. Bastarrachea-Magnani, P. Massignan, and G. Bruun, preprint (2023), arXiv:2305.04915 [cond-mat.quant-gas] .

[370] L. B. Tan, O. Cotlet, A. Bergschneider, R. Schmidt, P. Back, Y. Shimazaki, M. Kroner, and A. Imamoğlu, Phys. Rev. X **10**, 021011 (2020).

[371] J. B. Muir, J. Levinsen, S. K. Earl, M. A. Conway, J. H. Cole, M. Wurdack, R. Mishra, D. J. Ing, E. Estrecho, Y. Lu, D. K. Efimkin, J. O. Tollerud, E. A. Ostrovskaya, M. M. Parish, and J. A. Davis, Nat. Commun. **13**, 6164 (2022).

[372] M. Will, G. E. Astrakharchik, and M. Fleischhauer, Phys. Rev. Lett. **127**, 103401 (2021).

[373] A. Petković and Z. Ristivojevic, Phys. Rev. A **105**, L021303 (2022).

[374] J. Jager and R. Barnett, New J. Phys. **24**, 103032 (2022).

[375] N. T. Zinner, EPL **101**, 60009 (2013).

[376] M. Drescher, M. Salmhofer, and T. Enss, Phys. Rev. A **107**, 063301 (2023).

[377] S. McArdle, S. Endo, A. Aspuru-Guzik, S. C. Benjamin, and X. Yuan, Rev. Mod. Phys. **92**, 015003 (2020).

[378] I. Kassal, S. P. Jordan, P. J. Love, M. Mohseni, and A. Aspuru-Guzik, PNAS **105**, 18681 (2008).

[379] X. Xing, A. Gomez Cadavid, A. F. Izmaylov, and T. V. Tscherbul, J. Phys. Chem. Lett. **14**, 6224 (2023).

[380] R. Cleve, A. Ekert, C. Macchiavello, and M. Mosca, Proc. R. Soc. A: Math. Phys. Eng. Sci. **454**, 339 (1998).